Quaternary structural evolution and seismic hazards of the onshore Ventura basin, southern California, USA

Alex Hughes

Department of Earth Science & Engineering

Imperial College London

Submitted in fulfilment of the requirements for the award of the degree of

Doctor of Philosophy

10th June 2019

Declaration of Originality

I declare that this thesis is the result of my own work during my PhD and I have indicated work contributed by third parties in the relevant section of the text, for which I have provided full references. In addition, the work presented in this thesis has not been submitted for a degree in Imperial College London previously, or in any other institution.

Alex Hughes

10th June 2019

Copywrite Declaration

Abstract

Fault interactions cause variations in patterns of deformation and stress distribution, which control the location and magnitude of earthquakes and can also have a significant impact on the evolution of the landscape. Consequently, a better understanding of how patterns of deformation vary in time and space and the timescales over which fault interactions occur is of critical importance to a sizeable amount of the global population who live within earthquake-prone regions. Devastating earthquakes can occur on well-studied faults, or faults that are either blind or unknown prior to an earthquake. Furthermore, there are several recent examples where large-magnitude earthquakes are attributed to synchronous ruptures of multiple faults with complex subsurface geometry and kinematics. For example, the 2016 M_w 7.8 Kaikoura earthquake is thought to have ruptured up to twelve major faults, at least two of which were unknown before the event occurred. The observation that such complex earthquake ruptures can occur brings into focus the need to use geologic and geomorphic field data to accurately characterize parameters such as subsurface fault geometry and fault slip rates. Additional information on tectonic activity and patterns of deformation can also be acquired from a quantitative analysis of landscape morphology. However, even in well-studied areas such as southern California, fundamental data such as fault slip rates or subsurface fault geometry are often poorly understood, which undermines a complete analysis of seismic hazards.

This thesis integrates a multi-disciplinary approach incorporating geomorphic mapping, multiple cosmogenic isotope techniques to establish dates and rates of Earth surface processes, landscape topographic analysis, structural geology, and static Coulomb stress modelling. I investigate the degree to which patterns of deformation over multiple earthquakes cycles are variable in time and space and examine how potential variability in deformation controls the morphology of the landscape and impacts our interpretation of seismic hazards. I focus on the Ventura basin, southern California, USA, which is an ideal location to address such questions because despite an abundance of active reverse and thrust faults in proximity to major population centres, the subsurface geometry and slip rates for several key faults are not well quantified and there are few data on how the numerous active faults have shaped the evolution of the landscape.

First, I investigate evidence for a proposed blind fault in the Ventura basin, the Southern San Cayetano fault (SSCF), and the potential role of the SSCF in stress transfer between the Ventura fault and the San Cayetano fault in potential large-magnitude (M_w 7.5–8.0) multi-fault earthquakes. I examine late Quaternary alluvial fans and river terraces using field mapping, high-resolution lidar topographic data, ^{10}Be surface exposure dating, and subsurface well data to provide evidence for a young, active SSCF. I calculate a Holocene reverse slip rate of $1.3\ ^{+0.5}/_{-0.3}$ mm yr^{-1} and suggest that displacement rates for the SSCF have not varied significantly since the onset of activity on the SSCF around ~58 ka. I hypothesize that the SSCF could potentially act as a rupture pathway between the Ventura and San Cayetano faults in large-magnitude, multi-fault earthquakes in southern California.

In the second part of the thesis, I examine the subsurface geometry of the SSCF and the potential structural connectivity and stress interactions between the SSCF and neighbouring faults. I present a series of structural cross sections along strike of the SSCF and a 3D fault model for the SSCF. These results provide evidence for a low-angle SSCF that dips ~15° north and connects with the western San Cayetano fault (WSCF) around 1.5–3.5 km depth. I incorporate the 3D fault model for the SSCF in static Coulomb stress modelling and find that triggered seismicity may occur on the SSCF and the WSCF because of ruptures on the eastern section of the San Cayetano fault. However, my results indicate that the role of static Coulomb stress transfer in the potential occurrence of multi-fault earthquakes in the Ventura basin is critically dependent on fault model adopted for the deep structure of faults. The results demonstrate that an accurate characterization of three-dimensional subsurface fault geometry is important for reducing uncertainties when assessing future patterns of regional seismicity and highlight the importance of integrating field observations, surface data, and subsurface data to create realistic fault inputs when modelling static Coulomb stress transfer.

In the last section of the thesis, I investigate how fault evolution has controlled patterns of topographic relief development, channel morphology, and erosion in the Ventura basin. I employ cosmogenic isotope isochron burial dating of an important, yet poorly dated, Quaternary strain marker, the Saugus Formation, to reduce uncertainties in the assessment of rates of tectonic processes. My results confirm that the Saugus Formation increases in age from west to east along the axis of the Ventura basin with

ages for the top of the exposed Saugus Formation of 0.38 $^{+.017}/_{-0.23}$ Ma at Ventura and 2.49 $^{+0.25}/_{-0.29}$ Ma in the eastern Ventura basin. The burial ages for the base of shallow marine sands, which underlie the Saugus Formation throughout the basin are 0.55 $^{+0.80}/_{-0.10}$ Ma at Ventura and 3.30 $^{+0.30}/_{-0.42}$ Ma in the eastern Ventura basin. Burial ages for the Saugus Formation in conjunction with published fault offsets suggest long-term slip rates of 7.1 +/- 1.0 mm yr^{-1} for the San Cayetano fault since ~1.54 Ma. In addition, I calculate ^{10}Be-derived catchment-averaged erosion rates and compare erosion rates with fault displacement rates and the results of a morphometric landscape analysis. The comparison indicates a transient landscape response to tectonic forcing in the Ventura basin, where the erosion signal in fault hanging walls is not yet fully adjusted to various tectonic perturbations over the last ~1.5 Ma. These data demonstrate that on the local scale with uniform climate, such as the hanging wall of the San Cayetano, Ventura, and Southern San Cayetano faults, tectonic perturbations are the main drivers in patterns of topographic relief developments and highest stream gradients for periods up to 10^6 years.

Overall, my results demonstrate that patterns of deformation can demonstrate significant spatial variability on timescales between 10^3 to 10^6 years. I find that fault interactions and the migration of deformation exert significant control on rates of fault activity and landscape morphology, and that patterns of deformation must be accurately modelled for a robust analysis of seismic hazards.

Acknowledgements

I would like to thank my supervisors Dylan Rood, Rebecca Bell, and Alex Whittaker for helping develop my skills as a researcher and sharing with me their broad knowledge and understanding across range of research fields, but more importantly, for having the patience to put up with me over the last three and a half years! I would also like to thank my various collaborators Tom Rockwell, Yuval Levy, Klaus Wilcken, Lee Corbett, Paul Bierman, Duane DeVecchio, Scott Marshall, Larry Gurrola, Craig Nicholson, and Zoe Mildon for thoughtful discussions, contributions, and feedback on various parts of this thesis. Thanks also to Ruth Davey and Charlie Singer for helping me out with field work and sample collection, and special mention to Alex Seal for his contribution in the field in challenging circumstances during the ongoing Thomas fire in December 2017 and his subsequent advice in the laboratory during processing of the erosion rate samples.

Lastly, thanks to my parents who have always been there for me and have supported me throughout this PhD and provided me with a place to stay during these last few months writing up.

Table of Contents

List of Figures

List of Tables

Chapter 1: Introduction

1.1 Overview

An understanding of how the evolution and interaction of faults affects the location and magnitude of earthquakes is of critical importance to a sizeable amount of the global population who live within tectonically active regions. Total displacement on a fault is the sum of coseismic slip along its length, consequently, an accurate assessment of earthquake hazard requires a deep understanding of the processes that govern the spatiotemporal distribution of coseismic slip during earthquakes. The basic model for long-term fault behaviour states that over-time fault segments slowly accumulate elastic strain and when this accumulated strain reaches a threshold level greater than the rocks can sustain, rupture occurs and results in sudden relaxation of elastic stress during an earthquake (Reid, 1910; Scholz, 1990). Such stick-slip behaviour leads to certain simplified models of the earthquake cycle, which imply a degree of predictability to fault activity and resulting earthquakes (Shimazaki and Nakata, 1980). However, recent studies that investigate how fault activity is linked to earthquake hazards demonstrate that simple stick-slip earthquake behaviour and the implied predictability of fault behaviour is an oversimplification (Peltzer et al., 2001; Friedrich et al., 2003; Ganev et al., 2010; e.g., Dolan et al., 2016). The fundamental question that then arises is: **To what degree are patterns of deformation over multiple earthquake cycles variable in time and space and how do any potential variations impact our interpretation of seismic hazards?**

The end goal of seismic hazard assessment is to evaluate the potential for future earthquake effects, e.g., ground motion, for a specific site or area and in a given time period. Two key inputs are required to achieve this end goal: 1) an earthquake source model, and 2) an attenuation model for seismic waves affecting the site. The latter is an engineering parameter that has been characterized by other studies and will not be considered here (e.g. Anderson and Brune, 1999). Instead, this project will focus on quantitatively characterizing source models using geologic and geomorphic data. The Working Group on California Earthquake Probabilities have undertaken a comprehensive assessment of seismic hazards in California in the form of the Uniform California Earthquake Rupture Forecast, version 3 (UCERF3)

(Field et al., 2014; Field et al., 2015; Field et al., 2017). The framework for UCERF3 consists of 4 model components: a fault model (i.e., fault geometry), a deformation model (i.e., fault slip rate), an earthquake-rate model (i.e., earthquake frequency), and a probability model (Field et al., 2014). However, whilst the UCERF report is a comprehensive attempt to forecast fault activity in California, the models are limited by the availability of accurate data to input into the models. For example, there are a total of ~350 fault segments in the UCERF3 fault model, however, only 150 of these faults have well constrained slip rate data (Field et al., 2014). This study will focus on reducing uncertainties in the two most basic inputs in to the UCERF model, the fault models and the displacement models. To calculate these inputs, detailed studies of faults are required to characterize the fault surface trace, subsurface fault geometry, and fault slip rate.

I will focus on calculating slip rates on timescales of 10^3–10^5 years using offset geomorphic landforms and 10^5–10^6 years using offset geological bedrock surfaces. These data can be compared with contemporary slip rates based on GPS data or inferred from erosion rates to obtain a complete dataset over multiple earthquake cycles. In addition to applications in seismic hazard assessment, a high-resolution record of fault slip rates can also provide insights into how variations in stress and strain affect fault growth and interaction (Cowie, 1998; Gawthorpe and Leeder, 2000; Cowie and Roberts, 2001; Duffy et al., 2015) and to investigate the relationship between active faults and evolving landscapes (Wobus et al., 2006a; Whittaker et al., 2008; Whittaker and Walker, 2015).

Two inputs are required to calculate a fault slip rate: an offset feature and an age for that feature. Topographic or structural cross sections across geomorphic or geological features offset by active faults have long been analysed to extract data on fault displacement (Yeats, 1988; Huftile and Yeats, 1995; Frankel et al., 2007b; Amos et al., 2010). However, the ability to accurately quantify rates of fault activity are often hindered because of a lack of precise dates for key strain markers. For example, prior to the development of isochron burial dating techniques, the calculation of early Pleistocene or Pliocene fault displacement rates was often problematic because no reliable method was available to directly date certain strain markers, such as terrestrial sediments (Balco and Rovey, 2008; Balco et al., 2013). Recent advances in cosmogenic dating techniques (Balco and Rovey, 2008; Erlanger et al., 2012;

Granger et al., 2013), in combination with improvements to accelerator mass spectrometry (Rood et al., 2010; Wilcken et al., 2017), have provided geologists with an opportunity to produce high-resolution geochronology and to quantify variations in fault activity at high temporal resolutions (Rood et al., 2011b; Çiner et al., 2015; Bender et al., 2016). Such high-resolution temporal records of fault activity can be used as the basis to answer questions about how fault interactions affect variable rates of strain accumulation over multiple earthquake cycles and the implications for seismic hazards.

Cosmogenic isotopes can also be applied to quantify rates of erosion and incision (Bierman and Steig, 1996; Regalla et al., 2013; Portenga et al., 2015; Mudd et al., 2016), which can be compared to fault slip rates and provide insights into the landscape's response to growing fault networks (Stock et al., 2009; Cyr et al., 2010; Roda-Boluda et al., 2019). Catchment-averaged erosion rates are often analysed in tandem with morphological parameters of the landscape, such as relief (Densmore et al., 2009) and/or channel steepness (Cyr et al., 2010; DiBiase et al., 2010). Studies have shown that relief generation in active orogens may be driven by rock uplift, but lithology can also play a significant role in controlling maximum relief (Lavé and Avouac, 2001; Densmore et al., 2004; Finnegan et al., 2008; Whittaker and Walker, 2015). For landscapes in dynamic topographic equilibrium, channel steepness indices should also demonstrate a systematic correlation with patterns of rock uplift rates (Snyder et al., 2000; Kirby and Whipple, 2001; Cyr et al., 2010; D'Arcy and Whittaker, 2014).

In contrast, for relatively young (i.e. Neogene to Quaternary) orogens the landscape morphology and rates of erosion and incision may still be adjusting to new boundary conditions imposed by changing tectonic forcing (Tucker, 2009). Analysing these transient landscape responses is sometimes problematic because systematic correlations between different landscape parameters, such as rock uplift rates and erosion rates, can be more challenging to interpret (Wobus et al., 2006b; Stock et al., 2009; Whittaker, 2012; Roda-Boluda et al., 2019). Consequently, **understanding to what extent morphometric landscape parameters and erosion rates, in addition to other factors such as lithology, are suitable for extracting tectonic signals from the landscape is one of the most pertinent questions in tectonic geomorphology today.** The ability to extract a tectonic signal from the landscape is important, because such data can be used in combination with slip rate data to analyse

how variations in strain accumulation and stress distribution affect fault growth or seismic hazards over multiple seismic cycles.

Data from fault slip rates can provide a first order approximation of patterns in stress distribution and strain accumulation (Friedrich et al., 2003; Oskin et al., 2008; Marshall et al., 2013). Alternatively, stress distributions can be modelled directly to compare with spatial patterns in fault slip rates and assess an individual fault's contribution to regional strain accumulation in space and time. Static Coulomb stress modelling has been applied to model seismic hazards, with studies indicating that aftershocks or potential future earthquakes are more likely to occur on faults that are located in areas of positive Coulomb stress change (King et al., 1994; Harris, 1998; Freed, 2005). Coulomb stress change has also been demonstrated to exhibit a control on the growth and interaction of faults where fault linkage is thought to occur in areas of positive Coulomb stress change (Cowie, 1998; Gupta et al., 1998). Recent work indicates that changes in along-strike fault geometry can play a key role in modelled stress distributions (Mildon et al., 2016; Mildon et al., 2017). However, fundamental **questions remain about how non-planar fault geometry, particularly changes in fault geometry down-dip, affect models of static Coulomb stress transfer.**

Fault geometry also plays a key role in dynamic rupture propagation in potential large-magnitude (~M_w 7.5–8.0) multi-fault earthquakes. For example, a high degree of subsurface structural connectivity provided a dynamic rupture pathway between several faults during the 2008 M_w 7.9 Wenchuan earthquake in China (Xu et al., 2009; Densmore et al., 2010; Hubbard et al., 2010). Furthermore, previously unidentified faults are thought to have played a significant role in transferring stress during the 2017 M_w 7.8 Kaikōura earthquake including the Papatea fault (Hamling et al., 2017; Hollingsworth et al., 2017) and the Point Kean fault, which acted as a subsurface link between the Hundalee fault and faults to the north (Clark et al., 2017). Confirming potential structural connectivity of faults in the subsurface is, therefore, an important undertaking in areas such as the Ventura basin, southern California, USA, where large-magnitude earthquakes are not documented in the historical record, but are thought to be possible due to a proposed high degree of subsurface fault connectivity (Hubbard et al., 2014; Rockwell et al., 2016).

This project aims to tackle the broad research questions posed above. The primary aim of this project is to investigate the late Cenozoic evolution of the several important reverse and thrust faults within the onshore Ventura basin, California, USA and the implications of fault evolution for interpretations of contemporary seismic hazards. Despite an abundance of active reverse faults within a densely populated area, seismic hazards within the Ventura basin are not fully understood. The lack of understanding stems from limited and highly variable slip rate measurements for several key faults including the Ventura, Oak Ridge, Southern San Cayetano, and San Cayetano faults (e.g. Rockwell, 1988; Yeats, 1988; Hubbard et al., 2014). This variability in slip rates is partly a product of poorly-quantified age estimates for key strain markers. Furthermore, there is ongoing debate around the subsurface geometry and potential structural connectivity of faults within the Ventura basin that has important implications for the potential for large-magnitude multi-fault earthquakes (Hubbard et al., 2014; Nicholson et al., 2017b).

This project integrates a multi-disciplinary approach encompassing various cosmogenic isotope techniques, structural analysis, landscape analysis, and static Coulomb stress modelling to improve the spatial and temporal record of fault activity and characterize the subsurface geometry of faults within the onshore Ventura basin. I use high-resolution lidar data and cosmogenic ^{10}Be exposure dating to provide evidence for a recently identified thrust fault, the Southern San Cayetano fault (SSCF), and to calculate fault slip rates for the SSCF over multiple timescales (Chapter 2). The SSCF is suggested to have played role in transferring stress between the Ventura fault and the San Cayetano fault in large-magnitude (M_w 7.5–8.0) earthquakes in the Ventura basin (Hubbard et al., 2014). In chapter 3, I use evidence from subsurface well-log data to characterize the three-dimensional subsurface geometry of the SSCF and examine the subsurface structural connection of the SSCF with the San Cayetano fault and the Ventura fault. I use static Coulomb stress modelling incorporating non-planar reverse and thrust fault geometry to examine the potential stress distribution in the Ventura basin and to explore the possible role of static stress triggering in proposed multi-fault earthquakes (Chapter 3).

In chapter 4, I use isochron burial dating and exposure dating to re-evaluate existing fault slip rates for the Oak Ridge, San Cayetano, and Ventura faults on 10^5–10^6 year timescales. I compare fault slip rates

with ^{10}Be derived catchment-averaged erosion rates and the results of a morphometric landscape analysis and quantative analysis of knickpoints in stream profiles to examine the Quaternary evolution of the Ventura basin landscape. The results are synthesized in chapter 5 to examine how fault interactions have influenced patterns of deformation in time and space throughout the Quaternary and the implications for seismic hazard analysis.

1.2 Aims and objectives

The main goal of this project is to investigate spatial and temporal variations in strain accumulation between several key faults within the onshore Ventura basin and the implications that fault interactions have for seismic hazard assessment and landscape evolution. These aims are addressed in three individual research chapters of this thesis, which are outlined in section 1.3 below.

Aim 1: How do previously unrecognized faults impact regional seismic hazard assessment, and can small faults play significant roles in large-magnitude earthquake ruptures (Chapter 2)?

Aim 2: To what extent does fault connectivity and fault geometry affect spatial and temporal patterns of stress distribution and strain accumulation (Chapter 3)?

Aim 3: To what extent are variations in fault slip rates reflected in the landscape (Chapters 2 and 4) and which topographic metrics are most suitable to extract tectonic signals from the landscape (Chapter 4)?

Aim 1 requires identification of evidence for the SSCF and any other unrecognizesed faults in the Ventura basin and quantification of their slip rates, which can be used for comparison with slip rates of neighbouring faults and assessment of the potential for large-magnitude multi-fault earthquakes. The objectives to meet Aim 1 are addressed in Chapter 2 and are as follows:

1.1) Create geomorphic maps of alluvial fans and river terraces in the proximity of the proposed SSCF and San Cayetano fault. These maps will be used as the basis to identify and analyse geomorphic landforms offset by surface rupture on the SSCF and characterize the fault surface trace.

1.2) Employ cosmogenic ^{10}Be surface exposure dating to a time-series of landforms offset by activity on the SSCF to create a late Quaternary geochronology for alluvial fans and terraces in the study area.

1.3) Calculate a suite of late Quaternary fault slip rates for the SSCF based on quantative analysis of offset geomorphic landforms and ^{10}Be geochronology.

1.4) Compare slip rates with published rates for neighbouring faults and data from geodesy to explore the prospects for large-magnitude earthquakes.

Aim 2 necessitates characterization of the 3D geometry and the subsurface connectivity and stress interactions between faults in the Ventura basin. Aim 2 will be addressed in Chapter 3 via the following objectives:

2.1) Examine subsurface data for evidence for the SSCF to produce a series of cross sections and a 3D model to characterize the subsurface geometry for the SSCF and potential structural connectivity of the SSCF with surrounding faults.

2.2) Integrate surface data with subsurface data to investigate the distribution of strain and potential pathways for dynamic rupture propagation.

2.3) Employ the new 3D geometry for the SSCF in static Coulomb stress modelling using complex non-planar fault geometry to investigate spatial and temporal variations in static stress in the Ventura basin and provide further insights into seismic hazards and fault evolution.

Aim 3 requires quantification of rates of tectonic rock uplift throughout the study area and how these rates vary in space and time. It also demands extraction of various key morphometric paraments from the landscape, such as erosion rate, relief, and channel steepness. The following objectives associated with Aim 3 will be addressed in Chapter 4:

3.1) Characterize the age of the Saugus Formation across the Ventura basin using cosmogenic isotope isochron burial dating to use as a strain marker to calculate fault slip rates on various key faults throughout the late Quaternary.

3.2) Calculate ^{10}Be derived catchment-averaged erosion rates in the hanging wall of key faults to compare to fault slip rates and assess the balance between tectonic rock uplift and erosion in the study area.

3.3) Extract morphometric stream parameters, such as relief and channel steepness, from digital elevation models to compare with fault slip rates and erosion rates.

3.4) Extract river long-profiles from streams in the study area to identify knickpoints and compare knickpoint positions in the catchments to relief, channel steepness, and fault slip rates to examine how changing tectonic forcing has influenced Quaternary landscape evolution in the Ventura basin.

1.3 Thesis structure

This thesis comprises six chapters in total: an introduction chapter, three research chapters, a discussion chapter, and a conclusion. Each of the three research chapters are written in the style of a manuscript for publication (Chapters 2, 3, and 4). The three research chapters are synthesized in the discussion in Chapter 5 where I attempt to address some of the broad research questions outlined in section 1.4 and 1.5 below. The techniques and methods appropriate for the work in each chapter are included in the relevant chapters together with a review of literature pertinent to each chapter. Furthermore, because the research chapters are written in the style of an individual manuscript there may be some repetition between chapters.

Chapter 2 focuses on identification of surface evidence for the proposed SSCF and the implications of the apparent surface connectivity of faults for the prospects of multi-fault ruptures in the Ventura basin (Aim 1). I use high-resolution lidar data to map out late Quaternary river terraces and alluvial fans offset by activity on the SSCF (objective 1.1) and apply cosmogenic isotope surface exposure dating using depth profiles to generate a geochronology for alluvial surfaces in the study area (objective 1.2). By combining topographic profiles extracted from the lidar data with the geochronology, I calculate a high-resolution late Quaternary record of fault slip rates for the SSCF (objective 1.3). The resulting slip rates are compared with published slip rates for the Ventura fault and the San Cayetano fault, in combination with data from geodesy, to examine the potential for large-magnitude multi-fault earthquakes in the Ventura basin (objective 1.3). This work is now published: **Hughes, A**., Rood, D.H., Whittaker, A.C., Bell, R.E., Rockwell, T.K., Levy, Y., Wilcken, K.M., Corbett, L.B., Bierman, P.R., DeVecchio, D.E., Marshall, S.T., Gurrola, L.D. and Nicholson, C., 2018. *Geomorphic evidence for the geometry and slip*

rate of a young, low-angle thrust fault: Implications for hazard assessment and fault interaction in complex tectonic environments. Earth and Planetary Science Letters, 504: 198-210 https://doi.org/10.1016/j.epsl.2018.10.003.

Chapter 3 comprises a detailed analysis of onshore petroleum well-log data, which is used as the basis to draft four cross sections and a 3D model to characterize the subsurface geometry of the SSCF and examine the potential subsurface connectivity of the SSCF with neighbouring faults (objective 2.1). Well data are analysed in tandem with the surface data described in Chapter 2 to examine the potential distribution of strain and ruptures pathways between the SSCF and the San Cayetano fault during the Holocene (objective 2.2). Furthermore, subsurface data, microseismicity, and fault slip rates are examined to investigate the evidence for a potential blind fault at depth in the footwall of the San Cayetano fault, which may act as a potential rupture pathway for large-magnitude earthquakes in the Ventura basin (Aim 1 & Aim 2). The 3D model for the SSCF is combined with existing fault models for neighbouring faults and used in static Coulomb stress modelling employing complex non-planar reverse fault geometry (objective 2.3). The stress modelling is used to investigate spatial and temporal patterns in stress distribution within the Ventura basin, the potential for triggered seismicity on the SSCF from surrounding faults, and the role that fault geometry plays in controlling stress distribution and seismic hazards (Aim 2).

Chapter 4 focuses on quantifying changing rates of tectonic uplift and erosion on multiple timescales and the effect that changes in the rates of these competing forces have had on the landscape evolution of the Ventura basin (Aim 3). I use cosmogenic isotope isochron burial dating of the Saugus Formation in combination with published offsets for the San Cayetano, Oak Ridge, and Ventura faults to calculate fault slip rates over various time periods (objective 3.1). I then calculate ^{10}Be catchment-averaged erosion rates for catchments along strike in the hanging walls of the Ventura fault, the San Cayetano fault, and the SSCF (Objective 3.2). Data on hanging wall relief and channel steepness are extracted from a 30 m digital elevation model to compare with fault slip and uplift rates and catchment-averaged erosion rates in fault hanging walls (objective 3.3). Tectonic knickpoints are observed in river long profiles extracted from streams in the hanging wall of the San Cayetano fault (objective 3.4) and a

synthesis of fault uplift, throw, and slip rates, erosion rates, landscape analysis, and knickpoints is used to examine a transient response of the Ventura basin landscape to tectonic forcing through the Quaternary.

Chapter 5 combines the findings of the three research chapters to assess how the work contributes to wider research into rates of variability in strain accommodation and what the combined results imply for seismic hazard in the Ventura basin, and specifically the likelihood of large-magnitude multi-fault ruptures. The general findings are summarized in the conclusion in Chapter 6.

Due to the collaborative nature of science, and to acknowledge the assorted contributions from my supervisors, co-authors and collaborators for this work, I have chosen to use the pronoun ‘we’ instead of ‘I’ in the research chapters. The specific role that each person has contributed to the work is highlighted at the start of each chapter.

1.4 Research Background

1.4.1 Fault slip rates

A first-order observation from observed historical earthquakes and empirical modelling studies is that larger faults produce larger earthquakes (Wells and Coppersmith, 1994; Leonard, 2010; Leonard, 2014; Biasi and Wesnousky, 2017). The traditional model for fault growth and interaction states that as faults grow by segment linkage and fault tip propagation, fault length and the amount of displacement on the fault increase sympathetically in order to maintain the displacement-length scaling relationship (e.g., Cartwright et al., 1995; Dawers and Anders, 1995; Gupta et al., 1998; Gawthorpe and Leeder, 2000; Cowie and Roberts, 2001; Meyer et al., 2002). However, recent work has suggested an alternative model where individual fault segments establish their final length rapidly and fault slip gradually increases with minimal subsequent lateral propagation until an appropriate displacement-length relationship for the fault is achieved (Jackson and Rotevatn, 2013; Jackson et al., 2017; Nicol et al., 2017). Regardless of the exact model, the implication is that slip rates will vary in space and time, including potentially along parts of the fault where linkage has occurred, to compensate for a potential strain deficit in the area of deformation (Dawers and Anders, 1995; Whittaker and Walker, 2015).

Several methods of data collection exist for examining fault slip rates over various timescales. For example, contemporary rates of fault activity on decadal timescales can be resolved from mechanical models based on geodetic measurements (Donnellan et al., 1993b; Marshall et al., 2013; Marshall et al., 2017) and historical or prehistoric rates of fault activity over periods of 10^2–10^4 years can be resolved from paleoseismic studies (Rockwell et al., 2000; Dolan and Rockwell, 2001; Klinger et al., 2015). Fault displacement rates over timescales of 10^4–10^5 years can be resolved from offset geomorphic landforms (Amos et al., 2010; Rood et al., 2011b; Hughes et al., 2018) and for periods of 10^5–10^7 years geologic bedrock offsets are used to calculate fault displacement rates (Yeats, 1988; Çemen, 1989; Huftile and Yeats, 1996).

A common approach to assess regional strain accumulation through time is to compare the overall contemporary regional strain measured from geodesy to the sum of fault displacement rates measured

from geomorphology or geology (Donnellan et al., 1993a; Oskin et al., 2008; Cowgill et al., 2009; Marshall et al., 2013; Dolan et al., 2016). However, discrepancies often exist between slip rates derived from geodesy and slip rates derived from paleoseismic, geomorphic or geological methods (e.g. Donnellan et al., 1993a; Collier et al., 1998; Oskin et al., 2008; Bell et al., 2011). For example, in the Gulf of Corinth, Greece, extension rates measured in geodetic studies are interpreted to increase from east to west across the gulf (Clarke et al., 1998; Floyd et al., 2010), but this is not consistent with geological estimates of shortening that predict greatest long-term strain accumulation in the centre of the rift (Bell et al., 2011). This discrepancy has been attributed to strain migration resulting from fault growth and interaction (Bell et al., 2011)

It is important, therefore, to consider ambiguity that may arise when directly comparing results for a single fault obtained via different methods and averaged over different timescales relative to the repeat times. While some studies appear to demonstrate a first-order correlation between short-term geodetic and long-term geological slip rates (Collier et al., 1998; Cowgill et al., 2009; Marshall et al., 2013), uncertainties contained within the geological slip rates are often far too large for any comparison to be meaningful. Two key factors that lead to uncertainties within slip rates are unreliable or imprecise dates for key strain markers or uncertainties in the geological or geomorphic model used to calculate offsets (Zechar and Frankel, 2009; Behr et al., 2010). A good example is the Mission Creek strand of the San Andreas fault. Initial estimates of the fault slip rate from geological offsets suggested a slip rate of 15.9 +/- 3.4 mm yr^{-1}, which was much less than the amount of strike-slip indicated from geodetic data of between 23–26 mm yr^{-1} (Meade and Hager, 2005; Van Der Woerd et al., 2006). However, re-examination of the ^{10}Be geochronology and surface offset used to calculate the geological slip rate suggest that a proposed discrepancy of nearly 10 mm yr^{-1} between geologic slip rates and strike-slip across the fault measured from geodesy may not be real and could simply be a product of large uncertainties contained in a geological slip rate of between 12–22 mm yr^{-1} (Behr et al., 2010).

Within the study area, the San Cayetano fault is a similar example. The San Cayetano fault has a minimum slip rate estimate of 1.05 $^{+}$/- 0.2 mm yr^{-1} since 15–20 ka measured from offset of geomorphic surfaces dated using radiocarbon and soil profile development (Rockwell, 1988) and this rate is an order

of magnitude smaller than the maximum slip rate estimate of $11.4\ ^{+1.7}/_{-1.8}$ mm yr^{-1} since 975 ka measured from bedrock offsets (Huftile and Yeats, 1996). The short-term rate and the long-term rate were calculated at different locations along strike of the fault, therefore, the differences in rates could reflect spatial and temporal variations in activity on the San Cayetano fault, but the difference in rate could also be product of invalid assumptions or uncertainties contained in the age correlation for the strain marker used to calculate the long-term slip rate (Huftile and Yeats, 1996). At progressively smaller temporal and spatial scales data are lacking to assess whether the apparent discrepancy between the relatively fast long-term rate and the much slower short-term rate for the San Cayetano fault is reasonable. In this study, I will attempt to address this issue for the San Cayetano fault by re-examining existing fault slip rates and estimating new rates.

There are several other factors that can cause slip rates to vary in both space and time. Data on the periodicity of earthquake cycles are often obtained from paleoseismic studies, which demonstrate that earthquakes often occur in clusters (McGill and Rockwell, 1998; Rockwell et al., 2000; Klinger et al., 2015). Globally, inter-cluster timescales have been demonstrated to range from 10^3 to 10^4 years and inter-seismic periods within clusters are thought to range from 10^2 to 10^3 years (Wallace, 1987; Sieh et al., 1989; Rockwell et al., 2000; Klinger et al., 2015; Dolan et al., 2016). If earthquakes occur in clusters, then the signal from multiple earthquakes within a cluster may differ from a slip rate that is calculated from geomorphic surfaces or geological bedrock offsets over multiple earthquake cycles. Therefore, earthquake clusters can add an additional layer of complexity to seismic hazard assessment because they imply that fault slip rates will have significant temporal variability across a range of timescales from 10^3–10^6 years (Friedrich et al., 2003; Dolan et al., 2016). The potential occurrence of earthquakes in clusters necessitates an in-depth history of coseismic slip for a fault at various timescales to understand how fault evolution and interaction affect the location and magnitude of earthquakes.

Numerous other factors can give rise to apparent spatial and temporal variations in fault slip rates or misrepresentations of seismic hazard. For example, slip rate studies using offset geomorphic surfaces suggest high Pleistocene and Holocene slip rates for the Garlock fault in California, which range from 5–14 mm yr^{-1} (McGill et al., 2009; Ganev et al., 2012; Dolan et al., 2016). In contrast, geodetic studies

indicate that very little left-lateral contemporary strain is being accommodated on the Garlock fault (Meade and Hager, 2005; Loveless and Meade, 2011). This discrepancy has been attributed to the geodetic data being sampled at the beginning of a period of seismic quiescence after a cluster of earthquakes (Peltzer et al., 2001). Earthquakes in an elastic upper crust cause gradual relaxation of the underlying viscoelastic asthenosphere (Pollitz, 1992). Depending on the degree of coupling between the upper crust and the asthenosphere, viscoelastic relaxation has been linked to variations in transient deformation and strain accommodation following an earthquake and, accordingly, variations in fault slip rates (Dixon et al., 2003; Pollitz et al., 2003)

Significant strain can also be accommodated by ductile deformation such as folding (Suppe, 1983; Shaw and Suppe, 1994; Yue et al., 2005). Seismic data is a key tool for characterizing subsurface fault geometry and, therefore, for calculating fault slip rates (e.g., Bell et al., 2014). However, strain can be underestimated due to the presence of unmapped or blind faults (Shaw and Suppe, 1996; Dolan et al., 2003; Lu et al., 2016) and this is a particular problem in seismic data if the offset on the faults is smaller than the resolution of the data (Pei et al., 2018). Strain accommodation via folding or unmapped faults would not be observed in the signal of coseismic strain release obtained from fault slip but would be represented in regional geodetic studies. Moreover, the effects of unmapped or blind faults have particular significance for seismic hazard analysis. The 1994, M_w 6.7 Northridge earthquake in California serves as a poignant reminder that devastating earthquakes can occur on previously unrecognized blind faults in well-studied areas such as southern California (Yeats and Huftile, 1995; Tsutsumi and Yeats, 1999; Baldwin et al., 2000). Therefore, **identification and characterization of blind faults is of critical importance to a complete and accurate assessment of seismic hazard**.

The key points to consider when combining datasets covering different time scales in seismic hazard assessment is that slip rates will vary spatially and temporally. When considering whether a slip rate is appropriate for seismic hazard assessment, it is important to consider where along the faults length the slip rate is taken from and what specific process is recorded by the slip rate. **The crucial tool in accurate evaluation of the relationship between well-quantified short-term strain and less well-quantified long-term strain is the precise quantification of fault slip rates over various time scales.**

1.4.2 Stress distribution

A key assumption that underpins stick-slip earthquake models is that far-field strain accumulation is constant and equal to the total coseismic strain release. However, this assumption does not match the often-observed discrepancies between rates of fault activity and modelled strain accumulation derived from geodesy compared with rates derived from geological and/or geomorphic data (Donnellan et al., 1993a; Collier et al., 1998; Friedrich et al., 2003; Bell et al., 2011; Marshall et al., 2013). This mismatch implies that either far-field strain accumulation is non-uniform in time or the observed distribution of strain is affected by some other process such as stress diffusion in a viscoelastic weak zone in the lower crust (Hager et al., 1999; Kenner and Segall, 2000; Cowie et al., 2013). The prospect of non-uniform temporal strain accumulation is supported by the observation that earthquakes often occur in clusters (Wallace, 1987; Sieh et al., 1989; Rockwell et al., 2000; Klinger et al., 2015; Dolan et al., 2016).

Part of the reason that earthquakes occur in clusters is because earthquakes modify the surrounding stress field and influence the behaviour of neighbouring faults. An earthquake on one fault can either initiate or delay the occurrence of a subsequent earthquake on a neighbouring fault. One key component in determining the likelihood of a subsequent event occurring on a neighbouring fault is static Coulomb stress transfer (Harris and Simpson, 1992; King et al., 1994; e.g. Harris, 1998; Parsons et al., 1999; Toda et al., 2005). A large body of previous work has focused on modelling static stress changes resulting from an earthquake, or sequence of earthquakes, and identifying regions of positive stress change to explain the location and magnitude of subsequent earthquakes or aftershocks (e.g. Harris and Simpson, 1992; Stein et al., 1992; Stein et al., 1997; Lin and Stein, 2004; Pace et al., 2014; Mildon et al., 2017). Recent work has attempted to incorporate models of static Coulomb stress transfer into earthquake forecasting under the assumption that earthquakes are more likely to occur in areas of high Coulomb stress increase (Toda et al., 2005; Toda and Enescu, 2011; Woessner et al., 2011; Strader and Jackson, 2014; Strader and Jackson, 2015).

In addition to application in seismic hazard analysis and aftershock modelling, Coulomb stress change has also been applied to study the growth and interaction of faults (Cowie, 1998; Gupta et al., 1998; Wedmore et al., 2017). The rate at which fault segment linkage occurs is dependent upon a faults

proximity to other surrounding faults (Cowie, 1998). For earthquakes on all faults stress in regions around the fault tip is enhanced, whereas stress shadows are produced transverse to fault strike (King et al., 1994; Hodgkinson et al., 1996; Cowie, 1998). Consequently, the temporal evolution of fault slip for an individual fault depends on whether it undergoes a negative or positive stress feedback stemming from its position relative to surrounding faults. For example, Coulomb stress interactions between the Garlock fault and the San Andreas fault are suggested to be the cause for large temporal variations in slip recorded on the Garlock fault during the late Quaternary (McAuliffe et al., 2013; Dolan et al., 2016).

The observation that models of static Coulomb stress changes can be used to model seismic hazard and fault growth and interaction make Coulomb stress modelling an important tool to investigate how variable rates of strain accumulation and stress release affect fault interactions and seismic hazards. Models of static Coulomb stress change routinely employ overly simplistic planar fault geometry (Harris and Simpson, 1992; Lin and Stein, 2004; Pace et al., 2014). Studies of static Coulomb stress change consist of a source fault upon which the rupture is simulated and any number of receiver faults upon which changes in static stress are observed (King et al., 1994; Toda et al., 2005; Mildon et al., 2016). Recent studies have demonstrated that modelled static Coulomb stress change imparted on receiver faults is particularly sensitive to receiver fault strike (Mildon et al., 2016; Mildon et al., 2017). However, **so far studies investigating how non-planar fault geometry affects the distribution of static stress imparted on receiver faults have focused on normal faults and the application has not been rigorously tested on non-planar reverse faults**. Furthermore, while studies incorporating non-planar faults in static Coulomb stress modelling have concentrated on variations in strike, changes in fault dip with depth may also be significant (Mildon et al., 2016). **The effect of changes in fault dip with depth to models of static Coulomb stress transfer remains relatively unexplored.**

1.4.3 Landscape response to tectonics

Landscapes in tectonically-active regimes reflect a complex interplay between tectonics and climate, which both exert first-order controls on processes such as erosion, incision, and sedimentation. The ability to quantify rates and apply time constraints to erosional and depositional processes in active mountain belts is an essential tool to examine how the relative contribution of uplift and erosion control

landscape evolution through time (e.g. Clark et al., 2004; Finnegan et al., 2008; Wang et al., 2017). Recent developments in Quaternary dating techniques have provided geologists and geomorphologists with the tools to accurately quantify rates of rock uplift and erosion on various timescales between 10^2–10^7 years (Granger et al., 2013). Comparison of these rates with landscape analysis often forms the basis to examine spatial and temporal patterns in strain accumulation (Densmore et al., 2009; Whittaker and Walker, 2015), which can be used to model landscape evolution (e.g. Armitage et al., 2011) or seismic hazards (e.g. Kirby et al., 2008; Boulton and Whittaker, 2009).

Relief in active orogens can be driven by rock uplift so that areas of highest relief should correspond with area of highest uplift rates (Lavé and Avouac, 2001; Densmore et al., 2004; Finnegan et al., 2008; Whittaker and Walker, 2015). However, pre-existing topography can exert a significant control on current patterns of erosion and relief (Densmore et al., 2009) and, in steady state landscapes, topography can reach an erosionally controlled threshold elevation above which relief and becomes decoupled from rock uplift (Densmore et al., 2004; Densmore et al., 2007). Furthermore, because rivers play a key role in the erosion, transport, and deposition of sediment and erosion and deposition reflect the combined interplay between tectonics and climate, a wealth of information on the tectonic history of a landscape can be extracted from measurements of parameters such as stream morphology (Whipple and Tucker, 1999; Tucker and Whipple, 2002; Whipple, 2004; Wobus et al., 2006a; Whittaker et al., 2008; Kirby and Whipple, 2012).

Rivers respond to large scale changes in tectonic forcing on timescales of the order 10^5–10^6 years (Densmore et al., 1998; Whittaker et al., 2008; Armitage et al., 2011; Gudmundsdottir et al., 2013). Accordingly, on timescales of 10^6–10^7 years landscapes should reach a dynamic equilibrium where erosion and rock uplift rates become coupled (Ouimet et al., 2009; Cyr et al., 2010; DiBiase et al., 2010). Dynamic topographic equilibrium has been documented in parts of the Himalaya, where rock uplift has been occurring for the past 50 million years (Lavé and Avouac, 2001; Finnegan et al., 2008). For steady-state landscapes, morphometric stream parameters such as channel steepness indices should demonstrate systematic correlation with patterns of rock uplift rates (Snyder et al., 2000; Kirby and Whipple, 2001; Cyr et al., 2010; D'Arcy and Whittaker, 2014). In this case, stream parameters can either

be directly compared with rock uplift rates or used in place of measurements of rock uplift rates in areas where direct measurements of rock uplift rates are problematic to obtain (Kirby et al., 2003; Cyr et al., 2010; Miller et al., 2012).

In contrast, for orogens that have been active on timescales of 10^4–10^6 years erosion rates may be significantly less than rock uplift rates (Gudmundsdottir et al., 2013; Roda-Boluda et al., 2019) and comparing morphometric stream parameters with patterns of rock uplift rates becomes more challenging. The investigation of transient landscape responses to tectonic forcing is one of the most active areas of research in tectonic geomorphology today, and important outstanding questions include **over what timescales do landscapes respond to tectonic forcing and which topographic metrics are most suitable to record tectonic signals?**

Stream profiles can commonly be defined by a power law that relates channel gradient to upstream drainage area:

$$S = k_s A^{-\theta}$$

In the stream power law S is channel gradient (m/m), k_s is the steepness index which is a measure of both rock uplift rate and bedrock erodibility, A is upstream drainage area (m^2), and θ is the concavity index (m/n where m and n are constants) (Flint, 1974; Tucker and Whipple, 2002). Normalized steepness indices (k_{sn}) are commonly used in place of k_s to permit comparison of steepness indices between catchments and k_{sn} is calculated using a reference concavity index across a study area (Wobus et al., 2006a). In steady-state landscapes, river long profiles will be concave up (Tucker, 2009). However, a change in the rate of base level may result in a change in incision of the downstream section of the stream profile, causing a convex up section to develop as the channel system seeks a new equilibrium (Wobus et al., 2006a; Whittaker et al., 2008). The resulting upward convexity, or knickpoint, will separate an upstream reach with relatively low steepness index from a downstream reach with a relatively high steepness index (Whipple and Tucker, 1999; Whittaker et al., 2008; Kirby and Whipple, 2012). Low upstream steepness indices record the relict landscape that has yet to respond to the new erosional regime, whereas high downstream steepness indices record the erosional response

to the change in boundary conditions. Knickpoints can result as river channels adjust to new equilibrium conditions induced by either a change in tectonic rate (Whittaker et al., 2008; Boulton and Whittaker, 2009) or climate (Whipple, 2009), and over time knickpoints will propagate upstream through the landscape as an incisional wave (Whipple and Tucker, 1999; Niemann et al., 2001).

Field and modelling studies have identified various relationships that link the position of the knickpoint in the landscape to parameters such as rock uplift rate or upstream drainage area (Tucker and Whipple, 2002; Wobus et al., 2006b; Pritchard et al., 2009; Whittaker and Boulton, 2012). For example, the height of a knickpoint above a dip-slip fault should be independent of upstream drainage area and related to the change in uplift gradient along a stream as the stream crosses the fault (Whittaker et al., 2008; e.g. Whittaker, 2012). Knickpoint height above a normal fault will be related to catchment relief if footwall relief has not yet reached a threshold elevation above which relief is decoupled from erosion (Densmore et al., 2004; Densmore et al., 2007). Moreover, the distance a knickpoint has migrated upstream should scale with the square root of upstream area, assuming a uniform rock strength (Wobus et al., 2006b; Whittaker and Boulton, 2012; Whittaker and Walker, 2015).

Knickpoint analysis is strengthened if an accurate geochronology is available to compare knickpoint initiation with dated changes in sea-level (Crosby and Whipple, 2006; Mackey et al., 2014), isostatic rebound (Gomez and Livingston, 2012), large landslides (Lamb et al., 2007), or fault displacement rates (Wobus et al., 2006b). Furthermore, knickpoint analysis can provide additional insights into tectonic history where rock uplift rates are not available or the resolution of the record of rock uplift is insufficient to investigate whether variations in rock uplift rates have controlled river morphology through time (Whittaker and Walker, 2015).

In theory, the landscape response to rock uplift should be the similar irrespective of whether the landscape is responding to an extensional or contractional tectonic signal (Barnes et al., 2011) However, empirical relationships that link knickpoint propagation relative to tectonic processes have only been thoroughly tested on normal faults and **there is a paucity of studies which analyse how fault activity control knickpoints propagation through the landscape above active reverse faults** (e.g. Regalla et al., 2013; Dey et al., 2016). Complications arise from complex subsurface geometries

and interactions associated with reverse or thrust faults, which make attributing specific geomorphic indices over large areas to individual reverse faults problematic (Regalla et al., 2013). In compressional regimes, knickpoints have been used above surface folds to imply the presence of unmapped blind faults (Ahmad et al., 2015) or to characterize style of folding and hinge migration associated with buried faults (Ahmadi et al., 2006; Regalla et al., 2013). Moreover, recent work in the Himalaya has suggested that knickpoints and steepness indices above active thrust faults can be correlated with measures of long-term fault slip (Dey et al., 2016), but more studies are required to investigate this important relationship. Given that analysis of river long profiles and associated knickpoints can provide insights into important processes such as fault growth and interaction (Whittaker et al., 2008; Whittaker and Walker, 2015) or seismic hazard analysis (Boulton and Whittaker, 2009), **the degree to which active faulting controls knickpoint propagation through the landscape in the hanging wall of active reverse or thrust faults is a significant but relatively unexplored problem.**

1.4.4 Cosmogenic nuclide dating

Fault slip rates reflect a given amount of movement on a fault, within a specified period. Therefore, dating key regional strain markers is essential when calculating fault slip rates. Many methods are used for dating stratigraphic marker horizons in seismic hazard assessment. These include, but are not limited to, radiocarbon dating (e.g. McAuliffe et al., 2015), optically stimulated luminescence (e.g. DeVecchio et al., 2012a), amino acid racemization (e.g., Wehmiller, 1992), uranium-series dating (Schwarcz, 1989), biostratigraphy (Wagner et al., 2007), and magnetostratigraphy (e.g. Levi and Yeats, 1993). All Quaternary dating methods have respective strengths and weaknesses. However, existing methods for dating sediments within an age range from 100 ka to 5 Ma (i.e. the Plio-Pleistocene) are often affected by method-specific limitations. For example, uranium-series dating generally requires marine carbonate material and biostratigraphy requires preserved fossils. The recent advancement of the isochron method for cosmogenic isotope burial dating provides a wide-ranging tool for dating Plio-Pleistocene deposits (Balco and Rovey, 2008; Erlanger et al., 2012; Balco et al., 2013). When combined with the more established method of cosmogenic exposure dating, it is possible to obtain a complete Plio-Pleistocene chronology. This chronology can then be used to outline a detailed picture of variations in fault slip

rates over time, which can be used as the basis to examine spatial and temporal variations in strain accumulation and seismic hazards.

Numerous different cosmogenic dating techniques are applied in this project and specific considerations along with the background relevant for each technique are provided in the introduction to the chapter in which the specific technique is applied. Exposure dating using depth profiles is described in chapter 2 and isochron burial dating, exposure dating using boulders, and ^{10}Be catchment-averaged erosion rates are described in Chapter 4. The following text provides some background to the basic physics and development of cosmogenic dating theory.

Cosmogenic nuclides form in rocks via bombardment of minerals at the Earth's surface from secondary cosmic ray particles (Lal and Peters, 1967; Nishiizumi et al., 1989; Lal, 1991). Neutrons are the main secondary cosmic-ray particle responsible for cosmogenic nuclide production, but protons and muons contribute to a lesser extent (Lal and Peters, 1967; Nishiizumi et al., 1989). In theory, if the production rate for a cosmogenic nuclide is known, then the concentration of the cosmogenic nuclides within a rock should be a function of the time the rock has been exposed at the surface of the Earth:

$$N = P_{total} \times t \quad (1)$$

In equation 1, N is the total nuclide concentration in a sample, P_{total} is the production rate and t represents time.

Cosmogenic dating requires solving equation 1 for time:

$$t = \frac{N}{P_{total}} \quad (2)$$

N is measured by laboratory analysis (Kohl and Nishiizumi, 1992; Corbett et al., 2016b) but P_{total} needs to be modelled. In simple terms P_{total} is measured by taking a reference production rate (P_{ref}) and scaling for geographical variables (S_{geog}) and sample specific variables (S_{sam}) (Jull et al., 2015; Borchers et al., 2016).

$$P_{total} = P_{ref} \times S_{geog} \times S_{sam} \quad (3)$$

P_{ref} is a function of geomagnetic latitude, altitude, and depth below the surface. Primary cosmic rays are deflected by the Earth's magnetic field and the amount of deflection is termed 'cut-off rigidity' (Dunai, 2001). Convergence of the Earth's magnetic field at the poles dictates that the incoming cosmic ray flux needs to penetrate less of the magnetic field at the poles than at the equator (Dunai, 2000; Dunai, 2001). Hence, the intensity of the cosmic ray flux is dependent on cut-off rigidity, which in turn is dependent on latitude.

Primary cosmic rays react with the Earth's atmosphere to produce secondary cosmic rays (Lal and Peters, 1967). During this reaction, energy is scattered and absorbed. Therefore, at lower altitudes cosmic ray intensity is less than at high altitudes because cosmic rays have travelled through more atmosphere. Consequently, P_{ref} is scaled for latitude and altitude (Borchers et al., 2016), which are included in the term S_{geog} in equation 3. The slope of the sampled surface and shielding from surrounding topography and snow or water cover influence production rate to a lesser extent (Nishiizumi et al., 1989). These variables are included in the term S_{sam}. Finally, production of cosmogenic nuclides decreases rapidly with depth from the surface due to attenuation effects from the overlying material. Attenuation length depends on the density of the rock, but in general neutron flux is reduced to <1% below about 3 m (Gosse and Phillips, 2001).

A universal scaling model for production rates has proved problematic to produce. Lal (1991) used polynomial equations derived from atmospheric data to produce the first scaling model for global cosmogenic nuclide production, with reference to a common high latitude and sea level (Lal, 1991). Although Lal's model was a decent starting point, it overlooked subtle variations in global air pressure and muon concentration (Stone, 2000). The main drawback of Lal's scaling model, however, is that the model overlooked spatiotemporal variations in the Earth's geomagnetic field. Several studies have attempted to create scaling models based on neutron monitoring stations (e.g. Dunai, 2000; Dunai, 2001; Lifton et al., 2005). Neutron monitoring scaling models consider the spatiotemporal variations in both the intensity of the Earth's magnetic field and global variations in the dipole of the magnetic field. Neutron monitoring scaling models are, therefore, time-dependent in contrast to Lal's scaling model which is constant and based on a snapshot of atmospheric data from 1948-1949 (Lal, 1991).

The most up-to-date model for production rate scaling is the CRONUS-Earth (Cosmic Ray Produced Nuclide Systematics on Earth) project (e.g. Phillips et al., 2016). The CRONUS-Earth project has the broad aim of improving precision in cosmogenic nuclide dating by applying physics-based analytical methods to scaling nuclide production rates with respect to latitude, altitude and time. Geological calibration sites are combined with a physics-based model of cosmic ray fluxes for the main cosmic ray particles responsible for the production of cosmogenic nuclides (Lifton et al., 2014). CRONUS-Earth has the advantage of being able to model spatiotemporal variations in cosmic ray fluxes, calibrated against numerous different geographic localities on a nuclide-specific basis (Lifton et al., 2014).

The cosmogenic nuclides most commonly used for dating geological and geomorphic features are ^{10}Be, ^{26}Al, ^{36}Cl, ^{3}He, ^{21}Ne and ^{14}C. The two main nuclides utilized in this project will be ^{10}Be and ^{26}Al, which are formed by the interaction of cosmic rays with ^{16}O and ^{28}Si in quartz (Lal, 1988). Quartz is assumed to be ubiquitous throughout the Ventura basin because a large proportion of the Cenozoic bedrock is sourced from the San Gabriel Mountains (Levi and Yeats, 1993), which are composed of igneous and metamorphic rocks that provide abundant quartz (Campbell et al., 2014), and the Topatopa Mountains, which comprise a quartz-rich Tertiary sedimentary succession (Dibblee, 1979; Dibblee, 1987)

A large body of work has characterized the production rates for ^{10}Be and ^{26}Al (e.g. Nishiizumi et al., 1989; Balco and Shuster, 2009) and the currently accepted values stand at 3.92 atoms g^{-1} yr^{-1} for ^{10}Be (Phillips et al., 2016) and 26.5 atoms g^{-1} yr^{-1} for ^{26}Al at sea level and high latitude (Corbett et al., 2016a). The ratio of production rates for ^{10}Be relative to ^{26}Al is an essential component of the isochron burial method (Balco and Rovey, 2008). The exact value of the production rate ratio is a subject of ongoing research as the ratio is thought to vary with latitude and elevation (e.g. Borchers et al., 2016). Current estimates of the ratio range from ~6.6 to 7.3 (Lifton et al., 2015; Borchers et al., 2016). This project will use the current convention of 6.75 after Balco et al. (2008), which was validated in the study area using a sediment sample from the modern San Gabriel River (Chapter 4).

1.5 The Ventura basin

The Ventura basin is a fault-bounded, deep sedimentary trough situated in the Western Transverse Ranges, southern California (Fig. 1.1). It is bounded to the north by the Topatopa Mountains, to the east by the San Gabriel Mountains, and to the south by the Santa Monica Mountains and extends westward out to the Santa Barbara Channel via the Oxnard Plain (Fig. 1). Multiple active reverse faults in the Ventura basin are located in close proximity to major towns and cities (Fig. 1), which makes the Ventura basin a high value location to study how variable deformation rates can impact our understanding of seismic hazards.

The tectonic setting of what is now the Western Transverse Ranges (WTR) dates back to the early to mid-Miocene when subduction of the Farallon plate beneath North America was accompanied by the north-westward migration of the Pacific plate relative to North America (Atwater, 1970). The breakup of the subducting Farallon plate was followed by microplate capture of the fragmented remnants of the Farallon plate by the Pacific plate, which, along with shear between the North American and Pacific plates led to >90° of clockwise rotation of the WTR block from 20 Ma to 5 Ma (Luyendyk, 1991; Nicholson, 1994). Formation of the 'Big Bend' in the San Andreas fault (Fig. 1) caused a switch from Miocene extension and transtension to transpression and the inversion of Miocene transtensional basins in the WTR beginning in the late Miocene or early Pliocene (Crowell, 1976; Wright, 1991; Yeats et al., 1994). Transpression is currently accommodated by approximately north-south directed regional crustal shortening at rates of 7-10 mm yr^{-1} (Donnellan et al., 1993b; Marshall et al., 2013). This rapid shortening is accommodated by a series of east-west striking reverse faults and associated folds, including the north-dipping Red Mountain, Pitas Point, Ventura, and San Cayetano faults and the south-dipping Oak Ridge, Lion Canyon, Big Canyon, Padre Juan, Northridge, and Sisar faults and associated folds (Fig. 1) (Namson and Davis, 1988; Rockwell, 1988; Yeats et al., 1988; Sorlien et al., 2000; Hubbard et al., 2014; Sorlien and Nicholson, 2015; Rockwell et al., 2016; Nicholson et al., 2017b).

These faults are a significant source of historic seismic activity. The magnitude (M_w) 6.7 1994 Northridge earthquake was at the time the second costliest natural disaster in US history (Hall et al., 1994) and had its epicentre beneath the northern San Fernando valley (Fig. 1.1) to the east of the Ventura basin (Yeats and Huftile, 1995; Donnellan et al., 2002). The 1971 M_w 6.7 Sylmar (or San Fernando) earthquake had its epicentre beneath the southern San Gabriel Mountains just north of the San Fernando valley (Fig. 1.1) (Tsutsumi and Yeats, 1999). The earthquake was a result of slip on the Sierra Madre fault (Kamb et al., 1971), a north-dipping reverse fault similar in size, orientation, and geometry to most other major faults within the Ventura basin. Despite the moderate size (M_w 6.7) of both the 1971 Sylmar and 1994 Northridge earthquakes, the damage caused during both earthquakes was disproportionally large. The total cost of the 1971 Sylmar earthquake was estimated at $558 million (Dolan et al., 1995) (or ~$3.5 billion today) with the loss of 64 lives (Jennings, 1997). The total cost for the 1994 Northridge earthquake was estimated at $20 billion ($32 billion today) with the loss of 60 lives (Goltz, 1994; Hall et al., 1994). Part of the reason the damage caused by the Northridge and Sylmar earthquakes was so

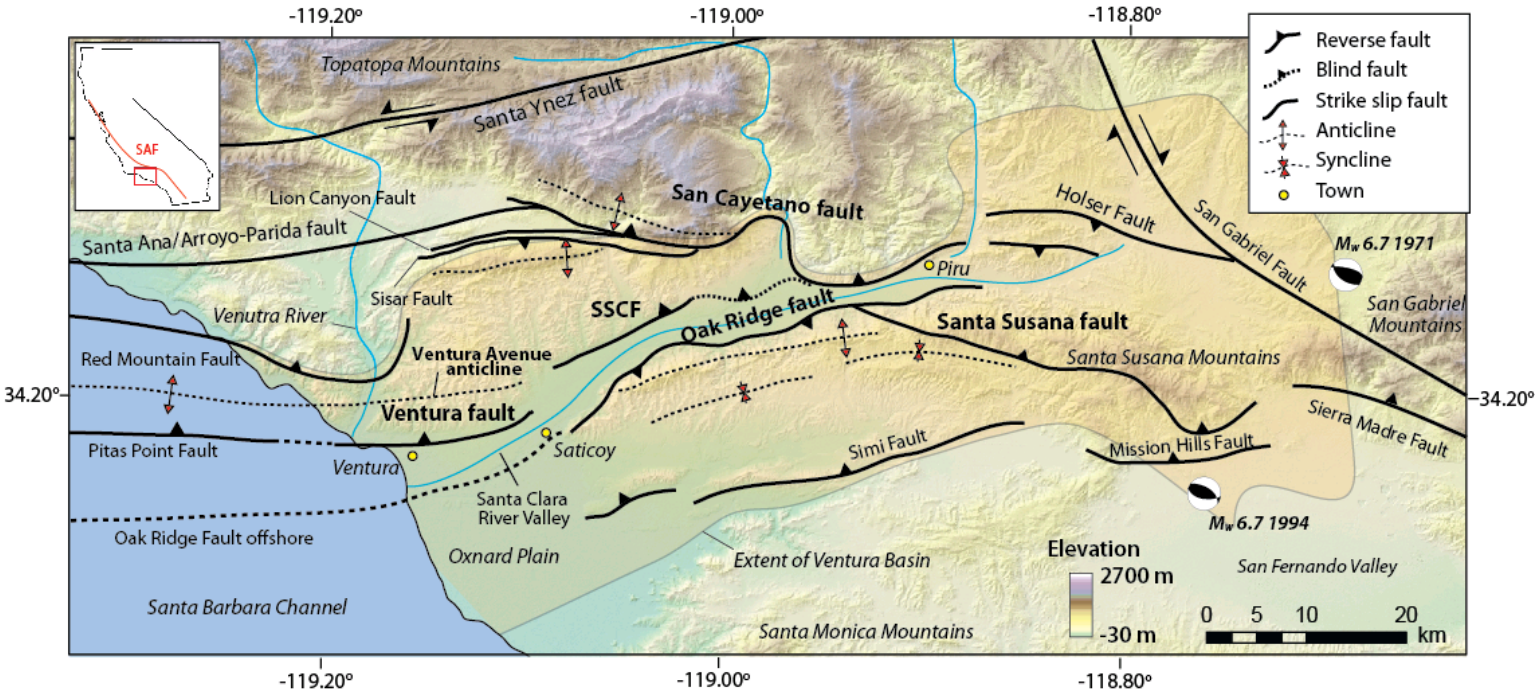

Figure 1.1 *Shaded relief map of the study area with major structures. Major faults are denoted with solid black lines with triangles on hanging wall of reverse faults. Key folds are denoted with thin dashed lines. The extent of the Ventura Basin is shaded in orange based on the extent of Plio-Pleistocene sedimentary deposits (Campbell et al. 2014). Yellow circles are towns mentioned in text. The location of the 1994 M_w 6.7 Northridge and 1971 M_w 6.7 San Fernando earthquakes are shown with the beachballs. SSCF = Southern San Cayetano fault, SAF = San Andreas fault. All fault traces based on Dibblee maps except SSCF based on work in this thesis.*

catastrophic was because the faults on which they occurred cut through or are in close proximity to major population centres within the San Fernando Valley and Los Angeles basin.

The Ventura fault is an east-west trending, blind reverse fault that cuts stratigraphy directly beneath the city of Ventura (Fig. 1.1) (e.g. Yeats, 1982; Hubbard et al., 2014). The city hall in downtown Ventura is built on a prominent fold scarp that represents the geomorphic surface expression of the blind Ventura fault (Sarna-Wojcicki, 1976; McAuliffe et al., 2015). Even a moderately sized earthquake on the Ventura fault would cause substantial damage to infrastructure and significant human casualties in Ventura and potentially across part of the wider Los Angeles metropolitan area.

1.5.1 Geological uncertainties within the Ventura basin

The Ventura basin contains significant economic petroleum reserves and consequently a wealth of subsurface well-log data and offshore seismic data is potentially available, which has been used to identify and characterize the subsurface structure of numerous faults (Yeats, 1982; Yeats et al., 1988; e.g., Hopps et al., 1992; Kamerling et al., 2003; Hubbard et al., 2014; Nicholson et al., 2017b). However, despite the large body of work there are still outstanding questions regarding the subsurface connectivity and rates of activity for several major faults. The following section will discuss some of these outstanding questions that I will attempt to address in Chapters 2, 3, and 4, and in the discussion in Chapter 5.

Significant regional crustal shortening within the Ventura basin has been measured by GPS to be around 7 mm yr^{-1} since 2001 (Marshall et al., 2013), but shortening rates measured over geological timescales (10^4 to 10^6 years) range from 10-14 mm yr^{-1} (Huftile and Yeats, 1995; Huftile and Yeats, 1996). It is currently not possible to ascertain whether this disparity is reflective of varying temporal rates of interseismic strain (Dolan et al., 2007; Dolan et al., 2016) or simply a result of large existing uncertainties in geological strain rates (assuming the geodetic estimates are reasonable).

A large body of work addresses the quantification of slip rates on various key faults within the Ventura basin (e.g. Rockwell, 1988; Rockwell et al., 1988; Yeats, 1988; Huftile and Yeats, 1995; Marshall et al., 2013; Hubbard et al., 2014; Rockwell et al., 2016; Nicholson et al., 2017b). However, uncertainties

still exist mainly as a result of poorly-defined temporal constraints on key strain markers (DeVecchio et al., 2012a; Marshall et al., 2013). A limited number of paleoseismic studies (Dolan and Rockwell, 2001; McAuliffe et al., 2015) and studies that use geomorphic surfaces to quantify slip rates on 10^3 to 10^4 year timescales (Rockwell, 1988; Rockwell et al., 1988; Hubbard et al., 2014) also contribute to a limited understanding of spatial and temporal variations in strain accumulation within the Ventura basin.

Many of the studies estimating slip rates in the Ventura basin have relied on using the youngest regionally deformed bedrock deposit, the Saugus Formation, as a regional strain marker (Yeats et al., 1988; Levi and Yeats, 1993; Tsutsumi and Yeats, 1999; DeVecchio et al., 2012b; Hubbard et al., 2014). This is because the Saugus Formation is regionally extensive and is often interpreted as the youngest syndeformational tectonic unit (e.g. Yeats, 1988; Meigs et al., 2003), even though deformation has continued post-Saugus Formation deposition. Despite its wide-ranging application in several studies, the precise age of the Saugus Formation and its spatial age variation remain poorly defined. Furthermore, despite limited chronology, the Saugus Formation is often referred to as time-transgressive with a decrease in age westward across the Ventura basin (Levi and Yeats, 1993; Campbell et al., 2014). The Saugus Formation is thought to range in age from 2.3–0.5 Ma in the eastern Ventura basin based on magnetostratigraphy and tephrochronology (Levi and Yeats, 1993). However, the magnetostratigraphic age assumed constant rates of sedimentation throughout the ~2.0 Myr period of deposition of the Saugus Formation. Whilst this may be the case locally, it is unlikely to be applicable across the entirety of the Ventura basin. A commonly cited upper age limit for the Saugus Formation around Ventura is 200-250 ka based on amino acid racemization on *Macoma* shells (Wehmiller et al., 1978; Lajoie et al., 1982). However, it is suggested that this age is potentially too young, due to the assumption that the Saugus Formation and overlying terrace deposits have the same thermal history despite being separated by an angular unconformity (Wehmiller, 1992). Additionally, recent work by DeVecchio et al., (2012a) used a combination of optically stimulated luminescence (OSL) and cosmogenic nuclide dating to calculate a lower age for the Saugus Formation in the southern Ventura basin of 125 ka and an upper age of 60-25 ka. The broad range of potential ages for the Saugus

Formation mentioned above, dictates the need to obtain a high-precision regional chronology for the Saugus Formation in order to use the Saugus Formation as a strain marker for seismic hazard assessment. **A detailed view of the potentially time-transgressive nature of the Saugus Formation from east to west across the Ventura basin is essential in order to accurately quantify Quaternary fault slip rates, assess contemporary seismic hazards, and aid in better understanding the Quaternary evolution of the Ventura basin.**

Another important source of debate in the Ventura basin is the deep structure of faults and potential for structural connectivity at depth. Two contrasting models exist for the deep structure of faults. In one interpretation, the Pitas Point, Ventura, Red Mountain, Lion Canyon, San Cayetano, and Arroyo Parida faults are connected via a mid-crustal detachment at ~7.5 km depth which dips gently north (Hubbard et al., 2014; Levy et al., in review). This interpretation is based primarily on 2D kinematic modelling, shallow onshore seismic reflection data, surface geological maps, and limited well control. In the alternative interpretation, the Pitas Point, Ventura, Red Mountain, and Arroyo-Parida faults form a flower structure, where the faults maintain a relatively constant dip down to ~10 km depth at which point they merge to form a master north-dipping fault that continues with a moderate-to-steep dip to maximum seismogenic depths of 18-20 km (Sorlien and Nicholson, 2015; Nicholson et al., 2017b). The deep geometry of this alternative interpretation is based on correlating fault geometry in the upper ~5 km based on well data and offshore 2D and 3D seismic reflection data with deep seismicity (Nicholson et al., 2017b).

The deep geometry of faults and the degree of subsurface connectivity provides a first-order control on the prospects for large-magnitude multi-fault earthquakes in the Ventura basin (discussed below). Therefore, **an accurate characterization of the deep structure of faults is essential to a complete analysis of seismic hazards in the Ventura basin**.

1.5.2 Prospects for large-magnitude (M_w 7.5–8.0) earthquakes

The size of a potential earthquake rupture for a given fault or system of faults, is partly dependent upon the amount of segmentation along a fault system (Wesnousky, 2006; Wesnousky and Biasi, 2011;

Manighetti et al., 2015; Biasi and Wesnousky, 2017). Faults do not need to be hard-linked in order for ruptures to propagate between them but the size of the steps between segments is also a crucial factor in determining the percentage of the fault or fault system that ruptures in any single event (Oglesby, 2008; Lozos et al., 2012; Biasi and Wesnousky, 2016; Hamling et al., 2017). Examples such as the 2017 M_w 7.8 Kaikōura earthquake in New Zealand (Hamling et al., 2017) and the 2010 M_w 7.2 El Mayor Cucapah earthquake in Mexico (Fletcher et al., 2014) provide evidence for large-magnitude earthquakes which involved slip on multiple faults and fault segments. Furthermore, during the Kaikōura earthquake, ruptures were suggested to have propagated across faults separated at the surface by as much as ~15 km (Hamling et al., 2017). These examples highlight the importance of characterizing potential structural connectivity between faults for robust analyses of seismic hazards.

The Ventura fault is a north-dipping reverse fault that runs east-west onshore for ~14 km from Saticoy at its eastern end, westward to the coast at Ventura (Fig. 1). The fault continues offshore into the Santa Barbara channel where the fault is termed the Pitas Point fault (Plesch et al., 2007), although there is some controversy about the degree of structural linkage between the Ventura and Pitas Point faults (Sorlien and Nicholson, 2015). Uplifted river terraces on the Ventura Avenue anticline show that the structure has been uplifting at a rate of 5 mm yr^{-1} since 30 ka (Rockwell et al., 1988). Hubbard et al. (2014) used seismic reflection profiles, well log data, and published interpretations of the fault to characterize a fault dip of 45-55° to the north. The Hubbard model builds on previous interpretations (Sarna-Wojcicki, 1976) to extend the Ventura fault beneath the Ventura Avenue anticline to around 7.5 km. At this depth the fault is proposed to connect with the San Cayetano, Red Mountain, and Lion Canyon faults along a gently north-dipping decollement surface (Hubbard et al., 2014). This decollement surface has been proposed to provide a pathway for large-magnitude multi-fault earthquakes between some combination of the Pitas Point, Ventura, Red Mountain, Lion Canyon, and San Cayetano faults (Rockwell, 2011; Hubbard et al., 2014; McAuliffe et al., 2015; Rockwell et al., 2016).

The prospect of large-magnitude earthquakes appears to be supported by observations that uplifted Holocene terraces on the Ventura Avenue anticline appear to be deformed in events with 5-10 m of

uplift via fault throw (Rockwell, 2011; Rockwell et al., 2016) and by paleoseismic trenching studies, which estimate fault throw events of between 5-6 m on the Ventura fault (McAuliffe et al., 2015) and 4–5 m on the San Cayetano fault (Dolan and Rockwell, 2001). Uplifts of this magnitude require earthquakes between M_w 7.5-8, greater than the potential magnitude that can be derived from scaling relationships based on the individual fault area (Wells and Coppersmith, 1994; Leonard, 2010; Leonard, 2014). However, recent work has questioned the likelihood of such large-magnitude earthquakes based on the observation that deep fault connectivity may be limited and large uplift events on the Ventura fault may be anomalous and caused by a restraining bend in the Pitas Point fault rather than a result of a continuous fault surface at depth and related large-magnitude earthquakes (Sorlien and Nicholson, 2015; Nicholson et al., 2017b).

The degree of subsurface structural connectivity is critical to the prospect of multi-fault earthquakes in the Ventura basin. A blind fault called the Southern San Cayetano fault (SSCF) was recently proposed, which links the Ventura fault with the San Cayetano fault in the subsurface and increases potential subsurface structural connectivity (Hubbard et al., 2014). However, despite this faults potentially important role in stress transfer and the prospect for multi-fault earthquakes, no geological field data was presented to prove the existence of the SSCF or characterize its geometry and slip rate. **Characterization of the surface expression, subsurface geometry, and the subsurface connectivity of the SSCF with neighbouring faults is key to investigating the potential for multi-fault earthquakes in the Ventura basin.**

1.6 Summary of key research questions

The literature review in sections 1.4 and 1.5 highlights several broad research questions and specific questions that relate to the Ventura basin that I will attempt to address in this thesis. These questions are summarised below.

Fault interactions and seismic hazards:

- *To what degree are patterns of deformation over multiple earthquake cycles variable in time and spaces and how do any potential variations impact our interpretation of seismic hazards?* (Chapters

2, 3, 4, and 5)

- *To what extent do unidentified faults and blind faults inhibit accurate analysis of seismic hazard and what role do smaller faults play in stress transfer during multi-fault earthquakes?* (Chapters 2, 3, and 5)
- *How does fault geometry effect stress transfer between faults?* (Chapter 3)
- *Is static stress transference between reverse faults highly sensitive to changes in fault geometry, as is the case for normal faults?* (Chapter 3)

Landscape evolution:

- *How effective are catchment-averaged erosion rates for tracking tectonic rock uplift in transient landscapes with multiple interacting reverse and thrust faults?* (Chapter 4)
- *Can morphometric landscape parameters such as relief and channel steepness be used to extract tectonic signals from the landscape in compressional regimes with multiple interacting reverse faults?* (Chapter 4)
- *How does fault activity control knickpoint propagation through the landscape above active reverse or thrust faults?* (Chapter 4)

Key questions within the Ventura basin:

- *What field evidence is there for the proposed existence of the SSCF, are there any other unidentified faults in the Ventura Basin, and could the SSCF provide a pathway for potential large-magnitude multi-fault ruptures?* (Chapters 2, 3, and 5)
- *What evidence is there for proposed subsurface connectivity for faults in the Ventura basin, and can we use data from fault slip rates, erosion rates, or geomorphology to provide insights into subsurface fault connectivity and fault evolution?* (Chapters 2, 3 and 5)
- *How likely are proposed multi-fault earthquakes in the Ventura basin?* (Chapters 2, 3, and 5)
- *Over what time and length scales does the Saugus Formation vary in age across the Ventura basin and how effective is the Saugus Formation as a strain marker for late Quaternary tectonics in the Ventura basin?* (Chapter 4)
- *To what extent have Quaternary fault interactions shaped the landscape evolution of the Ventura*

basin? (Chapter 4)

I will attempt to address some of these key questions in the research Chapters 2, 3, and 4 by focusing on the Ventura basin. I will then synthesize the findings of the research chapters for the discussion in Chapter 5 to address the key questions in the Ventura basin.

Chapter 2: Geomorphic evidence for the geometry and slip rate of a young, low-angle thrust: Implications for hazard assessment and fault interaction in complex tectonic environments+

Chapter Abstract

We present surface evidence and displacement rates for a young, active, low-angle (~20°) reverse thrust fault in close proximity to major population centres in southern California (USA), the Southern San Cayetano fault (SSCF). Active faulting along the northern flank of the Santa Clara River Valley displaces young landforms, such as late Quaternary river terraces and alluvial fans. Geomorphic strain markers are examined using field mapping, high-resolution lidar topographic data, ^{10}Be surface exposure dating, and subsurface well data to provide evidence for a young, active SSCF along the northern flank of the Santa Clara River Valley. Displacement rates for the SSCF are calculated over 10^3–10^4 year timescales with maximum slip rates for the central SSCF of 1.9 $^{+1.0}/_{-0.5}$ mm yr^{-1} between ~19–7 ka and minimum slip rates of 1.3 $^{+0.5}/_{-0.3}$ mm yr^{-1} since ~7 ka. The SSCF is interpreted as a young, active structure with onset of activity at some point after ~58 ka. The geometry for the SSCF presented here, with a ~20° north-dip in the subsurface, is the first interpretation of the SSCF based on geological field data. Our new interpretation is significantly different from the previously proposed model-derived geometry, which dips more steeply at 45–60° and intersects the surface in the middle of the Santa Clara River Valley. We suggest that the SSCF may rupture in tandem with the main San Cayetano fault. Additionally, the SSCF could potentially act as a rupture pathway between the Ventura and San Cayetano faults in large-magnitude, multi-fault earthquakes in southern California. However, given structural complexities, including significant changes in dip and varying Holocene displacement rates along strike, further work is required to examine the possible mechanism, likelihood, and frequency of potential through-going ruptures between the Ventura and San Cayetano faults. Confirmation of the SSCF in a previously well-studied area, such as southern California, demonstrates that identification of

young faults is critical for accurate seismic hazard assessment. We suggest that many young, active faults remain undetected in other structurally complex and tectonically active regions globally, and that significant seismic hazards can be overlooked.

+ A version of this chapter has been published in the following paper:

Hughes, A., Rood, D.H., Whittaker, A.C., Bell, R.E., Rockwell, T.K., Levy, Y., Wilcken, K.M., Corbett, L.B., Bierman, P.R., DeVecchio, D.E., Marshall, S.T., Gurrola, L.D. and Nicholson, C., 2018. *Geomorphic evidence for the geometry and slip rate of a young, low-angle thrust fault: Implications for hazard assessment and fault interaction in complex tectonic environments.* Earth and Planetary Science Letters, 504: 198-210 https://doi.org/10.1016/j.epsl.2018.10.003

AH conceived of the idea of the research and performed all the laboratory analyses with the exception of accelerator mass spectrometry analysis, which was performed by KMW and DHR. AH performed the data reduction and analysis, prepared the figures, and wrote the manuscript. DHR aided AH with the laboratory analysis and all authors discussed the science and commented on the manuscript.

2.1 Introduction

A growing body of evidence indicates that large-magnitude earthquakes can involve slip on multiple faults with complex geometries and kinematics (e.g., Yue et al., 2005; Hubbard et al., 2010). Several recent examples of large-magnitude multi-fault ruptures involve slip on young faults that were unrecognized prior to the earthquake, but acted as key rupture pathways and enhanced fault connectivity during the event (Densmore et al., 2010; Fletcher et al., 2014; Hamling et al., 2017). Previously unrecognized faults have also been identified as the seismic source for many recent, devastating, moderately-sized earthquakes, including the 2015 M_w 6.5 Pishan earthquake, China (Lu et al., 2016), and the 2011 M_w 6.2 Christchurch earthquake, New Zealand (Beavan et al., 2011). Consequently, identifying young or small offset faults and accurately characterizing key fault parameters, such as location and deformation rate, is a fundamental prerequisite for accurate seismic hazard assessment (e.g., Field et al., 2015).

Fault slip rates are key first-order inputs into seismic hazard assessment as they provide quantitative information on both the magnitude and frequency of potential earthquakes (e.g., Field et al., 2015). Records of fault slip rates over multiple timescales can be used to detect spatial and temporal variations in fault activity, thereby enhancing our ability to forecast future fault behaviour (Friedrich et al., 2003; Rood et al., 2011b). However, the processes that govern spatial and temporal variations in fault slip rates are poorly understood, partly because long-term records of fault slip often lack sufficient resolution (e.g., Friedrich et al., 2003). Improved understanding of fault activity within major fault systems is particularly important given new insights into how young, previously unrecognized, faults can potentially act as rupture pathways in large-magnitude earthquakes (Fletcher et al., 2014; Hubbard et al., 2014; Hamling et al., 2017).

Young faults can have little stratigraphic offset and subtle geomorphic expression, making them difficult to identify prior to earthquake rupture and can, therefore, be overlooked in seismic hazard assessments. For example, the Papatea fault in the northern South Island, New Zealand, is a recently identified, small offset fault with small stratigraphic offset that potentially enhanced fault connectivity

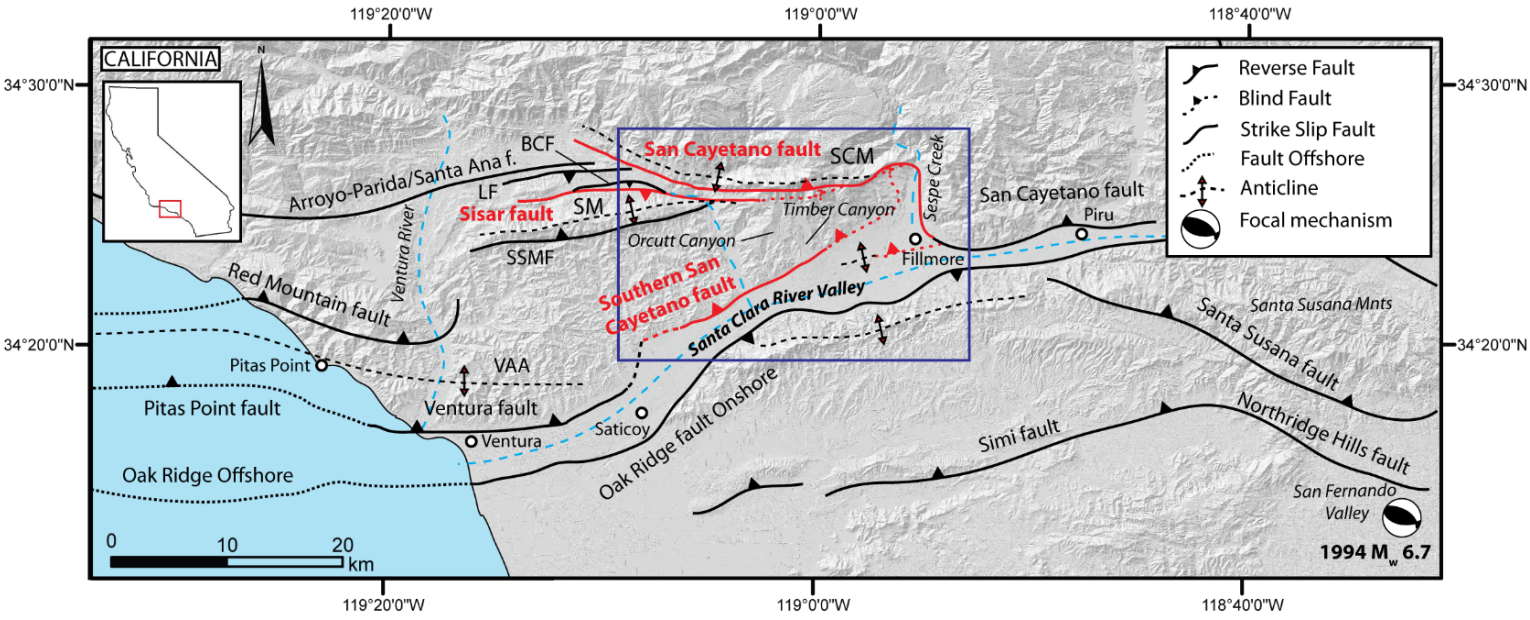

Figure 2.1 *Major onshore structures of the Western Transverse Ranges near the Southern San Cayetano fault (SSCF). The key faults discussed in this paper are highlighted with solid red lines with other major faults denoted using solid black lines. Fault surface traces are based on the Dibblee maps. Major regional folds are indicated by dashed black lines. The location of the focal mechanism for the 1994 M_w 6.7 Northridge earthquake is indicated by the beach ball. Dashed blue lines are the paths of major rivers. The blue box shows location of Figures 2.2 & 2.6. SCM = San Cayetano Mountain, SM = Sulphur Mountain, BCF = Big Canyon fault, LF = Lion fault, SSMF = South Sulphur Mountain fault, VAA = Ventura Avenue anticline.*

and increased earthquake magnitude during the 2017 M_w 7.8 Kaikōura earthquake (Hamling et al., 2017; Hollingsworth et al., 2017). Accordingly, identification of young faults prior to an earthquake can in theory improve understanding of structural connectivity in fault systems where no historical large-magnitude (M_w > 7) earthquakes are documented, and facilitate a more rigorous assessment of future potential earthquake magnitudes (e.g., Hubbard et al., 2014).

The Ventura Basin, southern California, provides an ideal location to investigate the significance of the identification of young faults to seismic hazard assessment for several reasons. The Ventura fault (Fig. 2.1) is a young, fault within the Ventura Basin with as little as 200–300 m of stratigraphic offset since 200–300 ka observed in subsurface well data (Hubbard et al., 2014). The geometry of the Ventura fault has proved controversial as small stratigraphic offsets within the upper 2–3 km made the Ventura fault difficult to identify in subsurface well data (Sarna-Wojcicki and Yerkes, 1982; Yeats, 1982). A proposed model for the Ventura fault, based on well-log and seismic reflection data, indicated that the Ventura fault may be deep-rooted and potentially connects with the San Cayetano fault (Hubbard et al., 2014) (Fig. 2.1). However, 2D structural kinematic modelling required an additional, steeply-dipping (45–60°) linking structure, which was referred to as the Southern San Cayetano fault (SSCF) (Hubbard et al., 2014) (Fig.1). Connection of the Ventura and San Cayetano faults via a model-derived SSCF creates a continuous ~150 km long fault system, between which the SSCF potentially acts as a rupture pathway during large-magnitude multi-fault ruptures (Hubbard et al., 2014; Rockwell et al., 2016; Marshall et al., 2017).

Previous geological mapping has included minor unnamed fault segments along a section of the proposed SSCF with no indication of the subsurface geometry or connectivity (Yerkes et al., 1987). Additionally, a structure named the Pagenkopp fault is mapped from well data at the eastern end of the proposed surface trace of the SSCF (Çemen, 1989; Hopps et al., 1992). However, despite much previous mapping within the Santa Clara River Valley (e.g., Rockwell, 1988; Dibblee, 1990b; Hopps et al., 1992) (Fig. 2.1), a continuous fault along the northern Santa Clara River Valley has not been characterized by any geological or geomorphic field evidence, or subsurface data. Furthermore, the proposed geometry of the SSCF (whether north or south-dipping) is unknown, and the faults age, surface expression,

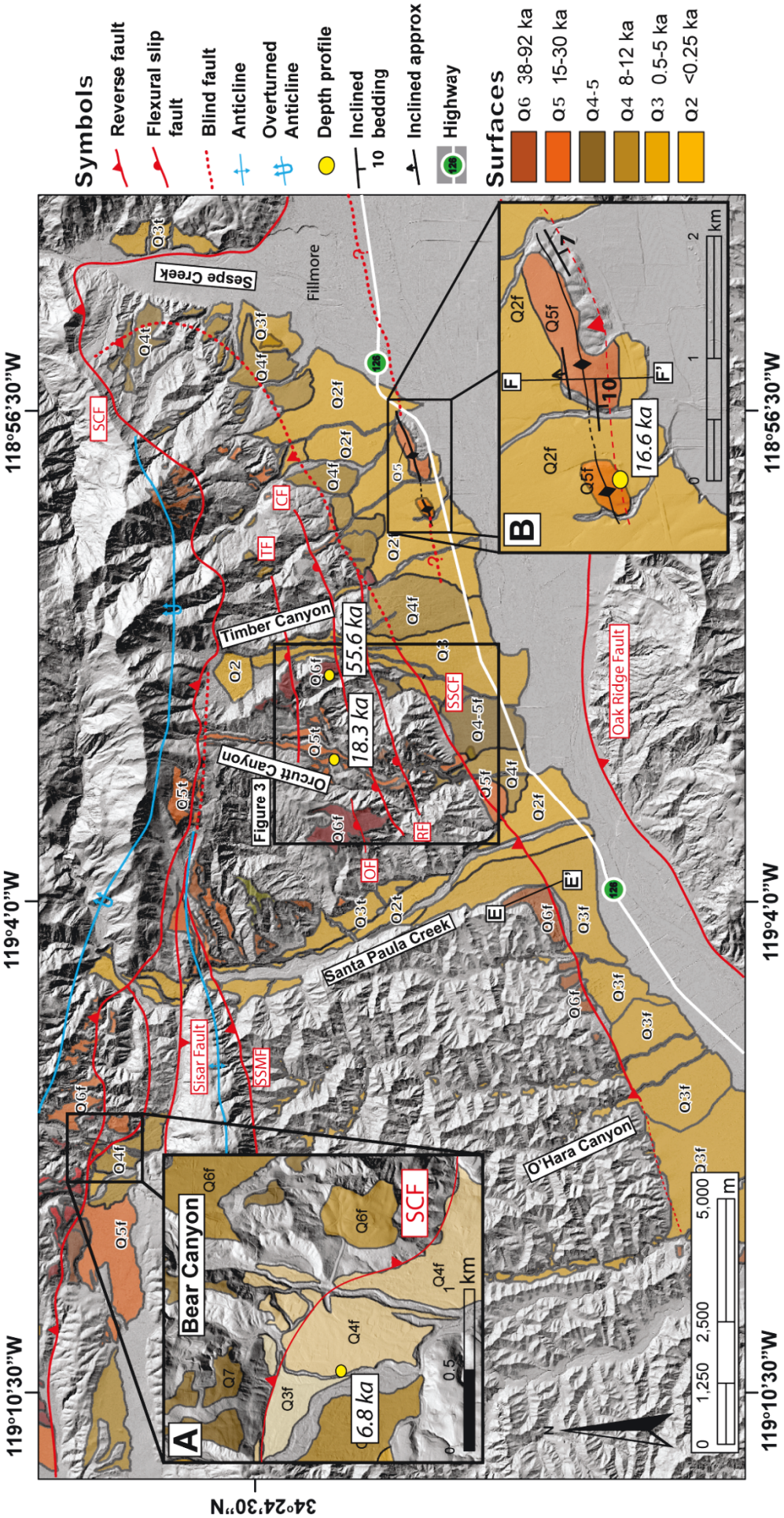
Symbols
Reverse fault
Flexural slip fault
Blind fault
Anticline
Overturned Anticline
Depth profile
Inclined bedding
10
Inclined approx
Highway
Surfaces
Q6 38-92 ka
Q5 15-30 ka
Q4-5
Q4 8-12 ka
Q3 0.5-5 ka
Q2 <0.25 ka
Sespe Creek
Fillmore
SCF
CF
TF
Timber Canyon
Orcutt Canyon
Figure 3
55.6 ka
18.3 ka
SSCF
RF
OF
Sisar Fault
SSMF
Santa Paula Creek
Oak Ridge Fault
O'Hara Canyon
Bear Canyon
6.8 ka
16.6 ka
A
B
E
E'
F
F'
118°56'30"W
119°4'0"W
119°10'30"W
34°24'30"N
0 1,250 2,500 5,000 m
0 0.5 1 km
0 1 2 km

Figure 2.2 *Hillshade map of river terraces and alluvial fans in the proximity of the Southern San Cayetano fault (SSCF). Faults are indicated with solid red lines. Triangles and semi-circles denote fault hanging walls where triangles are reverse faults and semi-circles are flexural-slip faults. Dashed lines are blind faults. Cosmogenic depth profile locations are indicated with yellow dots. The location of Figure 2.3 is indicated in the black box. Line of topographic profile E-E' in Figure 2.4e is shown and the line of section G-G' in Figure 2.7 is indicated. Extent of river terraces (t) and alluvial fans (f) and associated ages are from Rockwell [1988]. (A) Map of late Quaternary alluvial fans and location of Q4 depth profile at Bear Canyon. (B) Enlarged hillshade map of the fold in the Santa Clara River Valley. Bedding readings and fault surface traces for all faults (except the SSCF, which is based on data in this chapter) are from Dibblee [1992]. Line of section F-F' from Figure 2.4f is indicated with a black line. SCF = San Cayetano fault, TF = Thorpe fault, OF = Orcutt fault, CF = Culbertson fault, RF = Rudolph fault.*

subsurface dip, activity, and slip rate have not been thoroughly investigated. Without accurate characterization of the SSCF, a rigorous assessment of seismic hazard in this densely populated and tectonically active area of southern California remains incomplete.

In this paper, we use lidar topographic data, cosmogenic ^{10}Be surface exposure ages, and subsurface data to provide compelling evidence for the SSCF and characterize the surface trace, subsurface geometry, and deformation rate for the SSCF through time. Our results bring into focus the importance of accurately characterizing easily overlooked, young faults for seismic hazard assessment in densely populated areas. Confirmation of the SSCF in a previously well-studied area, such as the Ventura basin, leads us to suggest that unrecognized, young active faults may well remain undetected in many other well-studied tectonically active regions globally. Efforts should be made to identify young or small offset faults, particularly in areas with multiple interacting faults where young structures may enhance subsurface fault connectivity in potential multi-fault earthquakes.

2.1.1 Regional setting

The Ventura Basin is located within the Western Transverse Ranges, a fold and thrust belt in southern California, USA, resulting from regional transpression and 7–10 mm yr^{-1} of north-south directed crustal shortening (Marshall et al., 2013) caused by the restraining bend in the San Andreas fault (e.g., Wright, 1991). Range-front topography throughout most of the Ventura Basin is fault controlled and associated with uplift in the hanging wall of active, east-striking reverse faults (Fig. 2.1). One such fault, the San Cayetano fault, is often mapped as the most southerly fault along the northern flank of the Santa Clara River Valley (e.g., Rockwell 1988) (Fig. 2.1). However, recent fault modelling has suggested the existence of the SSCF farther south in the footwall of the San Cayetano fault (Hubbard et al., 2014).

The SSCF is not included in current seismic hazard mapping for California (e.g., Jennings and Bryant, 2010), published geological maps (e.g., Dibblee, 1990b), or the UCERF3 report for California (Field et al., 2015). However, the model-derived interpretation of the SSCF is included in the latest version of the Community Fault Model for Southern California (Nicholson et al., 2015).

A series of uplifted and tilted strath terraces, fill terraces, and alluvial fan deposits are preserved along the northern flanks of the east-west trending Santa Clara River Valley, in close proximity to the proposed SSCF (Fig. 2.2). Rock uplift has previously been attributed to activity on a 25 km long, south-dipping fault zone referred to as the Lion fault set, which includes the Sisar, Big Canyon, and Lion faults (e.g., Huftile and Yeats, 1995) (Fig. 2.1). Alternatively, uplift of terraces along the eastern section of the range front has been attributed to footwall deformation from the north-dipping San Cayetano fault (Rockwell, 1988).

2.1.2 Study location

We focused on Orcutt Canyon (Figs. 2.1 & 2.2) to investigate range-front faulting along the northern Santa Clara River Valley because several geomorphic observations point to active faulting in this area. Orcutt Canyon is a north-south-trending incised valley along the southern flank of San Cayetano Mountain (Fig. 2.1) that drains into the Santa Clara River Valley. The canyon is located in the central portion of the range front, and thus likely records close-to-maximum displacement if the range front were bounded by a laterally continuous fault (Fig. 2.2). Alluvial fans that cross the range front at the mouth of Orcutt Canyon are warped parallel to the range front creating north-side-up scarps (Fig. 2.3). A series of bedding plane parallel flexural-slip faults such as the Rudolph, Culbertson, and Thorpe faults are well-established in the footwall of the San Cayetano fault at Orcutt Canyon (e.g., Rockwell, 1983; Rockwell, 1988) (Figs. 2.2, 2.3, & 2.4). Additionally, ~3 km southeast of Orcutt Canyon in the Santa Clara River Valley, a ~2 km east-west trending fold is mapped warping Quaternary alluvial fan deposits above the valley floor (Rockwell, 1983; Dibblee, 1990a) (Fig. 2.2b).

A sequence of uplifted and tilted alluvial fill and strath terraces at various elevations within Orcutt Canyon have previously been mapped and numerically age dated (Rockwell, 1983; Rockwell, 1988).

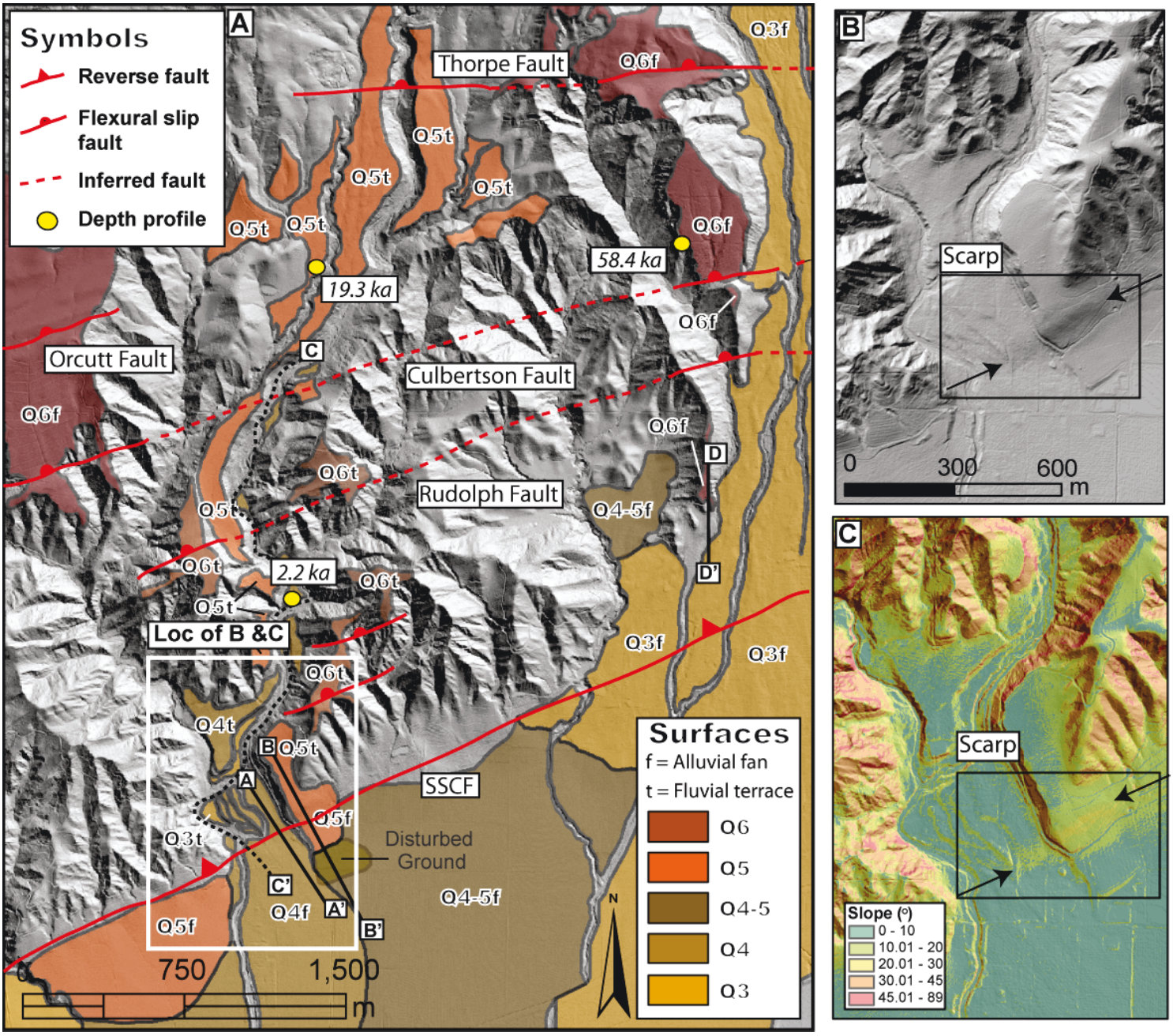

Figure 2.3 *Summary of active deformation at Orcutt Canyon. (A) Hillshade image with extent of mapped fluvial terraces (t) and alluvial fans (f) and the local surface trace of the Southern San Cayetano fault (SSCF) indicated with solid red line. Lines A-A' and B-B' show trace of topographic profiles through Q4 and Q5 surfaces at the mouth of Orcutt Canyon respectively. Topographic profiles are included in Figure 2.4. The trace of the modern-day stream used to calculate uplift of Q6 surfaces in Figure 2.4c is indicated by the dashed black line. (B) Hillshade map with 330° sun angle and 45° azimuth detailing scarp at the mouth of Orcutt Canyon indicated by the black arrows. (C) Hillslope map with Orcutt Canyon scarp highlighted as pale green high-angle slope against dark green low-angle slope detailing scarp at the mouth of Orcutt Canyon.*

The existing terrace chronology for the Santa Clara River Valley and Upper Ojai Valley is based upon dendrochronology, soil development, radiocarbon, and comparative rates of faulting on the Arroyo Parida-Santa Ana fault (Rockwell, 1983; Rockwell, 1988; DeVecchio et al., 2012a) (Fig. 2.1). Terraces are assigned a number that increases with increasing age, i.e., Q1 (youngest) to Q7 (oldest), and the existing terrace chronology is included in Figure 2.2.

The strength and thickness of soil profile development and, if appropriate, the elevation relative to the level of the modern Orcutt Canyon channel was used to field check the approximate age of geomorphic surfaces at Orcutt and Timber Canyons, following Rockwell (1983). Older surfaces are interpreted to have a strongly developed soil profile, including a well-developed argillic horizon and increasing development of the B horizon with increasing age (Rockwell, 1983). Surfaces previously mapped at Orcutt Canyon range from Q3 (0.5-5 ka) to Q6 (38-92 ka) (Rockwell, 1983; Rockwell, 1988). However, the majority of radiocarbon ages were taken from the Ventura River area and the existing soil chronology at Orcutt and Timber Canyons, particularly for the Q4, Q5, and Q6 surfaces, is generally based correlation with surfaces in the Ventura River. Consequently, there are few direct ages for the alluvial fans and river terraces at Orcutt Canyon. All deposits were poorly sorted and consist of a range of grain sizes from silt to boulders and Q4 surfaces at Orcutt Canyon are generally 6–10 m above the current stream level, Q5 terraces are generally situated 25–35 m above the current stream level, and the Q6 surfaces are up to 100 m above the current stream level.

2.2 Methods

2.2.1 Mapping

Lidar data covering Ventura County were acquired from the Ventura County Watershed Protection District (Airborne1, 2005) and imported into ArcGIS to create a 5 m digital elevation model (DEM). Digital geomorphic maps comprising bare earth hillshade images and topographic slope maps were extracted from the DEM and used to reinterpret the spatial extent and increase the resolution of existing geomorphic maps (Rockwell, 1983; Rockwell, 1988) (Figs. 2.2 & 2.3). The geomorphic maps detail a series of alluvial river terraces, which flank the various canyons created by tributary streams that drain

the south flank of San Cayetano Mountain (Fig. 2.1) and corresponding alluvial fans, which have been deposited south of the range front as the tributary streams open out into the Santa Clara River Valley (Fig. 2.2 & 2.3). 2.2.2 Depth profiles

To improve the accuracy and precision of age estimates for the Q4, Q5, and Q6 surfaces and accurately quantify slip rates at Orcutt Canyon, we measured *in-situ*-produced cosmogenic ^{10}Be surface exposure ages using depth profiles (e.g., Anderson et al., 1996; DeVecchio et al., 2012a). *In-situ* ^{10}Be is formed via the interaction of cosmic rays with minerals at the Earth's surface and the concentration of ^{10}Be decreases exponentially with depth. The surface ^{10}Be concentration represents the build-up of ^{10}Be since the time of surface abandonment and, if minimal erosion has occurred, the age of the surface. A depth profile accounts for substantial ^{10}Be acquired prior to deposition (inheritance) by estimating ^{10}Be concentration below the attenuation length of cosmic rays (Anderson et al., 1996).

Depth profile locations were selected based on the quality and completeness of soil profile development. A complete soil profile is interpreted to indicate a stable surface that has not undergone significant erosion since time of abandonment (Rockwell, 1983). We collected samples for depth profiles from an alluvial fan with Q4 soil development at Bear Canyon (Fig. 2.2a) and an alluvial fill terrace with Q4 soil development at Orcutt Canon (Fig. 2.3). Further samples for depth profiles were collected from a Q5 alluvial fill terrace at Orcutt Canyon (Fig. 2.3), the top surface of a folded Q5 alluvial fan in the Santa Clara River Valley (Fig. 2.2b), and an uplifted alluvial fan at neighbouring Timber Canyon, which was originally mapped as Q7 but we re-designated here to Q6 based on the results in section 2.3.2 (Fig. 2.3). A full description of field sampling methods is included in Appendix A1.

2.2.3 Laboratory methods

Quartz separation was undertaken in the CosmIC laboratory at Imperial College London. Bulk sediment samples were sieved to isolate the 250–1000 μm fraction and ~20 g aliquots of quartz were isolated and purified from the samples following the methodology of Kohl and Nishiizumi (1992). Beryllium isolation was carried out at the University of Vermont following the methods of Corbett et al. (2016). ^{10}Be/^{9}Be AMS measurements were made at the Centre for Accelerator Science at the Australian Nuclear

Science and Technology Organization using the 6 MV Sirius tandem accelerator (Wilcken et al., 2017). Measured $^{10}Be/^{9}Be$ ratios were calibrated to standard 01-5-2 with an assumed $^{10}Be/^{9}Be$ ratio of 8.558 x 10^{-12} (Nishiizumi et al., 2007). Measured AMS $^{10}Be/^{9}Be$ ratios were converted to concentrations and samples were blank corrected relative to the batch-specific process blank. The mean total ^{10}Be atoms for all process blanks was 9307 $^{+}$/- 2487 atoms (1σ). This background equates to a total of 0.2–9.9% of the total ^{10}Be atoms in the individual samples. A summary of sample details and concentrations are included in Table 1.

We calculated exposure ages and associated uncertainties by modelling depth profiles of measured ^{10}Be concentrations using a Monte Carlo simulator (Hidy et al., 2010). Simulations employed a constant production rate model (Stone, 2000) with a reference spallogenic ^{10}Be production rate of 4.24 +/- 0.12 atoms g^{-1} yr^{-1} based on inputting the Promontory Point reference production rate calibration dataset from Lake Bonneville, Utah, USA (Lifton et al., 2015) to the CRONUS online exposure age calculator version 2.3 (Balco, 2009). Density was modelled using a range of 1.7–1.8 g cm^{-3} and we employed an attenuation length of 160 g cm^{-2}. We used a ^{10}Be half-life of 1.387 +/- 0.012 My (Chmeleff et al., 2010), but applied a greater uncertainty of 5% to the half-life in our simulations. Muonogenic ^{10}Be production was modelled after Heisinger (2002a, 2002b). Further details on both laboratory methods and data reduction are included in appendices A2 and A3, respectively, and full samples parameters are included in Table ST1.

2.2.4 Scarp identification and fault activity

We extracted topographic profiles from the DEM and used these topographic profiles in combination with our digital geomorphic maps and field observations to confirm the presence of north-side-up tectonic scarps in Q4 and Q5 alluvial fans at the mouth of Orcutt Canyon (Fig. 2.3). Topographic profiles, geomorphic maps, and field observations were also employed to identify further alluvial surfaces offset by active faulting along the length of the proposed fault (Figs. 2.2 & 2.3).

Monte Carlo simulations, which account for uncertainties in all input parameters, were utilized to calculate slip rates and throw rates across the fault scarps. Monte Carlo simulations output a non-

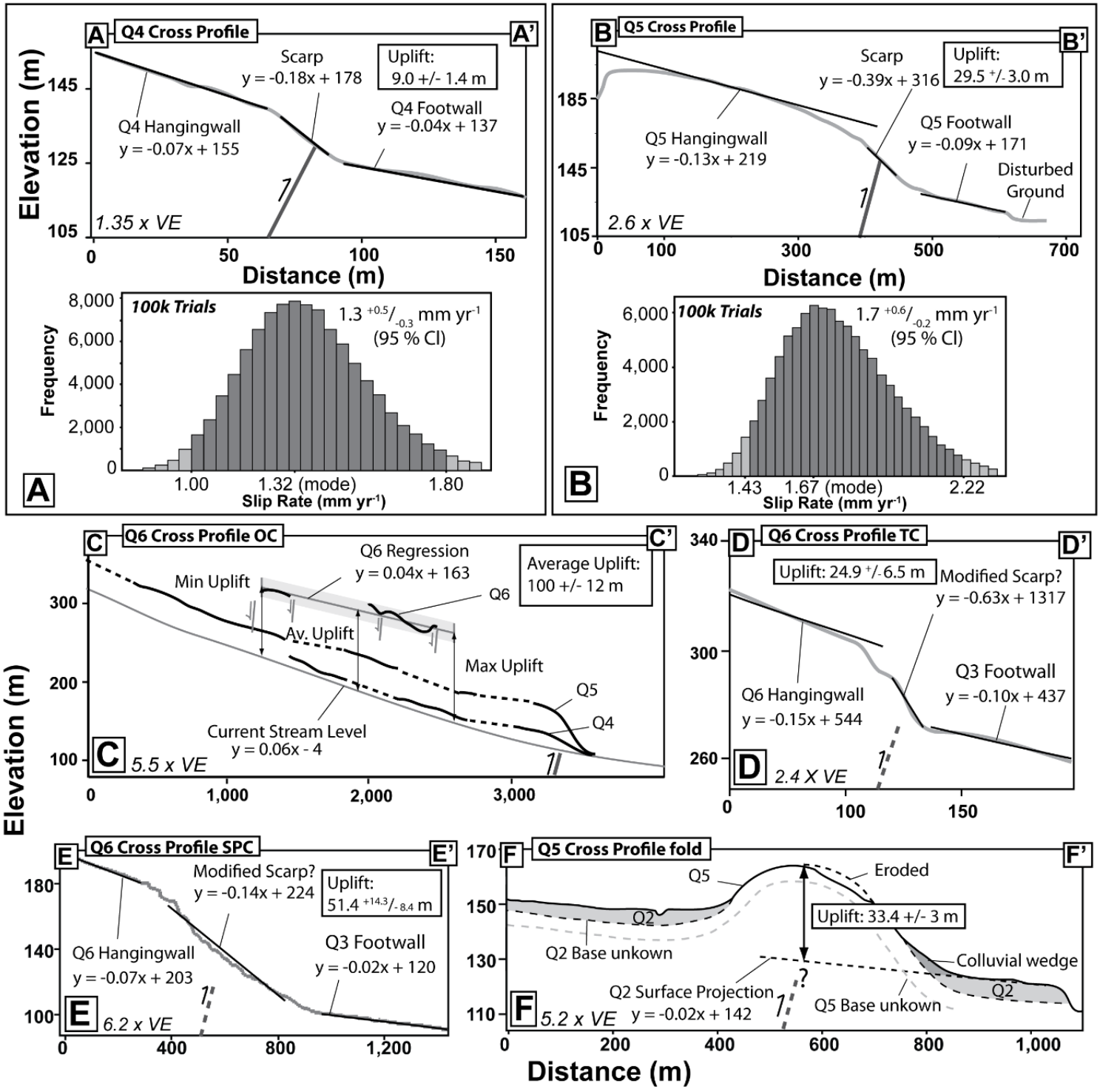

Figure 2.4 *Topographic profiles used to calculate displacement across the Southern San Cayetano fault (SSCF). Equations are linear regressions through geomorphic surfaces used in Monte Carlo simulations. A and B include topographic profiles A-A' and B-B' across the Q4 and Q5 surfaces at the mouth of Orcutt Canyon (lines of section in Figure 2.3) and frequency histograms of all slip rates output during Monte Carlo simulations. C includes section C-C' with a linear regression through the average elevation of the Q6 surface relative to the modern stream channel used to calculate average uplift and incision. The grey band either side of the regression denotes the vertical uncertainty. Bedding parallel flexural-slip faults are indicated with pale grey lines. D and E are topographic profiles D-D' and E-E' through Q6 surfaces at Timber Canyon (D) and Santa Paula Creek (E) used to calculate minimum throw for the Q6 surfaces relative to Q3 surfaces in the fault footwall. F is profile F-F', a topographic profile across the fold in the Santa Clara River Valley showing parameters used to calculate minimum uplift of the Q5 surface on the fold crest relative to the Q2 surface north and south of the fold. Lines of section for D-D' and C-C' are shown in Figure 2.3. Lines of section for E-E' and F-F' are shown in Figure 2.2. VE = Vertical exaggeration, OC = Orcutt Canyon, TC = Timber Canyon, SPC = Santa Paula Creek.*

normally distributed frequency histogram (Figs. 2.4a & 2.4b) encompassing all possible slip rate values calculated during 100,000 trial runs. The modal value was selected from the output frequency histogram to represent the most likely slip rate (e.g., Rood et al., 2011b). Input parameters used in Monte Carlo simulations to calculate slip rates at Orcutt Canyon were surface age, fault position, near-surface fault dip, geomorphic surface slope, and intercepts. See Appendix A4 for full details of how each input parameter was modelled during the simulation.

We improved the spatial resolution of our dataset by quantifying throw rates for Q6 alluvial fans at Timber Canyon and Santa Paula Creek (Fig. 2.2) east and west of Orcutt Canyon, respectively. At these locations Monte Carlo simulations were again utilized to calculate rock uplift rates (Figs. 2.4d & 2.4e); however, no Q6 deposits are preserved in the fault footwall at either Timber Canyon or Santa Paula Creek (Fig. 2.2). Therefore, our Monte Carlo simulations combine the hanging wall surfaces for Q6 alluvial fans with the top of the corresponding Q3 alluvial fans preserved in the footwall to give minimum fault throw rates (Figs. 2.4d & 2.4e). The most likely modal value for fault throw from the Monte Carlo simulation was taken to represent minimum rock uplift of Q6 surfaces relative to the modern-day Santa Clara River Valley. Rock uplift for a Q6 strath terrace at Orcutt Canyon was calculated by measuring incision of the terrace relative to the current stream level and assuming that rock uplift is in equilibrium with incision (Fig. 2.4c). Total incision was converted to a rate using the age of the uplifted Q6 alluvial fan from Timber Canyon. We acknowledge that the Q6 strath terrace at Orcutt Canyon is not necessarily coeval with the Q6 alluvial fan at Timber Canyon, but we have no direct date the strath terrace at Orcutt Canyon, so we rely on correlation of the soil profile development between the two surfaces to assume that the surfaces were abandoned at a similar time.

For the fold in the Santa Clara River Valley floor, we were unable to identify a burial depth for the top of the Q5 surface exposed at the crest of the fold beneath Q2 deposits that currently comprise the valley floor (Fig. 2.4f). Consequently, a topographic profile across the fold was used to calculate the maximum elevation of the fold relative to the current elevation of the Q2 surface on the modern valley floor and the value of maximum elevation of the fold was taken to represent minimum rock uplift (Fig. 2.4f).

Interval rock uplift rates, fault throw rates, and fault slip rates, which represent the rate of activity for time intervals between the formation of two proximal offset surfaces, were also calculated using Monte Carlo simulations. We use the output frequency histogram for the amount of total displacement (throw, rock uplift, or slip) between two surfaces and the probability density function output from the Monte Carlo simulation used to calculate the surface ages. Iterative Monte Carlo simulations were performed to model the most likely time interval between the terrace formation, and the most likely amount of displacement that has occurred during that time interval, all with associated uncertainties. The final interval displacement rates and uncertainties were calculated by combing the interval time and the amount of displacement (with uncertainties) output from the iterative simulation in a final Monte Carlo simulation.

Rates were calculated during Monte Carlo simulations by dividing either the total fault slip, fault throw, or minimum rock uplift at each location by our new cosmogenic exposure ages. We assumed a fault dip at the surface of 50–90° and modelled uncertainties accordingly from the simulation results. The basis for the 50–90° range in fault dips is provided in section 2.3.3 and a full breakdown of all equations and parameters used in displacement rate calculations is included in Appendix A5. We calculated tilt of geomorphic surfaces by plotting a linear regression for topographic profiles extracted from lidar data for both the base of the modern-day channel and the geomorphic surface. The slope of the modern-day stream was subtracted from the slope of the older geomorphic surface to give the tilt of the older geomorphic surface. Tilt calculations assumed that the older surface was deposited at the same angle as the current stream level.

2.2.5 Subsurface data

An approximately north-south oriented well-correlation section through Orcutt Canyon includes subsurface data for five wells down to ~3 km (Hopps et al., 1992). We reinterpreted well-log, lithological, and structural data contained in the correlation section to identify subsurface evidence for faulting at Orcutt Canyon. Additionally, two geotechnical reports encompassing trenching and/or

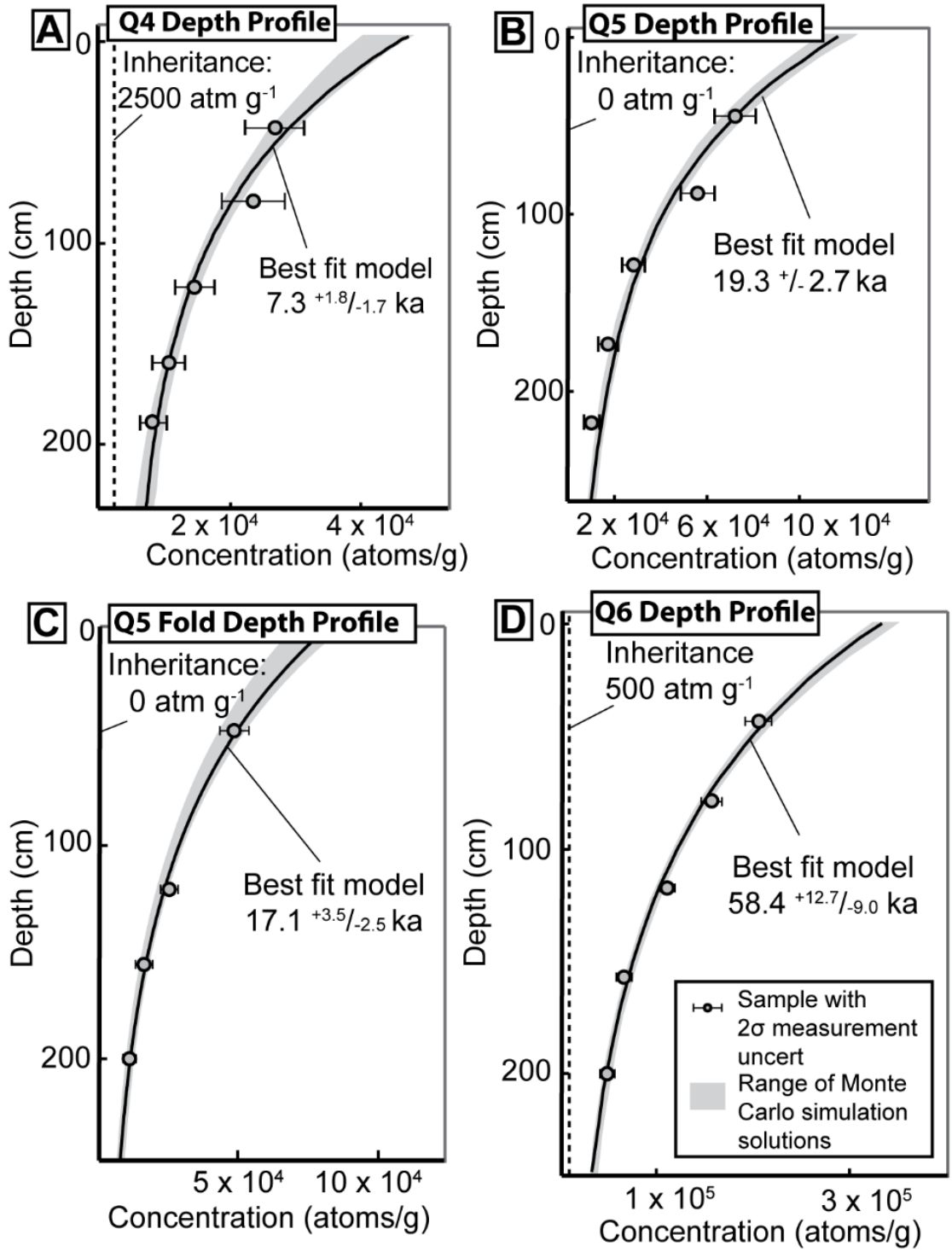

Figure 2.5 *Cosmogenic ^{10}Be depth profiles (see Figure 2.2 for sample locations). Gray circles are individual samples with error bars representing 2σ measurement uncertainties. Gray shaded area either side of the best fit profile represents the range of possible best fit solutions returned from Monte Carlo simulations. Depth profiles are calculated using a density of 1.7 - 1.8 g cm^{-3} and an attenuation length of 160 g cm^{-2}. (a) Q4 alluvial fan at Bear Canyon. (b) Q5 alluvial terrace at Orcutt Canyon. (c) Q5 fold in the Santa Clara River Valley. (d) Q6 alluvial fan at Timber Canyon. The depth profile for the Q4 fan at Orcutt Canyon, which we have not considered in our displacement rates, is included in Appendix A, Figure S2.*

shallow boreholes provide subsurface data along the western section of the range front and at Timber Canyon (Earth Systems Southern California, 2013; Earth Consultants International, 2015).

2.3 Results

2.3.1 Scarps

Bare earth hillshade imagery, topographic slope maps, topographic profiles, and field investigations confirm the presence of a north-side-up tectonic scarp in Q4 and Q5 alluvial fans at the mouth of Orcutt Canyon (Figs. 2.3, 2.4a, & 2.4b). The scarp warps Q4 and Q5 alluvial fans for ~420 m parallel to the trend of the range front (Figs. 2.3, 2.4a, & 2.4b). Additionally, soil profiles exposed in road cuts perpendicular to the scarp have Q4 soil profile development both north and south of the scarp. We take the fact that the scarps follow the orientation of the potential range-front fault, along with the similarity of soil profiles north and south of the fault, to indicate a tectonic rather than erosional origin for the scarp. We suggest the Orcutt Canyon scarp is a hanging wall collapse scarp based on our interpreted steep dip (>50°) for the fault at the surface and the poorly consolidated nature of the alluvial fan deposits in which the scarp is preserved (Carver and McCalpin, 1996) (Fig. 2.4). This model implies that faulting is emergent at Orcutt Canyon.

The flexural-slip faults at Orcutt and Timber Canyon create south-side-up scarps that are easily identifiable in both hillshade maps and in the field (Figs. 2.2, 2.3, & 2.4). The flexural-slip faults clearly offset Q6 surfaces at Orcutt and Timber Canyons. However, only one flexural-slip fault (the Thorpe fault) offsets Q5 terraces at Orcutt Canyon, and none of the flexural-slip faults offset Q4 or younger deposits. Moreover, paleoseismic trenching of a Q5 terrace that crosses the Culbertson fault revealed no evidence of Holocene activity (Earth Consultants International, 2015).

There is no clear surface deformation in the numerous alluvial fans along the eastern stretch of the range front between Timber Canyon and Sespe Creek (Fig. 2.2). A lack of surface deformation suggests either faulting is blind or inactive along the range front east of Timber Canyon.

Table 2.1 *Key sample details and ^{10}Be concentrations*

Sample name	Latitude (DD)	Longitude (DD)	Elevation (m)	Depth (cm)	Shielding Correction [a]	^{10}Be (atoms g^{-1})[b, c]
			Q4 Fan at Bear Canyon			
KR-1	34.4397	-119.1282	459	39	0.998	26925 +/- 1100
KR-2				74	0.998	23559 +/- 1205
KR-3				116	0.998	14560 +/- 681
KR-4				153	0.998	10496 +/- 681
KR-5				182	0.998	8028 +/- 743
			Q5 Terrace at Orcutt Canyon			
OCN- 1	34.3994	-119.0356	416	42	0.997	72312 +/- 2177
OCN- 2				84	0.997	55892 +/- 1699
OCN- 3				124	0.997	28230 +/- 1054
OCN- 4				169	0.997	17336 +/- 839
OCN- 5				212	0.997	10135 +/- 685
			Q6 Fan at Timber Canyon			
TC-1	34.4011	-119.0171	430	39	0.995	204712 +/- 6316
TC-2				76	0.995	156845 +/- 4986
TC-3				112	0.995	110114 +/- 3186
TC-4				153	0.995	62617 +/- 1942
TC-5				196	0.995	48588 +/- 1629
			Q5 Fold in Santa Clara River Valley			
FW-1	34.3832	-118.9784	139	41	0.999	48179 +/- 1720
FW-3				116	0.999	24940 +/- 978
FW-4				150	0.999	15717 +/- 927
FW-5				196	0.999	10662 +/- 614
			Q4 Terrace at Orcutt Canyon			
OC4 1	34.3859	-119.036	225	45	0.984	17849 +/- 790
OC4 2				82	0.984	16895 +/- 811
OC4 3				114	0.984	14733 +/- 720
OC4 4				160	0.984	13918 +/- 719
OC4 5				202	0.984	12866 +/- 670

[a] Calculated using the CRONUS-Earth Geometric Shielding Calculator version 1.1 (available online at: http://hess.ess.washington.edu/)

[b] ^{10}Be concentrations and associated measurement uncertainties are blank corrected relative to batch specific process blanks. Total atoms ^{10}Be in process blanks (atoms): KR & OC4 = 8857 $^{+}$/- 2288, OCN = 11187 $^{+}$/- 2388, TC & FW = 7876 $^{+}$/- 2786.

[c] Calculated using 07KNSTD ^{10}Be measurement and calibration standard number 01-5-2 with a assumed ^{10}Be/^{9}Be ratio of 8.558 x 10^{-12} (Nishiizumi et al., 2007).

2.3.2 ^{10}Be terrace geochronology

Our new surface cosmogenic exposure-age determinations generally fall within the range of published soil age estimates, but with improved precision (Rockwell, 1983; DeVecchio et al., 2012a) (Table 2.2, Fig. 2.2). Our ages for both Q5 deposits of 19.3 $^{+}/_{-}$ 2.7 ka (all ages are Bayesian most probable values with 2σ uncertainties throughout) for the Q5 terrace at Orcutt Canyon (Fig. 2.5b) and 17.1 $^{+3.5}/_{-2.5}$ ka for the folded Q5 fan in the Santa Clara River Valley (Fig. 2.5c) show good agreement and overlap with the existing age for Q5 deposits within the Ventura basin (15-30 ka) (Rockwell, 1983). We revise the original designation of the uplifted fan surface at Timber Canyon from Q7 (160–200 ka) to Q6 (38–92 ka) (Rockwell, 1983). Revision is based on re-evaluation of the soil profile in the field, the close match of the existing Q6 age of 54 ±10 ka (Rockwell, 1983) to our new cosmogenic numerical age (58.4 $^{+12.7}/_{-9.0}$ ka), and the similar value of tilt between a Q6 surface at Orcutt Canyon and the uplifted fan surface at Timber Canyon (Table 2.2). However, it is possible the Q6 fan surface we dated at Timber Canyon may include remnants of Q7 soils in places, as described in Rockwell (1983). We discount our age of 2.2 $^{+1.4}/_{-1.2}$ ka for the Q4 alluvial fill terrace at Orcutt Canyon (Appendix A, Fig. S2). Further investigation of the soil profile in the Q4 sample location leads us to suggest that a gravel channel in the top 1.5 m of the soil profile is a local, anomalously-young deposit and not representative of the age of the Q4 terrace we sampled as a whole. Therefore, we use our age of the Q4 fan at Bear Canyon of 7.3 $^{+1.8}/_{-1.7}$ ka (Fig. 2.2a) for our slip rate calculations at Orcutt Canyon, which is slightly lower than the previous age for Q4 surfaces of 8–12 ka (Rockwell, 1983) but overlaps with this age within the uncertainties of our measurements.

All samples used in the depth profiles show a good fit to an exponential profile, within individual sample 2σ measurement uncertainties (Figs. 2.5 & Appendix A, Fig. S2). Best-fit inheritance values are low with a maximum value of 11,500 atoms g^{-1} in the Q4 sample at Orcutt Canyon (Appendix A, Fig. S2) and minimum values that are indistinguishable from zero in both the Q5 sample locations (Fig. 2.5). Sediment stored deep within the hill slopes, beneath the attenuation length of cosmic rays, will not accumulate significant ^{10}Be prior to erosion and subsequent deposition within the terrace. Therefore, low inheritance values indicate that source material is rapidly eroded from material stored deep within

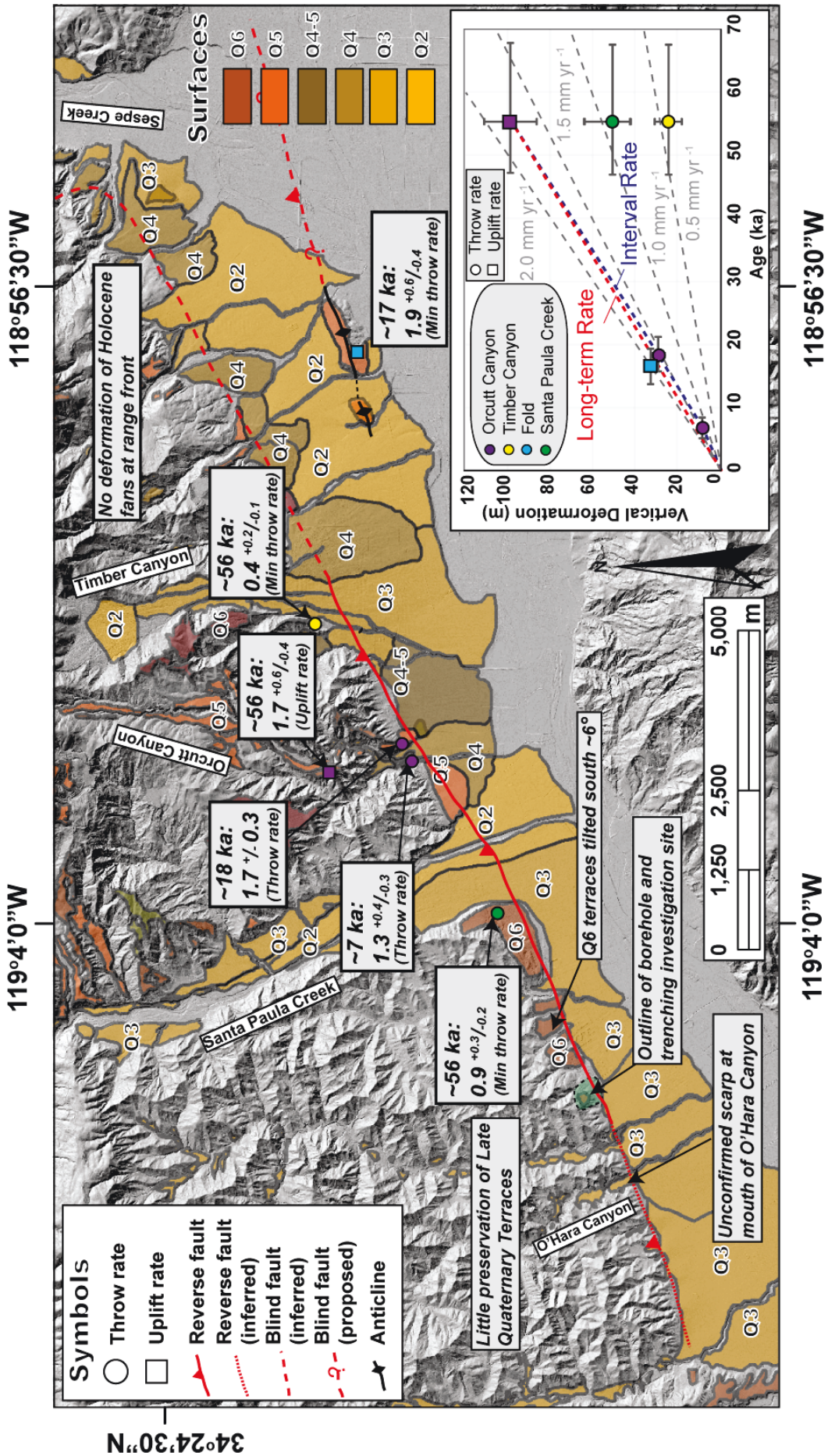
Surfaces
Q6
Q5
Q4-5
Q4
Q3
Q2
Sespe Creek
No deformation of Holocene fans at range front
Timber Canyon
Orcutt Canyon
Santa Paula Creek
O'Hara Canyon
~17 ka: 1.9 +0.6/-0.4 (Min throw rate)
~56 ka: 0.4 +0.2/-0.1 (Min throw rate)
~56 ka: 1.7 +0.6/-0.4 (Uplift rate)
~18 ka: 1.7 +/- 0.3 (Throw rate)
~7 ka: 1.3 +0.4/-0.3 (Throw rate)
~56 ka: 0.9 +0.3/-0.2 (Min throw rate)
Q6 terraces tilted south ~6°
Outline of borehole and trenching investigation site
Unconfirmed scarp at mouth of O'Hara Canyon
Little preservation of Late Quaternary Terraces
Symbols
Throw rate
Uplift rate
Reverse fault
Reverse fault (inferred)
Blind fault (inferred)
Blind fault (proposed)
Anticline
Vertical Deformation (m)
Age (ka)
Throw rate
Uplift rate
Orcutt Canyon
Timber Canyon
Fold
Santa Paula Creek
Long-term Rate
Interval Rate
2.0 mm yr-1
1.5 mm yr-1
1.0 mm yr-1
0.5 mm yr-1
0 1,250 2,500 5,000 m
N
118°56'30"W
119°4'0"W
34°24'30"N

Figure 2.6 *Summary of spatial and temporal fault throw rates for the Southern San Cayetano fault. Location of throw rate is indicated by coloured circles (squares denote uplift rates rather than fault throw): purple = Orcutt Canyon, yellow = Timber Canyon, green = Santa Paula Creek, and blue = Santa Clara River Valley. Inset graph shows fault throw (or uplift if appropriate) against surface age. Coloured circles are fault throw amounts (squares are uplift amounts) with colours corresponding to the location of the rate on the map. Error bars are uncertainty in amount of fault throw (vertical error bars) or age (horizontal error bars) derived from Monte Carlo simulations. Throw rates of 2.0, 1.5, 1.0, & 0.5 mm yr^{-1} are indicated with grey dashed lines. The red dashed line is the long-term rate and interval rates are denoted by the blue dashed lines.*

the landscape. A slightly higher inheritance value for the Q4 depth profile at Orcutt Canyon (11,500 atoms g^{-1} compared to 2,500-0 atoms g^{-1} for all other samples) (Figs. 2.5 & Appendix A, Fig. S2) is indicative of a potentially shallower source material or a slower erosion rate for source material within the gravel channel contained within the sampled Q4 terrace.

2.3.3 Fault Geometry

Data from well-correlation sections, shallow borehole at the range front, and surface observations form the basis for our interpretation of a north-dipping range-front fault at Orcutt Canyon with 50–90° dip from the surface to ~100 m depth, below which the fault dip decreases to ~20° (Fig. 2.7). We employ a fault dip of 50–90° in our Monte Carlo simulations and do not use the proposed subsurface dip of 20° in slip rate calculations because these rates are calculated from surface offsets at the range front where we interpret the fault to have steeper dip. On the well-correlation section through Orcutt Canyon, we note an abrupt change in dips that occurs at progressively shallower depths southwards for wells in the footwall of the San Cayetano fault (Hopps et al., 1992) (Fig. 2.7). The change in dips correlates to a fault with a shallow (~20°) north dip in the subsurface, with ~100 m of stratigraphic offset (Fig. 2.7). However, when projected to the surface, a fault with 20° north-dip that passes through the sections of variable dips observed in subsurface well-log data would steepen in dip in the upper ~100 m if it intersects with our preferred fault surface trace (Fig. 2.7). Fault evidence from borehole logs contained in a geotechnical report along the western section of the range front suggests a north-side-up sense of movement on three steeply-dipping northwest-southeast zones of faulting, with the majority of faults recording dips between 70–90° (Earth Systems Southern California, 2013) (Appendix A, Table ST3). Additionally, we suggest the linear nature of the range front (Fig. 2.2) is indicative of a steep fault dip at the surface (assuming that the location of the range front is fault controlled) and analysis of the

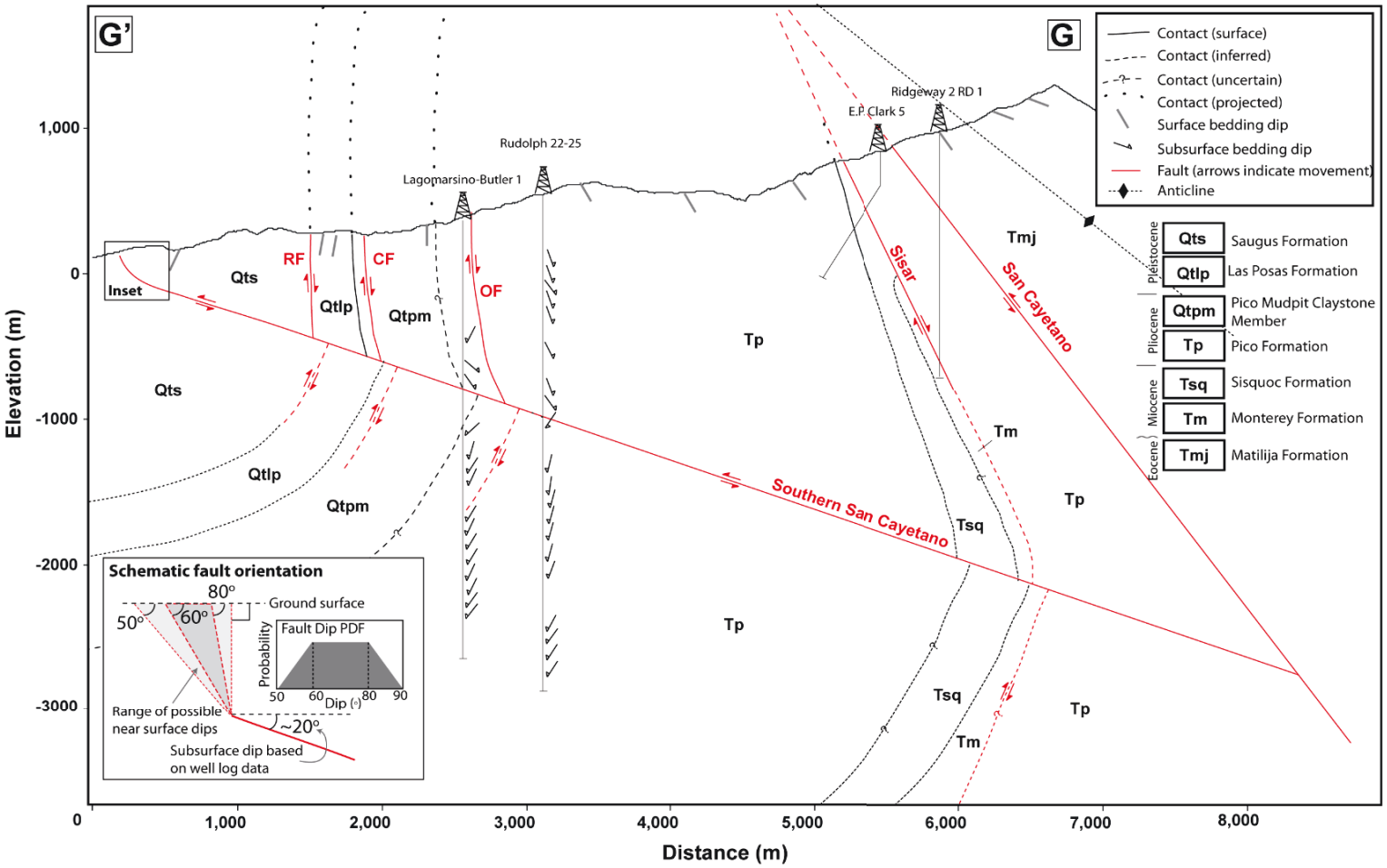

Figure 2.7 *Cross section G-G' showing our interpretation for the subsurface geometry for the Southern San Cayetano fault at Orcutt Canyon. The San Cayetano, Sisar, Rudolph (RF), Culbertson (CF), and Orcutt (OF) faults, along with the subsurface stratigraphy and the well data are taken from Hopps et al. (1992). The line of section is indicated in Figure 2.2. Surface dips and geology are from Dibblee (1990a). Inset shows schematic for the range of steepening fault dips we interpret in the shallow subsurface compared to the ~20° dip we interpret in the deeper subsurface. The custom trapezoidal probability density function used to model uncertainty in the near surface fault dip during Monte Carlo simulations is based on a range of fault dips observed in shallow subsurface boreholes (Earth Systems Southern California, 2013), and the range of potential apparent fault dips from analysis of the fault position within the scarps (Appendix A, Fig S1).*

intersection of the fault trace with the scarps suggests a range of apparent dips at the surface between 51–64° (Appendix A, Fig. S2).

We show the Sisar fault as offset, because we observe no evidence of Holocene activity on the Sisar fault in both digital geomorphic maps and in the field, which suggests that the Sisar fault is potentially inactive at Orcutt Canyon. Conversely, both the main strand of the San Cayetano fault (Rockwell, 1988) and the range-front fault at Orcutt Canyon demonstrate evidence for Holocene activity in the form of fault scarps cutting Holocene alluvial fans (Fig. 2.3. The fault we present in Figure 2.7 offsets the overturned Sisar fault and connects with the San Cayetano fault at ~3 km depth (Fig. 2.7).

2.3.4 Fault deformation rates

Within the resolution of our data, our results indicate that long-term average fault slip rates and fault throw rates at Orcutt Canyon have remained relatively constant for the last ~19 ka (Table 2.2, Fig. 2.6). The long-term average incision rate at Orcutt Canyon since ~58 ka, which we use as a proxy for rock uplift rate, overlaps with fault throw rates since ~19 ka, which indicates that activity on the SSCF has not varied significantly over the last ~58 ka (Fig. 2.6). Rock uplift amounts at Orcutt Canyon decrease with decreasing surface age, with 9.0 ± 1.4 m fault throw across the youngest Q4 scarp at the mouth of Orcutt Canyon and 99.7 ± 12.4 m average rock uplift of the oldest Q6 strath terrace relative to the modern-day stream level (Table 2.2). All fault throw rates at Orcutt Canyon overlap within uncertainties, with a maximum value of $1.7\ ^{+0.7}/_{-0.4}$ mm yr^{-1} for the interval ~19–7 ka (deformation rates are mode and 95% confidence interval throughout) and a minimum value of $1.2\ ^{+}/_{-}0.3$ mm yr^{-1} since ~7 ka (Table 2.2).

The fault slip rate from ~19 ka to the present day is $1.7\ ^{+0.6}/_{-0.2}$ mm yr^{-1} and from ~7 ka to the present day the average slip rate is $1.3\ ^{+0.5}/_{-0.3}$ mm yr^{-1}. The interval fault slip rate between ~19 ka and ~7 ka is $1.9\ ^{+1.0}/_{-0.5}$ mm yr^{-1}.

Q6 surfaces at Orcutt and Timber Canyons are tilted southwards more than the younger Q5 and Q4 surfaces (Table 2). Tilt rates at Orcutt Canyon remained constant during the Late Pleistocene at 0.14° ka^{-1} since ~58 ka and 0.12° ka^{-1} since ~18 ka (Table 2.2). Tilt rates at Orcutt Canyon then increased during the Holocene to 0.33° ka^{-1} since ~ 7 ka (Table 2.2). Additionally, we note that Q6 fan surfaces along the western range front are tilted southwards by ~6° relative to Q3 surfaces in the footwall.

The rock uplift rate for the Q6 alluvial fans at Timber Canyon and Santa Paula Creek are $0.4\ ^{+0.2}/_{-0.1}$ mm yr^{-1} and $0.9\ ^{+0.3}/_{-0.2}$ mm yr^{-1} since ~58 ka, respectively (Table 2). Both are lower than the Q6 rock uplift rate at Orcutt Canyon since ~58 ka, although the Q6 Timber Canyon fan is tilted slightly more than the Orcutt Canyon Q6 surface (Table 2). We consider the rock uplift rates for the Q6 alluvial fans at Timber Canyon and Santa Paula Creek to be minimum rates, as uplift is measured relative to younger Q3 deposits in the fault footwall (Fig. 2.6). All rates assume that multiple terrace treads are not sharing the

same strath, therefore overprinting the initial age signal with a younger age. We have not determined

Table 2.2 *Cosmogenic exposure ages, offset amounts, displacement rates, and tilting for the SSCF*

Surface	Age or Time interval (ka)			Throw (m)			Throw Rate (mm yr^{-1})			Slip (m)			Slip Rate (mm yr^{-1})			Tilt (°)	Tilt Rate (°/ka)
Q4 OC	7.3	+/-	1.8/1.7	9.0	+/-	1.4	1.2	+/-	0.3	9.7	+/-	2.6/1.7	1.3	+/-	0.5/0.3	2.3	0.33
Q5-Q4 OC	11.8^{++}	+/-	2.4/3.0	20.5	+/-	3.3/3.4	1.7	+/-	0.7/0.4	21.8	+/-	9.0/4.2	1.9	+/-	1.0/0.5	n/a	n/a
Q5 OC	19.3	+/-	2.7	29.5	+/-	3.0	1.5	+/-	0.3/0.2	31.7	+/-	8.8/3.6	1.7	+/-	0.6/0.2	2.2	0.12
Q6-Q5 OC	40.6^{++}	+/-	11.2/8.4	70.2	+/-	24.6	1.7	+/-	0.9/0.6	n/a	+/-	n/a	n/a	+/-	n/a	n/a	n/a
Q6 OC	58.4	+/-	12.7/9.0	99.7**	+/-	12.4	1.6+	+/-	0.6/0.4	n/a	+/-	n/a	n/a	+/-	n/a	7.6	0.14
Q5 SCRV	17.1	+/-	3.5/2.5	33.4*	+/-	3	1.9+	+/-	0.6/0.4	n/a	+/-	n/a	n/a	+/-	n/a	n/a	n/a
Q6 TC	58.4	+/-	12.7/9.0	24.9**	+/-	6.5	0.4	+/-	0.1	n/a	+/-	n/a	n/a	+/-	n/a	9.6	0.17
Q6 SPC	58.4	+/-	12.7/9.0	51.4**	+/-	14.3/8.4	0.9	+/-	0.3/0.2	n/a	+/-	n/a	n/a	+/-	n/a	2.9	0.05

* Uplift of the top of a folded Q5 surface relative to the corresponding unfolded Q2 surface in the fault footwall.

** Average of incision/uplift of the Q6 surface relative to the modern stream level in Orcutt Canyon or Q3 surfaces in the modern day Santa Clara River valley floor.

All throw rates are calculated using a Monte Carlo simulation by correlating offset surfaces across the fault. Rates indicated with a + denotes 'uplift' rate rather than fault throw rate because two surfaces were not present that could be correlated across the fault and these rates are based on offsets described in * and ** above.

All rates are calculated from the terrace age using the present day as a pin except time interval rates (indicated by++) which are calculated for the time interval between corresponding terrace ages.

OC = Orcutt Canyon, TC = Timber Canyon, SPC = Santa Paula Creek, SCRV = Fold in Santa Clara River Valley

for the top of the Q5 surface below the fold in the Santa Clara River Valley, therefore, our rock uplift rate is a minimum (Fig. 2.6).

2.4 Discussion and Implications

Our results provide the first geomorphic and subsurface well-log evidence for a young low-angle thrust fault beneath Orcutt Canyon. Despite a large amount of previous geologic, geomorphic, and subsurface investigation, the fault described here was previously undetected beneath Orcutt and Timber Canyons (Rockwell, 1988; Dibblee, 1990b; Hopps et al., 1992).

2.4.1 Fault activity

Given the subtle nature of geomorphic and subsurface expression associated with young faults, various datasets must be examined in detail to provide compelling fault evidence. Uplifted Late Pleistocene and Holocene alluvial surfaces (Fig. 2.2 & 2.3), tectonic scarps (Fig. 2.3), faults observed in shallow boreholes (section 2.3.3), and subsurface dip-data (Fig. 2.7) provide evidence for the existence of a young, continuous, north-dipping, low-angle fault along the northern Santa Clara River Valley (Figs. 2.6 & 2.7).

We suggest that our shallow, north-dipping, range-front fault at Orcutt Canyon could be the westward continuation of the Pagenkopp fault because the geometry we present in Figure 2.7 for the range front fault is almost identical to the Pagenkopp fault to the east (Çemen, 1989; Hopps et al., 1992). However, the lack of surface scarps east of Timber Canyon, combined with a lower rock uplift rate at Timber Canyon compared to Orcutt Canyon, suggests that the section of the range-front fault previously mapped as the Pagenkopp fault is either inactive, blind, or surface evidence for the Pagenkopp fault has been removed by erosion. However, we suggest that active deformation steps southwards east of Timber Canyon on a blind en-echelon fault splay beneath the Q5 fold in the Santa Clara River Valley (Fig. 2.6). Furthermore, we speculate that this blind fault splay continues eastwards in the subsurface, potentially as far as the eastern strand of the San Cayetano fault at Fillmore.

Evidence for faulting along the western range front, west of Santa Paula Creek, comprises steeply-dipping fault segments observed in trenching and borehole studies (Appendix A: Table ST3) (Earth

Systems Southern California, 2013) and southward tilting of Q6 fan surfaces (Fig. 2.6). We map very few uplifted and tilted alluvial terraces along the western section of the range front compared to the central and eastern sections (Fig. 2.6). The decrease in preservation along the western section is probably due to the lack of coarse clastic sediments being shed from Sulphur Mountain (Fig. 2.1), which primarily consists of fine-grained Miocene and Pliocene age sediments (Dibblee and Ehrenspeck, 1992b).

We interpret our results to suggest that the low-angle SSCF has been active since at most ~58 ka. This is based on the observation that the Orcutt, Rudolph, and Culbertson flexural-slip faults at Orcutt Canyon, and elsewhere, clearly offset Q6 surfaces and produce pronounced scarps (e.g., Fig. 2.4c). In contrast, only the Thorpe fault (Fig. 2.3) has expression in a surface younger than Q6 where the Thorpe fault creates a well-defined south-side-up scarp in a Q5 alluvial terrace towards the upper reach of Orcutt Canyon. None of the flexural-slip faults offset surfaces Q4 or younger (section 2.3.1). A decrease in activity on the flexural-slip faults is also demonstrated by a lack of evidence for active faulting recorded in paleoseismic trenching within Q5 soils that cross the Culbertson fault at Timber Canyon (Earth Consultants International, 2015). We speculate that the decrease in activity on the flexural-slip faults results from onset of activity on the SSCF, because the SSCF cuts across the flexural-slip faults. Therefore, in Figure 2.7, the Orcutt, Rudolph, and Culbertson flexural-slip faults are offset by the SSCF. The decrease in activity in the flexural-slip faults implies that the onset of activity on the SSCF occurred at some point after ~58 ka, the age of the Q6 fan at Timber Canyon, which is offset by the Culbertson fault (Fig. 2.3). A maximum ~58 ka age explains the small stratigraphic offset for the SSCF and why the SSCF has previously been overlooked in subsurface data at Orcutt Canyon.

We have adopted the name “Southern San Cayetano Fault” for the shallow north-dipping fault along the northern Santa Clara River Valley described here, as this is the most recent name suggested for a continuous, active fault in this area (Hubbard et al., 2014). However, we stress that our interpretation of the SSCF, with a ~20° north subsurface-dip along the range front, has a drastically different geometry from that used in previous modelling, which incorporated a continuous 40-65° north dip down to ~7 km and outcrops farther south in the centre of Santa Clara River Valley (Hubbard et al., 2014).

Additionally, the presence of north-side-up scarps and confirmation of a north-dip in subsurface data leads us to discount a south-dipping model of the SSCF (Hubbard et al., 2014).

2.4.2 Seismic hazard implications

Confirmation of an active, young, low-angle thrust in the well-studied Santa Clara River Valley provides a good example of how significant seismic hazards, in the form of young faults, can be overlooked in geologic, geomorphic, and subsurface datasets. The seismic source of the 1994 Northridge earthquake could potentially have been identified prior to the earthquake if it had been recognized that uplift of the footwall of the Santa Susana fault was a result of activity on the Northridge blind thrust (Yeats and Huftile, 1995). The footwall of the central San Cayetano fault is uplifted to high elevations above the Santa Clara River Valley, and footwall uplift has previously been attributed to activity on south-dipping blind thrusts, such as the Sisar fault (Yeats and Huftile, 1995). Here, we suggest that footwall uplift of the central San Cayetano fault prior to ~58 ka could have occurred on

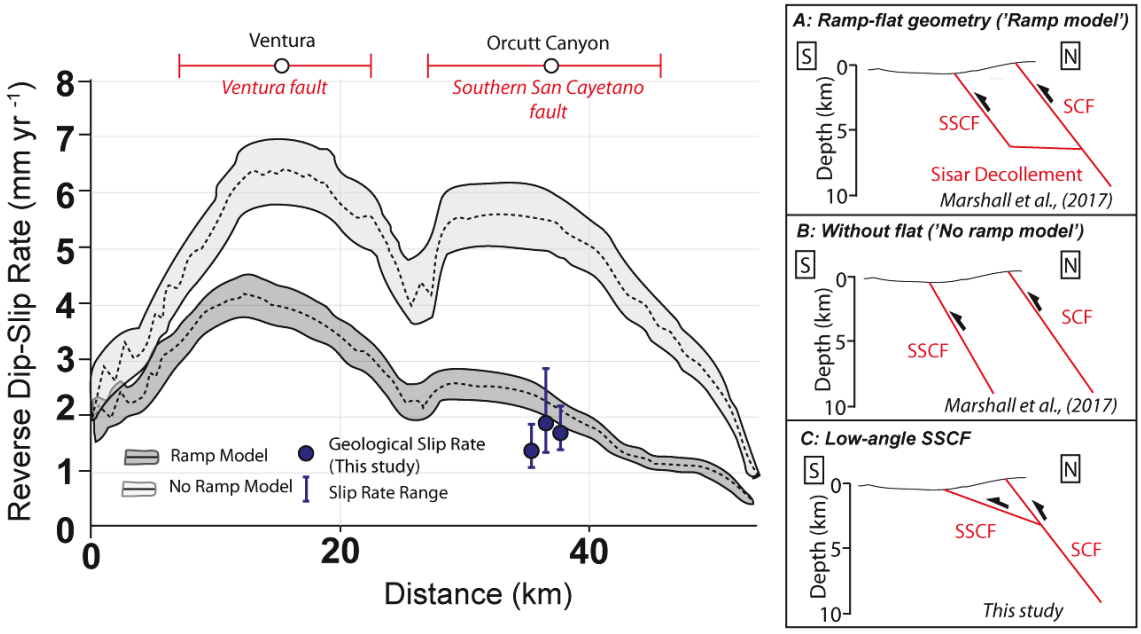

Figure 2.8 *Comparison of along-strike reverse fault slip rates for the Ventura, Pitas Point, and Southern San Cayetano faults (SSCF) assuming either a 'ramp' or 'no ramp' subsurface geometry (adapted from Marshall et al. [2017]). Dashed black lines trace best-fit model predicted along-strike reverse slip rate distributions measured from mechanical models based on GPS data. Gray ranges reflect regional strain rate boundary condition uncertainties. Dark grey represents 'ramp' model and light grey represents 'no ramp' model. Blue circles are geologically calculated reverse slip rates at Orcutt Canyon with blue lines for error bars (this study). (A) Schematic cross sections showing structure of the San Cayetano fault (SCF) and the connection with the SSCF used to calculate mechanical model derived slip rates from GPS data in the 'ramp' model (Marshall et al. [2017], after Hubbard et al. [2014]). (B) Schematic cross sections showing structure of the San Cayetano fault and the SSCF used in mechanical models to calculate slip rates for the 'no ramp' model (Marshall et al. [2017]). (C) Schematic cross section showing the geometry of the SSCF and the connection of the SSCF with the San Cayetano fault based on data from this study.*

south-dipping faults, but a component of any current footwall uplift must be due to fault activity in the hanging wall of the SSCF. This implies that any future earthquake could result from activity on the active SSCF, or some combination of the SSCF and the main strand of the San Cayetano fault.

2.4.3 Implications for multi-fault ruptures

In addition to posing significant individual seismic hazards, young faults or faults with small offsets can potentially act as rupture pathways during large-magnitude multi-fault ruptures (Fletcher et al., 2014; Hamling et al., 2017). For example, the Papatea fault is a small offset fault in central New Zealand, which was unrecognized prior to the 2017 M_w 7.8 Kaikōura earthquake, but played a key role in stress transfer during the event (Hamling et al., 2017; Hollingsworth et al., 2017). Our results provide confirmation of a young SSCF along the northern Santa Clara River Valley that fills in a 23 km gap that previously existed between the Ventura and San Cayetano faults at the surface (Fig. 2.1). The result is a continuous ~150 km surface trace including the Pitas Point, Ventura, Southern San Cayetano, and San Cayetano faults. Previous work has suggested that this fault system could potentially act as a pathway for large-magnitude multi-fault earthquakes (Hubbard et al., 2014; Rockwell et al., 2016; Marshall et al., 2017).

The only existing slip rate estimates for the SSCF are mechanical model-calculated slip rates based on a regional GPS derived strain rate tensor (Marshall et al., 2017). Our slip rates for the SSCF show good agreement with slip rates predicted by the Marshall et al. (2017) 'ramp' model and are significantly lower than slip rate estimates for the 'no ramp' model (Fig. 2.8). The ramp model of Marshall et al. (2017) (Fig. 2.8a) implies that the Pitas Point, Ventura, Southern San Cayetano, and San Cayetano fault system forms a single through-going plane at depth that may provide a potential multi-fault rupture pathway for past and future large earthquakes (Hubbard et al., 2014; Marshall et al., 2017). However, the interpretation of the SSCF used in three-dimensional mechanical models was not confirmed by geological field data and the results presented here suggest a change in dip of ~20–40° from the Ventura fault along-strike to the SSCF (Fig. 2.8a). A 20–40° change in dip does not represent a single through-going buried surface and could act as a potential stress barrier and decrease the likelihood of persistent through-going ruptures between the Ventura fault and the SSCF. Consequently, if through-going

ruptures do propagate between the Ventura fault and the SSCF, then we speculate a tear fault is present, which transfers strain during through-going ruptures similar to the style of interaction previously identified between faults elsewhere in the Ventura Basin (Thibert et al., 2005; DeVecchio et al., 2012b).

Assessing the possibility of through-going ruptures between the Ventura and San Cayetano faults is further complicated by a comparison of fault slip rates along-strike. Fault slip rates are 4.6–6.9 mm yr^{-1} since 30 +/- 10 ka for the Ventura fault (Hubbard et al., 2014) in the western Ventura Basin, 7.4 +/- 3 mm yr^{-1} since 500 ka for the eastern San Cayetano fault (Huftile and Yeats, 1996) in the eastern Ventura Basin, and 1.05 +/- 0.4 mm yr^{-1} up to 4.15 +/- 0.85 mm yr^{-1} since ~25 ka on the western San Cayetano fault (Rockwell, 1988) in the central Ventura Basin. These values are in contrast to a lower slip rate for the SSCF of 1.7 $^{+0.6}/_{-0.2}$ mm yr^{-1} since ~19 ka (this study) in the central part of the basin. Higher slip rates for the Ventura and eastern San Cayetano faults suggest that these faults individually accommodate a greater proportion of the 7-10 mm yr^{-1} of regional horizontal shortening suggested by GPS data (e.g., Marshall et al., 2013) than the SSCF or the western San Cayetano fault. However, the sum of slip rates for the SSCF and the western San Cayetano fault in the central Ventura Basin roughly equates to the individual Ventura and eastern San Cayetano faults, albeit within large associated uncertainties. Consequently, we suggest that strain in the upper ~3 km of the central Ventura Basin is partitioned between the SSCF and the western San Cayetano fault.

Alternatively, a lower slip rate for the SSCF could indicate that the SSCF is a rupture pathway that is predominantly, but not exclusively, active during through-going rupture between the San Cayetano and Ventura faults. Observations of up to 11 m coseismic throw events on the Pitas Point/Ventura fault (McAuliffe et al., 2015; Rockwell et al., 2016) and ~5 m coseismic slip events on the eastern San Cayetano (Dolan and Rockwell, 2001) indicate that large-magnitude (M_w 7–8) earthquakes can potentially occur between the Pitas Point, Ventura, and San Cayetano faults. However, these events do not necessarily always involve simultaneous rupture of all faults along-strike (McAuliffe et al., 2015). We propose that the lower slip rate for the SSCF may reflect a low frequency of large-magnitude through-going ruptures between the Ventura and San Cayetano faults. The Ventura and San Cayetano

faults may preferentially rupture independently or in combination with other proximal faults such as the Pitas Point, Red Mountain, or Arroyo Parida/Santa Ana faults (Fig. 2.1).

2.5 Conclusions

We incorporated lidar topographic data and a new ^{10}Be geochronology to provide geomorphic evidence for the existence of a low-angle (20°) Southern San Cayetano fault (SSCF). The SSCF is a young fault that has only been active since at most ~58 ka. Consequently, the SSCF has little stratigraphic offset in the subsurface and has been previously overlooked in geologic or geomorphic mapping and subsurface well-log data at Orcutt Canyon. Displacement rates averaged over multiple timescales for the SSCF have remained fairly constant since the Late Pleistocene with slip rates ranging from a maximum of 1.9 $^{+1.0}/_{-0.5}$ mm yr^{-1} since ~19–7 ka to 1.3 $^{+0.5}/_{-0.3}$ mm yr^{-1} since ~7 ka.

Confirmation of an active, young, low-angle SSCF along the length of the northern Santa Clara River Valley provides new insights into the nature of seismic hazards in a densely populated area of southern California. The SSCF may rupture synchronously with the well-established main strand of the San Cayetano fault and, furthermore, it is possible that the SSCF enhances fault connectivity and facilitates multi-fault ruptures including the San Cayetano, Ventura, and Pitas Point faults. However, given structural complexities, different slip histories, and different slip rates between the Ventura, San Cayetano, and Southern San Cayetano faults, these faults may be less prone to synchronous rupture than previously suggested.

Our results demonstrate that young, active, faults, such as the SSCF, can easily be overlooked in geomorphic and subsurface data, but may represent significant individual seismic hazards or potentially enhance structural connectivity in large-magnitude earthquakes in complex thrust fault systems.

2.6 Acknowledgments

The authors thank C. Singer and R. Davey for assistance in field work and sample collection, and A. Hidy for invaluable advice on plotting depth profiles. Work supported by funding from SCEC award numbers 15100 (to DHR and DDV), 17184 (to DHR), 16049 (to TKR), and 17024 (to TKR). The authors also acknowledge the financial support from the Australian Government for the Centre for

Accelerator Science at the Australian Nuclear Science and Technology Organization (ANSTO) through the National Collaborative Research Infrastructure Strategy (NCRIS). This work was completed thanks to ANSTO award number 10125 (to DHR). Additional funding was supplied by a Royal Geological Society post-graduate research grant (to AH) and a post-graduate research grant from the British Society for Geomorphology (to AH). Finally, we thank Richard Heermance for constructive comments and revisions of this article.

Chapter 3: The significance of non-planar three-dimensional fault geometry for static stress transfer and earthquake hazards on complex thrust faults in southern California[+]

Chapter Abstract

To investigate the degree to which small offset or young fault can enhance stress transfer, we present a series of cross sections and a three-dimensional fault model across the Southern San Cayetano fault (SSCF) based on integration of surface data with petroleum industry well-log data from the Ventura basin, southern California, USA. Our fault model for the SSCF is incorporated with other regional faults in static Coulomb stress modelling to test the application of such modelling to thrust faults using an unconventionally complex geometry and to further the understanding of stress distribution and seismic hazards in the Ventura basin. The results of the subsurface well investigation provide evidence for a low-angle SSCF that dips ~15° north and connects with the western San Cayetano fault around 1.5–3.5 km depth. A comparison of subsurface fault geometry with the spatial distribution of surface deformation leads us to suggest that Holocene deformation may have been focused on the SSCF rather than the upper ~3 km of the central section of the western San Cayetano fault. The results of the stress modelling indicate that static Coulomb stress transfer may increase the likelihood of potential multi-fault earthquakes between the Pitas Point, Ventura, Southern San Cayetano, and San Cayetano faults, in certain rupture scenarios. However, the degree to which static Coulomb stress transfer may enhance the prospect of multi-fault earthquakes in the Ventura basin is critically dependant on the subsurface structural model adopted for the Pitas Point and Ventura faults. Overall, our data demonstrate that an accurate characterization of three-dimensional subsurface fault geometry is important for reducing uncertainties when assessing future patterns of regional seismicity and highlights the importance of integrating field observations, surface data, and subsurface data to create realistic fault inputs when modelling static Coulomb stress transfer.

+ A version of this chapter is in preparation for submission to the *Journal of Geophysical Research: Solid Earth* with the following author list:

A. Hughes, R. E. Bell, Z. K. Mildon, D. H. Rood, A. C. Whittaker, T. K. Rockwell, Y. Levy, D. E. DeVecchio, S. T. Marshall, C. Nicholson

AH conceived of the idea of the research and performed all the data analysis, prepared the figures, and wrote the manuscript. RB aided AH with the analysis of subsurface data and the code for creating variable dip faults in *Coulomb 3.4* was written by ZM. All authors discussed the science and commented on the manuscript.

3.1 Introduction

Characterizing the 3D geometry of faults in the subsurface is crucial in order to determine how faults grow and interact (Cowie, 1998; Gupta et al., 1998; Wedmore et al., 2017) and to investigate how structural complexities in fault geometry can affect dynamic rupture propagation and static stress distribution (Oglesby et al., 1998; Oglesby and Day, 2001; Lozos et al., 2012; Mildon et al., 2016; Biasi and Wesnousky, 2017). The importance of having a good understanding of the 3D fault network geometry to improve seismic hazard analysis has been brought into focus by several recent large-magnitude, multi-fault earthquakes that propagated along multiple faults with complex geometry and kinematics. For example, both the 2016 M_w 7.8 Kaikōura earthquake, New Zealand (Hamling et al., 2017) and the 2010 M_w 7.2 El Mayor Cucapah earthquake, Mexico (Fletcher et al., 2014; Fletcher et al., 2016) involved slip on multiple faults with various orientations and senses of slip. During the Kaikōura earthquake, small faults that individually had been interpreted to represent low seismic hazard played a key role in enhancing both fault connectivity and stress transfer during the event (Clark et al., 2017; Hamling et al., 2017). However, despite potentially playing an important role in enhancing stress transfer, small offset and/or young faults are often overlooked because they may not have pronounced stratigraphic offset and are difficult to identify in subsurface data (Hughes et al., 2018; Pei et al., 2018).

The distribution of stress on a fault surface exerts a fundamental control on the nucleation, propagation, and size of earthquake ruptures (Rice, 1992; King et al., 1994; Rydelek and Sacks, 1999; Freed, 2005; Strader and Jackson, 2014; Biasi and Wesnousky, 2016). Although it is well-known that faults are non-planar (e.g., Candela et al., 2011; Brodsky et al., 2016) studies that model static Coulomb stress transfer have routinely employed simplified planar fault geometry (e.g., Harris and Simpson, 1992; Lin and Stein, 2004; Pace et al., 2014). Recent modelling has shown the significant role that fault geometry, particularly fault strike, may play in the magnitude of stress transfer between faults by altering the stress distribution on receiver faults (Marshall and Morris, 2012; Bie and Ryder, 2014; Mildon et al., 2016). Moreover, sensitivity analysis on faults with different dips indicates that changes in fault dip do alter the distribution of stress imparted on receiver faults (Mildon et al., 2016).

Despite these observations very few studies attempt to integrate field observations, surface data, and subsurface data in models of static Coulomb stress transfer and models that do incorporate non-planar fault geometry in stress modelling often rely on projecting surface observations, usually fault strike, down to seismogenic depths and do not necessarily incorporate changes down-dip changes in fault geometry (Marshall and Morris, 2012; Bie and Ryder, 2014; Mildon et al., 2017). This approach can result in faults employed in models of static stress transfer are often oversimplifications of complex structures. An understanding of how non-planar geometry faults affect models of static Coulomb stress transfer between thrust faults is important because static stress change is a key input when attempting to model future patterns in regional seismicity (Toda and Enescu, 2011; Strader and Jackson, 2015) and the growth and interaction of faults (Cowie, 1998; Gupta et al., 1998; Olson and Cooke, 2005).

This study focuses on the Ventura basin (Fig. 3.1), southern California, USA, to characterize the 3D geometry of an active fault system using sub-surface well-log data and then investigates how static stress may be transferred along the fault network for different rupture scenarios. Several authors have suggested that large-magnitude (M_w 7.5–8), multi-fault earthquakes may occur between the Pitas Point, Ventura, and San Cayetano faults (Fig. 3.1) based on a high degree of assumed structural connectivity between these faults at depth (Hubbard et al., 2014; Marshall et al., 2017) and > 5 m surface displacements suggested from paleoseismic studies (Dolan and Rockwell, 2001; McAuliffe et al., 2015;

Rockwell et al., 2016). Additionally, static stress triggering has been suggested as one possible method for enabling multi-fault earthquakes between the Pitas Point, Ventura, and San Cayetano faults (McAuliffe et al., 2015), although this suggestion has not been tested.

Alternatively, the potential for multi-fault ruptures on these faults has been questioned by other authors due to a lack of evidence for deep structural connectivity of these fault systems in seismicity data, the lack of evidence for synchronous fault displacements between these faults, and the suggestion that 5–10 m uplift events identified onshore are anomalous compared with the absence of similar fault-related vertical uplift events farther offshore (Nicholson et al., 2017b). The potential degree of multi-fault connectivity is critically dependent on the geometry inferred for the recently proposed low-angle Southern San Cayetano fault (SSCF) and the nature of its relationship with the neighbouring San Cayetano, Pitas Point, and Ventura faults (Hughes et al., 2018).

In this study, we examine petroleum industry well-log data and existing structural cross sections developed from well log data, in conjunction with geologic and geomorphic maps, to produce a series of cross sections across the northern boundary of the central Ventura basin and to characterize the 3D geometry of the SSCF. Using these data, we construct a 3D model of the SSCF to explore the possible subsurface structural connections of the SSCF to the San Cayetano fault. We then employ static Coulomb stress modelling, using the non-planar geometry for the faults based on surface and subsurface data, to explore whether the timing of subsequent earthquakes on the SSCF and the San Cayetano fault may be affected by static Coulomb stress changes as a result of modelled ruptures on the Pitas Point or Ventura faults.

3.1 Background and Geological setting

The Ventura basin is an approximately east-west trending, fault-bounded structural trough that contains up to 12 km of Neogene sediments (e.g., Yeats et al., 1994). Rapid convergence across the basin is the result of oblique transpressional deformation south of the “Big Bend” in the San Andreas fault (e.g., Wright, 1991) and geodetic studies suggest that current rates of shortening across the central and eastern basin range from 7–10 mm yr^{-1} (Donnellan et al., 1993; Marshall et al., 2013). High rates of shortening

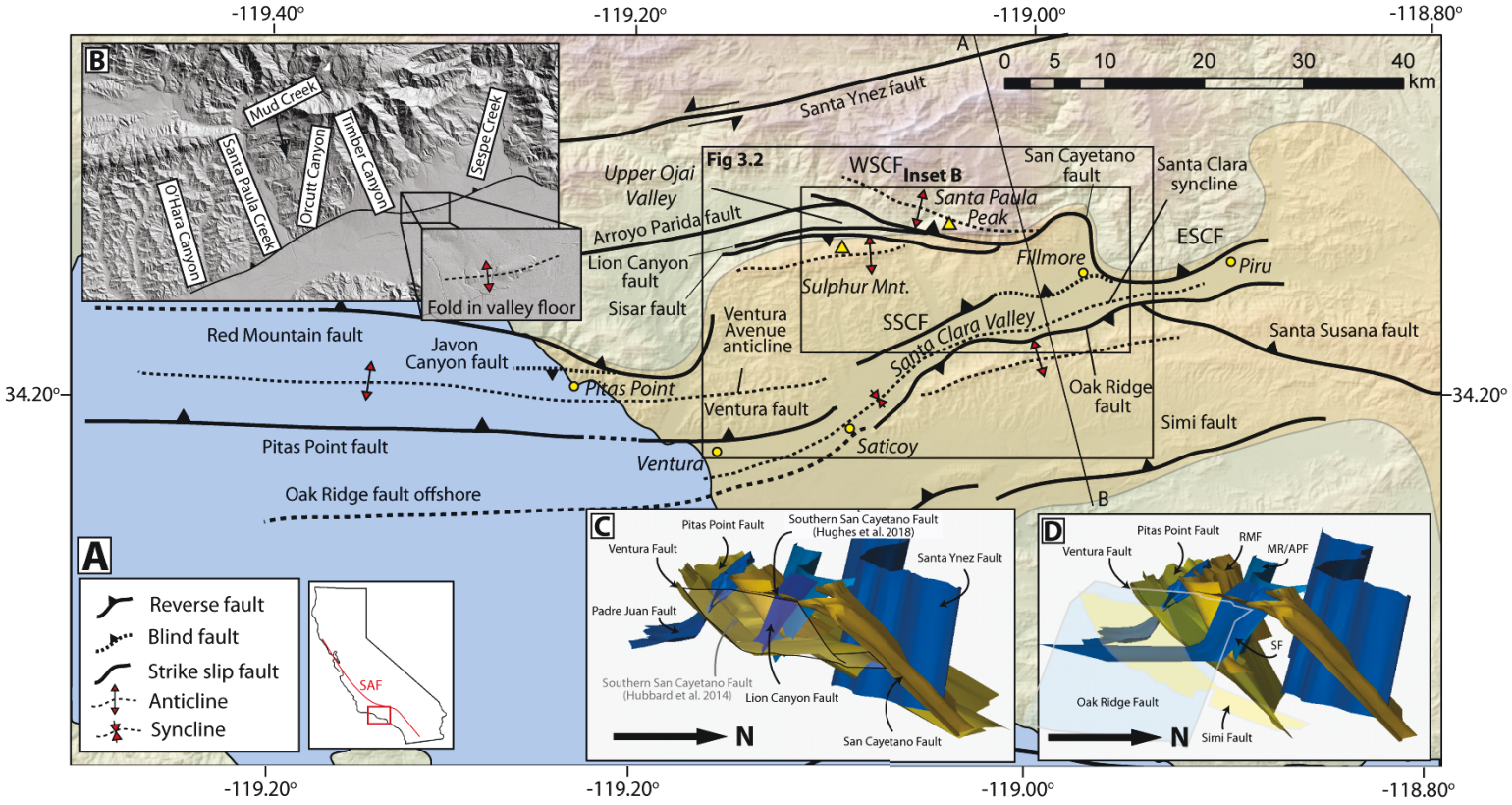

Figure 3.1 *A) Fault map of the study area. Solid lines are reverse faults with teeth on the hanging wall and black dashed lines are location of major folds. Yellow circles are location of major towns and the orange shaded area represents the outline of the Ventura basin and is defined by the limit of Plio-Pleistocene sedimentary basin fill (Swanson and Irvine, 2015). Yellow triangles are mountain peaks referred to in the text. Black boxes are limits of inset B and Figure 3.2. Line A-B is the line of section in Figure 3.10. Inset B is a hillshade map showing the location of various canyons and rivers mentioned in text and the fold in the Santa Clara valley. Insets C and D shows a comparison between the 'ramp-flat' model (C) and the 'no-flat' model (D) for the Pitas Points and Ventura faults looking west. Faults with north-dip are coloured in shades of yellow and faults with south-dip are coloured in shades of blue. WSCF = Western San Cayetano fault, ESCF = Eastern San Cayetano fault, SF = Sisar fault, RMF = Red Mountain fault, MR/APF = Mission Ridge/Arroyo Parida fault, SAF = San Andreas fault.*

are accommodated along the northern Ventura basin by activity on the north-dipping Red Mountain, Pitas Point, Ventura, and San Cayetano faults, and the south-dipping Oak Ridge, Lion Canyon, Big Canyon, Padre Juan, and Sisar faults and associated folds (Fig. 3.1) (Namson and Davis, 1988; Rockwell, 1988; Yeats et al., 1988; Sorlien et al., 2000; Hubbard et al., 2014; Sorlien and Nicholson, 2015; Rockwell et al., 2016; Nicholson et al., 2017b).

The Plio-Pleistocene stratigraphy of the Ventura basin consists of a progradational succession of deep marine to terrestrial strata that are highly deformed and locally overturned (Campbell et al., 2014; Swanson and Irvine, 2015). Various terminologies have been adopted to classify the Plio-Pleistocene sediments of the Ventura basin (Kew, 1924; Weber et al., 1976; Dibblee, 1990b; e.g. DeVecchio et al.,

2012a) and the nomenclature used in this study is based on a detailed synthesis of the existing literature (Campbell et al., 2014). The Plio-Pleistocene Pico Formation is a 4 km thick succession of deep marine sandstone, siltstone, and mudstone, which is exposed along the north flank of the Santa Clara Valley (Fig. 3.2) (Winterer and Durham, 1962). The mudstone dominated Mudpit Shale member of the upper Pico Formation interfingers with the overlying shallow marine sands of the lower Pleistocene Las Posas Formation, which is 100–300 m thick in the study area (Fig. 3.2). The youngest bedrock unit in the study area is the terrestrial Saugus Formation which is thought to be Pleistocene in age (Levi and Yeats, 1993) and comprises a ~2 km thick succession of heavily deformed mudstone, siltstone, sandstone, and conglomerate (Fig. 3.2) (Hopps et al., 1992). Overlying the basin fill on the northern flank of the Santa Clara River Valley is a series of uplifted and tilted late Pleistocene to Holocene alluvial fans and fluvial terraces (Rockwell, 1988; DeVecchio et al., 2012a; Hughes et al., 2018).

Fault geometry within the upper 7 km of the Ventura basin is relatively well-characterized (Plesch et al., 2007; Nicholson et al., 2017a) but there are competing models for the deep structure, geometry, and subsurface connectivity of various faults (Hubbard et al., 2014; Marshall et al., 2017; Nicholson et al., 2017b). For example, two contrasting models exist for the deep structure of the Pitas Point/Ventura, Red Mountain, and Lion Canyon faults (Fig. 3.1c and 3.1d). The differences in the two competing models are importance because the degree of structural connectivity at depth has implications for the likelihood of large-magnitude multi-fault earthquakes. In one model, the Pitas Point, Ventura, Red Mountain, and Lion Canyon faults all sole into an inferred shallowly north-dipping mid-crustal detachment at ~7.5 km depth (Fig. 3.1c), herein referred to as the 'ramp-flat' model in reference to the proposed ramp-flat-ramp geometry for the Pitas Point and Ventura faults (Hubbard et al., 2014). The 'ramp-flat' model is based primarily on 2D kinematic modelling, shallow onshore seismic reflection data, and limited well control. Moreover, the 'ramp-flat' model implies a high degree of structural connectivity at depth which it has been suggested provides a rupture pathway for large-magnitude earthquakes (Hubbard et al., 2014; Rockwell et al., 2016).

In the alternative model, the Pitas Point, Ventura, Red Mountain, and Arroyo Parida faults all maintain a relatively constant dip down to ~10 km depth where they merge to form a master N-dipping fault that

continues with moderate-to-steep dip to seismogenic depths of 18-20 km, herein referred to as the 'no-flat' model (3.1d) (Sorlien and Nicholson, 2015; Nicholson et al., 2017b). The deep geometry of the 'no-flat' model is based on correlating well data and offshore 2D and 3D seismic reflection data with deep seismicity (Nicholson et al., 2017b). The degree of subsurface structural connectivity is limited in the 'no-flat' model and the prospect for proposed large-magnitude earthquakes is diminished relative to the 'ramp-flat' model.

The San Cayetano fault is an active reverse fault that defines the northern margin of the central Ventura basin and is mapped for ~40 km trending east-west from Piru to the Upper Ojai Valley (Fig. 3.1). The fault has been well documented at both the surface (Çemen, 1977; Rockwell, 1983; Rockwell, 1988; Çemen, 1989; Dibblee, 1990a; Dibblee, 1990b; Dolan and Rockwell, 2001) and in the subsurface (Çemen, 1989; Hopps et al., 1992; Huftile and Yeats, 1995; Huftile and Yeats, 1996; Nicholson et al., 2007) with eastern and western segments of the fault separated by a pronounced bend in the surface trace north of the town of Fillmore (Fig. 3.1). The eastern San Cayetano fault (ESCF) has pronounced geomorphic expression in the form of a 5–8 m high scarp in late Holocene (<5 ka) deposits near the town of Piru (Fig. 3.1) (Dolan and Rockwell, 2001). Paleoseismic trenching across the fault scarp near Piru revealed evidence for at least one 4–5 m slip event on the ESCF within the last ~350 years (Dolan and Rockwell, 2001; Dolan, 2009). In contrast, there is a lack of prominent fault scarps in late Holocene deposits along the western San Cayetano fault (WSCF) (Rockwell, 1988) and no paleoseismic trenches have been excavated along the WSCF.

The SSCF is a ~20 km long, low-angle thrust in the footwall of the WSCF and is interpreted as a young structure, which has been active since ~58 ka with a slip rate of 1.3–1.9 mm yr^{-1} (Hughes et al., 2018). In addition, a blind splay of the SSCF was proposed to explain a pronounced surface fold at Fillmore (Fig. 3.1b) with a rock uplift rate of 1.9 mm yr^{-1} since ~17 ka (Hughes et al., 2018). This previous work on the SSCF focused on surface evidence for the fault, but the subsurface 3D geometry and structural connection of the SSCF with neighbouring structures require further investigation (Hughes et al., 2018). The work presented here is a follow up to the initial surface investigation and aims to explore the subsurface 3D geometry for the SSCF in detail.

3.3 Datasets and Methods

3.3.1 Datasets

We integrated various surface and subsurface datasets to produce a series of structural cross sections along strike of the SSCF and to generate a 3D model of SSCF geometry to demonstrate how the SSCF may connect with the San Cayetano fault in the subsurface. The full set of data sources, including both well data and geological maps, is as follows:

- *California Department of Conservation (Division of Oil, Gas and Geothermal Resources or DOGGR) online well database:* A comprehensive online record of almost all historical oil wells drilled in California including, but not limited to, oil and gas production records, resistivity logs, drillers logs, palaeontological data, and dipmeter data (available at: http://www.conservation.ca.gov/dog/Pages/WellFinder.aspx and herein referred to as 'the DOGGR online well database').
- *Ventura Basin Study Group well correlation sections*: The Ventura Basin Study Group (VBSG) provide a comprehensive review of the subsurface structure of the onshore Ventura basin comprising structural contour maps of key stratigraphic horizons and well-correlation sections across all major structures based on an integrated analysis of well data from 1200 petroleum industry wells (Hopps et al., 1992). Wells are typically tied or correlated in four directions with the next well along the line of section, to create a grid of correlation sections that allows for a unified 3D interpretation of subsurface structure and stratigraphy. Primary data extracted from the VBSG well correlation sections to characterize the SSCF included dipmeter data, dip data from core logs, and resistivity data.
- *Existing structural cross sections:* In addition to the VBSG, several previous researchers have examined the subsurface structure of the study area and produced structural cross sections (Schlueter, 1976; Çemen, 1977; Huftile, 1988; Rockwell, 1988; Çemen, 1989). Cross sections and interpretations of well data included on the cross sections (if present) were re-interpreted to characterize the SSCF.

- *Geological maps:* Numerous geologic maps have been drafted in the study area (Dibblee, 1987; Dibblee, 1990a; Dibblee, 1990b; Dibblee and Ehrenspeck, 1992b; Tan et al., 2004; Campbell et al., 2014). Data on outcrop patterns, mapped folds and faults, along with strike and dip data were extracted from maps and used to aid cross section construction.
- *Geomorphic maps:* A sequence of uplifted alluvial terraces and offset alluvial fans have been mapped in the hanging wall of the SSCF and in the Upper Ojai Valley (Rockwell, 1983; Rockwell, 1988; Hughes et al., 2018). These data helped quantify the surface expression of the SSCF to compare with results of the subsurface investigation.
- *Structural contour maps:* A structural contour map of the 'Top Pico horizon' based on resistivity data beneath Fillmore (Hopps et al., 1992) provided insights into basin development and stratigraphic geometry beneath the ~40 km axis of the Santa Clara Valley (Fig. 3.1).

3.3.2 Methods

The Ventura basin is a major onshore oil producing region and, consequently, oil wells are nearly ubiquitous throughout the study area (Fig. 3.2). Wells drilled around Fillmore have an average total depth of 4–5 km, but wells on the southern slopes of Santa Paula Peak (Fig. 3.1) in the hanging wall of the SSCF are generally only 1–3 km deep. A north-dipping SSCF combined with an increase in elevation northward from the Santa Clara Valley means that unless the fault is very low-angle (i.e. <5°) a large proportion of these wells are not deep enough to penetrate the SSCF (Fig. 3.2). Furthermore, many of the wells in the hanging wall of the SSCF are inactive historical wells and the associated data are often limited. Consequently, out of approximately one thousand wells that potentially penetrate the SSCF only around fifty contain data (e.g. dipmeter readings, core logs, or resistivity data) that can potentially be used to identify a fault. These fifty wells formed the basis for the SSCF interpretations in our study (Fig. 3.2, red and orange dots).

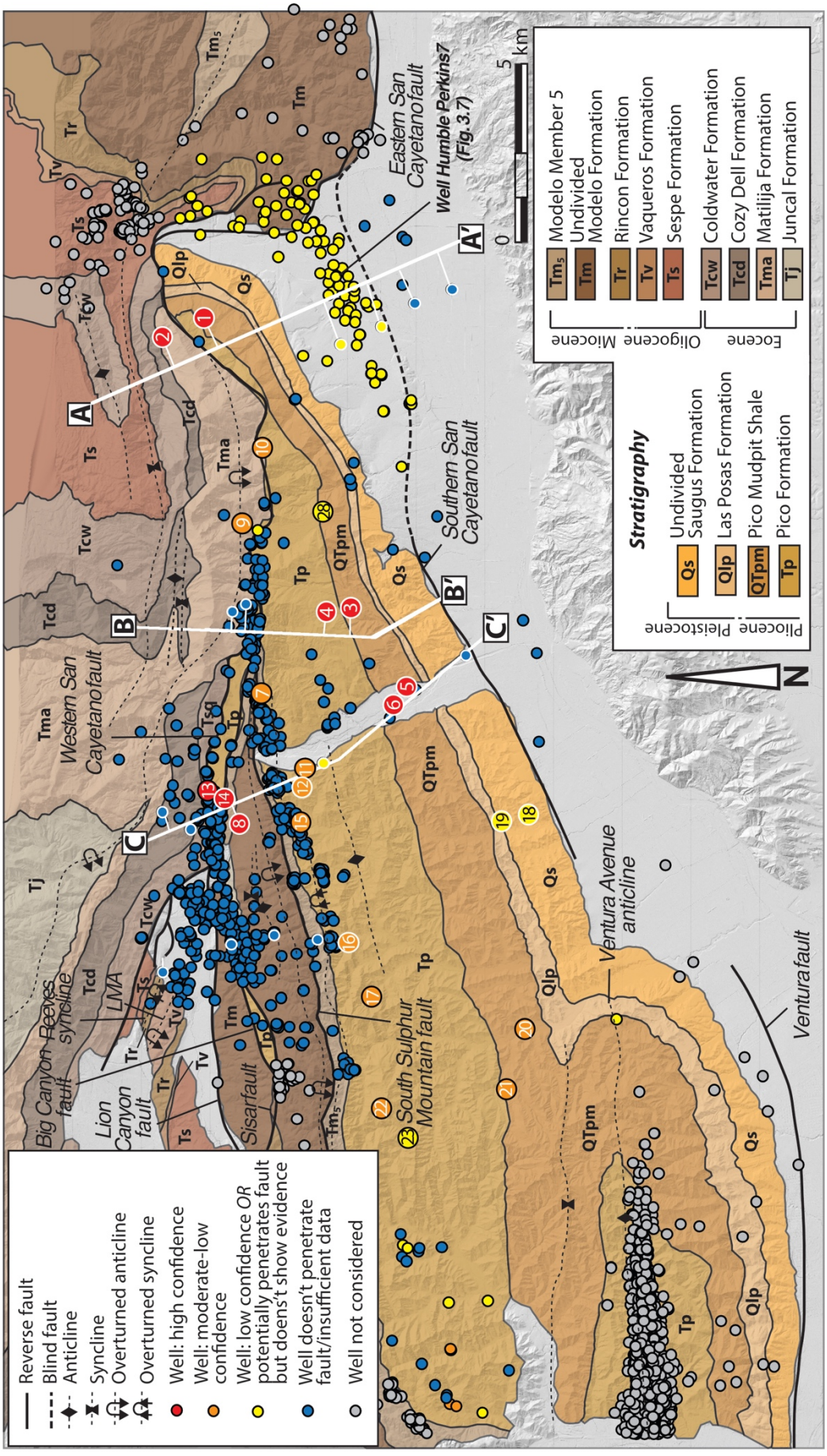
Reverse fault
Blind fault
Anticline
Syncline
Overturned anticline
Overturned syncline
Well: high confidence
Well: moderate-low confidence
Well: low confidence OR potentially penetrates fault but doesn't show evidence
Well doesn't penetrate fault/insufficient data
Well not considered
Big Canyon fault
Reeves syncline
Lion Canyon fault
LMA
Sisar fault
Western San Cayetano fault
Eastern San Cayetano fault
Southern San Cayetano fault
South Sulphur Mountain fault
Ventura Avenue anticline
Ventura fault
Well Humble Perkins7 (Fig. 3.7)
A
A'
B
B'
C
C'
0
5
km
N
Stratigraphy
Pliocene
Pleistocene
Qs Undivided Saugus Formation
Qlp Las Posas Formation
QTpm Pico Mudpit Shale
Tp Pico Formation
Oligocene
Miocene
Eocene
Tms Modelo Member 5
Tm Undivided Modelo Formation
Tr Rincon Formation
Tv Vaqueros Formation
Ts Sespe Formation
Tcw Coldwater Formation
Tcd Cozy Dell Formation
Tma Matilija Formation
Tj Juncal Formation

Figure 3.2 *Geological map of the study area showing major Cenozoic sedimentary units and the locations of petroleum wells discussed in the text. Geologic units are based on published maps (see section 3.3 for references) with the nomenclature of Campbell et al. (2014). Solid black lines are surface faults, dashed black lines are blind faults, and thin dashed black lines are folds. Wells are colour coded based on the degree to which the potential fault cuts in wells provide evidence for the low-angle Southern San Cayetano fault. Numbers in wells reference well evidence contained in Table 3.2 and Table S1 in Appendix B. The lines of section in bold white represent the cross sections included in Figures 3.4 and well projections on to the section line are represented with thin white lines. Well locations are from California Department of Conservation online well database. The location of well Humble Perkins 7, which is representative of the signal of the Top Pico horizon in resistivity data presented in Figure 3.7.*

3.3.2.1 Dipmeter data

With the onset of activity on the SSCF thought to have occurred within the last 58 kyr and with an inferred maximum surface slip rate of ~1.9 mm yr^{-1} (Hughes et al., 2018), the SSCF is expected to have accumulated a maximum displacement of ~110 m. Given such limited stratigraphic offset, methods of fault identification that rely solely on unambiguous identification of stratigraphic offsets in the subsurface (e.g. biostratigraphy or repetition of stratigraphy) may not be the most effective methods to identify the SSCF in well data. Disturbances in dipmeter trends are often associated with faulting and we interpret an abrupt change in dip, which can either be an abrupt decrease or increase in dip-angle with depth (or both if one follows the other), to represent potential evidence for a fault cut at or just below the change in dip (Devilliers and Werner, 1990; Adams et al., 1992; Hubbard et al., 2014). We focused primarily on disturbances in the dipmeter data at a depth that corresponded to the depth associated with the trend of the low-angle SSCF suggested by Hughes et al. (2018), which was only based on data from two wells at Orcutt Canyon (Fig. 3.1).

We assume an uncertainty of up to 20° is associated with individual dipmeter readings and only changes in down-well dipmeter data above 20° are considered significant. Sediment compaction, rather than faulting, could also alter the geometry of beds and related dipmeter data with depth (Nicholson et al., 2007). However, down-well changes in dipmeter data related to compaction would likely demonstrate a systematic, gradual change in bed geometry with depth, in contrast to a more abrupt change in dipmeter data associated with faulting (Devilliers and Werner, 1990; Adams et al., 1992). Original, uninterpreted dipmeter data are only sporadically available in the DOGGR online well database within the study area so we rely mainly on dip-data included in existing correlation and structural cross sections

that have been corrected for well drift from vertical and adjusted for the orientation of the cross section data panel (Fig. 3.3) (e.g. Schlueter, 1976; Huftile, 1988; Hopps et al., 1992).

3.3.2.2 Core logs

Many well records within the DOGGR online well database contain core logs that briefly describe the stratigraphy and note any specific features such as faults, fractures, gouge zones, slickensides, fossils, or traces of hydrocarbons. Core logs also contain dip-data annotations ascertained from the orientation of bedding, sedimentary structures, or fractures within the core. Such annotated dip data from core logs are typically low-resolution compared to the almost continuous readings from dipmeter data. However, changes in core log dips were used to either support interpretations from dipmeter data or in place of dipmeter data if dipmeter data were not available. Core logs were also examined for any first-hand observations of faulting, such as pervasive fracture zones or gouge zones.

3.3.2.3 Resistivity data

Resistivity data are available for many wells in the study area from the DOGGR online well database. Fluid migration along the fault plane can affect the resistivity signal, while fault gouge and/or fractures surrounding a fault zone can potentially cause the logging tool to fail (Hubbard et al., 2014). However, resistivity data alone from a single well are not normally used to suggest the presence of a fault (Devilliers and Werner, 1990). Sharp variations in resistivity have previously been used to support the identification of faults when they co-exist with other data that suggest the presence of a fault, for example dipmeter data (Devilliers and Werner, 1990). Changes in resistivity data, when they are observed at a depth roughly equal to the depth with abrupt variations in dip, were used to provide further supporting evidence for fault cuts related to the SSCF. Furthermore, the contact between the base of the Mudpit Shale member of the upper Pico Formation and the underlying Pico deposits (referred to as the 'Top Pico horizon' because the Mudpit Shale member was not attributed to the Pico Formation prior to the update to the nomenclature by Campbell et al. (2014)) is clearly visible in resistivity data in wells beneath Fillmore as a pronounced drop in resistivity and an increase in spontaneous potential (Hopps

et al., 1992). The 'Top Pico' horizon map (Hopps et al., 1992) was used investigate the presence of a potential blind fault at depth beneath Fillmore.

3.3.2.4 Well confidence categorization

The wells mapped in Figure 2 are colour coded based on a qualitative assessment of the degree of confidence to which the observations of possible fault cuts interpreted in the well data potentially provide evidence for the low-angle SSCF. Wells are classed as high-confidence if the inferred fault cut is based on multiple potential lines of evidence for faulting (e.g. change in trend of dipmeter and on resistivity logs) or if two wells are in close proximity and both show the same evidence for a fault cut (e.g. disturbance on dipmeter data at similar depth) (Fig. 3.3). Direct evidence of a fault (e.g. a fault zone or fault cut described in a core logs) is considered to have higher confidence than an indirect indicator such as core log dip data. Wells are assigned moderate confidence where the interpretation of the SSCF is based on one direct piece of evidence for the fault. Fault cuts in wells are assigned low confidence that they potentially provide evidence for the SSCF where a fault could be inferred but is not actually observed in the data (e.g. there is some evidence for a fault in terms of subtle dip changes, but where we may expect the fault cut there are data missing).

3.3.2.5 Cross sections and 3D fault model construction

We created four vertical structural cross sections and a 3D fault model for the SSCF (Fig. 3.4, 3.5 & 3.6) to map potential along-strike variations in the 2D and 3D subsurface structure of the SSCF and to present our interpretation of how the SSCF intersects previously mapped structures and stratigraphy. Cross section lines (Fig. 3.2) were selected to approximate the lines of section of the VBSG well-correlation sections within the study area (Hopps et al., 1992). The VBSG sections contain a large amount of well data corrected for well bore deviation onto section lines. By constructing our cross sections in a similar orientation to the VBSG sections, the cross sections followed the structural trend of the SSCF and the distance that well data needed to be projected onto the section was kept to a maximum of ~2 km. Whilst this method does involve some minor projection of well data onto the line of section, the wells used in construction of the 3D model are not projected. Utilizing this method, the

dip data contained in the VBSG sections could be used as a guide to model the subsurface geometry of the SSCF based on the fault evidence in Table 3.2.

We georeferenced geological maps containing the well locations in the 3D seismic interpretation software Petrel^{TM} to construct the 3D geometry of the SSCF. Fault intersections from the wells that we interpret to be related to activity on the SSCF were plotted as points in 3D and these points were gridded into a fault surface. The upper boundary of the fault surface was delineated using the mapped surface trace of the SSCF. The lower boundary was set as the intersection of the down-dip projection of the SSCF surface with the San Cayetano fault, which was extracted from the Southern California Earthquake Centre 3D Community Fault Model for Southern California (CFM) version 5.2 (Plesch et al., 2007; Nicholson et al., 2017a), a comprehensive representation of the 3D fault geometry based on geologic and seismologic evidence. The resulting 3D surface was used a template to reconstruct the 3D geometry for the SSCF in static Coulomb stress modelling.

3.3.2.6 Static stress modelling

The newly constructed 3D geometry for the SSCF was used in static Coulomb stress modelling (Harris and Simpson, 1992; King et al., 1994; e.g. Harris, 1998; Parsons et al., 1999; Toda et al., 2005) that included other faults with non-planar geometry both down-dip and along strike (Mildon et al., 2016; Mildon et al., 2017). Rupture scenarios were selected to investigate the potential for triggered seismicity on the SSCF and the WSCF following modelled earthquakes on the Pitas Point, Ventura, and eastern San Cayetano faults, based on the suggestion that static Coulomb stress transfer may play a role in multi-fault earthquakes between these faults (McAuliffe et al., 2015). No attempt was made to model dynamic stress effects or the current stress state of the faults resulting from historical ruptures (e.g. Deng and Sykes, 1997a; Deng and Sykes, 1997b), interseismic loading (e.g., Verdecchia and Carena, 2016; Mildon et al., 2017; Wedmore et al., 2017), or cumulative transferred stress over a longer time period from post seismic relaxation of the lower crust and mantle (e.g., Freed et al., 2007). In our simple model, we assumed an initial stress of zero on all faults and simulated reverse-slip ruptures on specific faults to observe patterns of modelled static stress changes on the SSCF and the WSCF.

3.3.2.6.1 Modelled fault surfaces

Faults were reconstructed in *Coulomb 3.4* (Lin and Stein, 2004; Toda et al., 2005) following the methodology of Mildon et al. (2016) for creating non-planar source and receiver fault inputs with variable strike. The original code for creating non-planar reverse faults in Coulomb 3.4 only facilitated the recreation of faults with variable strike and did not enable the recreation of faults that change their geometry down-dip. We updated the model to incorporate faults that change geometry both down-dip and along-strike (i.e. to be able to model listric or ramp-flat fault geometry). This is particularly useful for faults in the Ventura basin, as many faults such as the Pitas Point, Ventura, and Lion Canyon faults are documented to have complex down-dip geometry (Nicholson et al., 2017a). The code is described in detail in Mildon et al. (2016) and the updated version of the open source code is available from: https://github.com/ZoeMildon/3D-faults/tree/Variable dip faults.

An accurate set of 3D fault models are required as inputs to *Coulomb 3.4*. The 3D surface of the SSCF used in our Coulomb model is based on the analysis of subsurface data presented in section 3.4. We base the 3D geometry of the Pitas Point, Ventura, San Cayetano, Sisar, Lion Canyon, Padre Juan, and Red Mountain faults on surfaces provided in CFM 5.2 (Plesch et al., 2007; Nicholson et al., 2017a). Two alternative representations for the San Cayetano fault are presented in CFM 5.2, with 50° and 60° subsurface dips down to approximately 17 km (Nicholson et al., 2017a). Moreover, previous workers have matched shallow subsurface well-log data with deep seismicity to suggest a 40° subsurface dip for the San Cayetano fault (e.g. Huftile and Yeats, 1996). The intermediate value of 50° is adopted in our models as an average value between the two end members.

Currently, two deep-fault geometry models have been proposed and debated in the literature (see section 3.1). It is not our intention in this chapter to attempt to discriminate between these models (see Chapter 5), so instead we model the stress change associated with both the ‘ramp-flat’ and ‘no-flat’ models to investigate potential patterns of static Coulomb stress transfer in the central Ventura basin.

3.3.2.6.2 Coseismic ruptures

There are no published coseismic slip distributions for the faults in this study, and therefore the precise character of slip on the faults during potential large earthquake ruptures is not known. The observation of potential large paleoseismic uplift events (> 5 m) on the Pitas Point, Ventura, and San Cayetano faults (Table. 3.1) has led researchers to suggest that these faults may be linked in the subsurface (McAuliffe et al., 2015; Rockwell et al., 2016) but the timing of inferred uplift events is not consistent between faults, and the precise nature of any proposed deep structural linkage is controversial (Nicholson et al., 2017b). In this study, we want to test if earthquakes occurring on one part of the fault network are likely to affect the timing of an earthquake on a nearby fault due to static Coulomb stress transfer. Accordingly, we focus mainly on simulating hypothetical earthquakes on individual faults. We calculate maximum potential earthquake magnitude (M_w) for a specific fault using functions derived from regressions of M_w versus fault area (Table 3.1) (Leonard, 2014) and then model maximum slip on the fault to output the expected M_w from fault area (Table 3.1).

Maximum slip is modelled on the centre of the fault with a linear slip gradient that tapers to zero at the eastern and western fault tips and the base of the fault (Mildon et al., 2017). The base of all faults that do not terminate against another fault is modelled as 17 km in line with the depth of fault projections in the CFM (Nicholson et al., 2017a). Both the Pitas Point and Ventura faults are blind (Hubbard et al.,

Table 3.1 *Fault areas and potential earthquake magnitudes used in Coulomb modelling*

Fault	Area (km^2)[a]	Potential M_w from area scaling relationship	D_{max} from scaling relationships (m)	M_w output from Coulomb model using D_{max}	Max slip required in Coulomb to equal M_w from area (m)	Paleoseismic surface displacement (m)	Reference
'No-flat' Model							
Ventura	282	6.4	0.7	6.2	1.6	5.5-8.5	*McAuliffe et al (2015)*
Pitas Point	1197	7.1	2.2	6.8	5.7	10-16	*Rockwell et al (2016)*
'Ramp-flat' Model							
Ventura	789	6.9	1.6	6.6	4.5	5.5-8.5	*McAuliffe et al (2015)*
Pitas Point	2299	7.4	3.8	7.2	11.0	10-16	*Rockwell et al (2016)*
Ventura/Pitas Point	3088	7.5	4.8	7.4	11.3	5.5-16	*McAuliffe et al (2015), Rockwell et al (2016)*
ESCF	299	6.5	0.7	6.2	2.0	4.3-5.2	*Dolan & Rockwell (2001)*

a: Fault area calculated based on fault models contained in CFM 5.2 (Nicholson et al, 2015)
M_w calculated using $M_w = 4 + 1*\log(A)$ (Leonard 2015)
D_{ave} calculated using $M_w = 6.84 + 2 \log(D)$ (Leonard 2015)
D_{max} calculated using $\log(D_{max}) = -5.46 + (0.82*M_o)$ (Wells & Coppersmith, 1994)
ESCF = Eastern San Cayetano Fault

2014; Sorlien and Nicholson, 2015). Accordingly, the Ventura fault and the Pitas Point fault are modelled with slip tapering to zero at the surface and we do not account for half space or free surface effects in the modelled slip distributions. The San Cayetano fault is emergent, and we assume a large proportion of the slip (90 %) is transferred to the surface based on large observed surface slip in paleoseismic trenching (Table. 3.1) (Dolan and Rockwell, 2001).

3.3.2.6.3 Model parameters

The Coulomb failure function is defined by the following equation (Scholz, 1990):

$$\Delta\sigma_f = \Delta\tau + \mu'\Delta\sigma_n$$

where $\Delta\sigma_f$ is the Coulomb static stress change on the fault of interest , $\Delta\tau$ is the shear stress change, μ' is the effective coefficient of friction and incorporates pore pressure affects (e.g. Rice, 1992), and $\Delta\sigma_n$ is the change in normal stress. In the above equation, faults with a positive change in the Coulomb failure function (ΔCFF) after a nearby earthquake are hypothesized to be brought closer to failure and faults with negative ΔCFF are thought to be moved away from failure. During modelling an effective coefficient of friction of μ'= 0.8 was applied. A value of 0.8 is consistent with previous studies that have applied high values of $\mu'$to thrust faults based on the sensitivity of thrust or reverse faults to changes in normal stress (Lin and Stein, 2004) and because the relatively small fault offset of the Pitas Point, Ventura, and Southern San Cayetano faults in the upper ~7.5 km may result in a rough fault plane and, consequently, higher friction (Parsons et al., 1999; Toda and Stein, 2003; Lin and Stein, 2004).

The modelling employed here utilizes a uniform elastic half-space with a Poisson ratio of 0.25 and a shear modulus of 12 GPa. A map of modelled shear modulus values at 2 km depth within the study area, based on the Southern California Earthquake Committee Community Velocity Model version 4.0, shows that shear moduli increase northwards from approximately 5 GPa in the basin, to values > 30 GPa in the hanging wall of the San Cayetano fault (Marshall et al., 2013). Additionally, a shear modulus of 12 GPa has previously been applied to studies of stress transfer in the Los Angeles basin (Griffith and Cooke, 2004; Olson and Cooke, 2005), which is stratigraphically similar to the Ventura basin (Campbell et al., 2014). Therefore, a shear modulus of 12 GPa is selected as an average within the study

area and to be consistent with other studies of stress transfer in Neogene sedimentary basins in southern California. Because stresses are linearly related to fault slip, doubling the shear modulus would double the resultant stresses. We note that an increase in shear modulus across the San Cayetano fault (due to the stiffness contrast between sediment and rock) will likely affect the magnitude of stress transferred from ruptures on faults outside the Ventura basin to faults within the basin. The contrast in stiffness across the Ventura, Pitas Point, and SSCFs will be less pronounced as the faults have smaller offset.

We calculated ΔCFF on receiver faults resolved for an assumed fault rake of 90° (pure dip-slip reverse movement) across the entire fault plane. In contrast, many faults in the Ventura basin are thought to be oblique-reverse faults that include a significant component of lateral slip (Sorlien et al., 2000; Marshall et al., 2013). For example, microearthquakes associated with the Ventura fault (Sarna-Wojcicki, 1976) and the San Cayetano fault (Hauksson et al., 2016) have focal mechanism solutions with a large strike-slip component, and mechanical modelling based on horizontal GPS vectors indicates oblique reverse-slip for both the Ventura and San Cayetano faults (Marshall et al., 2013). In addition, given the non-planar geometry of faults in the Ventura basin, fault rake likely varies across the individual fault planes (Marshall et al., 2008). However, in the absence of large recent historical earthquakes and associated published slip distributions on the Pitas Point, Ventura, or San Cayetano faults there are no data to accurately quantify the precise direction of fault slip during large earthquake ruptures on these faults. Furthermore, there is no geomorphological evidence, such as offset river channels or shutter ridges that cross either the Ventura or San Cayetano faults, to facilitate quantification of the lateral component of fault slip. Consequently, slip is modelled as pure reverse dip-slip.

3.4 Characterizing the 3D geometry of the SSCF

3.4.1 Fault evidence from well data

Correlation of fault cuts from several wells within the study area shows clear evidence for the existence of a low-angle SSCF (Fig. 3.2). A description of the evidence in each well with ‘high’ confidence is provided below and in Table 3.2 and is illustrated in Figure 3.3. A description of fault evidence with ‘moderate’ to ‘low’ confidence is provided in Appendix B (Table S1).

Two wells north of Fillmore (*Santa Paula Unit 1, Pagenkopp 1*) contain fault cuts that can be attributed to the SSCF (Figs. 3.2 and 3.3; Table 3.2). In well *Santa Paula Unit 1,* there is an abrupt change in the dipmeter data from 70° N to 30° N at 1350 mbsl (meters below sea level) within a wider zone of disturbed dips that spans from 930–1350 mbsl (Hopps et al., 1992; Fig. 3.3, Table 3.2). Additionally, dips at ~1850 mbsl are considerably steeper (~50° N) than dips above (~15° N), indicating a possible fault somewhere in the intervening section (Fig. 3.3). We suggest a fault is present at ~1650 mbsl within the intervening section based on a downward decrease in both resistivity and spontaneous potential (Fig. 3.3). In well *Pagenkopp 1* at a depth of 450 mbsl, the Pico Formation is interpreted to occur above the younger Saugus Formation based on a sharp increase in resistivity and a decrease in spontaneous potential (Çemen, 1977; Hopps et al., 1992: this study). We interpret this upper repeated section to reflect the presence of the Pagenkopp fault. Another repeat section of Pico Formation ~120 m thick is interpreted as being thrust over the Saugus Formation from 1000–1120 mbsl, based on a sharp decrease in resistivity and an increase in spontaneous potential at ~1000 m depth (Hopps et al., 1992; this study). We interpret the SSCF to be at the base of this repeated section at 1120 mbsl (Fig. 3.3, Table 3.2). Dipmeter data in well *Pagenkopp 1* starts just below this repeat section at ~1200 mbsl and displays no abrupt changes below this depth.

At Orcutt and Timber Canyons there are also two wells (*Lagomarsino-Butler 1, Rudolph 22-25*) with fault cuts that may provide evidence for the SSCF (Fig. 3.2 and 3.3). The correlation of inferred fault cuts between these two wells was used as evidence to identify a shallow, low-angle (~20°) north-dip for the SSCF in previous work (Hughes et al., 2018). In well *Lagomarsino-Butler 1* there are abrupt changes in dipmeter readings from 45° S to 30° N at 480 mbsl and from 50° N to 40° S at 1055 mbsl. In well *Rudolph 22-25* an abrupt change in the dip-angle is observed at 811 mbsl which corresponds to a slight increase in resistivity (Fig. 3.3).

Table 3.2 *Well data with 'high confidence' used to characterise the subsurface geometry of the SSCF*

Well Name	Well No [a]	API	Latitude (°) [b]	Longitude (°) [b]	Possible Fault Evidence	Fault Depth (m [c])	Data Source	Confidence	Cross Section [d]
Pagenkopp 1	1	11106059	34.43843	-118.949713	*~120 m of Pico Formation interpreted within Saugus Formation in resistivity log from 1000-1120 m*	1120	Hopps et al (1992)	High	A-A'
Santa Paula Unit 1	2	11106064	34.448828	-118.955882	*Zone of highly disturbed dips in dipmeter data from 1000–1500 m, increase in dip from 15°–50° between ~1350–1850 m. Change in R and SP at 1650 m*	1650	Hopps et al (1992)	High	A-A'
Lagomarsino-Butler 1	3	11106073	34.399361	-119.038245	*Abrupt change in dip from 45°S to 30°N at 480 m and from 50°N to 40°S at 1055 m. Lower change in dip corresponds to disturbances in R & SP.*	1055	Hopps et al (1992)	High	B-B'
Rudolph 22-25	4	11120986	34.405526	-119.039616	*Abrupt change in dipmeter from 60°N to 50°S at 810 m. Increase in dip from 45°S to 75°S between 900 m and 1375 m.*	~1300	Hopps et al (1992)	High	B-B'
Sharp et al 1	5	11106076	34.384737	-119.062215	*Zone of highly disturbed dips in dipmeter data and highly variable R & SP from surface to 500 m. Abrupt decrease in dip from 60°N to 20°S at 280 m and 40°S to flat at 500 m.*	280	Hopps et al (1992)	High	C-C'
Signal-Powell 1	6	11106078	34.387442	-119.0688	*Abrupt decrease in dip from 60°S to 20°S at 250m and an increase in dip from 20°S to 45°S at 550 m which corresponds to a spike in SP.*	550	Hopps et al (1992)	High	C-C'
Ojai 67	8	11101069	34.426699	-119.105686	*Band of Miocene fossils sandwiched between Pliocene fossils correlating to change in R at 1800 m.*	1800	This study, Huftile (1988)	High	C-C'
Hamp B69	13	11121275	34.434858	-119.095644	*Abrupt decrease in dipmeter reading from 65°N to 17°N at 1990 m.*	1990	Huftile (1988)	High	n/a
Arco 6	14	11120471	34.43033	-119.09972	*Decrease in dipmeter readings from 85°N to 45°N at 2050 m*	2050	Hopps et al (1992)	High	C-C'

a: Well No refers to location on map in Figure 2 and is also noted in Figures 2.3, 2.4, & 2.5 (if applicable)
b: Latitude and longitude refer to the surface location of the well. The actual location of the fault evidence may be away from this location if the well has significant drift
c: Fault depth in meters below sea level
d: See Figures 2.4 and 2.5 for cross sections
R = Resistivity, SP = Spontaneous potential, API = American Petroleum Institute number

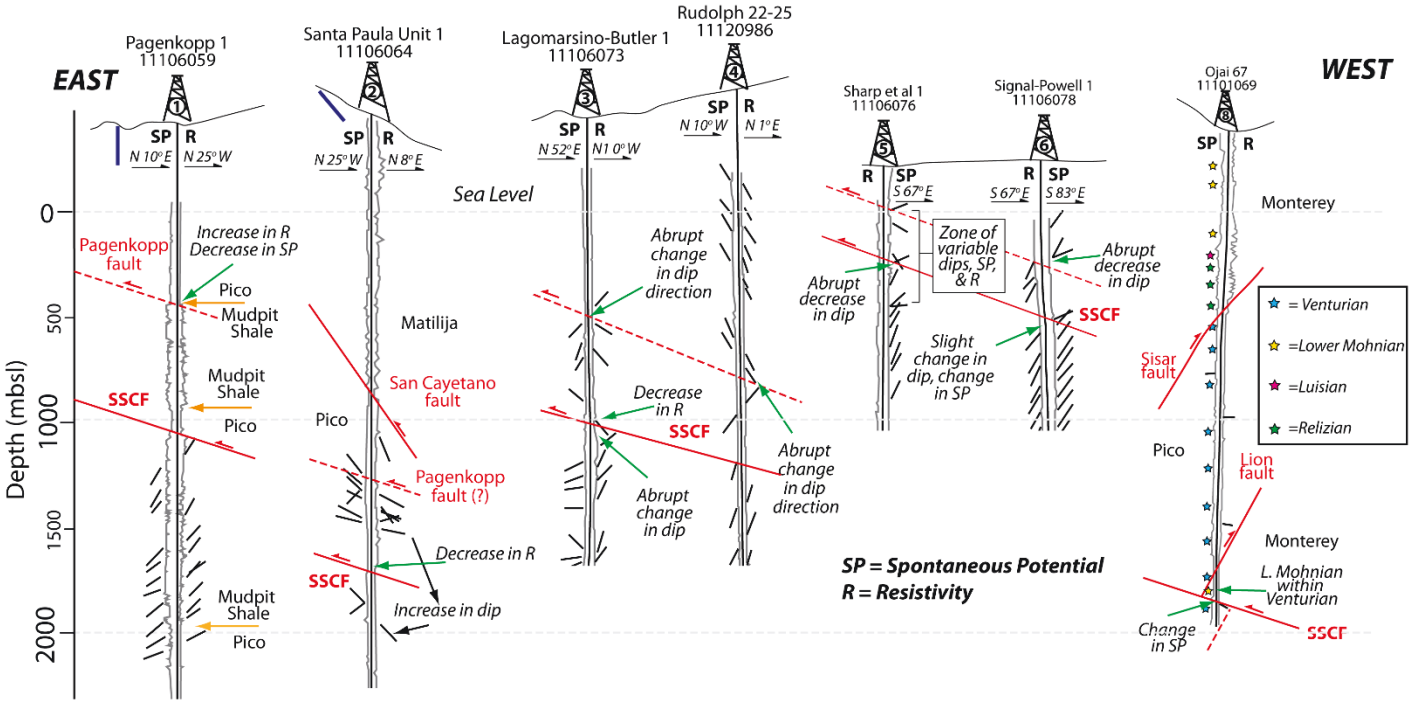

Figure 3.3 *Summary of key fault cuts from well data that we interpret to provide evidence the low angle Southern San Cayetano fault (SSCF). Blue lines are surface bedrock dips from published geological maps. Dipmeter data are taken from Hopps et al. (1992). Number of wells refers to number assigned to wells in Table 3.2 which contains full details of all wells. Location of wells is shows in Figure 3.2. SP = Spontaneous potential, R = Resistivity*

Three wells at Santa Paula Creek contain fault cuts that can be attributed to activity on the SSCF (*Sharp et al 1, Signal-Powell 1, and Ojai 67*). In well *Sharp et al 1* there is a zone of disturbed dipmeter readings accompanied by variations in resistivity and spontaneous potential from the surface down to ~500 mbsl, with abrupt change in dipmeter readings from 60° N to 20° S at 280 mbsl, and from 40° S to flat at ~500 mbsl. Roughly 1 km to the northwest, well *Signal-Powell 1* also exhibits a zone of disturbed dipmeter data with an abrupt decrease in dips from 60° S to 20° S at ~250 mbsl and an increase in dip from 20° S to 45° S at 550 mbsl. In well *Ojai 67* a bio-stratigraphic log suggests that lower Mohnian (Miocene) microfossils are logged within a continuous succession of Venturian microfossils that characterize the Pico Formation at 1800 mbsl (Fig. 3.3). We interpret the Miocene microfossils to be contained within a small section of Monterey Formation that has been faulted into the Pliocene succession by slip on the SSCF (Fig. 3.3). There is also a pronounced increase in spontaneous potential just below the section of the core log that contains the Miocene microfossils (Fig. 3.3).

On the southern slopes of Sulphur Mountain there are numerous mapped oil wells (Fig. 3.2). However, many of these wells have limited or no records in the DOGGR online well database meaning that there is limited data on fault dip or resistivity. If records are available, the maximum depth of any individual well does not exceed ~1350 mbsl (Appendix B, Table S1). There are only two wells north of the range front to the west of Santa Paula Creek, wells *Ex Mission X14* and *Ex Mission X17* (Fig. 3.2). Both wells should penetrate the SSCF if it were present this far west, but the available dipmeter data are either too sparse or too deep to provide evidence for the low-angle SSCF. We suggest that the SSCF does extend this far west because faults have been observed in shallow boreholes drilled in late Pleistocene alluvial fans along the range front immediately south of the location of wells *Ex Mission X14* and *Ex Mission X17* (Earth Systems Southern California, 2013; Hughes et al., 2018). Additionally, borehole and cone penetration test data indicate a buried fold scarp in latest Pleistocene to Holocene fans that cross the range front two kilometres farther west of wells *Ex Mission X14* and *Ex Mission X17* (McAuliffe, 2014).

3.4.2 Cross section A-A'

The eastern extension of the SSCF is difficult to define because there are few dip data (core or dipmeter) in the upper 1–2 km for the numerous wells at Fillmore that would help to characterize the subsurface structure at the eastern end of the SSCF (Fig. 3.2). Our interpretation for the SSCF involves a 15° north-dipping fault. that projects at constant dip to the surface fold in the Santa Clara Valley (Fig. 3.4a). This geometry is presented because there is no evidence for surface deformation in the many late Pleistocene and Holocene alluvial fans that cross the range front east of Timber Canyon, which would be expected if the SSCF crops out at the range front, or was blind in the shallow subsurface, north of Fillmore (Fig. 3.1). Furthermore, throw rates derived from a fault scarp within an alluvial fan at Orcutt Canyon of 1.5 $^{+0.3}/_{-0.2}$ mm yr^{-1} since ~19 ka overlaps with uplift rates for the fold in the Valley of 1.9 $^{+0.6}/_{-0.4}$ mm yr^{-1} since ~17 ka (Hughes et al., 2018), which may indicate that uplift of both the fold and the scarp could be occurring on the same structure.

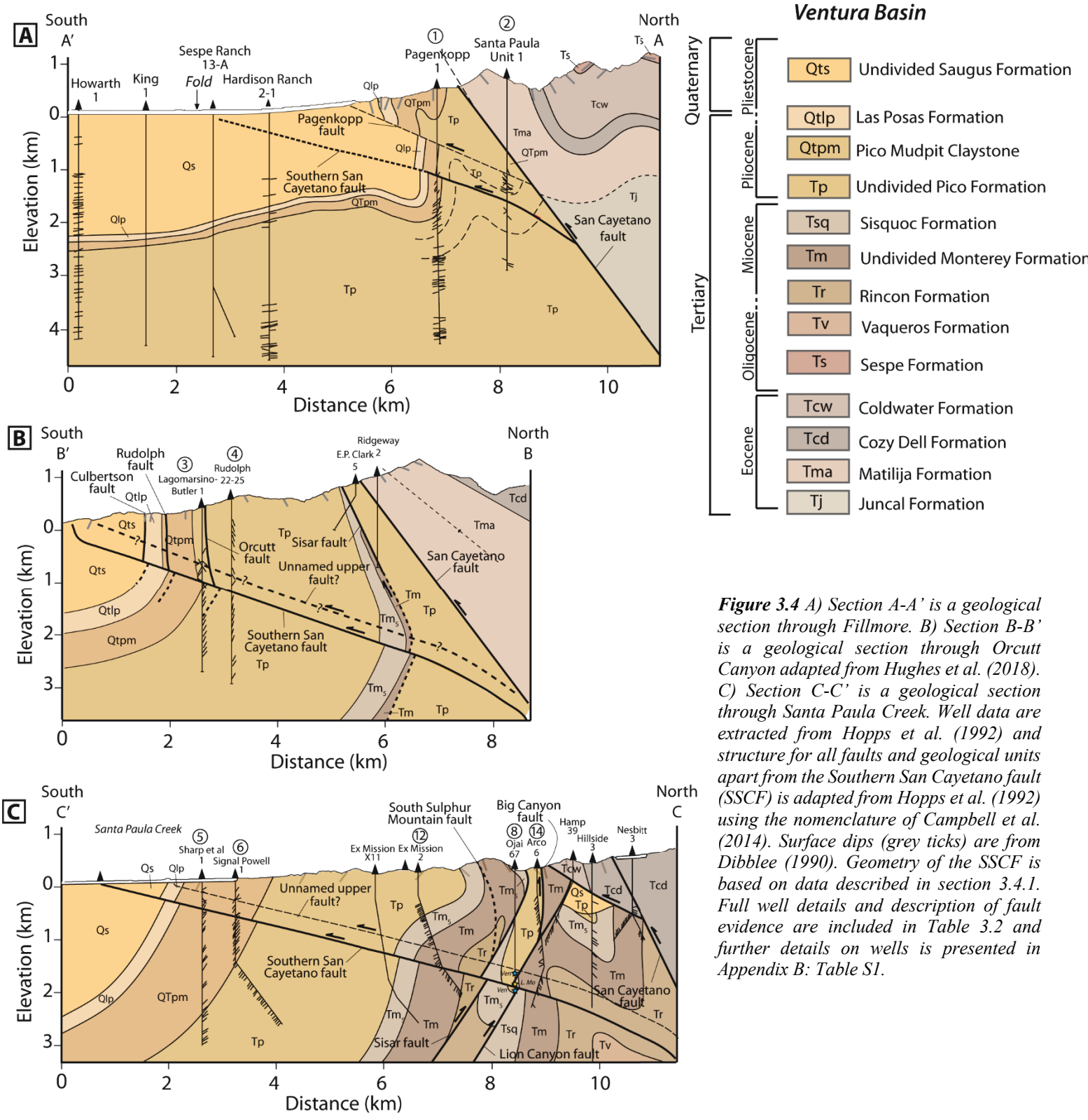

Figure 3.4 *A) Section A-A' is a geological section through Fillmore. B) Section B-B' is a geological section through Orcutt Canyon adapted from Hughes et al. (2018). C) Section C-C' is a geological section through Santa Paula Creek. Well data are extracted from Hopps et al. (1992) and structure for all faults and geological units apart from the Southern San Cayetano fault (SSCF) is adapted from Hopps et al. (1992) using the nomenclature of Campbell et al. (2014). Surface dips (grey ticks) are from Dibblee (1990). Geometry of the SSCF is based on data described in section 3.4.1. Full well details and description of fault evidence are included in Table 3.2 and further details on wells is presented in Appendix B: Table S1.*

3.4.3 Section B-B' and the Pagenkopp fault

A fault referred to as the Pagenkopp fault has been previously mapped in the footwall of the WSCF, based on the interpretation of the Pico Formation being thrust above the Saugus Formation in resistivity logs (Fig. 3.3 & 3.4a) (Çemen, 1989; Hopps et al., 1992). Well *Pagenkopp 1* is the only well in the study area where Pico Formation is interpreted to be thrust over Saugus Formation. However, in many logs we note a section of disturbed dips at 400–500 m above the SSCF that could be related to the Pagenkopp fault (Fig. 3.3 & 3.4b). Alternatively, the upper dip disturbance could be a separate structure that runs parallel to the SSCF in the fault hanging wall (Fig. 3.4b & 3.5a). There is no surface evidence to demonstrate that the Pagenkopp fault or a potential upper fault are active, and the upper dip disturbance is not traceable west of Santa Paula Creek (Fig. 3.1).

3.4.4 Cross section C-C'

The SSCF in Figure 3.4c is characterized by interpreted fault cuts in four separate wells and has a suggested dip of ~18° (Fig. 3.4c). However, to the west on the southern slopes of Sulphur Mountain many of the wells have limited or no records in the DOGGR online well database and if records are available, the maximum depth of any individual well does not exceed ~1350 mbsl (Appendix B: Table S3). There are only two wells north of the range front to the west of Santa Paula Creek, wells *Ex Mission X14* and *Ex Mission X17* (Fig. 3.2). Both wells should penetrate the SSCF if present this far west, but the available dipmeter data are either too sparse or too deep to provide evidence for the low-angle SSCF. We suggest the SSCF does extend this far west because faults have been observed in shallow boreholes drilled in late Pleistocene alluvial fans along the range front immediately south of the location of wells *Ex Mission X14* and *Ex Mission X1*7 (Earth Systems Southern California, 2013; Hughes et al., 2018). Additionally, borehole and cone penetration data indicate a buried fold scarp in latest Pleistocene to Holocene fans that cross the range front two kilometres farther west of wells *Ex Mission X14* and *Ex Mission X1*7 (McAuliffe, 2014).

There are possible fault cuts in several wells on the south flank of Sulphur Mountain (Fig. 3.2) but the dip of the SSCF would need to decrease to ~10° to correlate faults suggested in shallow boreholes at

the range front with fault cuts suggested in wells on Sulphur Mountain. West of O'Hara Canyon, the depth of potential fault cuts becomes inconsistent between wells and the number of wells that could potentially penetrate the low-angle SSCF but show no evidence of faulting increases (Fig. 3.2). Consequently, we suggest activity on the low-angle SSCF dies out 2–3 km west of O'Hara Canyon (Fig. 3.1). This interpretation indicates that the SSCF is likely not hard-linked with the Ventura fault, nor does the SSCF represent an eastern extension of Ventura fault geometry.

3.4.5 3D fault model

The 3D model of the SSCF presented in Figure 3.6 encompasses all of the data from all wells described below and presented in Figures 3.3, 3.4 and 3.5 and in Table 3.2, in addition to the surface trace of this fault (c.f. Hughes et al., 2018). When the combined fault evidence from well data is plotted, the resulting fault surface can be defined by a surface with an average dip around ~15° north that ranges in dip from 12–20°. The steepest dips occur in the centre of the fault beneath Orcutt Canyon and the dip shallows

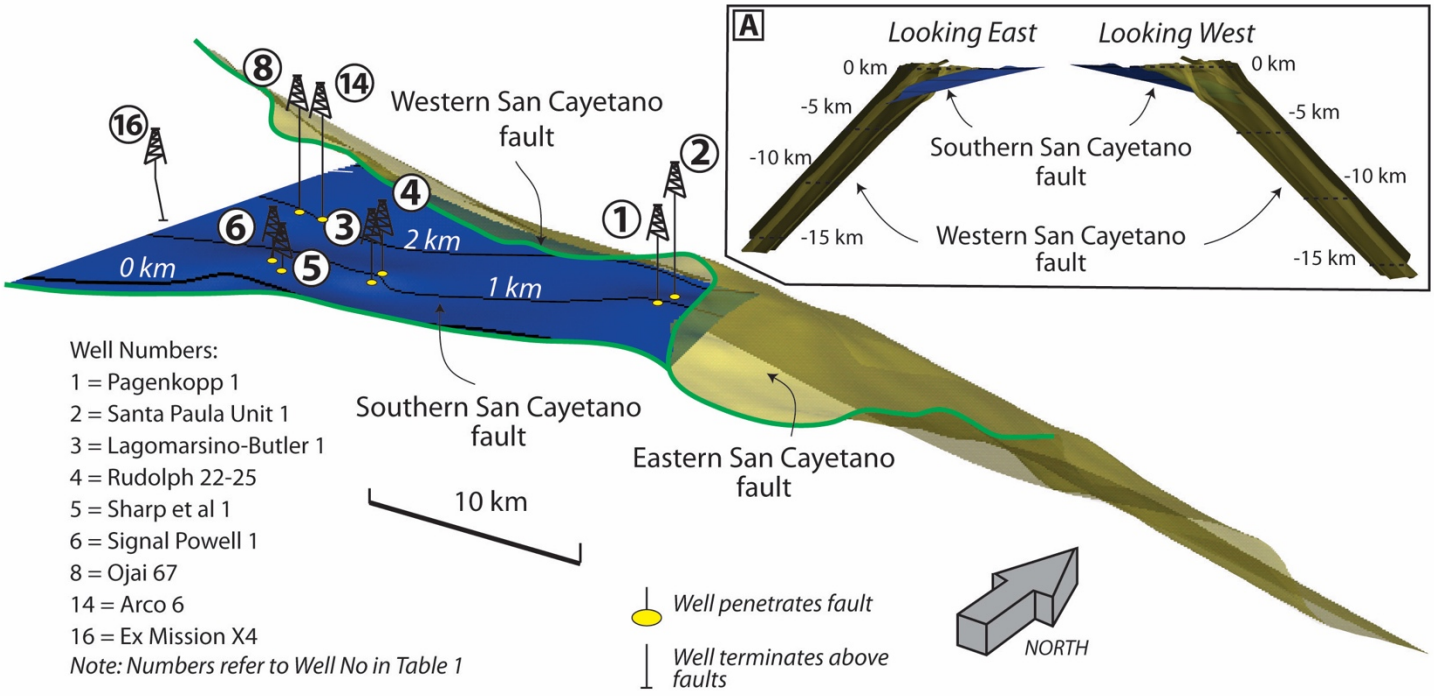

Figure 3.5 *Oblique 3D view of the Southern San Cayetano Fault (SSCF) looking northwest down-dip of the San Cayetano fault. Well numbers refer to well details described in Table 3.2. Green lines are surface traces of faults. Yellow circles denote where well penetrates fault. Cross sections in the top right are looking west and east to demonstrate the connection of the SSCF with the San Cayetano fault at depth.*

slightly at the eastern and western ends (Fig. 3.5). The SSCF connects with the WSCF at a depth of ~1.5 km at its eastern end, increasing to ~3.5 km in the west (Fig. 3.5).

3.4.6 The Top Pico horizon

The digitized contour map of the Top Pico horizon records an open anticline with an east-west striking axial plane around 2100–2300 mbsl and an associated syncline just to the north (Hopps et al., 1992). Just south of Fillmore, the depth of the Top Pico horizon increases to approximately 2500-2750 mbsl producing a northeast trending kink in the Top Pico surface on the south limb of the anticline that trends approximately 260° (Fig. 3.6). The open fold trends roughly parallel to the San Cayetano fault and the Santa Clara syncline but is not traceable farther west than where the Top Pico horizon is cut by the San Cayetano fault (Fig. 3.6). The density of wells decreases drastically westward of Fillmore (Fig. 3.2) and the 'kink' on the south limb of the fold is not traceable much farther west than Timber Canyon using resistivity data (Hopps et al., 1992). This fold and associated 'kink' could indicate the presence of a

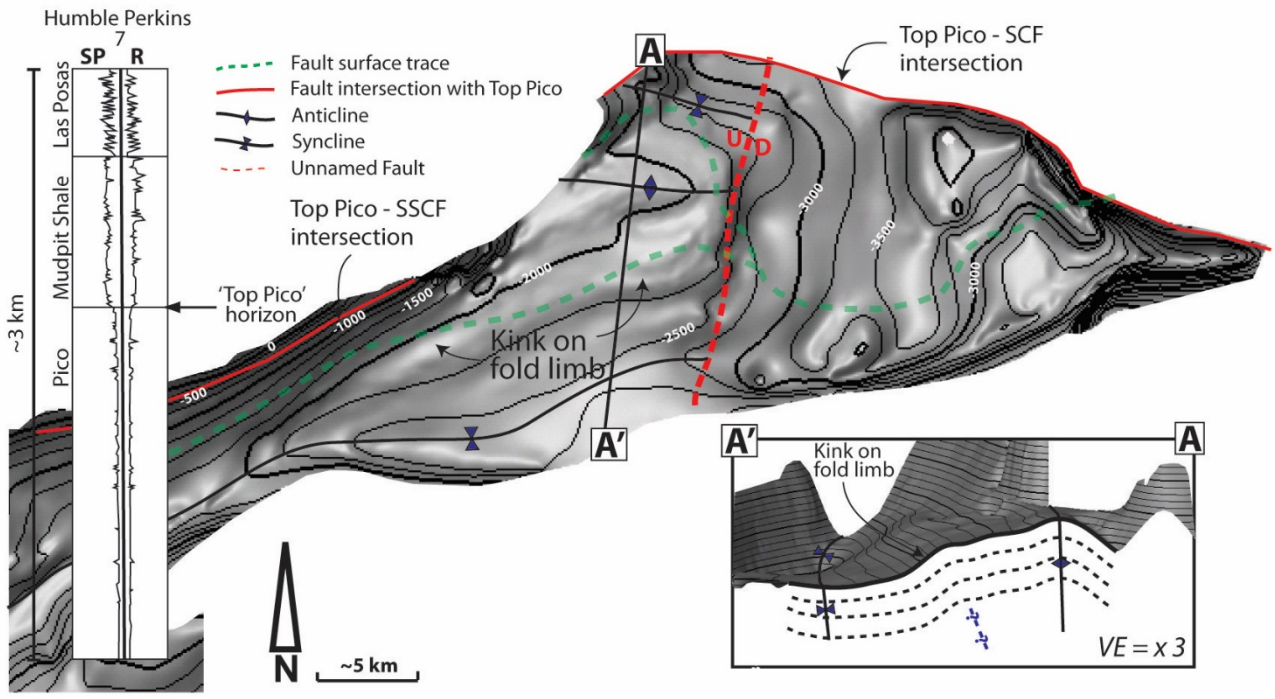

Figure 3.6 *Shaded relief contour map of the 'Top Pico horizon' showing folding of the horizon in the footwall of the San Cayetano fault (SCF). Fault surface traces are indicated with a dashed green lines and fold traces are shown with solid black lines. Solid red lines are intersections of 3D fault geometry presented in this study with the Top Pico horizon. The well-log shows resistivity (R) and spontaneous potential (SP) signal from well Humble Perkins 7, which demonstrates the characteristic decrease in R and increase in SP that signifies the top of the Pico formation (Hopps et al., 1992). Location of Humble Perkins 7 is included in Figure 3.2. Section A-A' is a cross section through the Top Pico surface with three times vertical exaggeration (VE) which shows the kink on the south limb of an open anticline.*

buried fault at depth with strike of approximately 260°, similar to the previous interpretation of a buried fault beneath the fold (Hopps et al., 1992).

3.5 Coulomb modelling results

In addition to the increase in fault dip where the SSCF connects with the WSCF (Fig. 3.5), many of the other faults contained in the CFM have non-planar geometry that demonstrate marked changes in down-dip and along-strike geometry, notably, the Pitas Point, Ventura, and eastern San Cayetano faults (Fig. 3.1) (Nicholson et al., 2017a). Consequently, the incorporation of variable geometry for faults in the Ventura basin in static Coulomb stress modelling is particularly significant. This section focuses primarily on the patterns in ΔCFF that occur on the SSCF and WSCF as a result of modelled ruptures on the Pitas Point, Ventura, and eastern San Cayetano faults. The stress on modelled receiver faults is used to assess the prospect of triggered seismicity on the SSCF and WSCF. Values for the maximum, minimum, and average ΔCFF imparted on the SSCF and the WSCF for the various earthquake rupture scenarios explored are included in Table 3.3.

In general, ruptures simulated on the 'ramp-flat' models for the Pitas Point or Ventura fault induce larger ΔCFF on the SSCF than the WSCF because the 'ramp-flat' geometry means the Ventura fault is physically closer to the SSCF and WSCFs at depth and modelled ΔCFF decreases with distance from the source fault (e.g., King et al., 1994). Ruptures simulated on the Pitas Point fault result in small positive ΔCFF on the SSCF and the WSCF regardless of whether the mid-crustal flat at 7 km is included in the Pitas Point fault or not (Fig. 3.7a). The key difference between the 'ramp-flat' and 'no-flat' models for ruptures on the Pitas Point fault is the value of ΔCFF imparted on the Ventura fault (Fig. 3.7a and 3.7b). For ruptures on the Pitas Point fault when the 'no-flat' model is employed most of the Ventura fault experiences negative ΔCFF with an average of -0.11 bars (Fig. 3.7a). When ruptures are simulated on the 'ramp-flat' version of the Pitas Point fault the upper 7 km of the Ventura fault, which has a modelled dip of 50° also experiences negative ΔCFF (Fig. 3.7b); however, below 7 km the Ventura fault exhibits positive ΔCFF with a maximum value of 18.63 bars where the modelled fault dip decreases to 6° and then increases to 35° (Fig. 3.7b).

Table 3.3 *Selected results from static Coulomb stress modelling*

Receiver Fault	Maximum ΔCFF (Bar)	Minimum ΔCFF (Bar)	Average ΔCFF (Bar)	Figure number
5.7 m maximum slip on Pitas Point fault (no-flat model)				
WSCF	0.07	-0.02	0.02	8a
SSCF	0.05	0.01	0.03	
Ventura fault	0.13	-0.37	-0.11	
11.0 m maximum slip on Pitas Point fault (ramp-flat model)				
WSCF	0.20	-0.09	0.03	8b
SSCF	0.11	0.03	0.07	
Ventura fault	18.63	-0.84	0.88	
1.6 m maximum slip on Ventura fault (no-flat model)				
WSCF	0.16	-0.11	0.01	8c
SSCF	0.08	-0.06	0.02	
4.5 m maximum slip on Ventura fault (ramp-flat model)				
WSCF	1.66	-2.10	-0.33	8d
SSCF	1.09	-1.28	0.20	
11.3 m maximum slip on entire Pitas Point/Ventura fault (ramp-flat model)				
WSCF	0.42	-2.56	-0.38	8e
SSCF	1.40	-0.22	0.42	
2.0 m maximum slip on ESCF				
WSCF	4.20	-0.27	0.40	8f
SSCF	2.87	-0.91	0.22	

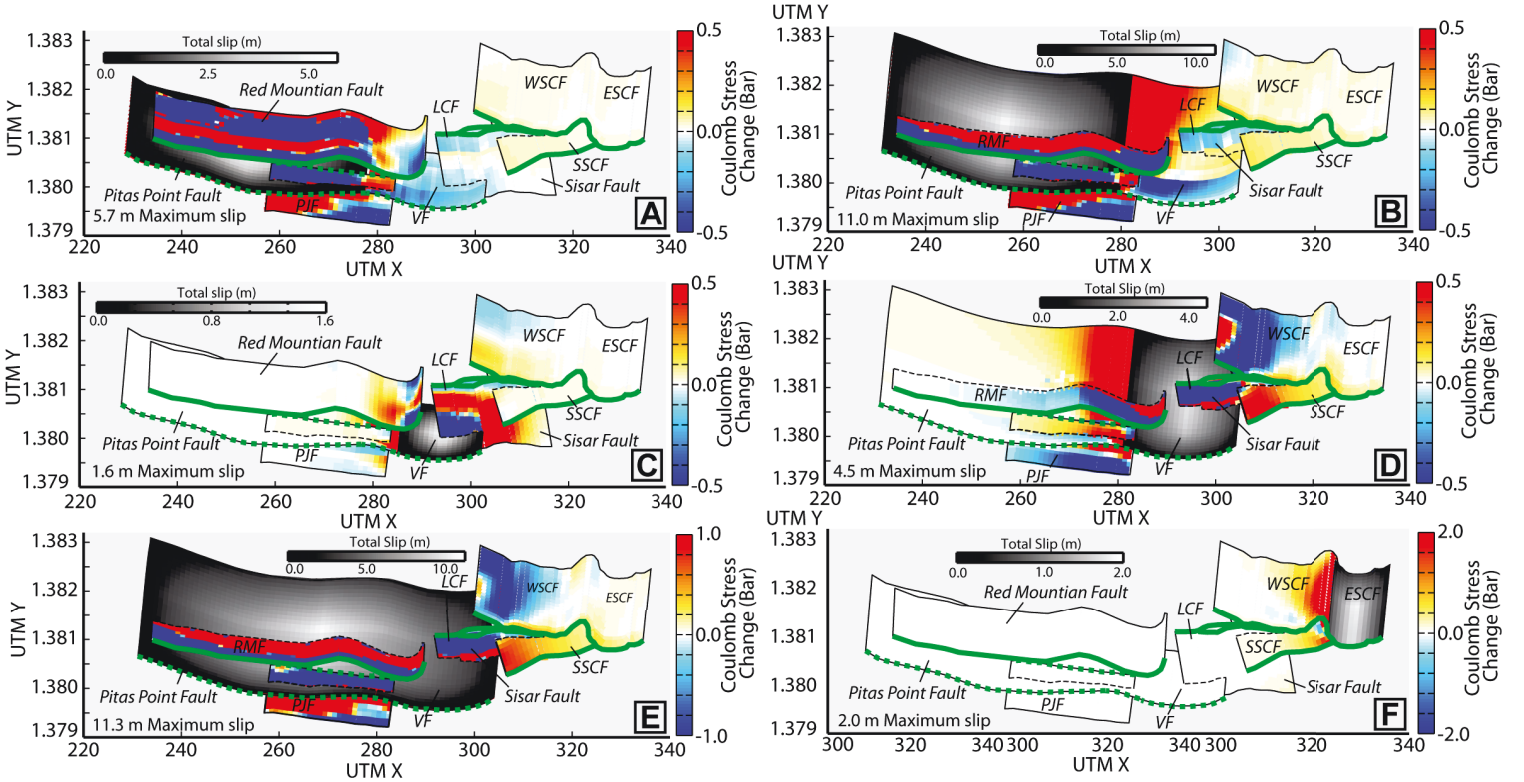

Figure 3.7 *Map views showing static stress imparted on various faults from ruptures simulated on the Pitas Point fault ('no-flat' model) (A), Pitas Point fault ('ramp-flat' model) (B), Ventura fault ('no-flat' model) (C), Ventura fault ('ramp-flat' model) (D), Entire Pitas Point/Ventura fault ('ramp-flat' model) (E). (F) The stress imparted on receiver fault for ruptures on the ESCF. Green lines are surface traces of faults. SSCF = Southern San Cayetano fault, ESCF = Eastern San Cayetano fault, WSCF = Western San Cayetano fault, RMF = Red Mountain fault, RMF = Red Mountain Fault, ORF = Oak Ridge Fault, SF = Sisar Fault, LCF = Lion Canyon fault, PJF = Padre Juan fault.*

When ruptures are simulated on the Ventura fault there are also key differences in the pattern of stress transfer if the 'ramp-flat' or the 'no-flat' models are adopted for the Pitas Point and Ventura faults. For example, when the 'no-flat' model is adopted for the Ventura fault, the upper ~7 km of the WSCF experiences a slight positive ΔCFF but the WSCF below ~7 km experiences slight negative ΔCFF (Fig. 3.7c). In contrast, when the 'ramp-flat' model is adopted for the Ventura fault most of the WSCF experiences negative ΔCFF with the exception of a patch of positive ΔCFF that has a maximum value of 1.66 bars along the western edge of the WSCF between 3.5 km to 10 km depth (Fig. 3.7d, Table. 3.3). Ruptures on the Ventura fault impart limited positive ΔCFF on the SSCF if the 'no-ramp' model is adopted for the Ventura fault with a maximum value of 0.08 bars (Fig. 3.7c) and greater ΔCFF with a maximum value of 1.09 bars if the 'ramp-flat' model is adopted (Fig. 3.7d, Table. 3.3).

A large rupture of the entire Pitas Point/Ventura fault in the 'ramp-flat' model with 11.3 m of maximum slip exerts mostly negative ΔCFF on the WSCF with a small section of slight positive ΔCFF along the western edge of the WSCF. Positive ΔCFF is observed across the entire SSCF (Fig. 3.7e). When ruptures are simulated on the ESCF there is positive ΔCFF across most of the SSCF with a maximum value of 2.87 bars and across the lower section of the WSCF with a maximum value of 4.2 bars (Fig. 3.7f, Table. 3.3).

3.6 Discussion and implications

The following discussion focuses on the implications that the non-planar fault geometry of faults in the Ventura basin affects stress transfer and potential earthquake hazards. We consider Holocene rupture pathways between the SSCF and the WSCF in the context of non-planar down-dip fault geometry, and between the SSCF, the WSCF, and the Ventura fault in the form of a proposed blind fault in the footwall of the SSCF. Static stress change effects are considered by using the results of the static Coulomb stress modelling to investigate the possibility that earthquakes on the SSCF and WSCF can occur as triggered seismicity (King et al., 1994; e.g., Freed, 2005) induced by events on the Pitas Point, Ventura, and eastern San Cayetano faults.

3.6.1 Holocene strain distribution and rupture dynamics

Large to moderately sized earthquakes (i.e. > M_w 6) generally nucleate at depths near the base of the seismogenic zone and faults present in the upper 3 km of the crust, such as the SSCF, are not capable of storing sufficient elastic strain energy to generate large earthquakes (e.g. Das and Scholz, 1983). Consequently, any large earthquake that propagates to the surface on SSCF would probably nucleate at depth on the lower WSCF, to which the SSCF is connected at 1.5–3.5 km depth (Fig. 3.5). The results

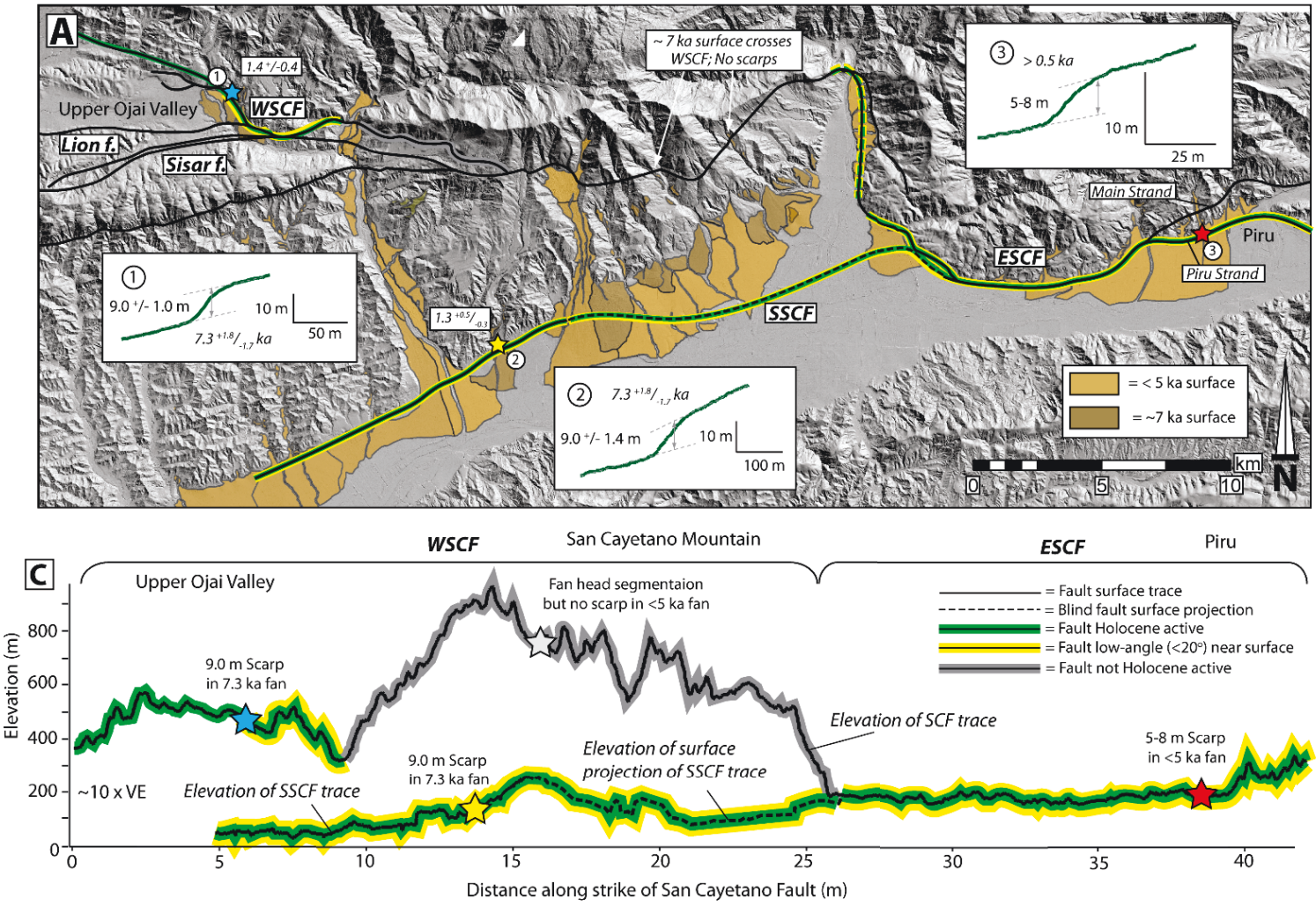

Figure 3.8 *Summary of Holocene geomorphic expression and stress distribution for the Southern San Cayetano (SSCF) and San Cayetano faults. (A) Hillshade map with Holocene alluvial terraces and fans in proximity to the SSCF and San Cayetano fault. Major reverse faults are denoted with black lines (dashed where blind) and where fault traces are outlined in green indicates Holocene active and outlined in yellow indicates low angle (<20°) in the shallow subsurface. Coloured stars show the locations of fault scarps in Holocene alluvial fans topographic profiles across the scarps numbered 1–3 (Yellow = SSCF, red = eastern San Cayetano fault (ESCF), blue = western San Cayetano fault (WSCF)). The age of the surface is in italics and uplift amount is in standard text. (C) Topographic profile along the trace of the San Cayetano and SSCF faults demonstrating where the WSCF has been uplifted by activity on the south-dipping Sisar and Lion faults with locations of Holocene fault scarps along strike. Uplift across scarp for the WSCF from Rockwell (1988), for the SSCF from Hughes et al., (2018), and for the ESCF from Dolan and Rockwell (2001).*

of the static stress modelling can be compared with evidence from geomorphology to provide further insights into the partitioning of strain between the SSCF and the WSCF and possible rupture pathways for earthquakes that nucleate at depth on these faults.

The youngest fault scarp associated with the SSCF observed in the field records ~9 m total uplift of a 7.3 $^{+1.8}/_{-1.7}$ ka Holocene alluvial fan at Orcutt Canyon, although there is no paleoseismic data to confirm how may events created this scarp or when the most recent rupture occurred (Hughes et al., 2018) (Fig. 3.8). Pronounced fault scarps in Holocene deposits are also recorded along the WSCF in the Upper Ojai Valley and along the ESCF at Piru (Fig. 3.8) (Rockwell, 1988; Dolan and Rockwell, 2001). Along the ~15 km central section of the San Cayetano fault where the fault trace is uplifted by south dipping faults on Santa Paula Peak (Fig. 3.1), there are no fault scarps in Holocene alluvial surfaces that cross the San Cayetano fault (Fig. 3.8), although possible fan head segmentation across a ~5 ka alluvial fan at Timber Canyon could be related to activity on the WSCF (Rockwell, 1988).

It is possible that events have occurred on the uplifted section of the WSCF during the Holocene that were too small or too infrequent to leave a scarp, or the scarps may have been eroded by fluvial activity or buried by subsequent deposition. Alternatively, the lack of fault scarps in Holocene deposits on the uplifted central section of the WSCF could indicate that this section of the WSCF has been inactive during the Holocene and ruptures in the central Ventura basin preferentially propagate to the surface along the SSCF. If it is the case that Holocene ruptures are propagating to the surface along the SSCF, the lower Holocene slip rate of 1.3 mm yr^{-1} for the SSCF (Hughes et al., 2018) compared to a rate possibly as high as 7.5 mm yr^{-1} for the ESCF (Cemen, 1989) and a rate of 4.4–6.9 mm yr^{-1} for the Ventura fault (Hubbard et al, 2014) could indicate that a large portion of strain in the hanging wall of the SSCF is accommodated by folding rather than slip on the SSCF. Alternatively, a portion of slip could be partitioned onto a possible blind fault in the footwall of the SSCF (Fig. 3.6).

The pattern of ruptures preferentially travelling up-dip from depth along low-angle reverse faults near the surface has previously been documented on the ESCF (Dolan and Rockwell, 2001; Dolan, 2009). As the ESCF approaches the surface, the fault bifurcates into a low-angle ‘Piru strand’ with a dip of 10–30° and a ‘main strand’ that dips ~50° (Çemen, 1989; Huftile and Yeats, 1996). The Piru strand

exhibits a 5–8 m high multi-event scarp in late Holocene alluvial fans (Fig. 3.8), whereas the main strand is thought to be inactive and demonstrates no evidence of Holocene or recent activity (Dolan and Rockwell, 2001). Dynamic rupture simulations of slip propagating up-dip over a decrease in fault dip show that slip is increased on low-angle sections of faults, due to a dynamic unclamping and decreased normal stress on the low-angle fault (Ryan et al., 2015). Dynamic unclamping, in combination with the positive ΔCFF recorded on the ~15° SSCF in all the earthquake rupture scenarios in Figure 8, provide one potential explanation as to why Holocene activity appears to have been concentrated on the low-angle SSCF and ESCF compared to the existing higher-angle upper sections of the eastern and western San Cayetano.

3.6.2 Potential for multi-fault earthquake by static stress triggering

The above discussion in section 3.5.1 examines potential rupture scenarios between the SSCF and the WSCF. However, triggered seismicity from static stress change has been suggested as one possible mechanism for multi-fault earthquakes between the Pitas Point, Ventura, and San Cayetano faults (McAuliffe et al., 2015).

The value of ΔCFF that represents a triggering threshold (i.e. changes above which are thought to be sufficient to trigger seismicity) is poorly understood, with estimates ranging from 1 bar (Kilb et al., 2002), 0.5 bars (King et al., 1994), 0.2 bars (Toda et al., 1998), to values as low as 0.01 bars (Rydelek and Sacks, 1999; Ziv and Rubin, 2000; Ogata, 2005). Ruptures on the ESCF impart large positive ΔCFF on the WSCF and the SSCF with maximum ΔCFF values of 4.20 bars on the WSCF and 2.87 bars on the SSCF (Table. 3.3). These values are well above even the largest triggering threshold estimates of 1 bar (Kilb et al., 2002) and could well trigger an earthquake that nucleates along the WSCF at depth. Such an event may propagate to the surface along the SSCF rather than the upper WSCF, given the effect of dynamic unclamping and reduced normal stress on the 15° SSCF compared to the 40–50° upper WSCF (Oglesby et al., 1998; Ryan et al., 2015).

Maximum ΔCFF on the WSCF when ruptures are simulated on the Pitas Point fault are 0.07 bars in the ‘no-flat’ model and 0.20 bars in the ‘ramp-flat’ model (Table.3) and these values are at the lower end

of those considered a triggering threshold (e.g. Ziv and Rubin, 2000). Consequently, the likelihood of triggered seismicity on the SSCF and the WSCF from ruptures on the Pitas Point fault may depend on the current stress state on the fault at the time of rupture, which plays an important role in whether triggered seismicity will occur on a fault and how large the resulting earthquake will be (Deng and Sykes, 1997a; Rydelek and Sacks, 1999; Freed et al., 2007).

For ruptures that are simulated on the Ventura fault in the 'no-ramp' model the lower section of the WSCF experiences negative ΔCFF and the prospect of triggered seismicity is decreased. In contrast, if the 'ramp-flat' geometry is adopted for the Ventura fault, then maximum ΔCFF of 1.66 bars in the patch of positive ΔCFF between 3.5–10 km depth along the western section of the WSCF (Fig. 3.7d) could potentially trigger an event on the WSCF. If a large rupture were to occur on the entire Pitas Point/Ventura fault in the 'ramp-flat' model, then most of the WSCF experiences negative ΔCFF (Fig. 3.7e). An area of positive ΔCFF along the western edge of the WSCF only extends to a depth of 8 km (Fig. 3.7e). Even if this small patch of positive ΔCFF is sufficient to trigger seismicity on the WSCF, which seems unlikely given that stress heterogeneities on a fault plane can inhibit rupture propagation (Rydelek and Sacks, 1999; Mildon et al., 2017), then the resulting event may be small given the relatively shallow depth of around 7 km that the triggered event would nucleate. In summary, for ruptures on the Pitas Point and Ventura fault the prospect of triggered seismicity on the WSCF and SSCF could depend on where exactly along the Pitas Point/ Ventura fault the rupture occurs, the precise geometry for the Pitas Point and Ventura faults at depth, and the pre-existing stresses on the WSCF and SSCF at the time of rupture.

In the simplified models presented here ruptures have only been simulated on the Pitas Point, Ventura, and ESCFs. However, the current stress state of the SSCF and the WSCF will of course be a product the total ΔCFF imparted on these faults by earthquakes on all the potentially active faults in the Ventura basin including the Oak Ridge, Simi, Red Mountain, Padre Juan, and Arroyo Parida faults (Fig. 3.1). Furthermore, potential stress changes induced by large-magnitude events on the San Andreas fault (e.g., Deng and Sykes, 1997a) and long-term stresses due to plate boundary interactions (Freed et al., 2007) will also exert significant control on the stress state of the SSCF and the WSCF.

Additionally, we note that there is large positive ΔCFF imparted on the Lion Canon and Sisar faults when ruptures are simulated on the Ventura fault. Ruptures on the Sisar fault were not considered in the analyses conducted here because is thought to be inactive, or at least no longer active at the surface, due to a lack of surface scarps associated with the fault trace and the interpretation that the SSCF cross cuts the Sisar fault in the subsurface (Hughes et al., 2018). However, even if the Sisar fault is still active at depth, we note that ruptures on the Sisar fault would impart strongly negative ΔCFF on the WSCF at depth and would not likely trigger seismicity on the SSCF and WSCF (Fig. S1).

Although not the primary focus of this study, insights into the possibility of multi-fault earthquakes can be made by examining the static stress transfer between the Pitas Point and Ventura faults (Fig. 3.7a and 3.8b). In the 'no-flat' model ΔCFF for the Ventura fault is negative across most of the fault for ruptures of the Pitas Point fault (Fig. 3.7a), but if the 'ramp-flat' model is adopted then the lower section of the Ventura fault experiences positive ΔCFF (Fig. 3.7b). This distinction is important because the negative ΔCFF on the Ventura fault implies that in the 'no-flat' model the Ventura fault is located in a stress shadow of the Pitas Point fault (e.g. Harris, 1998). Therefore, static stress effects decrease the likelihood of multi-fault earthquakes in the 'no-flat' model. A deceased likelihood of multi-fault earthquakes is also suggested by the lower degrees of fault connectivity at depth, which decreases the likelihood for dynamic rupture propagation along the Pitas Point and Ventura faults in the 'no-flat' model compared to the 'ramp-flat' model (Nicholson et al., 2017b). Conversely, the positive ΔCFF on the lower Ventura fault in the 'ramp-flat' model from ruptures on the Pitas Point fault suggest that static Coulomb stress triggering could be a factor in facilitating multi-fault earthquakes between the Pitas - Points and Ventura faults (Hubbard et al., 2014; Rockwell et al., 2016).

These contrasting conclusions that can be drawn from whether the 'ramp-flat' model or the 'no-flat' model are adopted highlight the need for further work to characterize the deep structure of these faults. Furthermore, the results presented here assume all slip on the fault is pure reverse despite the suggestion that there may be a significant oblique component to slip on some of these faults (e.g., Sorlien et al., 2000, Marshall et al., 2013). We acknowledge that modelling slip as pure reverse is a simplification and

suggest that data to accurately quantify the proposed lateral component of slip on the Pitas Point, Ventura, or San Cayetano faults would strengthen the static Coulomb stress modelling conducted here.

3.6.3 A potential blind fault beneath Fillmore

The potential for static stress triggering for earthquakes on the SSCF and the WSCF for could depend on various factors, including the deep structure of the Pitas Point and Ventura faults. However, the presence or absence of a blind fault in the footwall of the San Cayetano fault is important, because such as structure may increase the deep connectivity of the Pitas Point, Ventura, and San Cayetano faults and potentially provide a pathway for dynamic rupture propagation between these faults (e.g., Hubbard et al, 214). The contour map of the 'Top Pico' horizon indicates a low-amplitude anticline and a

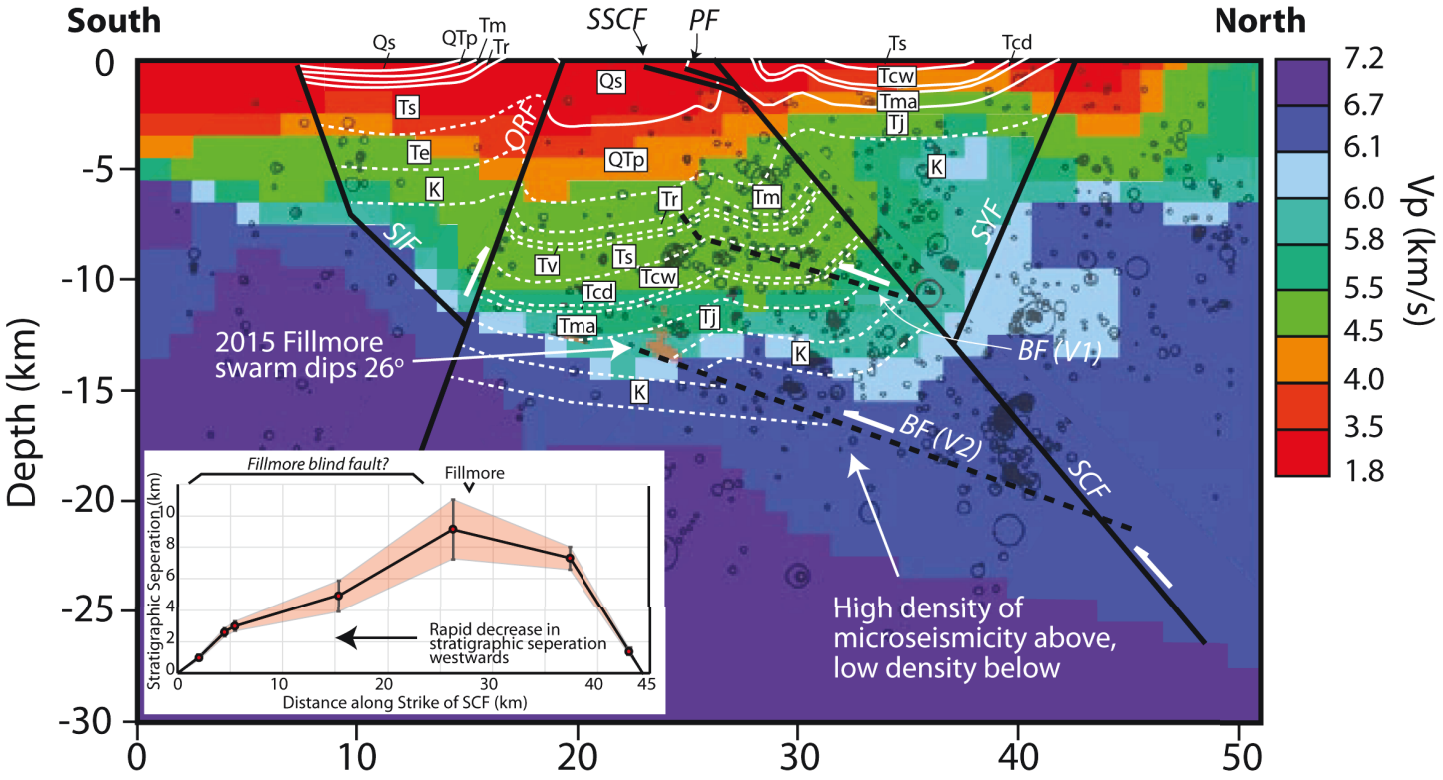

Figure 3.9 *Deep cross section amended from Hauksson et al, (2016) which shows a high concentration of microseismicity (black circles) in the footwall of the San Cayetano fault (SCF) compared to the hanging wall of the San Cayetano and Oak Ridge (ORF) faults. Section is colour coded by seismic p-wave velocity taken from Shaw et al,. 2015. Solid black lines are faults and the dashed black lines show two possible geometry for a potential blind fault. The upper interpretation is based on the depth for a blind fault in the footwall of the San Cayetano from 2D structural modelling and cross section balancing (Yeats et al., 1988; Hubbard et al., 2014) and the lower interpretation is based on microseismicity and is similar to the interpretation of Huftile and Yeats (1996). The inset graph shows stratigraphic separation along strike of the San Cayetano fault, which drop off sharply westward from a maximum at Fillmore. Stratigraphic separation values across the SCF surface trace and associated uncertainties are from Rockwell (1988) and Cemen (1989) and if no uncertainty was provided in the reference then a 10% uncertainty was applied. Abbreviations for stratigraphic units are included in Figure 3.2, BF = Blind fault, PF = Pagenkopp fault, SSCF = Southern San Cayetano fault, SYF = Santa Ynez fault*

corresponding syncline that run parallel to the San Cayetano fault in the fault footwall with a kink on the southern limb of the anticline that could be related to the presence of a blind fault at depth (Fig. 3.6). An initial interpretation attributed this fold to a low-angle eastward continuation of the Ventura fault (Hopps et al., 1992). However, there is no evidence in the well-log data between Fillmore and the western end of the Ventra fault to suggest that the Ventura fault extends as far east a Fillmore. Additionally, there is little evidence for a low-angle fault in well data from the upper 5 km beneath the Ventura basin despite the numerous deep wells (max depth ~5 km) drilled in the Santa Clara valley (Fig. 3.2). Therefore, we speculate that if the fold in the Top Pico is a product of folding above a blind fault, then the potential blind fault may be located below 5 km, which is the maximum depth of well control.

There are several additional independent lines of evidence for a blind fault in the footwall of the San Cayetano fault. For example, stratigraphic separation values calculated by summing the total stratigraphic thickness separating equivalent stratigraphy in the footwall and hanging wall of the San Cayetano fault, suggest that displacement on the WSCF decreases significantly west of Fillmore (Rockwell, 1988; Çemen, 1989) (Fig. 3.9). The sudden westward decrease in stratigraphic separation, could be a result of slip being partitioned between the WSCF and a possible blind fault in the footwall of the WSCF west of Fillmore (Fig. 3.9). Additionally, a 2.4 km north-south high-resolution seismic reflection survey across the topographic range front north of Saticoy (Fig. 3.1), identifies a north-dipping synclinal axial surface that is potentially associated with a blind fault at depth (McAuliffe, 2014).

It is possible that the fold in the Top Pico is non-tectonic and related to processes of differential subsidence and compaction in the footwall of the San Cayetano fault (Nicholson et al., 2007). However, the fact that the fold runs parallel to the other major structures in the area, such as the San Cayetano fault and the Santa Clara syncline, and the fact that all of folds in the region are associated with thrust faults, suggest a potential tectonic origin for the fold. Furthermore, in a cross section through the central Ventura basin the highest density of microseismicity is located in the footwall of the San Cayetano fault (Fig. 3.9) (Hauksson et al., 2016). The microseismicity includes a 2015 micro-earthquake cluster

beneath Fillmore that defines a smooth plane which dips 26° north at 12 km depth (Hauksson et al., 2016). It is possible that this plane is related to the potential blind fault which folds the Top Pico horizon but the high density of micro-seismicity in the footwall of the San Cayetano fault indicates a potentially active blind fault could be at any depth between the depth of well control at ~5 km and the base of seismicity at ~15 km (Fig. 3.9).

Other workers have included a low-angle north dipping blind fault in the footwall of the San Cayetano fault to accommodate folding on the south verging Lion Mountain anticline and Reeves syncline (Fig. 3.4) (Yeats et al., 1988; Huftile and Yeats, 1996). These blind faults are based on 2D kinematic modelling and cross section balancing. The strike of the axial plane of the folds in the Top Pico horizon runs roughly parallel to the strike of the San Cayetano fault in the same way that the strike of the Lion Mountain anticline and Reeves syncline run parallel the San Cayetano fault in the Upper Ojai valley (Fig. 3.2). Furthermore, the Lion Mountain anticline and Reeves syncline are projected eastwards to the footwall of the ESCF at depth (Huftile and Yeats, 1996). We suggest that the anticline and syncline pair observed in the Top Pico horizon could be the top of the eastward projection of the Lion Mountain anticline and the Reeves syncline and that a blind fault underlies this fold pair, similar to previous interpretations which have attributed folding in the footwall of the San Cayetano fault to a blind fault (Yeats et al., 1988; Huftile and Yeats, 1996).

In summary, there are no data to accurately characterize the precise depth or geometry of a potential blind fault beneath Fillmore but there are several independent, albeit indirect, observations that can be used to argue in favour of a blind fault at some depth in the footwall of the San Cayetano fault. These observations include folding in the footwall of the San Cayetano fault, a sudden decrease in stratigraphic separation on the San Cayetano fault west of Fillmore, and the high density of micro-seismicity in the footwall of the San Cayetano fault (Fig. 3.9).

3.7 Conclusions

Results from an integrated analysis of well data, geological maps, cross sections, and structural contour maps reveal evidence for the 3D geometry of the Southern San Cayetano fault (SSCF) and outline the

potential subsurface connection of the SSCF with the San Cayetano fault. The SSCF has a 12–20° north dip along the northern Santa Clara River Valley and connects with the western San Cayetano fault (WSCF) at depths of 1.5–3.5 km. A comparison of models of static Coulomb stress changes along regional faults with evidence from geomorphology indicate that Holocene ruptures may propagate to the surface along the SSCF rather than the upper WSCF. Static Coulomb stress modelling also indicates that triggered seismicity may occur on the SSCF and the WSCF as a result of ruptures on the ESCF. However, different conclusions can be drawn on the role of static stress in the prospect for multi-fault earthquakes in the Ventura basin depending on whether a mid-crustal flat is included in the Pitas Point and Ventura faults. These results serve as a good example of how variation in fault dip can exert a strong control on stress distribution of receiver faults and highlights the importance of incorporating variable dip faults into static Coulomb stress modelling. In addition, the results also indicate that an accurate understanding of 3D subsurface fault geometry is critical to a proper understanding of fault behaviour, the likelihood of multi-fault ruptures, and the long-term seismic hazard associated with faults. However, even in relatively well studied areas such as the Ventura basin the deep geometry of faults is often not fully understood.

Chapter 4: Tectonically-dominated Quaternary landscape evolution of the Ventura basin, southern California, quantified using cosmogenic isotopes with topographic analyses+

Chapter Abstract

Understanding how spatial and temporal variations in fault activity effect local patterns of relief generation and channel morphology has important implications for natural hazards and landscape evolution. Here, we quantify the complex interplay between tectonic uplift, the growth of topography, and erosion recorded in the hanging walls of several important seismically active reverse faults in the Ventura basin, southern California to investigate how Quaternary fault evolution and lithological distribution have controlled patterns of relief generation and erosion. First, we present the results of cosmogenic isotope isochron burial dating of an important, but poorly dated, Quaternary strain marker, the Saugus Formation. We then use this chronology to calculate tectonically-driven rock uplift rates and reduce uncertainties in fault slip rates. The results of the burial dating confirm that the Saugus Formation is time-transgressive with ages for the top of the exposed Saugus Formation of 0.38 $^{+0.17}/_{-0.23}$ Ma (mode and 95% confidence interval) at Ventura and 2.49 $^{+0.25}/_{-0.29}$ Ma in the east Ventura basin. The burial ages for the base of shallow marine sands, which underlie the Saugus Formation throughout the basin are 0.55 $^{+0.80}/_{-0.10}$ Ma at Ventura and 3.30 $^{+0.30}/_{-0.42}$ Ma in the eastern Ventura basin. In addition, we calculate ^{10}Be catchment-averaged erosion rates, characterise patterns of catchment relief and channel steepness indices, and analyse river long-profiles in fault hanging walls in order to compare the results with patterns of fault displacement on various temporal scales. The results of the landscape analysis indicate that relief, channel steepness, and erosion rates are still adjusting the new tectonic boundary conditions imposed by different tectonic perturbations that have occurred since ~1.5 Ma including fault initiation and fault linkage. The data presented here suggests that for transient landscapes on the local scale with uniform

climate, fault activity is the primary control on patterns of relief generation and channel morphology over periods of 10^4 to 10^6 years.

+ A version of this chapter is in preparation for submission to *The Geological Society of America Bulletin* with the following author list:

A. Hughes, D. H. Rood, A. C. Whittaker, R. E. Bell, K. M. Wilcken, L. B. Corbett, P. R. Bierman, D. E. DeVecchio, T. K. Rockwell

AH conceived of the idea of the research and collected the samples and performed the laboratory analyses for the ^{10}Be catchment averaged erosion rate samples, the boulder samples, and isochron burial sample suites HCR, SI5, and SLC. Isochron burial sample suites STL, SVF, SGR, SCQ were collected and processed in the laboratory before the commencement of my PhD by DHR and DDV. Accelerator mass spectrometry for samples HCR, SI5, and SLC was conducted by KMW. AH performed the all the data reduction and analysis, prepared the figures, and wrote the manuscript. DHR aided AH with the laboratory analysis, ACW aided AH with landscape analysis and all authors discussed the science and commented on the manuscript.

4.1 Introduction

The characterization of temporal variations in the competing forces of tectonic uplift and erosion within active mountain belts is essential to examine how variability in tectonic forcing, lithological distribution, and climate affect rates of erosion and relief generation. A common approach for investigating the relationship between rock uplift and erosion is to compare tectonic uplift and fault displacement rates with catchment-averaged erosion rates and morphometric landscape parameters such as relief and/or channel steepness (Vance et al., 2003; Densmore et al., 2009; Cyr et al., 2010; Miller et al., 2013; D'Arcy and Whittaker, 2014). In transient landscapes, these data are often supported by a quantitative analysis of river long-profiles and knickpoints upstream of faults (Whittaker et al., 2008; Miller et al., 2012; Roda-Boluda et al., 2019). However, questions remain about the effectiveness of catchment-averaged erosion rates and morphometric landscape parameters, such as topographic relief and normalised channel steepness indices, as a tool for tracking tectonics in rapidly eroding transient

landscapes (Kirby and Whipple, 2012; Gudmundsdottir et al., 2013; Ellis and Barnes., 2015; Whittaker and Walker, 2015; Kent et al., 2017; Wang et al., 2017; Roda-Boluda et al., 2019).

The key starting point for any thorough assessment of landscape response to tectonic forcing is a high-resolution record of fault activity, e.g., tectonic rock uplift and/or fault slip rates, and an accurate quantification of erosion rates (e.g. Cyr et al., 2010; Roda-Boluda et al., 2019). Developments in Quaternary dating techniques over the past twenty years have provided geoscientists with the ability to accurately quantify rock uplift rates via the precise dating of strain markers, and erosion rates on various timescales between 10^2–10^6 years (Granger and Muzikar, 2001; Balco and Rovey, 2008; Balco et al., 2008; Granger et al., 2013). Such comparisons enable us to address questions about whether present-day relationships between rock uplift, erosion, and sedimentation are representative of a long-term signal, which can be applied to model landscape evolution (Armitage et al., 2011; DeVecchio et al., 2012a; Corbett et al., 2016a) or quantify seismic hazards (Kirby et al., 2008; Boulton and Whittaker, 2009).

Despite the importance of a high-resolution record of Quaternary fault activity to an analysis of landscape evolution, prior to the development of cosmogenic isotope isochron burial dating the calculation of early Pleistocene or Pliocene fault displacement rates was often problematic because no reliable method was available to directly date certain strain markers such as terrestrial sedimentary deposits (Balco and Rovey, 2008; Balco et al., 2013). A good example of an important but poorly-dated strain marker is the Saugus Formation in the Ventura basin, southern California (Fig. 4.1), which is a deformed sequence of terrestrial fluvial and alluvial sediments of presumed Pleistocene age (Levi and Yeats, 1993; Swanson and Irvine, 2015). The Saugus Formation is a key strain marker within the Ventura basin because the formation is often described as the youngest of the deformed bedrock strata and is argued to record the Pleistocene onset of activity on several major active faults and related drainage reorganizations (Levi and Yeats, 1993; DeVecchio et al., 2012a; DeVecchio et al., 2012b).

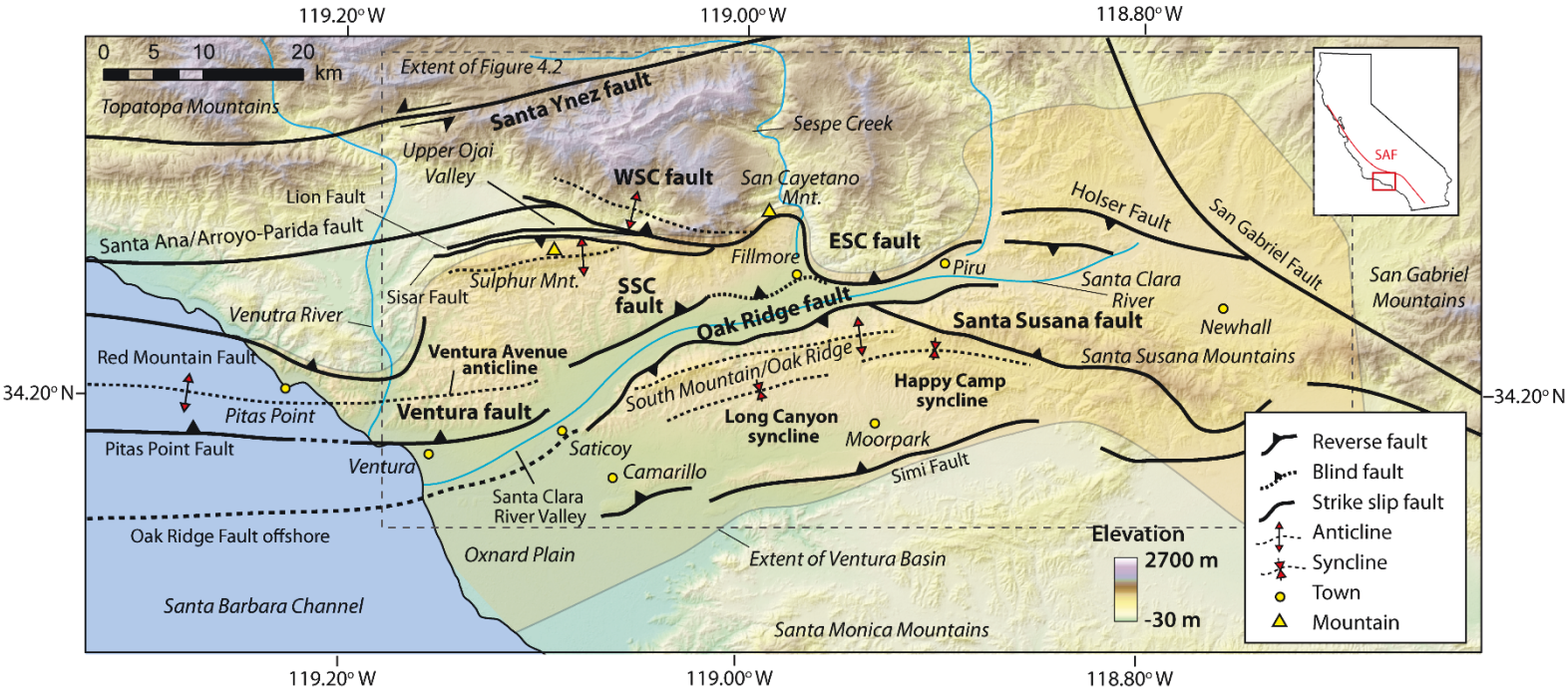

Figure 4.1 *Shaded relief map of the study area with major structures. Major faults are denoted with solid black lines with triangles on hanging wall of reverse faults. Key folds are denoted with thin dashed lines. The extent of the Ventura Basin is shaded in orange based on the extent of Plio-Pleistocene sedimentary deposits (Campbell et al. 2014). The dashed box denotes the location of Figure 4.3. Fault surface traces are based on the Dibblee maps. WSC = Western San Cayetano fault, ESC = Eastern San Cayetano fault, SSC = Southern San Cayetano fault, SAF = San Andreas fault.*

However, while that the Saugus Formation is thought to be time-transgressive, few direct ages for the Saugus Formation exist (Wagner et al., 2007; DeVecchio et al., 2012a).

Improvements in the chemistry required for isochron burial dating (Corbett et al., 2016b) and accelerator mass spectrometry techniques (Rood et al., 2010; Wilcken et al., 2017) along with recent validation of the isochron burial dating method via a comparison with existing K–Ar and $^{40}Ar/^{39}Ar$ chronology (Zhao et al., 2016) provide the necessary tools to create a high-resolution geochronology for previously undatable Quaternary sedimentary deposits, including the Saugus Formation. The resulting chronology can be used to quantify Quaternary fault displacement rates and investigate the landscape response to active faulting, including in complex compressional tectonic regimes such as the Ventura basin.

The primary aim of this work is to re-evaluate tectonic deformation rates for the Ventura basin and use these rates as the basis to investigate how tectonic and lithological factors control erosion rates

topographic development over various temporal scales. We apply cosmogenic isotope isochron burial dating to quantify spatial variation in the age of the Saugus Formation, and use the resulting geochronology to calculate slip rates for several regionally important reverse faults in the Ventura basin. To compare with fault displacement rates, we calculate terrestrial cosmogenic nuclide (TCN)-derived erosion rates for catchments along strike and undertake a morphometric landscape analysis in the hanging wall of active reverse and thrust faults. The erosion rates and the results of the morphometric landscape analysis are then compared with fault slip rates to quantify the landscape response to tectonic forcing. The results provide further evidence that over the local scale (< ~100 km^2) where climate can be considered uniform, tectonic and lithological variations exert a strong control on the distribution of erosion rates, channel steepness, and topographic relief development.

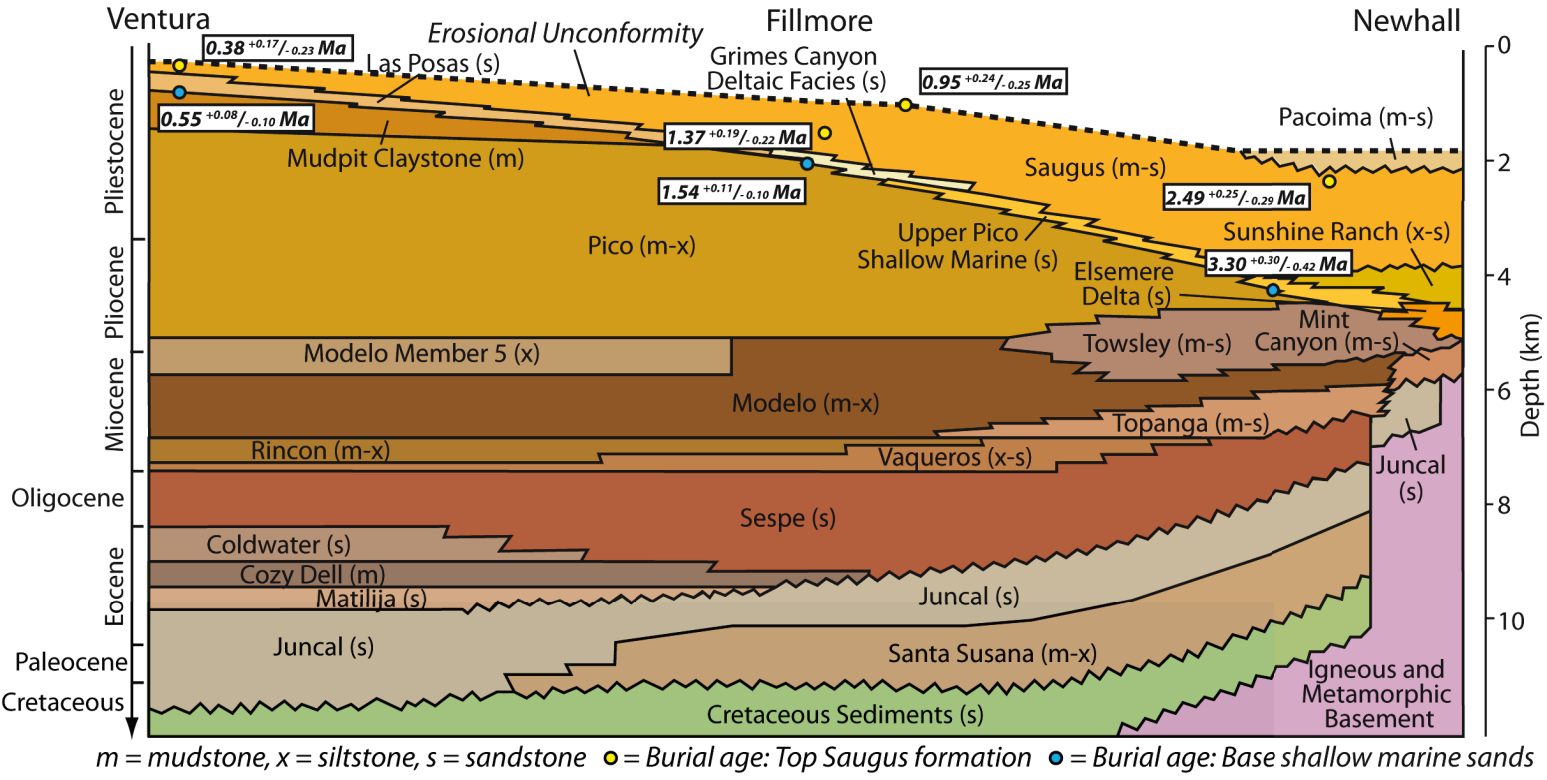

Figure 4.2 *Idealised stratigraphic section across the Ventura basin amended from Swanson and Irvine (2015). Letters in brackets denote the primary lithology within the unit (m = mudstone, x = siltstone, and s = sandstone). Circles are the stratigraphic location and burial age of the isochron burial samples from this study, with yellow circles denoting a burial age for the top of the exposed Saugus Formation and blue circles denoting the burial age for the base of the shallow marine sand units which underlie the Saugus Formation throughout the Ventura basin.*

4.2 Tectonic and stratigraphic setting

4.2.1 Late Cenozoic geological setting

The Ventura basin is an east-west trending, fault-bounded, sedimentary trough situated in the Western Transverse Ranges of southern California (Fig. 4.1). It is bounded to the north by the Topatopa Mountains, to the east by the San Gabriel Mountains, to the south by the Santa Monica Mountains, and extends westward offshore into the Santa Barbara Channel (Fig. 4.1). Within the basin, the marine Modelo Formation accumulated during the Miocene in a transtensional regime (Yeats et al., 1994) above an Oligocene-Eocene sedimentary succession (Fig. 4.2 and 4.3) (Bailey, 1947; Dibblee, 1950; Vedder et al., 1969). Subsequently, a switch to transpressional deformation occurred in the late Miocene to early Pliocene with the formation of the 'Big Bend' in the San Andreas Fault (e.g. Crowell, 1976; Wright, 1991). Consequently, the current structural framework of the Ventura basin is largely a product of post-Miocene inversion of transtensional basins in a transpressional regime (Crowell, 1976; Yeats et al., 1994).

Up to 7 km of heavily tilted and overturned Pliocene-Pleistocene stratigraphy was deposited after the onset of transpression (e.g., Yeats et al., 1994) as part of a marine regression from a deep water basinal setting to terrestrial alluvial deposits (Fig. 4.2 and 4.3) (Campbell et al., 2014; Swanson and Irvine, 2015). Transpressional deformation is currently expressed by north-south directed regional crustal shortening at rates of 7–10 mm yr^{-1} (Donnellan et al., 1993b, Marshall et al., 2013), which is accommodated by a series of east-west striking folds and reverse faults (Fig. 4.1).

Here, we focus on the San Cayetano, Southern San Cayetano, Ventura, and Oak Ridge faults (Fig. 4.1), which are all thought to represent significant contemporary earthquake hazards (Field et al., 2014; Field et al., 2015) and are believed to have contributed significantly to the landscape evolution of the onshore Ventura basin (Rockwell et al., 1984; Azor, 2002; DeVecchio et al., 2012a). Furthermore, activity on the San Cayetano, Ventura, and Southern San Cayetano faults is thought to have initiated at different times within the same tectonic setting and a similar lithologic setting (Rockwell et al., 1984; Rockwell, 1988; Cemen, 1989, Hubbard et al., 2014; Hughes et al., 2018), which makes these faults an ideal case

study in which to examine how lithology and tectonics control topographic relief development through time. For example, the San Cayetano fault is a north-dipping reverse fault that runs east-west for ~40 km from Piru to the Upper Ojai Valley (Fig. 4.1) (Rockwell, 1988). The San Cayetano fault is often separated into an eastern section (ESCF) and a western section (WSCF) (Fig. 4.1), which are thought to have different slip rates and geomorphic expression (Rockwell, 1988; Dolan and Rockwell, 2001). The onset of surface uplift related to the San Cayetano fault is not well quantified, but estimates range from commencement at around 1 Ma (Cemen, 1989), to as long ago as ~3.3 Ma (Rockwell, 1983). Furthermore, recent structural modelling suggests that during the Pliocene the San Cayetano fault may have continued westward for tens of kilometres west from the Upper Ojai Valley as a blind thrust, although there is no evidence that this section of the fault is currently active (Levy et al., in review).

The Ventura fault is a north-dipping reverse fault that is mapped onshore for 17 km from Saticoy to the coast and westward from the coast the offshore equivalent is referred to as the Pitas Point fault (Fig. 4.1) (Sarna-Wojcicki, 1976; Sarna-Wojcicki and Yerkes, 1982; Hubbard et al., 2014). Surface uplift related to the Ventura fault is thought to have begun with the commencement of uplift of the Ventura Avenue Anticline at around 250 ka (Sarna-Wojcicki, 1976; Sarna-Wojcicki and Yerkes, 1982; Rockwell et al., 1988). The Southern San Cayetano fault (SSCF) is a low-angle thrust fault that was recently identified immediately east of the Ventura fault in the footwall of the San Cayetano fault (Hubbard et al., 2014; Hughes et al., 2018) and is thought to have been active since ~58 ka (Hughes et al., 2018). Along the southern margin of the Ventura basin, the south-dipping Oak Ridge fault is mapped as a reverse fault for 40 km trending east-west from the towns of Piru to Saticoy, respectively, and is responsible for the uplift of South Mountain-Oak Ridge (Fig. 4.1) (Yeats, 1988; Azor, 2002). The Oak Ridge fault continues westwards through the Oxnard plain (Fig. 4.1) and offshore into the Santa Barbara Channel as a primarily strike-slip fault (Fig. 4.1) (Kamerling et al., 2003).

4.2.2 The Saugus Formation

The primary stratigraphic unit investigated in this study is the terrestrial Saugus Formation, although the underlying Las Posas Formation and the deep marine sandstone, siltstone, and mudstone of the

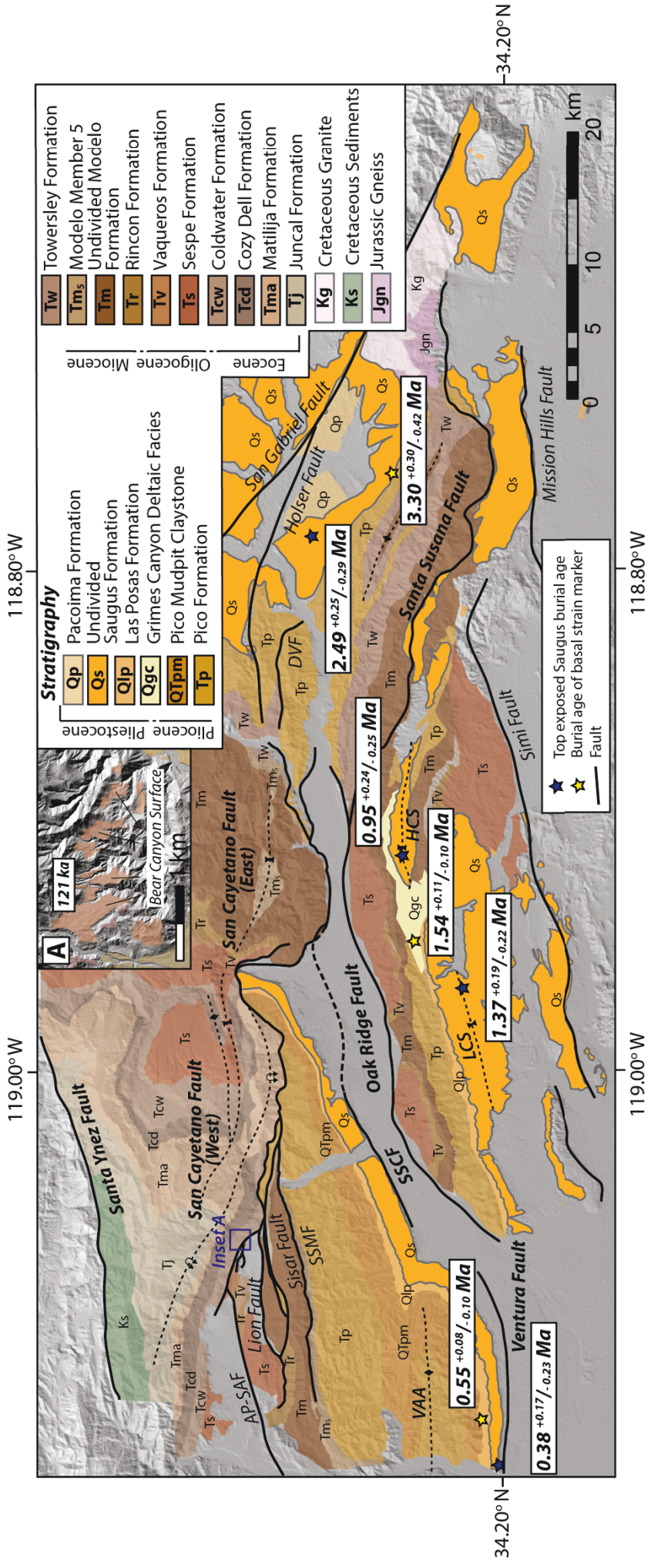
Stratigraphy
Pleistocene
Pliocene
Qp Pacoima Formation
Undivided
Qs Saugus Formation
Qlp Las Posas Formation
Qgc Grimes Canyon Deltaic Facies
QTpm Pico Mudpit Claystone
Tp Pico Formation
Eocene
Oligocene
Miocene
Tw Towersley Formation
Tm5 Modelo Member 5
Undivided Modelo
Tm Formation
Tr Rincon Formation
Tv Vaqueros Formation
Ts Sespe Formation
Tcw Coldwater Formation
Tcd Cozy Dell Formation
Tma Matilija Formation
Tj Juncal Formation
Kg Cretaceous Granite
Ks Cretaceous Sediments
Jgn Jurassic Gneiss
A
121 ka
Bear Canyon Surface
km
Santa Ynez Fault
San Cayetano Fault (West)
San Cayetano Fault (East)
Inset A
AP-SAF
Lion Fault
Sisar Fault
SSMF
Oak Ridge Fault
SSCF
VAA
Ventura Fault
DVF
HCS
LCS
San Gabriel Fault
Holser Fault
Santa Susana Fault
Simi Fault
Mission Hills Fault
0.55 +0.08/-0.10 Ma
0.38 +0.17/-0.23 Ma
0.95 +0.24/-0.25 Ma
1.54 +0.11/-0.10 Ma
1.37 +0.19/-0.22 Ma
2.49 +0.25/-0.29 Ma
3.30 +0.30/-0.42 Ma
Top exposed Saugus burial age
Burial age of basal strain marker
Fault
0 5 10 20 km
119.00° W
118.80° W
34.20° N

Figure 4.3 *Geological map of the study area showing locations of isochron burial dating samples. Solid black lines are major faults. Blue stars represent samples taken from the top of the Saugus Formation and yellow stars represent the base of the underlying shallow marine equivalent. Extent of mapped units in the east of the map is based on the mapping of Campbell et al., (2014) and the western half of the map is based on the Dibblee geological maps (see text for references). HCS = Happy Camp syncline, LCS = Long Canyon syncline, VAA = Ventura Avenue anticline, AP-SAF = Arroyo Parida/Santa Ana fault, DVF = Del Valle fault, SSCF = Southern San Cayetano fault, SSMF = South Sulphur Mountain fault.*

Pliocene Pico Formation (Fig. 4.2 and 4.3) are also important strain markers (Winterer and Durham, 1962). There are different interpretations for which specific lithological units or depositional environments should be included in the Saugus Formation. For example, shallow marine sands underlie the terrestrial Saugus Formation throughout the basin (Fig. 4.3) and previous researchers have included both the underlying shallow marine sands and terrestrial deposits within the Saugus Formation (e.g., Kew, 1924; Yeats, 1988; Huftile and Yeats, 1996). However, the current convention, adopted here, is to apply the term Saugus Formation only to terrestrial deposits and use separate terms for the underlying shallow marine deposits (Campbell et al., 2014; Swanson and Irvine, 2015). In the western basin, shallow marine deposits are assigned to the Las Posas Formation, mentioned above, whereas in the central basin the underlying marine deposits comprise the Grimes Canyon deltaic facies (Fig. 4.2 and 4.3) (Dibblee and Ehrenspeck, 1988b; Campbell et al., 2014). In the eastern basin shallow marine deposits include the Sunshine Ranch Member and the Elsmere Canyon delta plain facies (Fig. 4.3) (Campbell et al., 2014).

The Saugus Formation has been assumed to be entirely Pleistocene in age with a current estimated age range in the east Ventura basin of 0.5–2.3 Ma, based on magnetostratigraphy and an assumption of constant sedimentation rates projected above the 0.76 Ma Bailey ash (Levi and Yeats, 1993). An upper age limit for the Saugus Formation at Ventura of 250 +/- 50 ka is based on amino acid racemization (AAR) on *Macoma* mollusc shells (Wehmiller et al., 1978; Lajoie et al., 1982; Yerkes et al., 1987). More recent work used a combination of optically stimulated luminescence (OSL) and cosmogenic nuclide dating to calculate a lower age for the Camarillo member of the Saugus Formation in the southern Ventura basin of 125 ka and an upper age of 60-25 ka (DeVecchio et al., 2012a; DeVecchio et al., 2012b), significantly younger than previously thought. Based on these data, the base of the Saugus Formation is argued to be time-transgressive and to increase in age from west to east along the length of the Ventura basin (Yeats, 1988; Campbell et al., 2014; Swanson and Irvine, 2015), but the top of the

Saugus Formation is often modelled as synchronous across the entire basin (Yeats, 1988; Huftile and Yeats, 1995; Huftile and Yeats, 1996).

The broad range of chronological constraints described here highlights a substantial variation in the age of the Saugus Formation across the Ventura basin. The main problem with the existing chronology is that there are insufficient data points to directly quantify the spatial variability in the age of either the top or base of the exposed Saugus Formation across the entire basin. Despite the fact that there are very few direct ages for either the top or the base of the exposed Saugus Formation, slip rates for multiple faults in the Ventura basin are calculated using the Saugus Formation as a strain marker because the Saugus Formation is mapped as the youngest bedrock unit deformed by Quaternary faulting and folding, As a result, slip rates for several key faults, such as the Oak Ridge (Yeats, 1988; Yeats et al., 1994) and San Cayetano faults (Huftile and Yeats, 1995; Huftile and Yeats, 1996), are based on projecting ages of a time-transgressive unit over tens of kilometres resulting in large inherent uncertainties in the fault slip rates. Therefore, in order to use the Saugus Formation to track patterns of late Quaternary deformation across the Ventura basin a robust chronology of direct ages across the entire Saugus Formation is required.

4.3 Methods

4.3.1 Study design

In this study, we synthesize various complementary datasets to quantify fault activity for several active reverse and thrust faults, and to assess how the interaction and evolution of these faults has exerted a first-order control on Quaternary landscape evolution. A schematic representation of how competing signals of tectonic uplift rates and erosion can be extracted from the landscape by combining different cosmogenic nuclide dating techniques with morphometric landscape analysis is included in Figure 4.4.

Isochron burial dating is used to date the Saugus Formation and the resulting geochronology is employed to model Quaternary fault displacement rates, which characterize the tectonic uplift signal on timescales of 10^5–10^6 years (black arrows, Fig. 4.4). Additional insights addressing tectonically-driven uplift are extracted from catchment relief and channel steepness indices, which are compared with TCN-

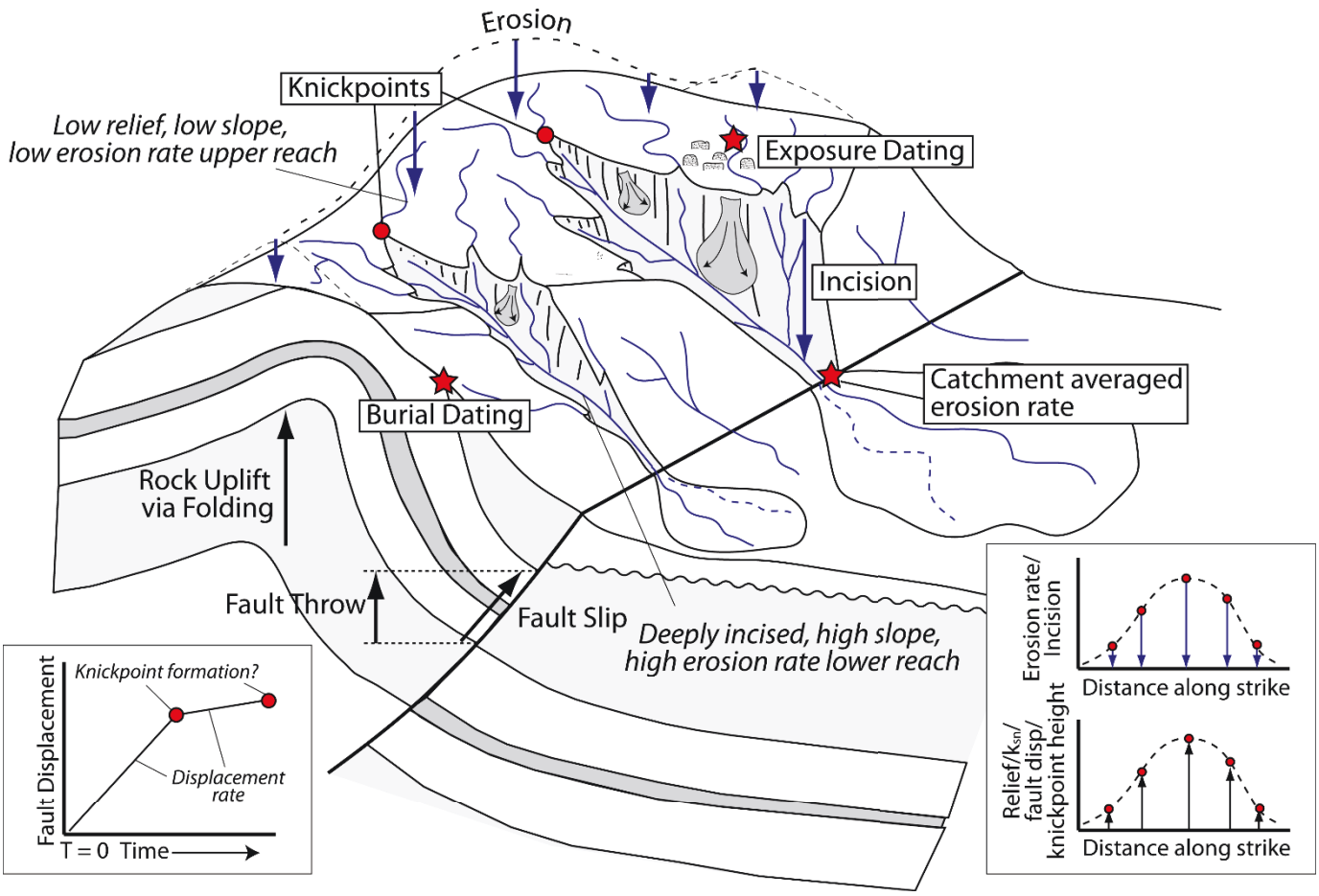

Figure 4.4 *Schematic summary of the various datasets used in the study to illustrate how a synthesis of these datasets can be used to extract the tectonic signal from the landscape and investigate the landscape response to active reverse faulting. Tectonic uplift forces are indicated with black arrows and the forces of erosion and incision, which remove sediment in response to the tectonic forcing, are indicated with blue arrows. Idealized sample locations for various cosmogenic nuclide dating techniques which are used to calculate the rate of rock uplift and/or erosion are indicated with red stars. The location of illustrative knickpoints, which separate a relatively uneroded upper reach from a deeply incised lower reach, are indicated with red circles. (Bottom right) Idealized graphs which indicate how various metrics of tectonic uplift or erosion used in this study would vary along strike if they are responding to the uplift or erosion signal of an individual fault. (Bottom left) Theoretical plot of fault displacement through time, which demonstrates how knickpoint formation can be related to changes in fault displacement rates if an increase in fault slip rate is identified.*

derived catchment-averaged erosion rates and incision rates that quantify the rate of sediment removal as the landscape adjusts to tectonic forcing on timescales of 10^2–10^4 years (blue arrows, Fig. 4.4). Finally, non-lithological knickpoints are extracted from river long-profiles and compared with fault initiation timings and possible changes in displacement rates to provide further insights into how fluvial networks are responding to tectonic forcing on 10^5–10^6-year timescales (Fig. 4.4). When synthesized, the combination of fault displacement rates, erosion rates, landscape analysis, and river long-profile analysis provides a wealth of information that can be used to gain insights into how the Ventura basin landscape has responded to changing tectonic forcing through the Quaternary.

4.3.2 Cosmogenic dating techniques

The sampling strategy associated with each cosmogenic nuclide technique is described separately below, followed by a general description for the extraction of ^{10}Be or ^{26}Al, which is applicable to all three techniques.

4.3.2.1 Isochron burial dating

We performed isochron burial dating on samples from the eastern, central, and western Ventura basin to track the spatial variation is age of the Saugus Formation and the underlying shallow marine deposits across the basin. Isochron burial dating is a key tool for dating late Quaternary sediments and has been applied to a wide range of terrestrial and marine deposits (e.g. Balco and Rovey, 2008; Erlanger et al., 2012; Balco et al., 2013; Çiner et al., 2015; Bender et al., 2016). At the time of deposition, the slope of a line in ^{10}Be–^{26}Al space reflects the surface production ratio of ^{10}Be and ^{26}Al. When the unit is buried to a depth below the penetration depth of cosmic rays, the slope evolves due to the differing half-lives of the two nuclides so that the difference between the slope of the isochron and the surface production ratio is indicative of the burial age of the sample (Balco and Rovey, 2008; Balco et al., 2013). The currently-accepted value for the half-life of ^{10}Be is measured at 1.387 +/- 0.012 x 10^6 yr^{-1} (Chmeleff et al., 2010) and for ^{26}Al the half-life is 0.708 +/- 0.017 x 10^6 yr^{-1} (Nishiizumi, 2004). Any post-burial nuclide production will uniformly increase the concentrations of ^{10}Be and ^{26}Al but will not affect the slope. Hence, post-burial production can be treated as a constant, defined by the intersect of the linear regression with the y-axis. The burial time, t_b, of the deposit is obtained using the following equation (Balco and Rovey, 2008):

$$t_b = \frac{-\ln\left(\frac{R_m}{R_{in}}\right)}{\lambda_{26} - \lambda_{10}} \qquad \text{(Equation 4.1)}$$

where R_{in} is the ^{26}Al/^{10}Be ratio at the time of deposition, R_m is the measured ^{26}Al/^{10}Be ratio, and λ_{26} and λ_{10} are the decay constants for ^{26}Al and ^{10}Be, respectively, derived from the half-lives of the two isotopes.

For each isochron the goal is to collect around eight individual cobble-sized samples, an amalgamated sample of approximately fifty pebble-sized clasts, and a bulk sample (~ 2 kg) of sand to capture a wide range of erosional processes and ensure a variety of nuclide concentrations to plot on an isochron. Unweathered quartz-rich cobbles and pebbles were selected to maximize the amount target mineral for ^{10}Be and ^{26}Al analyses. Sixty-four individual samples were collected from key stratigraphic horizons at eight individual sampling localities across the Ventura basin (Fig. 4.3). All samples were collected from the same depth horizon > 2 m from the surface to ensure minimal post burial production. Samples were collected over a depth range of +/- ~0.3 m, and from within the same stratigraphic unit to ensure a similar shared burial history across the individual samples.

Sampling localities were selected to represent either the top of the exposed Saugus Formation or the base of various shallow marine units that underlie the Saugus Formation throughout the Ventura basin (e.g. Las Posas Formation, Grimes Canyon deltaic facies) (Fig. 4.2). We refer to the top of the Saugus Formation as the top of the 'exposed' Saugus Formation because in no location do we have any quantification of the amount of material eroded from above the sample location. The base of the shallow marine sands was preferred to the base of the terrestrial Saugus Formation to track the age of the first coarse clastic input into the basin but also to be consistent with previous work which classified the underlying shallow marine together with terrestrial deposits within the Saugus Formation (e.g., Kew, 1924; Yeats, 1988; Huftile and Yeats, 1996). Additional information on burial dating of the Saugus Formation is included in Appendix C1, and sample details are summarized in Table 4.1.

A Bayesian approach was adopted to incorporate all uncertainty in linear regressions when plotting isochrons (Muzikar, 2011; Bender et al., 2016), which incorporates a standard reference surface production ^{26}Al/^{10}Be ratio of 6.75 in the sediment at the time of deposition (Balco and Rovey, 2008). To validate our choice of initial surface production ratio within the study area, a suite of sediment samples of different grain sizes was collected from the modern San Gabriel River. The Bayesian approach resolves a correlation between slope and intercept for numerous different regressions within a predefined set of errors in x–y data (i.e. ^{10}Be–^{26}Al concentration space). For burial isochrons, the maximum slope of the regression is set at 6.75 which represents the assumed production ratio at time

of deposition and is the current standard surface production ratio of $^{26}Al/^{10}Be$ (Balco and Rovey, 2008). The minimum slope is zero. The likelihood of each regression of slope and intercept is recorded in normalized probability histograms, which also illustrate whether the set of regressions represents a Gaussian distribution.

The calculations were performed with a Matlab script that runs Monte Carlo simulations to conduct 100,000 trial runs to calculate slope and intercept values from ^{10}Be and ^{26}Al concentrations and associated 1σ measurement errors (Bender et al., 2016). The Matlab script also calculates the likelihood of each slope and intercept value, assuming a Gaussian distribution (Bender et al., 2016). Output values for most likely estimate of slope (the modal value) are input into Equation 4.1 to calculate the burial age and uncertainties are plotted by inputting 95 % confidence values into Equation 4.1.

4.3.2.2 Surface Exposure Ages

I calculated an exposure age for an extensive uplifted alluvial fan surface above Bear Canyon, previously termed the 'Bear Canyon surface' (Fig. 4.3) (Rockwell, 1988). The Bear Canyon surface is a useful strain marker for activity on the WSCF because the surface is thought to date to around 80–100 ka based on soil correlation with what was thought to be a similar aged terrace uplifted on the flanks of the Ventura River (Fig 4.1) (Rockwell, 1983). In the absence of preserved Plio-Pleistocene bedrock in the hanging wall of the WSCF (Fig. 4.3), the uplifted Bear Canyon surface can potentially provide a measure of relatively long-term rock uplift or incision rates for the WSCF over 10^5-year timescales. Long-term rock uplift or incision rates can then be compared with fault throw rates obtained from the offset across a fault scarp in a younger ~7.3 ka alluvial fan at the mouth of Bear Canyon (Hughes et al., 2018).

Boulder height above the current fan surface was measured from ten large boulders standing > 1 m proud above the fan surface to minimize the chance that boulders had been exhumed or rotated since deposition. ^{10}Be exposure ages were calculated using version 3.0 of the online exposure age calculator formerly known as the CRONUS-Earth online exposure age calculator (Balco et al., 2008). Topographic shielding corrections were made using the CRONUS-Earth online geometric shielding calculator,

version 2 (available at: http://stoneage.ice-d.org/math/skyline/skyline_in.html). We employed a reference production rate for ^{10}Be of 4.22 +/- 0.16 atoms g^{-1} based on the Promontory Point (PPT) reference production rate calibration data from Lake Bonneville, Utah, USA (Lifton et al., 2015) and used the production rate scaling scheme of Lal (1991) and Stone (2000). Whilst care was taken to select boulders that had experienced minimal weathering, no accurate quantification of the amount of erosion on the boulder surface is available. Consequently, zero erosion is assumed in age calculations and the boulder age is inferred to be a minimum age.

A large inherited nuclide concentration will artificially increase the apparent exposure age of the boulder surface, but no precise quantification of the inherited nuclide concentration is available for the boulders. Accordingly, the boulders on the Bear Canyon surface are assumed to have low inheritance and inheritance is not included in the boulder age calculation. We note that inheritance values estimated from cosmogenic isotope depth profiles calculated using sand sized particles from elsewhere in the Ventura basin are all low, implying high past erosion rates for sand sized particles in the study area (DeVecchio et al., 2012a; Hughes et al., 2018). While the low inheritance values for sand sized particles do not necessarily apply to the boulders, they do indicate rapid erosion rates and transport times within the study area that could possibly also favour low-inheritance values for the boulders. Details for each boulder sample are included in Table 4.2 and further background and details on sampling strategy for the boulder samples is included in Appendix C1.2.

4.3.2.3 ^{10}Be derived catchment-averaged erosion rates

The goal of the erosion rate sampling was to sample from multiple catchments along strike of the Ventura, San Cayetano, and Southern San Cayetano faults to track fault-parallel patterns in erosion rates and compare results with published uplift rates and lithological distribution. In total 18 samples of ~2 kg of sand sized sediment were collected for catchment-averaged erosion rates from bars and active channels at the mouths of fault-bounded catchments just upstream from a fault. The 250–500 μm sand fraction was isolated and processed for ^{10}Be analysis (Carretier et al., 2015). Catchment-averaged erosion rates were calculated from ^{10}Be concentrations using the Catchment-Averaged Denudation Rates from Cosmogenic Nuclides (CAIRN) method (Mudd et al., 2016). A description of the CAIRN

method is provided in Appendix C1 and sample parameters for the erosion samples and inputs to CAIRN are included in Table 4.3.

Landslides are present throughout the study area (e.g., Tan et al., 2004) and must be considered when calculating catchment-averaged erosion rates because sediment from a deep seated landslide may artificially decrease the modelled erosion rate relative to the true signal if sourced from beneath the penetration depth of cosmic rays (Niemi et al., 2005; West et al., 2014). A preliminary version of the California Landslide Inventory Database (CaLSI) represents a consolidation of various landslide maps from southern California drafted over the past fifty years (available at: http://maps.conservation.ca.gov). Mapped landslides were also checked in the field, on Google Earth™, and where available with a high resolution DEM derived from lidar data with a 5 m horizontal accuracy and 0.45 m vertical accuracy that covers part of the study area (Airborne1, 2005). These data were used in conjunction with landslides mapped in the CaLSI to avoid sampling immediately downstream from major mapped landslides and artificially increasing modelling erosion rates.

4.3.2.4 Laboratory analysis

Quartz separation and chemistry for the erosion rate samples, the isochron burial dating samples, and the surface exposure age samples were carried out in laboratories at the Scottish Universities Environmental Research Centre (SUERC), the University of Vermont, and Imperial College London, but the methodology adopted at each laboratory was broadly similar. Bulk sediment samples were first sieved to isolate the 250–500 μm fraction and ~10–30 g of quartz were isolated and purified from the samples following the methodology of Kohl and Nishiizumi (1992). All Be and Al isolation was undertaken following the method of Corbett et al., (2016), which is described in full in Appendix C2.

Ratios of $^{10}Be/^{9}Be$ and $^{26}Al/^{27}Al$ for the exposure age samples and the burial dating samples were measured by accelerator mass spectrometry (AMS) at the Centre for Accelerator Science at the Australian Nuclear Science and Technology Organization (ANSTO) using the 6 MV Sirius tandem accelerator (Wilcken et al., 2017) and at SUERC (Xu et al., 2015). AMS ratios for the erosion rate samples were measured at the Lawrence Livermore National Laboratory AMS facility (Rood et al.,

2010). Details for measurement standards, beam currents, process blanks, and backgrounds for each AMS run are included in Appendix C2.

4.3.3 Displacement rates

We re-examined published slip rates and rock uplift rates for the San Cayetano, Ventura, and Oak Ridge faults using our new TCN chronology (section 4.5 below). Slip rates and rock uplift rates were calculated in order to improve the accuracy and resolution for the record of Quaternary displacement rates along the northern onshore Ventura basin and to facilitate a direct comparison with erosion rates to help understand the influence of tectonic and lithological variability on topographic development in the Ventura basin. In this study, fault slip is defined as the amount of displacement along the fault place (dip slip displacement) and the vertical component of fault slip (fault throw) was calculated by multiplying dip slip displacement by the sine of fault dip. Uplift via folding is termed 'rock uplift'.

We extracted dip-slip offsets and associated uncertainties for the Oak Ridge and eastern San Cayetano faults (ESCF) from cross sections through the Happy Camp syncline (Fig. 4.1) contained in Huftile and Yeats (1996). For the San Cayetano fault (ESCF and WSCF), slip rates were converted to throw rates to facilitate a direct comparison with erosion rates using a fault dip of 50˚. This value of fault dip was extracted from the Southern California Earthquake Centre 3D Community Fault Model for Southern California (CFM) version 5.2 (Plesch et al., 2007; Nicholson et al., 2017a) for consistency with the fault geometry in Chapter 2. The relevant cross sections from which dip slip amounts were extracted are included in Appendix C3. To revise the Holocene throw rate and slip rate for the WSCF, the fault offset across a Holocene alluvial fan at the mouth of Bear Canyon from Rockwell (1988) was used in combination with a depth profile age from the same fan of 7.3 $^{+1.8}/_{-1.7}$ ka (Hughes et al., 2018). Incision into the uplifted 'Bear Canyon surface' in the hanging wall of the San Cayetano fault was calculated by subtracting channel incision into the surface from maximum relief, which was determined using maximum and minimum elevation values extracted from a swath profile parallel to the stream. Maximum incision was combined with the TCN exposure age from boulders on the uplifted Bear Canyon surface to calculate an incision rate at Bear Canyon, which is used as a proxy for the minimum Late Pleistocene rock uplift rate.

For the Ventura fault, rock uplift rates are taken from uplifted terraces of the Ventura River (Rockwell et al., 1988; Hubbard et al., 2014). However, the long-term uplift rate based on rock uplift of the top of the Saugus Formation in the Ventura Avenue anticline (Rockwell et al., 1984) was recalculated by incorporating the isochron burial age for the top of the Saugus Formation at Ventura. All offset amounts, associated ages, and rates are included in Table 4.4.

Stratigraphic separation is a measure of fault activity calculated by comparing sediment thickness separating mapped geologic units in the hanging wall and footwall of a fault and provides an additional, relatively continuous measure of along-strike activity that covers the entire time-span of activity on the San Cayetano fault. Here, we use stratigraphic separation values taken from Rockwell (1988) and Cemen (1989) along strike of the San Cayetano fault to compare with fault slip rates and erosion rates.

4.3.4 Geomorphic analysis

The goal of the geomorphic analysis was to quantify various morphometric landscape parameters in the hanging wall of the San Cayetano, Southern San Cayetano, and Ventura faults for comparison with data on erosion rates, lithology, and fault displacement rates. An analysis of stream profiles and knickpoints in fault hanging walls was undertaken to compare with fault displacement rates and provide further insights on how tectonic perturbations have controlled the landscape evolution of the Ventura basin and to investigate how tectonic and lithological factors can control temporal variability in erosion rates and topographic development more generally.

4.3.4.1 Stream power

On timescales of 10^6–10^7 years, landscapes might be expected to reach a dynamic equilibrium where erosion and rock uplift rates become coupled, similar to the relationship documented in parts of the Himalaya (Lavé and Avouac, 2001; Finnegan et al., 2008) and the Basin and Range (Densmore et al., 2004). In steady-state landscapes, long-profiles of bedrock rivers are usually concave up (Tucker, 2009). However, a change in base level following a tectonic perturbation may result in faster incision of the downstream section of the stream profile causing a convex up section, or knickpoint, to develop.

The resulting knickpoint may then propagate upstream as the channel system seeks a new topographic steady state (Tucker and Whipple, 2002; Crosby and Whipple, 2006; Kirby and Whipple, 2012).

In both transient and steady state landscapes, longitudinal stream profiles can be defined by a power law function that relates channel gradient, *S*, at a particular down-system point to upstream drainage area, *A*. For a simple stream power model in a steady state landscape this can be expressed as

$$S = \left(\frac{U}{K}\right)^{\frac{1}{n}} A^{\frac{-m}{n}} \qquad \text{(Equation 4.2)}$$

where *U* is an uplift rate, *K* is a coefficient that represents bedrock erodibility amongst other factors and *m* and *n* are exponents related to erosional dynamics and hydraulic geometry (e.g., Whipple and Tucker, 1999; Tucker and Whipple, 2002). The term $\left(\frac{U}{K}\right)^{\frac{1}{n}}$ can be described as the channel steepness index, k_s, and the ratio of *m/n* as the channel concavity, θ. For a classic unit stream power model, $m = 0.5$, $n = 1$, and $\theta = 0.5$. Nonetheless, a reference value of θ is typically used to estimate a normalized channel steepness index, k_{sn}, allowing comparisons in steepness between neighbouring river channels with different concavities (e.g., Snyder et al., 2000; Wobus et al., 2006a). The steepness index fundamentally reflects how steep a river is for a given drainage area and has been shown in numerous studies to be sensitive to both uplift and bedrock erodibility (Kirby and Whipple, 2001; Kirby et al., 2003; Cyr et al., 2010; DiBiase et al., 2010; DiBiase and Whipple, 2011; D'Arcy and Whittaker, 2014).

Knickpoints can result as river channels adjust to new equilibrium conditions induced by either a change in tectonic rate (Boulton and Whittaker, 2009; Whittaker et al., 2008) or climatic changes (Whipple, 2009). In the case of a tectonic perturbation, an increase in fault slip rate resulting from fault linkage can cause knickpoints to form in river profiles where the knickpoint separates different zones of high and low channel steepness as the river adjusts to the changing rate of fault motion (Boulton and Whittaker, 2009; Whittaker and Walker, 2015, Kent et al., 2017). Following a change in displacement rate on a fault, a knickpoint can propagate upstream through an upland landscape as an incisional wave (Whipple and Tucker, 1999; Niemann et al., 2001). Both field and modelling studies have identified clear relationships that link the current position of the knickpoint in the landscape to both fault uplift

rate or upstream drainage area (Tucker and Whipple, 2002; Wobus et al., 2006b; Pritchard et al., 2009; Whittaker and Boulton, 2012). In the former case, the vertical elevation of the knickpoint upstream of the fault scales with the displacement rate since the knickpoint was generated (Crosby and Whipple, 2006; Wobus et al., 2006b; Whittaker et al., 2007; Whittaker and Walker, 2015). In the latter case, the position of the knickpoint upstream after a finite period of time should scale as A^m where the power-law exponent derived from a plot of knickpoint distance from the fault against upstream area should equal the exponent *m* from the simplified stream power equation presented in Equation 4.2 (Tucker and Whipple, 2002; Wobus et al., 2006b; Whittaker and Boulton, 2012; Whittaker and Walker, 2015). These relationships can be used in conjunction with data on landscape morphology and a detailed record of fault displacement rates to investigate the extent to which tectonic perturbations have controlled the landscape evolution of the Ventura basin.

4.3.4.2 Landscape analysis

A DEM was constructed from 30 m SRTM data for the study area and used as a basis for river long-profile analysis in the hanging wall of three major reverse faults: The San Cayetano, Southern San Cayetano, and Ventura faults (Fig. 4.1). Fault traces from existing geologic mapping of the study area were mapped in ArcGIS and overlain on the DEM (Dibblee, 1987; Dibblee and Ehrenspeck, 1988a; Dibblee, 1990a; Dibblee, 1990b; Dibblee and Ehrenspeck, 1992b; Tan et al., 2004; Campbell et al., 2014). Using the ArcGIS hydrology toolbox, twenty-five catchments > ~4.0 km^2 and covering the entire length of the hanging walls of the San Cayetano, Southern San Cayetano, and Ventura faults were extracted to analyse how various geomorphic and topographic characteristics may change along strike. Catchment relief, R, was measured as the maximum difference in elevation of the catchment measured upstream from the fault to the drainage divide, calculated using the zonal statistics tool.

Channel long-profiles were extracted from the DEM using the 'Stream Profiler' toolbar (Whipple et al., 2007) with a smoothing window of 150 m and a default contour sampling interval of 12 m. "Slope-break" knickpoints, associated with a difference in steepness index upstream and downstream of the knickpoint, were identified by matching abrupt changes in gradient in the long-profiles with the position of abrupt breaks in slope on slope-area plots (Wobus et al., 2006a; Kirby and Whipple, 2012).

Knickpoints that could be attributed to discrete heterogeneities in the long profile, such as those in close proximity to changes in mapped lithology (Haviv et al., 2010; Kirby and Whipple, 2012) or at the foot of mapped landslides (Korup, 2006), were excluded from the analysis. Knickpoint locations were assigned generous horizontal and vertical uncertainties of +/-50 m to account for noise in the long-profiles resulting from either landslides, lithological variability, or mismatches between the channel extracted from the DEM and the channel location observed in aerial photography.

Normalized channel steepness indices (k_{sn}) were calculated using the Stream Profiler toolbar from plots of log-slope vs log-area using a reference concavity of 0.5, which is the average concavity from all channels within the study area. If only one knickpoint was present, k_{sn} values were calculated above the uppermost slope-break knickpoint for the upper reach and below the uppermost slope break knickpoint for the lower reach. If more than one knickpoint was present, the maximum k_{sn} value from either the middle reach or the lower reach was reported as the 'lower reach' k_{sn} value. This approach was taken because only two out of nine catchments analysed in the hanging wall of the San Cayetano fault had two tectonic knickpoints, whereas the majority (seven out of nine catchments) only had one. A detailed analysis of the lower knickpoints was not possible with a sample size of two so these lower knickpoints were not analysed. Full details of catchment and knickpoint parameters are included in Table 4.5.

4.4. Cosmogenic dating and displacement rate results

4.4.1 Isochron burial ages of the Saugus Formation

Samples collected from the modern San Gabriel River produced an isochron with a slope of 7.00 +/-0.32 (uncertainty in slope is 95 % confidence interval), which overlaps with the standard reference production $^{26}Al/^{10}Be$ ratio of 6.75 (Fig. CS1). This result validates the use of this standard reference production ratio as the initial slope used to calculate the isochron burial ages for the Saugus Formation discussed in the following section.

The isochron burial age for the base of the Las Posas Formation was derived from samples taken from a bed of pebbles and cobbles immediately above the contact between the Las Posas Formation and the underlying Mudpit Claystone member of the Pico Formation identified in the field. The resulting

Table 4.1 *Full sample parameters for isochron burial samples*

Stratigraphy	Sample	Type	Latitude °N (DD.DD)	Longitude °W (DD.DD)	Altitude (m.a.s.l)[a]	Depth (m)	Isochron Age (Ma) [b]
Top Saugus, VF+	SVF-A	Clast	34.2841667	119.2922222	56	2.0 +/- 0.2	0.38 +0.17/-0.23
	SVF-B	Clast					
	SVF-C	Clast					
	SVF-D	Clast					
	SVF-E	Clast					
	SVF-F	Clast					
	SVF-P	Pebbles					
	SVF-S	Sand					
Base Las Posas, VF+	HCR-2	Clast	34.29398	119.25771	104	3.5 +/- 0.4	0.55 +0.08/-0.10
	HCR-3	Clast					
	HCR-6	Clast					
	HCR-7	Clast					
	HCR-8	Clast					
	HCR-10	Clast					
	HCR-S	Sand					
	HRC-P	Pebbles					
Top Saugus, ORF+	SCQ-A	Clast	34.34104	118.875349	488	2.0 +/- 0.2	0.95 +0.24/-0.25
	SCQ-E	Clast					
	SCQ-F	Clast					
	SCQ-P	Pebbles					
	SCQ-S	Sand					
Top Saugus, ORF+	SLC-A	Clast	34.31528	118.933334	273	3.8 +/- 0.3	1.37 +0.19/-0.22
	SCL-B	Clast					
	SLC-C	Clast					
	SLC-D	Clast					
	SLC-I	Clast					
	SLC-J	Clast					
	SLC-P	Pebbles					
	SLC-S	Sand					
Base GCDF, ORF+	TP-A	Clast	34.3427778	118.9075	323	2.0 +/- 0.2	1.54 +0.11/-0.10
	TP-B	Clast					
	TP-C	Clast					
	TP-D	Clast					
	TP-F	Clast					
	TP-G	Clast					
	TP-H	Clast					
	TP-I	Clast					
Top Saugus, EVB+	STL-3	Clast	34.40399	118.60884	450	4.0 +/- 0.2	2.49 +0.25/-0.29
	STL-6	Clast					

	STL-1	Clast					
	STL-2	Clast					
	STL-5	Clast					
	STL-7	Sand					
	STL-8	Pebbles					
Base Saugus, EVB+	SI5-F	Clast	34.36167	118.55417	415	25 +/- 1.0	3.30 +0.30/0.42
	SI5-M	Clast					
	SI5-N	Clast					
	SI5-O	Clast					
	SI5-P	Pebbles					
	SI5-S	Sand					
	SI5-U	Clast					
	SI5-V	Clast					
	SI5-X	Clast					

a: Meters above sea level

b: Age calculated using Bayesian regression Matlab script (Bender et al., 2016)

+Abbreviations: VF = Ventura Fault, ORF = Oak Ridge Fault, SSCF = Southern San Cayetano Fault, GCDF = Grimes Canyon Deltaic Facies, EVB = East Ventura Basin

Table 4.1 *Continued*

Sample	Quartz mass (g)	Be Carrier [a] (g)	$^{10}Be/^{9}Be$ AMS [b,c]	^{10}Be Concentration (atoms g^{-1} SiO_2) [d]	^{10}Be 1σ uncert (atoms g^{-1} SiO_2) [e]	^{10}Be 1σ uncert (%)	Total Al (µg)	$^{26}Al/^{27}Al$ AMS [c,f]	^{26}Al Concentration (atoms g^{-1} SiO_2) [g]	^{26}Al 1σ uncert (atoms g^{-1} SiO_2) [e]	^{26}Al 1σ uncert (%)
SVF-A	20.9960	1.0059	1.29179E-14	7145	468	6.5	2124	2.1208E-14	46002	5269	11.5
SVF-B	11.9290	1.0069	8.20287E-15	7163	672	9.4	2001	8.9947E-15	30554	6061	19.8
SVF-C	17.1940	1.0062	6.0534E-15	3252	469	14.4	2292	1.2681E-14	35241	5814	16.5
SVF-D	25.9510	1.0052	9.25566E-15	3843	330	8.6	2207	1.3835E-14	24677	3907	15.8
SVF-E	32.0420	1.0055	1.54125E-14	5747	392	6.8	2117	2.9908E-14	42863	3844	9.0
SVF-F	21.7560	1.0049	1.46804E-14	7998	504	6.3	2157	2.4295E-14	51918	5090	9.8
SVF-P	9.1140	1.0042	6.16626E-15	6292	1571	25.0	2183	1.0021E-14	49105	9688	19.7
SVF-S	36.5640	1.0046	4.27286E-14	15262	556	3.6	2590	5.728E-14	89224	6042	6.8
HCR-2	13.7900	0.8414	4.689E-15	4779	579	12.1	2415	1.2901E-14	46014	9086	19.5
HCR-3	11.8968	0.8396	2.917E-15	3125	3639	116.4	2451	5.0087E-15	17829	6700	36.2
HCR-6	20.8499	0.8414	1.1E-13	84818	2355	2.8	2518	1.6734E-13	447930	17177	3.8
HCR-7	18.5203	0.8391	1.922E-14	16199	830	5.1	2425	2.7258E-14	76340	8146	10.6
HCR-8	21.3362	0.8388	1.229E-14	8821	3998	45.3	2461	1.5824E-14	37824	4962	13.0
HCR-10	17.1301	0.8409	4.06E-15	3252	372	11.5	2371	7.0213E-15	18196	4765	25.5
HCR-S	21.0057	0.8347	2.476E-14	18437	814	4.4	2475	2.7017E-14	68073	6203	9.1
HCR-P	18.4683	0.8401	1.206E-14	10006	2117	21.2	1976	4.1269E-14	95852	10018	10.4
SCQ-A	30.7230	1.0056	3.07817E-14	12852	463	3.6	1973	5.2547E-14	74119	5044	6.8
SCQ-E	32.0030	1.0052	6.65609E-14	27652	1044	3.8	2253	9.1874E-14	143058	9338	6.5
SCQ-F	22.9320	1.0043	1.80388E-14	9589	544	5.7	1251	6.0064E-14	72119	4960	6.9
SCQ-P	6.4370	1.0064	8.52606E-15	13957	1696	12.2	1965	1.1682E-14	73898	11862	16.1
SCQ-S	37.8470	1.0057	7.06304E-14	24868	577	2.3	2325	7.5817E-14	102796	6856	6.7
SLC-A	16.3937	0.8365	2.401E-14	23546	1140	4.8	2231	4.2486E-14	125635	8185	6.5
SLC-B	20.2337	0.8338	3.203E-14	25534	942	3.7	2437	5.6293E-14	148287	10286	6.9
SLC-C	21.3569	0.8345	6.319E-14	46982	1473	3.1	2905	7.2419E-14	216399	11751	5.4
SLC-D	19.2653	0.8477	2.988E-14	24744	1195	4.8	2299	5.5101E-14	143756	11269	7.8
SLC-I	14.8049	0.8430	2.09E-14	22196	917	4.1	2413	3.3891E-14	119184	10713	8.9
SLC-J	19.8994	0.8399	3.299E-14	26258	1229	4.7	2505	5.557E-14	152940	9046	5.9
SLC-P	11.5116	0.8399	1.179E-14	15670	880	5.6	2390	2.7327E-14	121401	19112	15.7
SLC-S	17.5294	0.8380	3.769E-14	34057	1166	3.4	2472	5.0678E-14	155944	12951	8.3
TP-A	56.0810	1.0058	1.41453E-13	34061	1318	3.9	1365	3.7891E-13	205019	6003	2.9
TP-B	31.7300	1.0063	6.7239E-14	28147	1200	4.3	2062	1.1687E-13	167232	7704	4.6
TP-C	17.5360	1.006	5.022E-14	37605	1823	4.8	2479	7.204E-14	222374	12603	5.7
TP-D	13.7580	1.0069	3.348E-14	31274	1916	6.1	1902	6.1267E-14	184233	13283	7.2
TP-F	10.6630	1.0062	2.37987E-14	27871	2032	7.3	2145	4.4416E-14	192478	14448	7.5
TP-G	20.4660	1.0062	1.78002E-13	117865	3073	2.6	2989	1.4212E-13	458118	18948	4.1
TP-H	23.0920	1.0066	1.47591E-13	86433	2577	3.0	2210	1.7477E-13	370027	13089	3.5

TP-I	33.8740	1.0045	7.4214E-14	29138	1086	3.7	2099	1.461E-13	199886	8392	4.2
STL-3	12.7896	1.000	9.0117E-15	7034	841	12.0	1983	1.525E-14	51141	7718	15.1
STL-6	22.7830	1.000	2.24037E-14	12664	850	6.7	1993	2.6968E-14	51735	3917	7.6
STL-1	13.2606	1.000	9.486E-15	7338	1090	14.9	1921	1.2549E-14	39058	5943	15.2
STL-2	21.9948	1.000	1.31688E-14	6908	532	7.7	1991	1.9646E-14	38750	4371	11.3
STL-5	6.3629	1.000	1.00998E-14	16712	1651	9.9	2056	1.3958E-14	97261	13268	13.6
STL-7	21.9246	1.000	3.4317E-14	21024	853	4.1	2055	3.1197E-14	64293	5142	8.0
STL-8	15.6834	1.000	1.26108E-14	9215	679	7.4	1938	1.7005E-14	45616	5585	12.2
SI5-F	29.5560	0.335	6.8681E-15	3230	328	10.2	1573	7.6433E-15	7634	1783	23.4
SI5-M	30.1570	0.336	1.5837E-14	8203	475	5.8	2380	8.4618E-15	12763	2616	20.5
SI5-N	25.7140	0.335	1.0372E-14	6025	436	7.2	2708	6.4894E-15	12396	3130	25.3
SI5-O	13.8850	0.335	4.6307E-15	4096	538	13.1	2757	2.6451E-15	6336	3859	60.9
SI5-P	30.6980	0.336	7.237E-15	3296	340	10.3	2414	5.6011E-15	7698	2237	29.1
SI5-S	26.7690	0.337	1.563E-14	9137	507	5.5	1968	5.6245E-15	7235	2009	27.8
SI5-U	24.7900	0.337	5.1157E-15	2642	354	13.4	2505	4.0293E-15	6347	2411	38.0
SI5-V	15.1400	0.336	3.0392E-15	1981	405	20.4	2751	2.6691E-15	5896	3801	64.5
SI5-X	28.6000	0.335	6.4381E-15	3072	291	9.5	2607	4.9936E-15	7687	2539	33.0

a: Samples SVF, SCG, TP, and STL used an in-house produced Be carrier with a density of 1.000 g ml^{-1} and Be concentration of 300 µg ml^{-1}. Samples HCR, SLC, and OCS used an in-house produced Be carrier with a density of 1.012 g ml^{-1} and Be concentration of 291 µg ml^{-1}. Sample SI5 used an in-house Be carrier with a density of 1.000 g ml^{-1} and a Be concentration of 758 µg ml^{-1}

b: Be ratios normalized to standards of Nishiizumi et al., (2007)

c: All uncertainties are 1σ confidence level

d: ^{10}Be concentrations and associated measurement uncertainties for samples are blank corrected using the average value from all blanks processed in the same AMS run. Average total atoms ^{10}Be in process blanks: HCR, SLC, and OCS = 9970 +/- 964, SI5 = 22489 +/- 2725, SVF, SCQ = 27114 +/- 3906, TP = 29245 +/- 8120, STL = 43510 +/- 2955

e: Propagated uncertainties include 1σ error in AMS measurements, error in the blank, carrier mass (1%), and counting statistics

f: Al ratios normalized to standards of Nishiizumi et al., (2004)

g: ^{26}Al concentrations and associated measurement uncertainties for samples are blank corrected using the average value from all blanks processed in the same AMS run. Average total atoms ^{26} in process blanks: HCR, SLC, and OCS = 54534 +/- 10062, SI5 = 72572 +/- 36293, SVF, SCQ = 36414 +/- 21028, TP = 65073 +/- 26582, STL = 20263 +/- 7011

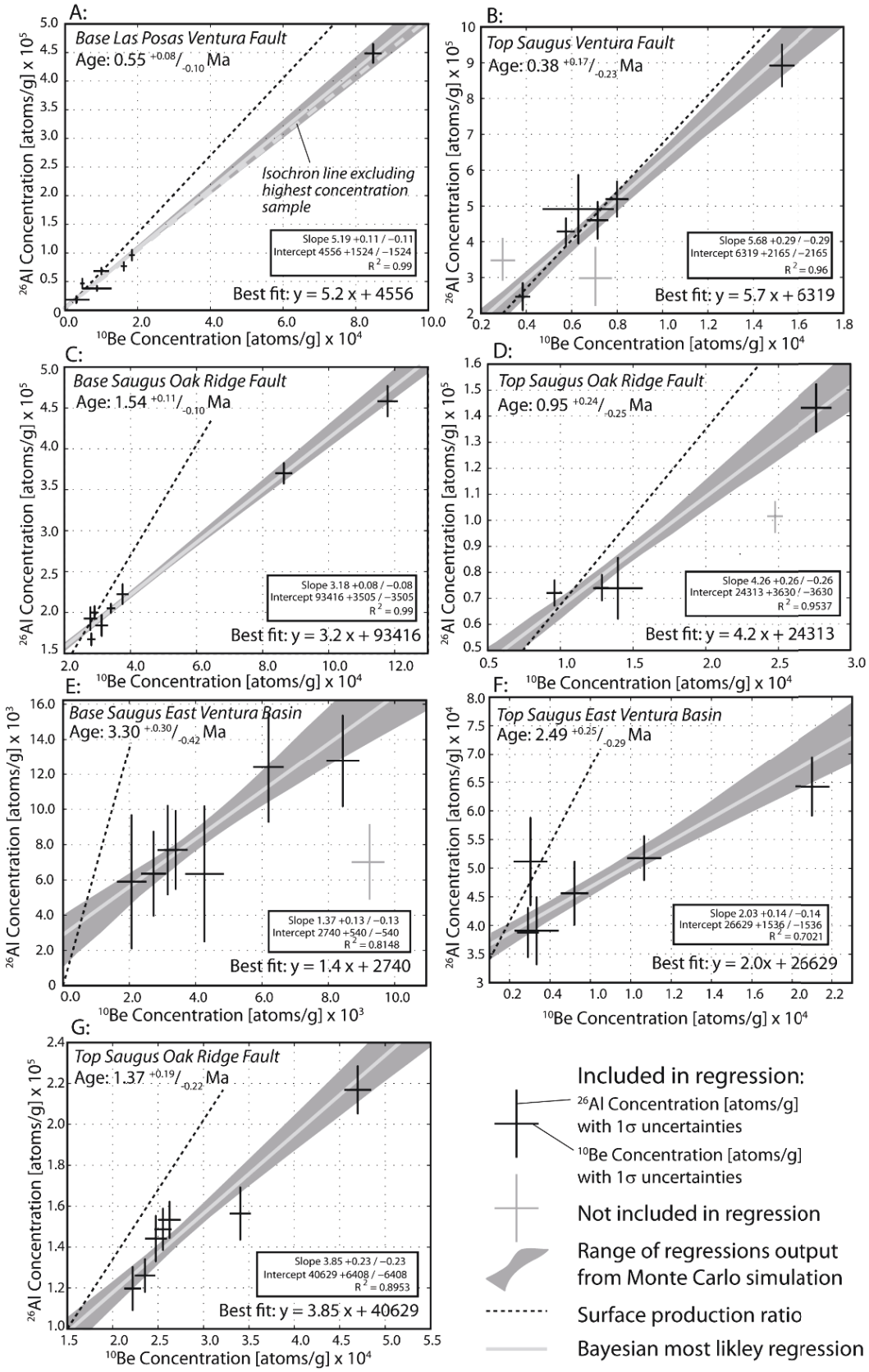

Figure 4.5 *^{26}Al-^{10}Be isochrons for the top Saugus Formation, Las Posas Formation, and the Grimes Canyon Deltaic facies. Isochrons were constructed using a Bayesian linear regression Matlab script (Bender et al. (2016)). Grey polygons are the range of results of 100,000 trial runs which fit the isotope data. Black crosses represent 1σ uncertainties in ^{26}Al or ^{10}Be concentrations and pale grey crosses represent outliers (>1σ from the mode line of best fit) omitted from the isochron analysis. Slope and ages are most likely (modal) values and uncertainties are based on the 95% confidence limits of the data.*

isochron burial age is 0.55 $^{+0.08}/_{-0.10}$ Ma (Fig. 4.5a, Table 4.1) (all burial ages are mode and 95% confidence limits throughout). Previous age constrains for the base of Las Posas Formation at Ventura were provided by the Lava Creek B ash, which is present 60 m above the base of the Las Posas Formation (Sarna-Wojcicki, 1984; Sarna-Wojcicki et al., 1987) and is dated at around 0.63 Ma (Matthews et al., 2015). Our burial age of 0.55 $^{+0.08}/_{-0.10}$ Ma overlaps with the 0.63 Ma age of the Lave Creek B ash within uncertainties and is the first direct age for this horizon.

The sample suite to date the top of the exposed Saugus Formation at Ventura was taken from approximately 50 m below the top of the mapped extent of the Saugus Formation (Dibblee and Ehrenspeck., 1988a). However, it is unknown exactly how much material has been eroded from above the sample location. The isochron burial dating age for the top of the exposed Saugus Formation at Ventura is 0.38 $^{+0.17}/_{-0.23}$ Ma (Fig. 4.5b, Table. 4.1). The large uncertainties associated with this age result from low nuclide concentrations (Table. 4.1) because the top of the Saugus Formation is near the minimum age limit for these sediments using the $^{26}Al/^{10}Be$ nuclide pair. A commonly-cited age for the top of the Saugus Formation near Ventura is 0.25 +/- 0.05 Ma based on amino acid racemization on mollusc shells (Wehmiller et al., 1978; Lajoie et al., 1982; Yerkes et al., 1987) and the isochron burial age agrees with the amino acid racemization age within the uncertainties.

Three isochron burial dating samples for the age of the top of the exposed Saugus Formation and the base of the underlying Grimes Canyon deltaic faces (GCDF) were collected from the hanging wall of the Oak Ridge fault (Fig. 4.3). The GCDF interfingers with upper Pico Formation on the north flank of Oak Ridge-South Mountain (Fig. 4.1) and samples for burial dating the age of the base of the GCDF was taken from ~5 m above the mapped contact between the GCDF and the Pico Formation (Campbell et al., 2014). The resulting isochron burial age for the base of the GCDF is 1.54 $^{+0.11}/_{0.10}$ Ma (Fig. 4.5c, Table 4.1). In the hanging wall of the Oak Ridge fault, the upper Pico Formation is bracketed by the Bailey and Thin White ash layers at Balcom Canyon (Fig. 4.6), approximately 6 km west of our sample location (Sarna-Wojcicki, 1984; Sarna-Wojcicki et al., 1987). The Bailey ash at Balcom Canyon is dated at 1.2 +/- 0.2 Ma (Izett et al., 1974) and the Thin White Ash is dated at 1.4–1.5 Ma (Sarna-

Wojcicki, 1984). Hence, the isochron burial age for the GCDF overlaps with ages for both these ash layers within the uncertainties (Fig. 4.6).

Two samples to date the top of the exposed Saugus Formation in the hanging wall of the Oak Ridge fault were collected from the axes of the Long Canyon and Happy Camp synclines (Fig. 4.3). Both sample suites were collected from as close as possible to what is mapped as the core of the two synclines, with the goal of sampling the youngest preserved sediments which, in theory, should be preserved in the core of the syncline. The isochron burial age for the top of the exposed Saugus Formation from the Happy Camp syncline is 0.95 $^{+0.24}/_{-0.25}$ Ma (Fig. 4.5d). Ages from a mammoth fossil assemblage and magnetostratigraphy at Moorpark date the Saugus Formation in the hanging wall of the Oak Ridge fault to 0.78–0.85 Ma (Wagner et al., 2007). Additionally, the base of the Saugus Formation at South Mountain has previously been estimated to be 0.975 +/- 0.075 Ma based on the proximity of the base of the Saugus Formation to the Jaramillo magnetic subchron in well-log data at the western end of South Mountain (Yeats, 1981). While the most likely age for the top of the Saugus Formation from the isochron burial dating of 0.95 $^{+0.24}/_{-0.25}$ Ma overlaps with the 0.78–0.85 Ma age within uncertainties, the isochron burial age for the top of the Saugus Formation is the same age as the basal age of 0.975 Ma calculated from magnetostratigraphy (Fig. 4.6).

An additional sample to date the top of the exposed Saugus Formation in the hanging wall of the Oak Ridge fault was collected from the axis of the Long Canyon syncline and gives a burial age of 1.37 $^{+0.19}/_{-0.22}$ Ma (Fig. 4.3 & 4.5g). The age for the top of the exposed Saugus Formation in the Long Canyon syncline is chronostratigraphically consistent with the age for the base of the underlying GCDF (1.54 Ma) (i.e., the age for the top is younger than the base) and overlaps with the age from the Happy Camp syncline of 0.95 $^{+0.25}/_{-0.24}$ Ma within the uncertainties (Fig. 4.6). However, the Long Canyon syncline burial age is considerably older than existing fossil and magnetostratigraphy age estimates (Fig. 4.6), which suggest that the top of the Saugus Formation in the hanging wall of the Oak Ridge fault is between 0.78–0.85 Ma (Wagner et al., 2007).

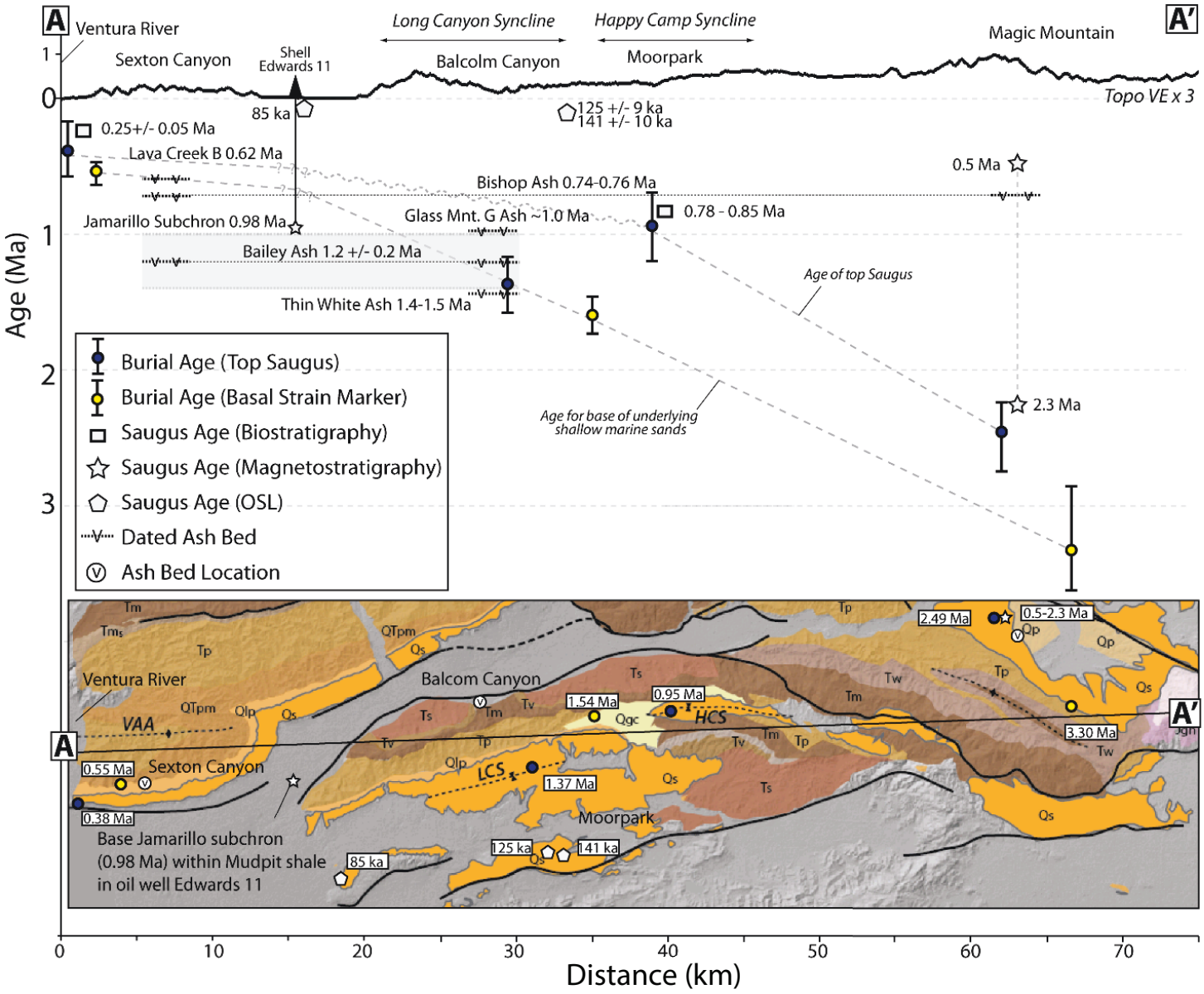

Figure 4.6 *Comparison of isochron burial ages for the Saugus Formation and underlying shallow marine equivalent with existing tephrochronology, biostratigraphy, and magnetostratigraphy across the Ventura Basin. Isochron burial ages for the top of the Saugus Formation (blue circles) and underlying shallow marine equivalent (yellow circles) are from this study and described in the text. Tephrochronology is dashed blacklines with 'v' (Sarna-Wojcicki, 1984; Sarna-Wojcicki et al., 1987), biostratigraphy is squares (Wehmiller et al., 1978; Wagner et al., 2007), and magnetostratigraphy is stars (Levi and Yeats, 1993). Optically stimulated luminescence ages for the Camarillo member are pentagons taken from DeVecchio et al (2012a & b). The map in the bottom indicates the line of the east-west transect relative to the location of each age marker.*

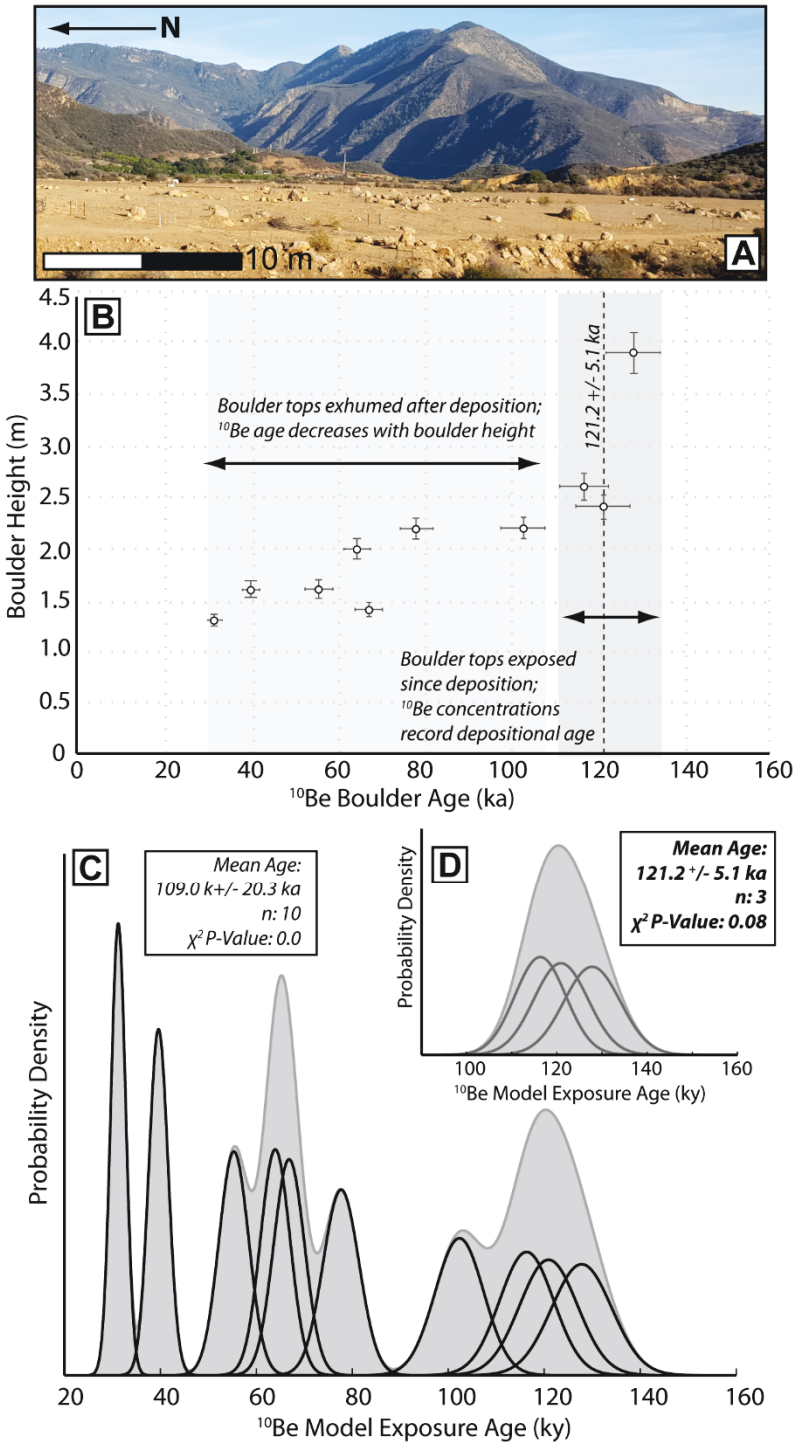

Figure 4.7 *Summary of ^{10}Be exposure age from boulders on the Bear Canyon surface. A) Photo of the boulders on the Bear Canyon surface. The location of the Bear Canyon surface is included in Figure 4.3. B) Plot of boulder height against boulder age which shows a systematic decrease in boulder age for boulders less than ~2 m in height. This plot demonstrates that boulders <2 m tall have likely been exhumed from below the surface by erosion and do not represent the true exposure age of the surface. C) Probability density function and associated ages incorporating all ten samples. D) Probability density function incorporating the oldest three samples from the surface, which are used to derive the preferred age for the surface. Note that these ages assume no erosion of the boulder surface.*

Two suites of samples for isochron burial dating of the Saugus Formation were taken from sites in the eastern Ventura basin. The sample suite to date the top of the exposed Saugus Formation was taken at mapped location of the contact between the Saugus Formation and the overlying Pacoima Formation (Campbell et al., 2014) and yielded a burial age of 2.49 $^{+0.25}/_{-0.29}$ Ma (Fig. 4.5f). The sample to date the shallow marine sands that underlie the Saugus Formation in the east Ventura basin was taken from a pebble and cobble horizon at the base of sediments mapped as the Sunshine Rach Member of the Saugus Formation, approximately 10 m above the contact with the underlying Pico Formation (Campbell et al., 2014). The corresponding burial age for the base of the Sunshine Ranch Member is 3.30 $^{+0.30}/_{-0.42}$ Ma (Fig. 4.5e). These burial ages for the east Ventura basin are considerably older than the existing age range for the Saugus Formation in this area of 0.5–2.3 Ma based on magnetostratigraphy, tephrochronology, and modelled sedimentation rates (Levi and Yeats, 1993).

4.4.2 Exposure Age of the Bear Canyon surface

When boulder height standing proud above the uplifted Bear Canyon surface is plotted against ^{10}Be boulder age, the ages for the tallest three boulders all overlap within the uncertainties, but boulder ages decrease systematically for the seven boulders below 2.4 m height (Fig. 4.7b). If boulders are exhumed after deposition, then measured ^{10}Be concentration will be lower than the ^{10}Be concentration that reflects the true exposure age of the surface because the nuclides that would have accumulated from the time of deposition to the time of exhumation are not accounted for (e.g. Behr et al., 2010; Heyman et al., 2016). Accordingly, based on our analysis the preferred exposure age for the uplifted Bear Canyon alluvial fan surface in the hanging wall of the WSCF is 121.2 ka +/- 5.2 ka (N = 3 average of oldest boulders, uncertainties are one standard deviation) (Fig. 4.7, Table 4.2). Our exposure age is based on the most likely exposure age for the three oldest boulders assuming that the remaining seven samples have been exhumed by erosion of alluvial fan surface material surrounding the boulders since their time of deposition (Fig. 4.7d) (Behr et al., 2010).

Table 4.2 *Sample parameters for the exposure samples from the Bear Canyon surface*

Sample	Cathode Number	Location °N	Location °W	Elevation above Sea Level (m)	Thickness (cm)	Shielding Factor [a]	Denudation Rate (mm yr^{-1})	Quartz (g)	Be Carrier [b] (g)	Standard	$^{10}Be/^{9}Be$ [c,d]			^{10}Be Concentration (atoms g^{-1} SiO_2) [e, f]			Model Age (yrs) [g,h]		
BCB-1	BE800	34.44493	-119.1145	622	4	0.995	0.	2.0931	0.8088	07KNSTD	4.49E-14	+/-	1.729E-15	325944	+/-	13171	55332	+/-	3107
BCB-3B	BE765	34.44451	-119.1143	619	3	0.976	0	6.6529	0.8407	07KNSTD	1.611E-13	+/-	4.26E-15	387155	+/-	11007	66839	+/-	3219
BCB-5	BE766	34.44271	-119.1127	606	4	0.997	0	7.0463	0.8409	07KNSTD	1.63E-13	+/-	4.31E-15	372036	+/-	10575	63953	+/-	3078
BCB-7	BE767	34.44148	-119.1118	604	4	0.989	0	7.5634	0.8421	07KNSTD	2.731E-13	+/-	7.7E-15	584101	+/-	17526	102334	+/-	5074
BCB-8	BE768	34.4414	-119.1118	604	7	0.996	0	7.4074	0.8387	07KNSTD	3.113E-13	+/-	8.769E-15	676762	+/-	20282	120903	+/-	6020
BCB-9	BE770	34.44353	-119.1124	610	6	0.997	0	8.9269	0.8390	07KNSTD	1.017E-13	+/-	2.933E-15	181156	+/-	5589	31245	+/-	1538
BCB-10	BE771	34.44361	-119.1124	612	7	0.988	0	7.5474	0.8374	07KNSTD	1.072E-13	+/-	3.323E-15	225948	+/-	7431	39628	+/-	2008
BCB-13	BE772	34.44484	-119.1135	621	3	0.998	0	7.0039	0.8391	07KNSTD	2.963E-13	+/-	7.714E-15	681441	+/-	19062	116332	+/-	5640
BCB-14	BE773	34.4447	-119.1140	618	7	0.998	0	6.6030	0.8382	07KNSTD	1.833E-13	+/-	4.833E-15	445125	+/-	12619	77672	+/-	3747
BCB-15	BE774	34.44581	-119.1141	627	5	0.990	0	6.1815	0.8355	07KNSTD	2.835E-13	+/-	7.558E-15	733279	+/-	20945	127806	+/-	6261

a: Calculated using the CRONUS-Earth Geometric Shielding Calculator version 1.1 (available online at: http://hess.ess.washington.edu/)

b: In-house produced Be carrier has density of 1.012 g ml^{-1} and Be concentration of 291 µg ml^{-1}

c: AMS measured ratios were normalized to standard 01-5-2 with an assumed $^{10}Be/^{9}Be$ ratio of 8.558 x 10^{-12} (Nishiizumi et al., 2007)

d: All uncertainties are 1σ confidence level

e: ^{10}Be concentrations and associated measurement uncertainties are blank corrected relative to batch specific process blanks. Total atoms ^{10}Be in process blanks (atoms): BCB-1 = 10701 +/- 3102, all other samples = 12107 +/- 4037

f: Propagated uncertainties include error in the blank, carrier mass (1%), and counting statistics

g: Age calculated using version 3.0 of the online exposure age calculator formerly known as the CRONUS-Earth online exposure age calculator (available online at: https://hess.ess.washington.edu/)

h: Constant (time-invariant) scaling scheme of Lal (1991) and Stone (2000) with a reference production rate of 4.24 +/- 0.16 atoms g^{-1} yr^{-1} based on Promontory Point (PPT) calibration data from Lifton et al., (2015)

Table 4.3 *Summary of ages, published offsets, and displacement rates*

Fault	Offset Reference	Location	Age (ka)	Dip Slip (m)	Slip rate (mm yr^{-1})	Throw or Rock Uplift (m)	Throw or Rock Uplift Rate (mm yr^{-1})
			Rates calculated in this study				
San Cayetano	Rockwell (1988a)	WSCF: Bear Canyon	7.3 +1.8/-1.7	12.7 +/- 1.4[a]	1.7 +0.8/- 0.5[a]	9.0 +/- 1.0	1.2 +0.6/-0.4
			121.2 +/- 5.2	246.8 +/- 12.7[a]	2.0 +/- 0.2[a]	174.5 +/- 9[b]	1.4 +/- 0.2[b]
	Huftile and Yeats (1996)	ESCF: Hopper Canyon	950 +240/-250	2200–5200	3.9 +3.5/-2.0	1700–4000[c]	3.0[+] +2.7/-1.6[c]
			1540 to 950	6600–7900	12.3 +2.0/-1.6	-	-
			1540 +110/100	10100–11800	7.1 +/- 1.0	7700–9000[c]	5.5[+] +/- 0.8[c]
Oak Ridge	Huftile and Yeats (1996)	Happy Camp Syncline	950 +240/-250	1700–2100	2.0 +1.0/-0.6	-	-
			1540 +110/100	3900–4000	2.6 +/- 0.2	-	-
Ventura	Rockwell (1988b)	Ventura River	384 +170/-230	-	-	2773	7.0 +11.9/-2.5
			Rates used in this study but not calculated here				
San Cayetano	Rockwell (1988a)	Sisar Creek (WSCF)	15–20	-	1.05 +/- 0.2[a]	13.0	0.75 +/- 0.15
		Mud Creek (WSCF)	15–20	-	2.35 +/- 0.55[e]	32.0 +/- 3.0	1.87 +/- 0.44
		Timber Canyon (WSCF)	5000	16–20	3.6 +/- 0.4	-	-
Ventura	Hubbard et al., (2014) after Rockwell (1988b)	Ventura River Terrace H–F [d]	105 or 80 to 38 +/- 1.9	-	-	440 +/- 10	4.8–13.7
		Ventura River Terrace F–E [d]	38 +/- 1.9 to 29.7 +/- 1.25	-	-	54 +/- 20	3.0–14.4
		Ventura River Terrace E–B [d]	29.7 +/- 1.25 to 15.9 +/- 0.2	-	-	66 +/- 20	3.0-6.9
		Ventura River Terrace B–Present [d]	15.9 +/- 0.2 to present	-	-	68 +/- 10	3.6-4.9

a: Values for dip slip and slip rate were calculated from fault throw or incision by diving by the sine of fault dip. Offsets for the western San Cayetano fault (WSCF) were measured at the surface, therefore, a dip of 45˚ was used for the WSCF to be consistent with the fault dip in the shallow surface based on structural contours (Rockwell, 1983 after Schlueter, 1976)

b: Incision amount used as a proxy for rock uplift

c: Values for fault throw were derived by multiplying measure dip-slip component by the sine of fault dip. Offsets for the eastern San Cayetano fault (ESCF) were measured along the fault plane at depth, therefore, a fault dip of 50˚ was used for the ESCF to be consistent with the deep geometry of the fault outlined in Chapter 2

d: River terrace annotations refer to uplifted alluvial terraces on the flanks of the Ventura River described in Rockwell (1988b)

e: Slip rate from Rockwell (1988a) based on vertical separation of a terrace across the WSCF with a local fault dip of 53˚ measured from structural contours

A previously published age estimate for the extensive uplifted Bear Canyon alluvial fan surface is 80–100 ka (Rockwell, 1988). However, the existing age is not a direct age for the surface, but is based on soil correlation with what was argued to be a similar aged terrace on the Ventura River (Rockwell, 1983). This 80–100 ka Ventura terrace was itself dated by extrapolating a slip rate of 0.37 +/- 0.02 mm yr^{-1} for the Arroyo Parida/Santa Ana fault from ~38 ka using the relative height of the terrace above the modern day Ventura River (Rockwell, 1983). Given numerous assumptions associated with the previous 80–100 ka age and the fact that the boulder age is directly taken from the uplifted Bear Canyon alluvial fan surface, our boulder age of ~121 ka is preferred for this fan surface.

4.4.4 Displacement rates

We re-calculated existing displacement rates for the San Cayetano, Ventura, and Oak Ridge faults by incorporating the results of the new TCN burial and surface exposure dating chronology presented above to better define stratigraphic marker ages. Details of marker horizons and ages used to make the slip rate calculations are shown in Table 4.3.

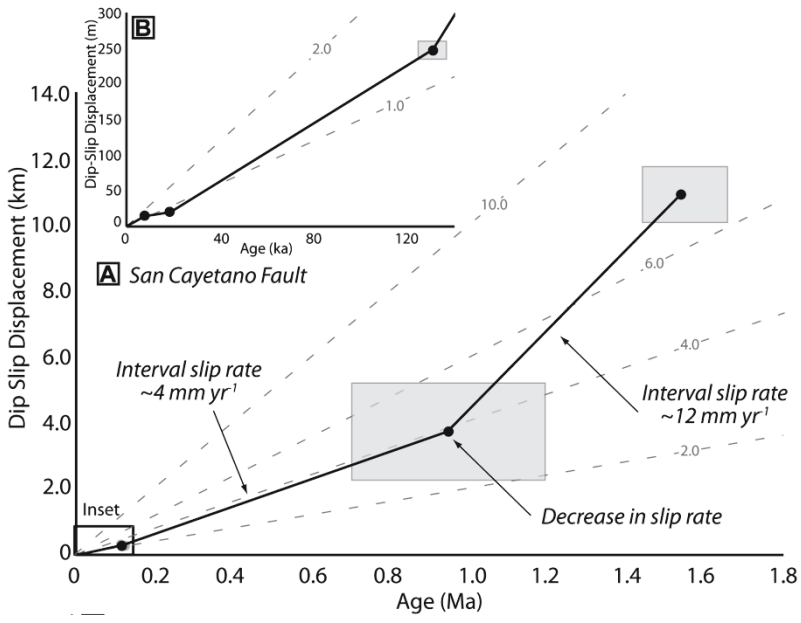

Figure 4.8 *Plots of slip rates over time for the San Cayetano fault. The solid line is the rate based on the most likely modal burial age and the average offset from the appropriate reference. Light grey boxes are the range of rates based on uncertainty in the age calculation and the offset amount. References for all offset amounts and ages are included in Table 4.3.*

Eastern San Cayetano fault:

Dip-slip separation across the ESCF of 2.2–5.0 km for the top of the Saugus Formation and 10.1–11.8 km (Table 4.3) for the base of the underlying shallow marine sands (Huftile and Yeats, 1996) were divided by the burial ages for the top of the Saugus Formation of 0.95 $^{+0.24}/_{-0.25}$ Ma and the base of the GCDF of 1.54 $^{+0.11}/_{0.10}$ Ma (Fig. 4.8a). Average slip rates for the ESCF calculated here are 3.9 $^{+3.5}/_{-2.0}$ mm yr^{-1} since ~0.95 Ma, and 7.1 +/- 1.0 mm yr^{-1} since ~1.54 Ma. The upper uncertainty bound for all rates stated here uses the maximum possible offset from the relevant reference (Table 4.3) and the youngest age value from the uncertainty associated with the appropriate age (Table 4.1). The lower uncertainty value uses the minimum possible offset from the relevant reference (Table 4.3) and the oldest age value from the uncertainty associated with the appropriate age (Table 4.1).

Western San Cayetano fault:

For the WSCF, 9.0 +/- 1.0 m vertical offset across a Holocene alluvial fan at the mouth of Bear Canyon (Rockwell, 1988) is divided by the depth profile age for the alluvial fan of 7.3 $^{+1.7}/_{-1.8}$ ka (Hughes et al., 2018) to give a Holocene slip rate of 1.8 $^{+0.7}/_{-0.5}$ mm yr^{-1} since 7.3 ka across a fault with and assumed 45° fault dip (Rockwell, 1988) (Fig. 4.8b, Table 4.3). We also calculated an incision rate into the uplifted Bear Canyon surface of 1.4 +/- 0.1 mm yr^{-1} based on maximum incision into the surface of 174.5 +/- 9.0 m (we assign a +/- 5% uncertainty to incision calculated using a swath profile) divided by the 121.2 +/- 5.2 ka boulder age of the Bear Canyon surface (Fig. 4.8b, Table. 4.3). The incision rate was used as a proxy for uplift but was also converted into a slip rate of 2.0 +/- 0.2 mm yr^{-1} using an assumed fault dip of 45° (Fig 8b, Table 4.3) for comparison with other rates.

Oak Ridge and Ventura faults:

Slip rates for the Oak Ridge fault through the Happy Camp syncline are based on 1.7–2.1 km of dip slip separation of the top of the exposed Saugus Formation calculated by restoring movement on the Oak Ridge fault so that the top of the currently exposed Saugus Formation in the fault hanging wall onlaps onto the Saugus Formation in the footwall (Huftile and Yeats, 1996). Our burial age for the top of the

Table 4.4 *Parameters for ^{10}Be erosion rate samples and inputs to CAIRN*

Catchment	Latitude (°N)	Longitude (°W)	Elevation (m.a.s.l) [a]	Quartz Mass (g)	Be Carrier (g)[b]	$^{10}Be/^{9}Be$ [c]	^{10}Be Concentration (atoms g^{-1} SiO_2) [d, e]	Av. Production Scaling	Av. Topographic Shielding	Erosion rate (mm yr^{-1}) [f]	^{10}Be Erosional Timescale (years) [g]
A	34.46800	119.17200	453	9.14	0.3374	9.57E-15	14508 +/- 1444	2.1231755	0.97007111	0.41 +/- 0.09	1450
C	34.44366	119.13450	521	16.58	0.3375	1.20E-13	122110 +/- 2850	2.2869962	0.96897949	0.05 +/- 0.01	11652
D	34.44136	119.12214	506	17.49	0.3371	2.40E-14	21664 +/- 1006	1.9042472	0.96345373	0.25 +/- 0.05	2413
E	34.43133	119.09092	175	17.75	0.3375	2.83E-15	975 +/- 532	2.2360063	0.96863021	6.46 +/- 5.19	93
G	34.41244	118.89864	209	9.74	0.3365	2.48E-15	1147 +/- 1029	1.5439849	0.96715678	3.95 +/- 18.18	152
H	34.41669	118.83309	209	16.94	0.3374	4.38E-15	2584 +/- 613	1.6988443	0.97477503	1.92 +/- 0.63	313
I	34.42757	118.77036	255	17.40	0.3396	3.64E-15	1816 +/- 593	1.3510503	0.96259496	2.21 +/- 0.95	271
K	34.41200	118.97500	270	16.75	0.3363	9.67E-15	7984 +/- 816	1.8035558	0.96278031	0.64 +/- 0.15	931
M	34.37748	119.04046	139	18.10	0.3371	1.40E-14	11492 +/- 1049	1.3573963	0.98756061	0.36 +/- 0.09	1680
N	34.40111	119.07000	225	16.20	0.3327	3.82E-15	2067 +/- 651	1.487846	0.97982125	2.14 +/- 0.88	280
Q	34.34894	119.11119	102	18.89	0.3363	1.85E-14	15072 +/- 911	1.0582481	0.9916808	0.22 +/- 0.05	2708
R	34.33776	119.14217	113	15.92	0.3368	9.74E-15	8505 +/- 1197	1.151546	0.98956297	0.42 +/- 0.12	1423
S	34.3176	119.14462	99	18.18	0.3352	9.94E-15	7590 +/- 969	1.1656873	0.98861027	0.48 +/- 0.13	1258
T	34.31034	119.15312	90	18.18	0.3355	2.14E-14	18294 +/- 1250	1.0741646	0.99313518	0.18 +/- 0.05	3248
W	34.28601	119.25642	63	19.16	0.3356	7.42E-15	8815 +/- 746	1.0641152	0.98182844	0.38 +/- 0.10	1584
X	34.34259	119.28571	75	17.57	0.3349	7.42E-15	5411 +/- 660	1.1576936	0.98601051	0.66 +/- 0.18	903
Y	34.35331	119.26002	133	16.86	0.3467	9.84E-15	8422 +/- 841	1.1007105	0.9862446	0.41 +/- 0.11	1467

a: m.a.s.l = Meters above sea level

b: b: In-house produced Be carrier has density of 1.000 g ml^{-1} and Be concentration of 758.9 µg ml^{-1}

c: AMS measured ratios were normalized to standard 01-5-2 with an assumed $^{10}Be/^{9}Be$ ratio of 8.558 x 10^{-12} (Nishiizumi et al., 2007)

d: All uncertainties are 1σ confidence level

Table 4.4 *Parameters for ^{10}Be erosion rate samples and inputs to CAIRN (continued)*

e: ^{10}Be concentrations and associated measurement uncertainties are blank corrected relative to batch specific process blanks. Total atoms ^{10}Be in process blanks (atoms): Catchments A-K 31126 +/- 4227, catchment M-Y = 30933 +/- 4391

f: Erosion rates calculated using the CAIRN method Mudd et al., (2016). Calculation use a density of 2.65 g cm^{-3}, a ^{10}Be half-life of 1.39 +/- 0.01 (Chmeleff et al., 2010) and a SLHL reference ^{10}Be production rate of 4.30 at g^{-1} yr $^{-1}$

g: Time required to remove one mean attenuation path length, $T=z*/e$, using $z = 60$ cm (typical for silicate rocks)*

exposed Saugus Formation in the Happy Camp syncline of ~0.95 Ma was combined with the dip-slip offset to give a slip rate of 2.0 $^{+1.0}/_{-0.6}$ mm yr^{-1} since ~0.95 Ma (Table 4.3).

The long-term rock uplift rate via folding for the Ventura fault is 7.0 $^{+11.9}/_{-2.5}$ mm yr^{-1} based on the burial age for the top of the Saugus Formation at Ventura of 0.38 $^{+0.17}/_{-0.23}$ Ma and 2.7 +/- 0.2 km maximum uplift of the Saugus Formation in the Ventura Avenue anticline (Table 4.3) (Rockwell et al., 1988). The large range in the uplift rate results primarily from the large uncertainty in the burial age (Table 4.1 and 4.3). All displacement rates calculated here along with additional displacement rates for the San Cayetano and Ventura faults, which are not re-evaluated in this study but are used in our analysis, are included in Table 4.1

4.5 Erosion rates and landscape analysis results

4.5.1 ^{10}Be erosion rates

Catchment-averaged erosion rates for the 18 studied catchments range from 0.05–6.45 mm yr^{-1} (Fig. 4.9, Table 4.4). Values from three catchments in the hanging wall of the WSCF range from 0.05 +/- 0.01 mm yr^{-1} up to 0.41 +/- 0.09 mm yr^{-1} (all uncertainties associated with erosion rates are 1σ) and are almost an order of magnitude lower than two catchments in the hanging wall of the ESCF, which have erosion rates of 1.92 +/- 0.63 mm yr^{-1} and 2.21 +/- 0.95 mm yr^{-1} (Fig. 4.9b, Table 4.4). Lower erosion rates for the WSCF compared to the ESCF mirror the pattern of Pleistocene displacement rates and total stratigraphic separation, which are also markedly lower in the west than the east (Rockwell, 1988; Çemen, 1989) (Table 4.3 and 4.4). Uncertainties for the erosion rates along the ESCF overlap with large uncertainties of the throw rate of 3.0 $^{+2.7}/_{-1.6}$ mm yr^{-1} since 0.95 Ma (Table 4.3 and 4.4), whereas erosion rates for catchments draining the hanging wall of the WSCF are generally two to four times lower than the Holocene fault throw rates of 1.3 mm yr^{-1} (Table 4.3 and 4.4).

Erosion rates for the Ventura fault are consistent along strike with five of the six catchments recording erosion rates in the range 0.38–0.66 mm yr^{-1} (Fig. 4.9a, Table 4.4). The only erosion rate for the Ventura fault that lies outside of this range is a rate of 0.18 +/- 0.05 mm yr^{-1} from catchment T, which is

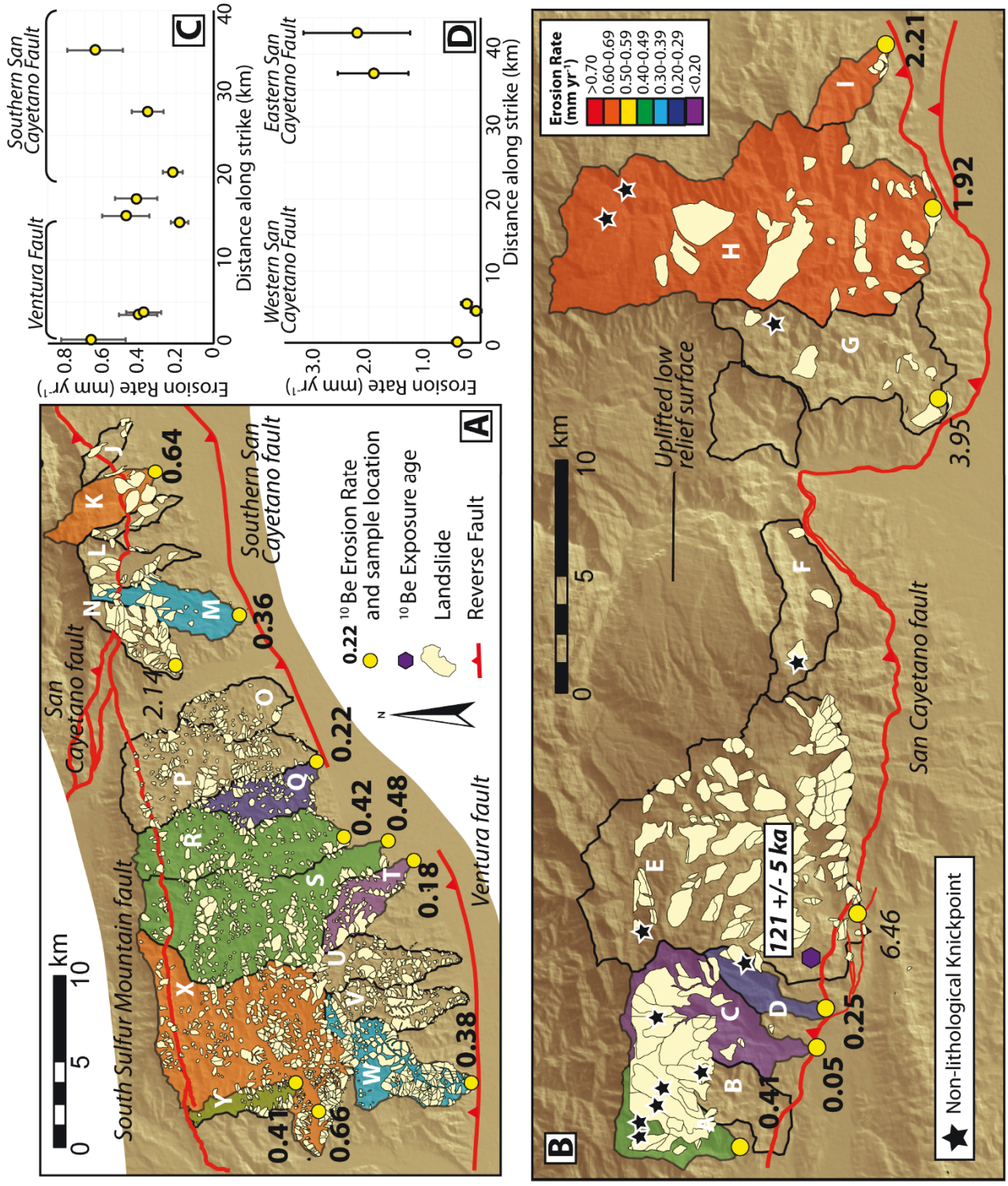

Figure 4.9 *A & B) Catchments and erosion rates in the hanging wall of the San Cayetano (B), Ventura, and Southern San Cayetano (A) faults. Catchments are colour coded by erosion rate. ^{10}Be derived erosion rate sample locations at catchment outlets are denoted with yellow circles and the associated rate is listed next to the sample location. Rates in italics may have been artificially increased by landslides in proximity to the sample location (see text). Non-lithological knickpoints locations are denoted with black stars. Letters in the catchments correspond to data in Tables 4.5 & 4.6. C & D) Erosion rates along strike for the hanging wall of the Ventura and Southern San Cayetano (C), and San Cayetano faults (D).*

situated at the eastern tip of the fault (Fig. 4.9). The late Pleistocene rock uplift rate for the Ventura fault at Ventura is 3.6–4.9 mm yr^{-1} (Hubbard et al., 2014) and the majority of erosion rates that lie in the range 0.4–0.6 mm yr^{-1} are an order of magnitude lower than the uplift rates. Erosion rates from catchments in the hanging wall of the SSCF demonstrate no discernible pattern along strike and range from 0.22 +/- 0.05 mm yr^{-1} up to 0.64 +/- 0.15 mm yr^{-1} (Fig. 4.9, Table. 4.4). The erosion rate values in the hanging wall of the SSCF are lower by a factor of 2–3 than throw rates, which range from 1.2–1.6 mm yr^{-1} (Hughes et al., 2018).

Erosion rates of 6.46 +/- 5.19 mm yr^{-1} in catchment E, 3.95 +/- 18.18 mm yr^{-1} in catchment G, and 2.14 +/- 0.88 mm yr^{-1} in catchment N are anomalously high compared to the surrounding catchments and have large associated uncertainties (Fig. 4.9, Table 4.3). Further analysis of the sample locations using a lidar derived DEM and Google Earth™ suggested the presence of recent landslides immediately adjacent to the sample locations of catchments E, G, and N, some of which are not recorded in the CaLSI digital landslide database. We suggest that the high catchment-averaged erosion rates in catchments E, G, and N result from sampling immediately downstream of landslides. The consequence of sampling downstream of landslides is that the sediment sampled for the erosion rate calculation may be locally sourced from below the penetration depth of cosmic rays and, consequently, may be depleted in ^{10}Be relative to the ^{10}Be concentration of well mixed sediment that is representative of the entire catchment (Niemi et al., 2005; Yanites et al., 2009; West et al., 2014). The high uncertainties associated with the erosion rates in catchments E, G, and N also result from sampling sediment with extremely low ^{10}Be concentration due to increased measurement uncertainties associated with low nuclide concentration samples. The erosion rates for catchments N, E and G are not compared with uplift rates given their high uncertainties and because their geomorphic context is not consistent with the assumption of well mixed sediment sourced from the entire catchment inherent to our erosion rate calculations (Table 4.3). The effects of landslides on measured erosion rates and the evolution of the landscape are discussed further in section 4.6.3 below.

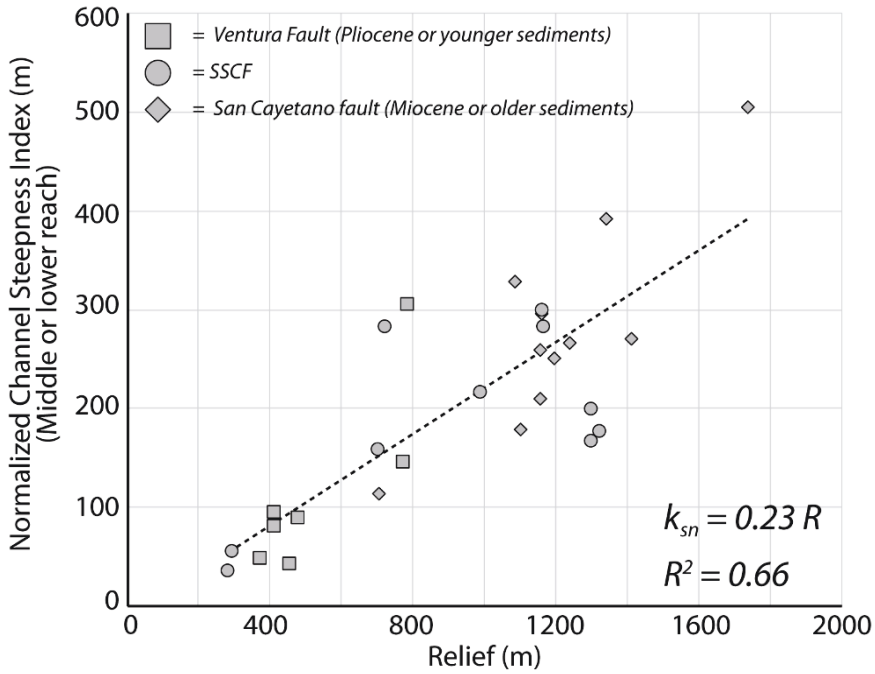

Figure 4.10 *Plot of normalized steepness indices (k_{sn}) against relief for the lower and (if applicable) middle reach of catchments in the hanging wall of the San Cayetano (diamonds), Ventura (squares), and Southern San Cayetano faults (circles). Ksn shows a positive correlation with relief but also with lithology. The lithology in the hanging wall of the Ventura fault is dominated by Pliocene or younger sediments with low ksn and low relief but the lithology in the hanging wall of the SCF is dominated by Miocene or older sediments with high ksn and high relief. Sediments in the hanging wall of the Southern San Cayetano fault have mixed lithology and a mixture of values of ksn and relief.*

4.5.2 Hanging wall relief, normalized steepness, fault activity

A plot of hanging wall relief (R) and k_{sn} in the hanging walls of the Ventura, San Cayetano, and SSCF shows a positive correlation and suggests that R and k_{sn} are coupled throughout the study area in a similar manner to that observed across various climates and tectonic regimes (Cyr et al., 2010; DiBiase et al., 2010; D'Arcy and Whittaker, 2014) (Fig. 4.10). Furthermore, k_{sn} values and relief are generally higher in the hanging wall of the San Cayetano fault compared to the hanging walls of the Ventura fault and the SSCF, with an average k_{sn} value for the lower reach of 260 m in the hanging wall of the San Cayetano fault and 116 m in the hanging wall of the Ventura fault (Fig. 4.11).

The strong correlation between R and k_{sn} is also evident in a plot of R and k_{sn} along-strike for the San Cayetano, Ventura, and SSCFs (Fig. 4.11). Along the San Cayetano fault, catchment maximum relief of ~1700 m and maximum k_{sn} of 505 m are recorded in catchment E in the WSCF (Fig. 4.11). Relief is

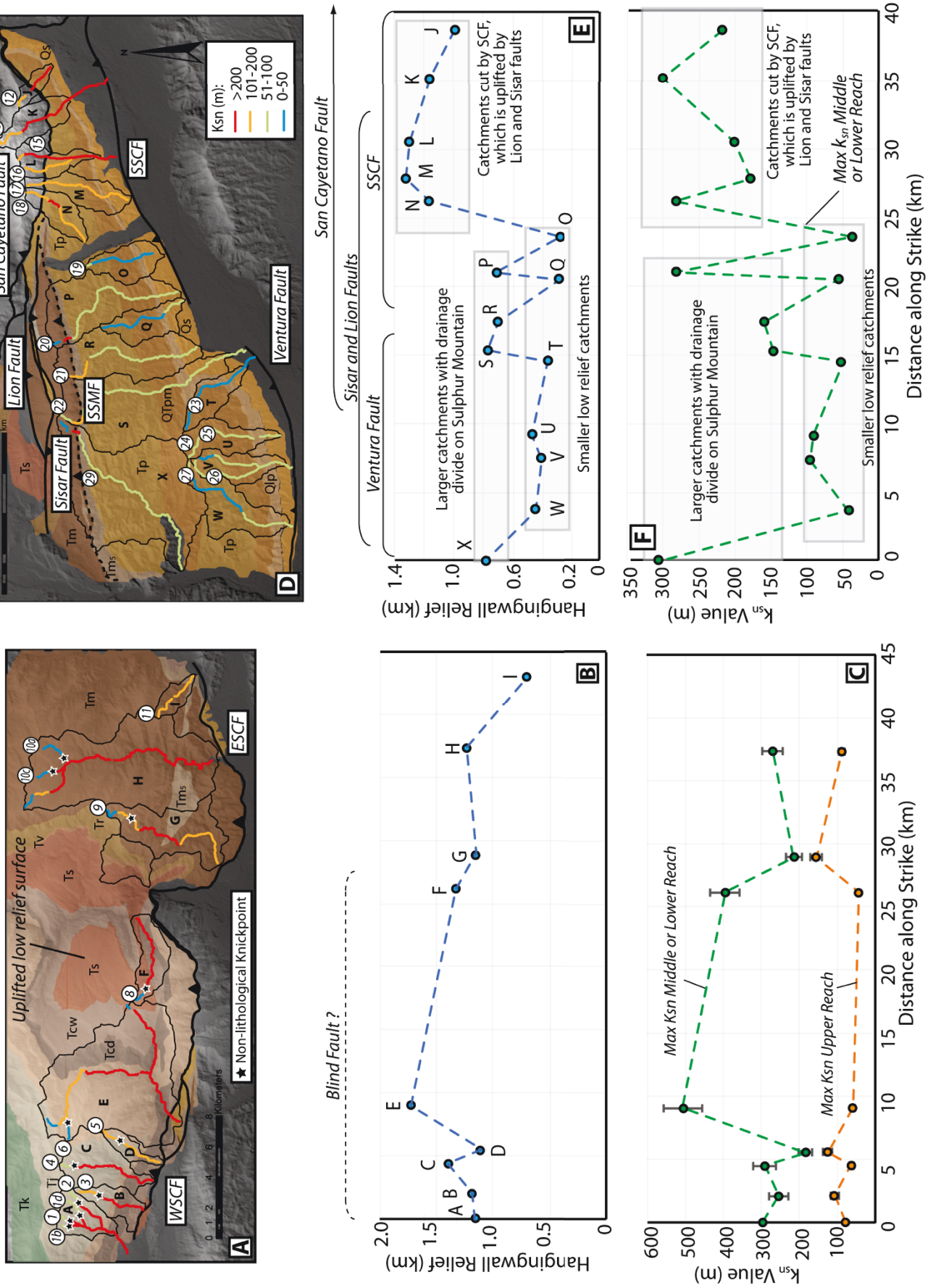
A
Uplifted low relief surface
Non-lithological Knickpoint
WSCF
ESCF
Kilometers
B
Blind Fault ?
Hangingwall Relief (km)
C
Max Ksn Middle or Lower Reach
Max Ksn Upper Reach
Ksn Value (m)
Distance along Strike (km)
D
San Cayetano Fault
Lion Fault
Sisar Fault
SSMF
SSCF
Ventura Fault
Ksn (m):
>200
101-200
51-100
0-50
E
Sisar and Lion Faults
Ventura Fault
SSCF
Larger catchments with drainage divide on Sulphur Mountain
Smaller low relief catchments
Catchments cut by SCF, which is uplifted by Lion and Sisar faults
F
Max ksn Middle or Lower Reach

Figure 4.11 *Relief, normalized steepness indices (k_{sn}), and knickpoint heights along strike in the hanging walls of the San Cayetano (SCF), Ventura and Southern San Cayetano (SSCF) faults. A) Catchment map in the hanging wall of the SCF with streams colour coded by k_{sn} value. Location of non-lithologic knickpoints is indicated by black stars and numbers in circles refer to stream in Table 4.5. Faults are denoted by solid black lines. B) Catchment relief along strike of the hanging wall of the San Cayetano fault. Letters refer to catchments in Table 4.5. C) Along-strike k_{sn} values in the hanging wall of the San Cayetano fault. D) Catchment map in hanging wall of the Ventura fault and the SSCF. Numbers in circles refer to streams and catchments in Table 4.6. E) Hanging wall relief along strike of the Ventura fault and SSCF. The lateral extent of various faults within the catchments is included above. Letters refer to catchments in Table 4.6. C) Along-strike k_{sn} values in the hanging wall of the Ventura fault and the SSCF. ESCF = Eastern San Cayetano fault, WSCF = Western San Cayetano fault, SSMF = South Sulphur Mountain fault. Abbreviations for stratigraphic units are included in key in Figure 4.3.*

near uniform in the central portion of the San Cayetano fault, where a large, uplifted, low-relief surface is preserved (Fig. 4.11a). The hanging wall of the San Cayetano fault has generally low k_{sn} for the upper reach (45–126 m) and higher k_{sn} for the lower reach (166–505 m) (Table. 4.5). Both R and k_{sn} in the hanging wall of the San Cayetano fault do not decrease significantly towards the western tip of the fault (Fig. 4.11). The highest uplift rates of 4.7–6.3 mm yr^{-1} and stratigraphic separation values of 7.3–11 km are recorded along the ESCF (Fig. 4.12, Table 4). This is in contrast to maximum R and k_{sn} values along strike, which are located along the WSCF (Fig. 4.12).

Relief in the hanging wall of the Ventura fault has a maximum value of ~780 m in catchments S and X at the eastern and western fault tips (Fig. 4.11e, Table 6). The remaining catchments in the centre of the fault have R values consistently lower at around 400–450 m (Fig. 4.11e). However, the two catchments at the fault tips with the largest R (catchments S and X) extend ~7 km farther north than catchments in the central Ventura fault and have their drainage divide on Sulfur Mountain (Fig. 4.11d). The pattern of k_{sn} values across the hanging wall of the Ventura fault is broadly similar to the pattern of relief across the fault (Fig. 4.11e and 4.11f). Both R and k_{sn} in the hanging wall of the SSCF demonstrate a marked increase from west to east (Fig. 4.11e and 4.11f). The larger catchments with drainage divides on Sulfur Mountain have relief of ~700 m and the smaller catchments, which do not reach as far north, generally have relief around 300 m (Fig. 4.11f). Along the eastern section of the SSCF catchment drainage divides are located in the hanging wall of the central San Cayetano fault. Patterns of relief and k_{sn} the hanging wall of the Ventura fault and the SSCF, with highest values in the larger catchments, are similar to patterns observed in the Basin and Range Province in the western United States (Densmore et al., 2004) and may be indicative of pre-existing topography prior to surface uplift related to the Ventura fault and

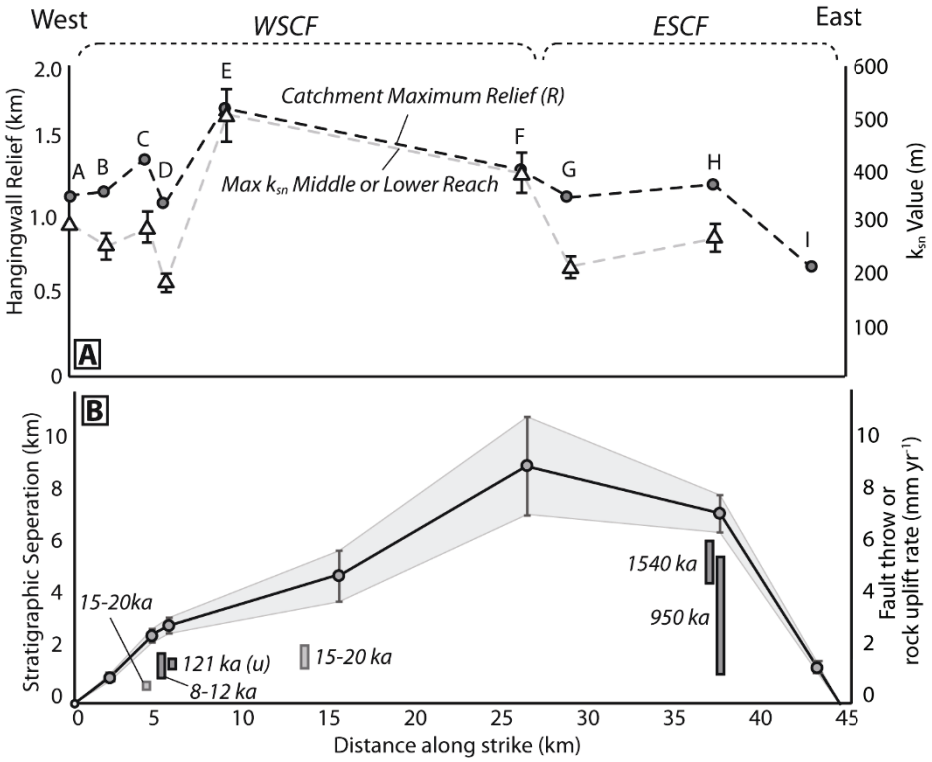

Figure 4.12 *Comparison of stratigraphic separation, fault throw or rock uplift rates, relief, and channel steepness along strike in the hanging wall of the San Cayetano fault. A) Plots of relief and normalized channel steepness along strike of the San Cayetano fault (see Figure 4.11). Letters refer to catchments in Table 4.5. B) Stratigraphic separation (circles) and uncertainties along strike with values taken from Rockwell (1988a) and Cemen (1989). If no uncertainty is described in the reference, then a 10% uncertainty is allocated. Grey rectangles are uplift or throw rates along strike with the number next to the rate denoting the age. Dark grey rates are from this study and light grey rates are from Rockwell (1988a).*

the SSCF. Stream parameters and relief data for the San Cayetano fault are included in Table 4.5 and the corresponding data for the Ventura fault and SSCF in included in Table 4.6.

4.5.3 Stream profiles and associated knickpoints

Stream profiles extracted from catchments in the hanging wall of the San Cayetano fault are not smoothly concave, and often contain several knickpoints (Fig. 4.13a). However, our analysis of these knickpoints suggest that many correspond to either mapped changes in lithology or are at the base of mapped landslides. Removing these lithological or landslide-related knickpoints leaves a total of twelve knickpoints in the hanging wall of the San Cayetano fault (stars, Fig. 4.9b and 4.13), which we interpret to be recording a transient response of the landscape to tectonic activity on the San Cayetano fault (Table. 4.5) (e.g. Boulton and Whittaker, 2009; Miller et al., 2012; Whittaker and Walker, 2015). In

the hanging walls of the Ventura fault and the SSCF, all knickpoints in the river long-profiles can be attributed to mapped changes in lithology so we therefore focus our analysis on the San Cayetano Fault (Fig. 4.13). Some catchments analysed in this study contain multiple streams e.g., catchment A (Fig. 4.11a), therefore, we applied numerical identifiers to the individual streams presented in Figure 4.13 and Tables 4.5 and 4.6.

In principle, for migrating knickpoints the difference in vertical elevation between a knickpoint extracted from river long profiles or slope-area plots, and the elevation of a fault (herein referred to as knickpoint height) should be independent of catchment area and related to the difference in uplift rate experienced by a channel when its course crosses a fault (Wobus et al., 2006a; Wobus et al., 2006b; Whittaker, 2012). Therefore, knickpoints in the hanging wall of the San Cayetano fault can potentially provide insights into past variations in rock uplift rates for the fault.

Figure 4.14a shows that knickpoint height along strike mirrors the pattern of relief and k_{sn} along strike. As with relief, the highest knickpoints are present in the west-central San Cayetano fault in catchment E, stream 6, and the only catchment that contains a stream without a non-lithologic knickpoint is catchment I, stream 11 located at the eastern tip of the San Cayetano fault (Fig. 4.11a). In another similarity with relief, knickpoint height does not systematically decrease towards the western tip but is consistently between ~700–900 m for streams 1, 1b, 1d, 2, 3, and 4 (Fig. 4.14a, Table 4.5). Streams in two of the larger catchments (G and H) contain a lower second knickpoint, however, a sample size of two is not sufficient to analyse these data in any detail and these knickpoints are not considered further (Table 4.5). Figure 4.14b demonstrates a positive correlation between knickpoint height and catchment relief with an R^2 value of 0.7. The analogous patterns of knickpoint height in the hanging wall of the San Cayetano fault with patterns of relief and k_{sn}, and the positive correlation between knickpoint height and relief in Figure 4.14b indicates that stream gradients may be responding to the same signal as relief and k_{sn}.

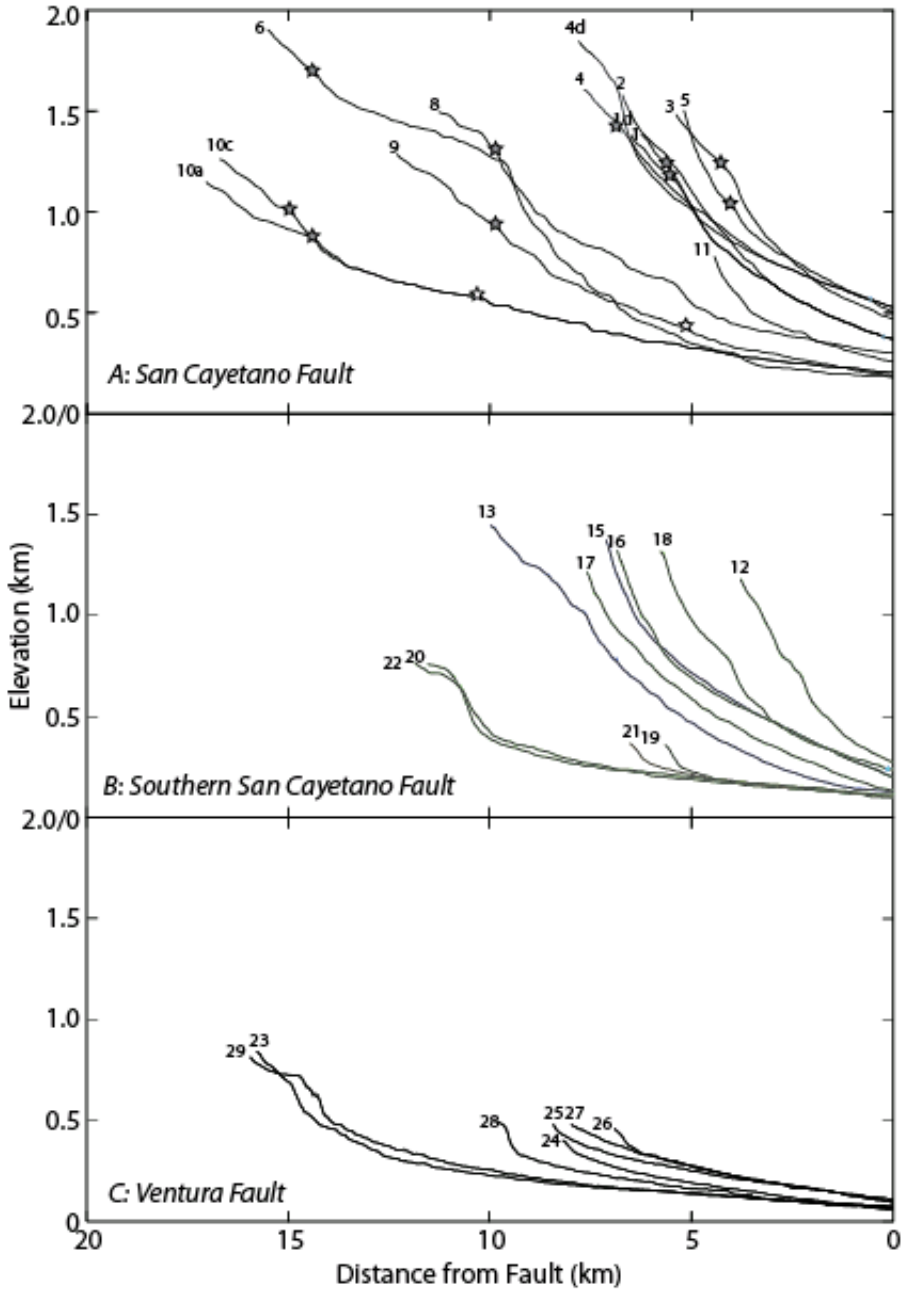

Figure 4.13 *River long profiles in the hanging wall of the San Cayetano (A), Southern San Cayetano (B), and Ventura faults (C). Non-lithological knickpoints in streams in the hanging wall of the San Cayetano fault are included as grey stars in A. Stream numbers refer to streams on maps in Figure 4.11 and details are included in Tables 4.5 and 4.6.*

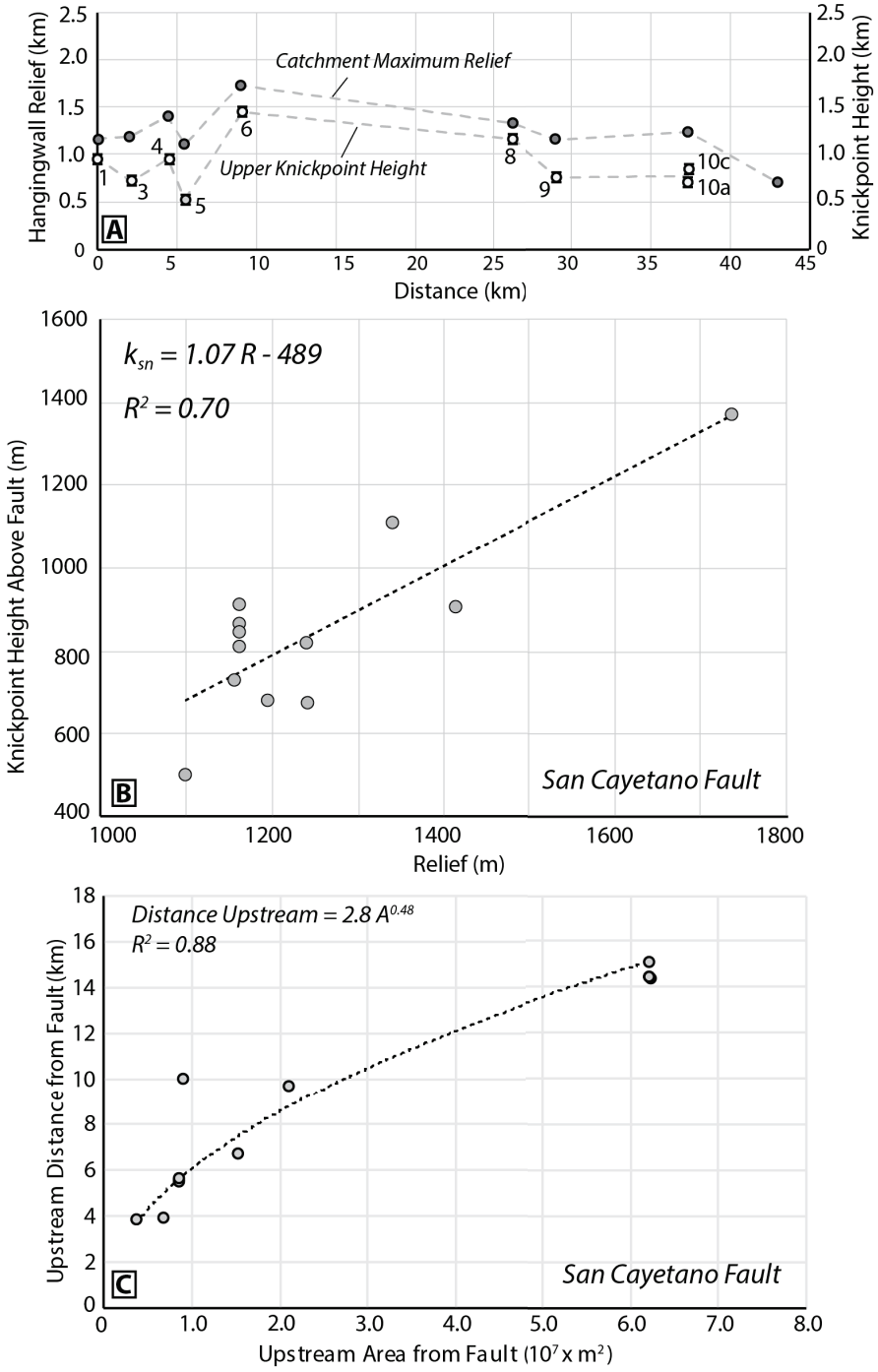

Figure 4.14 *Comparison of knickpoints positions in the streams relative to the San Cayetano fault. A) Relief and normalized channel steepness along strike of the San Cayetano fault from Figure 4.10. Numbers refer to streams in Table 4.5. (B) Plot of knickpoint heights relative to the fault against relief for streams in the hanging wall of the San Cayetano fault. The intercept value of 489 m suggests that and average of this amount of relief was present in the hanging wall of the San Cayetano fault when the knickpoints formed, assuming that all knickpoints formed at the same time. C) Plot of upstream distance of the knickpoint from the fault against upstream drainage area from the fault. The power law exponent of 0.48 is the same as the power law exponent for knickpoint celerity (0.5) in a simplified version of the stream power equation presented in section 4.3.4.1 and is taken to indicate that all the knickpoints were formed synchronously by the same change in base level event.*

Table 4.5 *Stream and knickpoint parameters for catchments in the hanging wall of the San Cayetano fault*

Catchment	*Stream Number*	*Outlet Distance Along Strike (m)*	*Relief (m)*	*Fault Elevation (m)*	*Upstream Drainage Area (km²)*	*Presence of Knickpoint [a]*	*Knickpoint Height from Fault (m)*	*Knickpoint Upstream Distance from Fault (m)*	*k_{sn} Above Knickpoint (m)*	*k_{sn} Below Knickpoint (m)*
A	1	0	1162	372	9*	1	864	5601	87	297
	1b					1	847	5519	46	293
	1d					1	807	5497	99	216
	2					1	913	5627	79	259
B	3	2030	1195	471	6	1	683	3911	107	252
C	4	4451	1413	513	16	1	906	6746	64	288
D	5	5473	1100	499	4	1	503	3898	126	179
E	6	9029	1736	328	62	1	1374	14381	59	505
F	8	26172	1339	194	9*	1	1109	9843	45	393
G	9	28993	1155	181	21	2	726	9732	156	186
	9					1	237	5039	186	210
H	10	37382	1240	195	62	1	393	10202	267	233
	10a					2	678	14406	69	211
	10c					2	819	15070	89	256
I	11	43000	704	237	4	0	-	-	110	114

a: Presence of knickpoint 0 = no knickpoints, 1 = lowermost of two knickpoints or only knickpoint, and 2 = uppermost of two knickpoints. Knickpoints listed here are knickpoints that cannot be attributed to lithology.

** Denotes catchments that have outlets set slightly north of the mapped fault trace. Accordingly, these areas are minimum values.*

In contrast to the height of a knickpoint relative to a fault, which is independent of upstream drainage area, the distance a knickpoint has travelled upstream from a fault after a finite period of time has been demonstrated to scale as A^m (Tucker and Whipple, 2002; Wobus et al., 2006b; Whittaker and Walker, 2015). To test whether the knickpoints in the hanging wall of the San Cayetano fault formed synchronously, the distance a knickpoint is currently located from the fault was plotted against upstream area from the fault (Fig. 4.14c). The upper set of knickpoints show a strong power-law correlation on a plot of distance upstream versus upstream area (Fig. 4.14c). The measured power law exponent of 0.48 is practically indistinguishable from the power law exponent for knickpoint celerity (m = 0.5) in a simplified version of the stream power equation (equation 4.1).

The correlation between the knickpoint position upstream and upstream area from the fault indicates that the knickpoints may have a tectonic origin rather than a climatic origin (Fig. 4.14c). If the knickpoints formed as a result of a climate induced change in base-level, then they would not necessarily have formed at the fault trace before migrating upstream and there would be no systematic relationship between distance from the fault and upstream area from the fault. Accordingly, we infer that the upper set of knickpoints in the hanging wall of the San Cayetano fault can all be attributed to the same event, which changed the base-level of streams currently draining the hanging wall of the San Cayetano fault, and we suggest that this base-level change event may have been related to a tectonic rather than climatic perturbation.

The relationship between catchment relief and knickpoint height can provide insights into the morphology of the landscape at the time the knickpoints formed (Whittaker and Walker, 2015). Average catchment relief in the hanging wall of the San Cayetano fault is 1288 m and knickpoint height is generally around 70 % of catchment relief, with a range between 46–87 % (Table. 4.5). This implies that and average along-strike of ~900 m of relief has been generated since the knickpoint formed and that there was an average along-strike of ~400 m of relief present at the time the knickpoints formed assuming that all knickpoints formed at the same time, which appears to be the case based on the analysis in Figure 4.14c.

Table 4.6 *Stream and knickpoint parameters for catchments in the hanging wall of the Ventura and Southern San Cayetano faults*

Catchment	*Stream Number*	*Outlet Distance along strike (km)* [a]	*Relief (m)*	*Upper Reach k_{sn} (m)*	*Lower Reach k_{sn} (m)* [b]
J	12	39	989	124	218
K	13	35	1155	100	300
L	15	31	1299	122	201
L	16	31	1299	154	168
M	17	28	1320	169	178
N	18	26	1164	122	283
O	19	24	282	73	37
P	20	21	719	30	284
Q	21	21	292	40	56
R	22	17	701	25	159
S	23	15	773	52	147
T	24	15	371	44	49
U	25	9	475	54	91
V	26	7	411	31	82
V	27	7	411	53	95
W	28	4	452	86	43
X	29	0	783	98	306

a: Distance is measured from west the east starting at the Ventura River and rounded to the nearest kilometre
b: Lower reach is the maximum ksn values from either the middle or lower reach

4.6 Discussion

The overall aim of this chapter is to synthesize a geochronology, fault displacement rates, erosion rates, and landscape analysis to evaluate the relative contribution of tectonic and lithological factors to patterns of erosion and relief generation across various temporal scales. However, in order to compare fault activity with erosion rates and the landscape morphology it is first necessary to evaluate uncertainties associated with the various results and how the results compare with the existing literature. The following discussion section examines the results presented in sections 4.4 and 4.5 in the context of the existing literature and presents explanations for potential divergences between the results of our study and previously published results.

4.6.1 Age of the top of the Saugus Formation

The isochron burial dating in section 4.4 indicates that the top of the exposed Saugus Formation and the base of the underlying shallow marine equivalent increase in age from west to east, with modal ages for the top and the base, respectively, of ~0.38–0.55 Ma at Ventura, ~0.95–1.54 Ma at Oak Ridge, and ~2.49–3.30 Ma in the eastern Ventura basin (Fig. 4.6). While the base of the Saugus Formation has often previously been described as increasing in age from west to east (e.g. Yeats, 1988; Levi and Yeats, 1993), the age of the top of Saugus Formation was previously poorly defined and has been modelled as synchronous across the entire basin in previous displacement rate calculations (Yeats, 1988; Huftile and Yeats, 1995; Huftile and Yeats, 1996).

The burial ages for the top of the exposed Saugus Formation presented in this study get systematically older from west to east (Fig. 4.6) and potentially indicate that the end of Saugus Formation deposition was not synchronous across the Ventura basin, but was progressively older from west to east. It is important to note that the results of this study provide no quantification for how much material has been eroded from above the currently exposed Saugus Formation, therefore, we cannot say for sure that the end of Saugus Formation deposition was not synchronous across the entire Ventura basin. However, the difference in age of ~2 Ma between the top of the exposed Saugus Formation at Ventura and the top in the eastern Ventura basin suggests a synchronous end to deposition is unlikely. Variations in the age

for the top of the Saugus Formation have also been suggested by optically stimulated luminescence and TCN dating south of the study area in the Camarillo fold belt, which record an age for the Saugus Formation of 125–65 ka, and possibly as young as 25 ka in places (DeVecchio et al., 2012a; DeVecchio et al., 2012b). These combined observations support the suggestion that locally derived ages for the Saugus Formation should be used when calculating displacement rates.

A commonly-cited age for the top of the exposed Saugus Formation near Ventura is 250 +/- 50 ka (Wehmiller et al., 1978; Lajoie et al., 1982; Yerkes et al., 1987) and this age has been employed by other researchers to calculate displacement rates for the Ventura fault (Rockwell et al., 1988; Hubbard et al., 2014). The 250 +/- 50 ka age is based on a set of early attempts at amino acid racemization on mollusc fossils in shallow marine sands of the 'San Pedro Formation' (Las Posas equivalent) on the southern flank of the Ventura Avenue anticline (Wehmiller et al., 1978). However, the amino acid racemization age has been questioned by various authors (Yeats, 1988; Wehmiller, 1992; Huftile and Yeats, 1995) and could be an underestimate because both the kinetic and thermal models employed in the calculation assumed the same thermal history for the Saugus Formation as the overlying marine terrace, despite an obvious angular unconformity being present between the two units. Given these questionable assumptions, previous researchers have indicated that an age of 0.4 Ma for the top of the Saugus Formation at Ventura could be more realistic (Yeats, 1988). Accordingly, the preferred isochron burial age of $0.38\ ^{+0.17}/_{-0.23}$ Ma could be a better estimate of the true age for the upper Saugus Formation at Ventura compared to the 0.25 Ma amino acid racemization age, despite the apparent overlap between the uncertainties associated with the two ages.

At first glance, our age for the top of the Saugus Formation in the Happy Camp syncline of $0.95\ ^{+0.25}/_{-0.24}$ Ma is not compatible with the previous basal age estimate for the Saugus Formation at South Mountain of 0.975 Ma (Yeats, 1981; Yeats, 1988). However, the isochron burial ages for the base of the Saugus Formation of ~0.55 Ma at Ventura and ~1.54 Ma at Oak Ridge confirm that the basal age increases significantly from west to east (Fig. 4.6) (e.g. DeVecchio et al., 2012a; Swanson and Irvine, 2015; this study). The oil well from which the 0.975 Ma age of Yeats (1981) is derived is located ~25 km to the west of the location of our isochron burial dating sample location in the Happy Camp syncline

(Fig. 4.6). Consequently, the isochron burial ages from the Happy Camp syncline would be expected to be significantly older than the 0.975 Ma age from the western end of South Mountain. Additionally, all the burial ages presented here for the top of the exposed Saugus Formation are maximum ages because there is no quantification of the amount of Saugus Formation above the sample locations that has been removed by erosion.

The two isochron burial dating ages for the upper exposed Saugus Formation in the hanging wall of the Oak Ridge fault are 0.95 $^{+0.24}/_{-0.25}$ Ma in the Happy Camp syncline and 1.37 $^{+0.19}/_{-0.22}$ Ma in the Long Canyon syncline (Fig. 4.5). Bedding orientations in the vicinity of the Long Canyon syncline have shallow dips that range from 0 to 10° (Dibblee, 1992; Campbell et al., 2014) and, consequently, the location of the axis of the Long Canyon syncline is difficult to locate precisely in the field. Therefore, it is possible that our sample location for the top of the exposed Saugus Formation in the Long Canyon syncline is on the limbs of the syncline and does not record the age of the youngest preserved strata. If it was the case that the Long Canyon syncline sample was taken from the limbs of the syncline this may partly explain the discrepancy between the two burial ages because the Long Canyon syncline and the Happy Camp syncline samples would have been taken from different stratigraphic positions. Alternatively, differential erosion could have removed more material from above the sample location in the axis of the Long Canyon syncline than in the Happy Camp syncline, although it is unclear why such a pattern of differential erosion would develop. Regardless, the age for the top of the Saugus Formation from the Happy Camp syncline (0.95 $^{+0.19}/_{-0.22}$ Ma) is preferred in displacement rate calculations because the Happy Camp syncline age overlaps the age range for the Saugus Formation at Moorpark (0.78–0.85 Ma) based on biostratigraphy (Wagner et al., 2007).

The isochron burial age for the base of the Saugus Formation in the eastern Ventura basin of 3.30 $^{+0.30}/_{-0.42}$ Ma is significantly older than the previous estimation of 2.3 Ma based on magnetostratigraphy and tephrochronology (Fig. 4.6) (Levi and Yeats, 1993). Our burial age for the underlying shallow marine sands in the eastern Ventura basin was sampled from strata that are either mapped as the brackish water Sunshine Ranch Member of the Saugus Formation (Dibblee and Ehrenspeck, 1992a) or a coarse-grained upper facies of the Pico Formation (Campbell et al., 2014). The coarse-grained upper facies of the Pico

Formation is mapped as interfingering with the Sunshine Ranch Member in the area from which our basal isochron burial dating sample was taken (Dibblee and Ehrenspeck, 1992a; Campbell et al., 2014) and it has previously been suggested that the Sunshine Ranch Member is late Pliocene based on its stratigraphic position, although there was no direct age data to confirm this suggestion (Campbell et al., 2014). Considering all the above, a late Pliocene age of ~3.30 Ma for the underlying shallow marine sands in the east Ventura basin appears consistent with previous work.

The burial age for the top of the exposed Saugus Formation in the eastern Ventura basin of $2.49\ ^{+0.25}/_{-0.29}$ Ma is considerably older than the previous age of 0.5 Ma (Levi and Yeats, 1993). The 0.5 Ma age for the top of the Saugus Formation is based on a projection of constant sedimentation rates above an ash layer identified in the upper Saugus Formation, which has 'chemical affinities' to the Bishop ash which is dated at 0.74–0.76 Ma (Izett, 1981; Sarna-Wojcicki, 1984; Levi and Yeats, 1993). Moreover, Saugus Formation strata were assigned to the Matuyama reversed magnetic chron based on the identification of mainly reverse polarity sediments in a magnetic transect (Levi and Yeats, 1993). Neither the ash layer within the upper Saugus Formation nor the magnetostratigraphy data provide direct ages for the Saugus Formation strata; both are based on semiquantitative correlations and assumptions. Our burial age for the top of the exposed Saugus Formation of $2.49\ ^{+0.25}/_{-0.29}$ Ma is the first direct age in the east Ventura basin and indicates that certain assumptions in the previously published ages of 0.5–2.3 Ma, such as the correlation of the ash layer in the upper Saugus Formation with the Bishop ash (Levi and Yeats, 1993), may have been invalid. Nevertheless, further geologic mapping and additional paleomagnetic samples are required near the sample locations to confirm whether the burial ages for the Saugus Formation in the eastern Ventura basin reflect the true age.

4.6.2 Displacement rates

Displacement rates calculated here are based on dip-slip offsets across the San Cayetano fault extracted from published cross sections (Table 4.4) (Huftile and Yeats, 1996). There are no strata younger than Miocene preserved in the hanging wall of the San Cayetano fault (Fig. 4.3); therefore, it is not possible to quantify post-Saugus Formation movement on the San Cayetano fault without several assumptions. The maximum offset value from previously published offsets for the ESCF of 5.2 km since 0.95 Ma

(Table 4.3) assumed that the same thickness of Saugus and Pico Formations was deposited in the hanging wall as is currently observed in well-log data in the footwall of the San Cayetano fault (Huftile and Yeats, 1996). However, this cannot be the case if slip on the San Cayetano fault occurred either before or during deposition of the Saugus Formation or shallow marine equivalent (Çemen, 1989; Yeats et al., 1994) because the thicknesses of the syndeformational units would thin across the fault.

The minimum offset value of 2.2 km since 0.95 Ma is based on isopach contours for the Pico Formation in the footwall of the Holser fault (Fig. 4.1), ~10 km eastwards of the ESCF, which increase in thickness southwards from 0.9 km at the Holser fault to a maximum thickness of 2.5 km in the basin (Huftile and Yeats, 1996). These isopach contours project eastwards to the hanging wall of the ESCF and the minimum thickness of 0.9 km is assumed to be the minimum thickness of Pico Formation that could have been deposited in the hanging wall of the ESCF. Furthermore, the northwards thinning from 2.5 to 0.9 km is attributed to sediment thickness decreasing across the fault due to uplift to the north (Yeats et al., 1994; Huftile and Yeats, 1996). We assume an intermediate value of 3.7 km offset since 0.95 Ma, which is between the two endmember scenarios described above in our slip rate calculation. This intermediate value is in line with the suggestion of Yeats et al., (1994) who attributed folds in the hanging wall of the ESCF to folding above an initially blind ESCF resulting in uplift to the north of the current ESCF.

In addition, there is ongoing debate about proposed rotation of the Western Transverse Ranges during the Quaternary (Luyendyk et al., 1980; Nicholson, 1994; Levi and Yeats, 2003; Schwartz et al., 2018). Displacement rates calculated from two-dimensional cross section restoration may underestimate fault slip because a potentially significant lateral component of slip may not be included in the offset. However, oblique movements are not well quantified for the Ventura basin and we observed no evidence for significant lateral offset in drainages or shutter ridges either in geomorphic maps or in the field. Therefore, our rates only consider the reverse component of movement.

4.6.3 Landslide effects on ^{10}Be erosion rates

Landslides can be a major contributor to uncertainties in catchment-averaged erosion rate calculations (Niemi et al., 2005; Densmore et al., 2009; Yanites et al., 2009; Roda-Boluda et al., 2019). In landslide-dominated landscapes, the assumption that sediment has undergone a steady transition through the attenuation length of the production pathway on hillslopes may not be applicable (e.g., Niemi et al., 2005; Yanites et al., 2009) because nuclide production at depths below the penetration depth of cosmic ray neutrons will be dominated by muon production, which occurs at much slower rates than production by neutron spallation (Braucher et al., 2013). Consequently, erosion rates calculated using standard methods in areas of deep-seated landslides could overestimate the true erosion rate, because deep-seated landslides can mobilize low-concentration sediment sourced from beneath the penetration depth of cosmic ray neutrons (Niemi et al., 2005; Yanites et al., 2009; West et al., 2014). Alternatively, where deep-seated but infrequent landslides are in fact the dominant erosional process, measured erosion rates can be low if samples are collected at a time interval between these large landslide events (Niemi et al., 2005; Ouimet, 2010).

With the exception of catchments N, E, and G, where we interpret the erosion rates to have been artificially increased by deep-seated landslides in proximity to the sample locations (section 4.5.1), the erosion rates measured in the Ventura basin (Table 4.4) generally record similar values to rates measured elsewhere in the Transverse Ranges, such as the San Gabriel Mountains (DiBiase et al., 2010; DiBiase and Whipple, 2011). However, we note that landslides are ubiquitous throughout all catchments in the study area (Fig. 4.9). Therefore, for catchment-averaged erosion rates derived from TCN concentrations in the Ventura basin to be a true reflection of the average erosion signal from across the catchments requires that landslides are high-frequency but low-volume and sediment can be mixed within catchment or hillslope 'storage' reservoirs (Niemi et al., 2005; Yanites et al., 2009; Roda-Boluda et al., 2019).

The surface area and quantity of landslides can potentially provide some insight into how landslides are influencing catchment-averaged erosion rates in the Ventura basin. In general, for catchments along strike of the Ventura fault and the SSCF landslides have smaller surface area but are more numerous

(Fig. 4.9a) when compared to catchments in the hanging wall of the San Cayetano fault, where landslides have larger surface area but are less numerous (Fig. 4.9b). Erosion rates along strike of the Ventura fault, and to a lesser extent the SSCF, are generally between 0.2–0.6 mm yr^{-1} (Fig. 4.9c). We interpret the generally consistent erosion rates along strike of the Ventura fault, and to a lesser extent the SSCF, to reflect the time-averaged erosion rate from the numerous small surface area landslides (Fig. 4.9a) (Yanites et al., 2009; Roda-Boluda et al., 2019).

In the hanging wall of the San Cayetano fault, the quantity of mapped landslides decreases from west to east along strike (Fig. 4.9a) but the erosion rates increase from west to east (Fig 4.9d), similar to the pattern of fault throw rates and stratigraphic separation values, which also increase from west to east (Fig. 4.12b). This apparent disconnect between the concentration of mapped landslides and the increase in erosion rates from west to east may indicate that landslides are not significantly affecting the catchment averaged erosion rates in the hanging wall of the San Cayetano fault. The relatively small contribution of landslides on catchment-averaged erosion rates in the hanging wall of the San Cayetano fault could be explained if the landslides were older than the ~10^3-year period over which the catchment-average erosion rates are measured (Table 4.4). Unfortunately, we have no data to constrain the age of the landslides but we suggested that the apparent increase in erosion rates from west to east is caused by higher slip rates along the eastern San Cayetano compared to the western San Cayetano fault based on the similar pattern of fault slip rates, stratigraphic separation, and erosions rates along-strike. Further information on the age and volume of the landslides would help to strengthen this analysis and provide insight into how temporal variations in landslide activity may have affected the modelled erosion rates.

4.7 Landscape response to active faulting

In the following discussion, our new data and analyses are combined to characterize the Quaternary response of the Ventura basin landscape to tectonic forcing with implications for how tectonic signals can be extracted from transient landscapes above reverse and thrust faults with complex surface and subsurface expression.

4.7.1 Transient landscape response to tectonic forcing

Variations in normalized steepness index (k_{sn}) and relief (*R*) are often analysed to characterize the landscape response to tectonics under the assumption of a topographic steady state (Densmore et al., 2004; Whittaker et al., 2008; Cyr et al., 2010; DiBiase et al., 2010; DiBiase and Whipple, 2011; Whipple et al., 2017). However, they can also be applied to transient landscapes if analysed carefully in tandem with other parameters, such as catchment relief, lithology, uplift rates, or knickpoint distribution (e.g. Densmore et al., 2007; D'Arcy and Whittaker, 2014; Whittaker and Walker, 2015; Roda-Boluda et al., 2019).

The presence of non-lithological knickpoints in the hanging wall of the San Cayetano fault provides possible evidence of a transient landscape response to tectonic forcing (Tucker and Whipple, 2002; e.g. Crosby and Whipple, 2006; Whittaker, 2012). Erosion rates that are generally 2–3 times less than uplift rock rates in the hanging wall of the WSCF also appear to support the suggestion of a transient response (Fig. 4.9 & 4.11). Conversely, erosion rates for the ESCF show good agreement with the long-term fault throw rate, although both throw rates and erosion rates for the ESCF have large uncertainties (Table 4.4 & 4.5). The pattern of higher erosion rates for the ESCF compared to the WSCF suggests that erosion rates in the hanging wall of the San Cayetano fault are responding to rock uplift rates (Fig. 4.9 and 4.12).

Further information about the nature of the landscape response is provided from the distribution of relief. A relatively continuous plateau of relief in the central section of the fault can indicate that footwall uplift has become decoupled from fault activity because an erosional threshold limit of elevation has been attained (Densmore et al., 2004; Densmore et al., 2007; Barnes et al., 2011). Relief is generally consistent along most of the San Cayetano reverse fault (Fig. 4.11b). However, the preservation of a large, uplifted, low-relief plateau in the hanging wall of the central San Cayetano fault (Fig. 4.9b & 4.11a) suggests that erosion has not yet fully adjusted to tectonic forcing (Whipple et al., 2017). If erosion had adjusted to tectonic forcing, then channel downcutting would have caused significant relief to develop on the uplifted plateau and the plateau would likely not be preserved in its current low-relief morphology. A similar example is the 'Big Bear Plateau' in the San Bernardino

Mountains, which is a large uplifted low-relief surface that is interpreted to indicate that the landscape has not adjusted to regional base level (Spotila et al., 1998).

Erosion rates in the hanging wall of the SSCF of 0.22 +/- 0.05 mm yr^{-1} up to 0.64 +/- 0.15 mm yr^{-1} (Fig. 4.9) are significantly lower than uplift rates of 1.2–1.6 mm yr^{-1} (Hughes et al., 2018) (Fig. 4.9 and 4.11), which is evidence that erosion rates are lagging behind fault displacement rates and further evidence of a transient response to tectonic forcing. However, it has been demonstrated that in the early stages of fault development erosion rates should reflect pre-faulting relief (Densmore et al., 2009). The highest erosion rates, relief, and channel steepness indices documented in the hanging walls of the Ventura fault and the SSCF correspond to the larger catchments and these larger catchments also include the Lion Canyon, Sisar, or San Cayetano faults (Fig. 4.9). The Lion Canyon, Sisar, and San Cayetano faults probably controlled relief in what is now the hanging wall of the Ventura fault prior to the onset of the activity on the Ventura fault and the SSCF. Taken together, these data suggest that the erosional response of catchments in the hanging wall of the Ventura fault and the SSCF are still recording the uplift signal from the Lion Canyon, Sisar, and San Cayetano faults, in addition to a potential blind fault in the footwall of the San Cayetano (Chapter 3).

An apparent discrepancy is recorded between the TCN derived erosion rates for catchments in the hanging wall of the Ventura fault (Fig. 4.9) and long-term erosion rates implied from the amount of material potentially removed from Ventura Avenue anticline (Rockwell et al., 1988). It has been previously estimated that the Saugus Formation has been uplifted via folding to a maximum of 2.7 km across the Ventura Avenue anticline since the end of Saugus Formation deposition at ~380 ka (Fig. 4.5). The 2.7 km was calculated based on projecting the tilt of bedding values on the fold limb to the fold hinge (Rockwell et al., 1988). If true, this would imply that a maximum of ~2.2 km of structural relief generated by folding of the Saugus Formation could have been eroded from the hanging wall of the Ventura fault, which requires extremely high long-term erosion rates of ~5–6 mm yr^{-1} based on maximum current topographic relief of 475 m on the Ventura Avenue anticline in catchment U (Fig. 4.11, Table 4.6). This is in sharp contrast to the TCN derived erosion rates in the hanging wall of the Ventura fault of 0.18–0.66 mm yr^{-1} (Fig. 4.9a).

Given that the erosion rates calculated here are applicable over the last ~1000–3000 years (Table 4.3) it is possible that erosion rates have decreased since the late Pleistocene or that erosion rates during the current warm and dry interglacial period are lower than longer-term rates (DeVecchio et al., 2012a). Alternatively, the maximum uplift amount for the Saugus Formation based on projection of bedding values in the limbs to the fold hinge could be an overestimate because the graphical reconstructions used to project the bedrock dips were an oversimplification of the actual structure (Rockwell et al., 1988). Further work is required to better characterize this apparent discrepancy.

4.7.2 Tectonic and lithologic controls on landscape response

Section 4.7.1 above established the transient nature of the Ventura basin landscape in response to tectonic forcing. The following discussion combines the results of the landscape analysis, the knickpoint analysis, the geochronology, and displacement rates to examine specifically how tectonic and lithologic effects may have controlled patterns of erosion and relief development within the study area.

4.7.2.1 Lithological controls on relief and channel steepness

A comparison of relief and k_{sn} with values with the distribution of mapped geological units indicates that lithology is an important control on patterns of relief generation and erosion in the Ventura basin. A thick sequence of siltstone-dominated Pliocene to Pleistocene sedimentary deposits is present in the hanging wall of the Ventura fault compared with an Oligocene to Miocene succession of sandstone and siltstone in the hanging wall of the San Cayetano fault (Fig. 4.3). Rock strength values measured by Schmitt hammer tests in the Santa Ynez Mountains, just west of the study area, suggest that in high uplift settings the Pico Formation has a significantly lower mean rock strength value of 15.0 +/- 0.3 when compared to mean rock strength values for the Monterey Formation (Modelo Formation equivalent) of 30.8 +/- 1.6 (Duval et al., 2004). Rock strength has been demonstrated to strongly influence channel morphology (e.g., Duval et al., 2004; Pike et al., 2009; Allen et al., 2013), therefore, the generally lower relief and k_{sn} values in the hanging wall of the Ventura fault and the SSCF, compared to the San Cayetano fault (Fig. 4.12) may, in part, be explained by a difference in rock strength in the respective fault hanging walls.

Lithology has also been demonstrated to modulate the abundance of landslides (Korup, 2008; Peruccacci et al., 2011; Borgomeo et al., 2014; Roda-Boluda et al., 2019). Therefore, the less-indurated and younger Pliocene sediments in the hanging wall of the Ventura fault are likely to have a higher erodibility than the older and well-lithified Oligocene–Miocene sediments in the hanging wall of the San Cayetano fault (Fig. 4.3). This contrast in lithology may partly explain why smaller but more numerous landslides are mapped in the hanging wall of the Ventura fault compared to larger and less numerous landslides in the hanging wall of the San Cayetano fault (Fig. 4.9a and 4.9b).

While the distribution of lithological units may be linked to patterns of relief and k_{sn}, and may also partly explain the distribution and surface area of mapped landslides, the distribution of lithological units in the Ventura basin is largely controlled by tectonics (Yeats, 1994). For example, the Oligocene to Miocene succession of sandstone and siltstone in the hanging wall of the San Cayetano fault (Fig. 4.3) has been faulted into contact with the younger Plio-Pleistocene deposits in the fault footwall by activity on the San Cayetano fault (Fig. 4.3) (Rockwell, 1988; Cemen, 1989). Likewise, the thick sequence of Pico formation in the hanging wall of the Ventura fault has been uplifted to the surface by uplift of the Ventura Avenue anticline resulting from slip on the Ventura fault (Hubbard et al., 2014). Therefore, while the distribution of lithology is an important consideration in the development of topographic relief and channel morphology, tectonic forcing may be a more significant contributor to the general landscape evolution of the Ventura basin.

4.7.2.2 Tectonic control on relief and channel steepness

The contrast between the large amount of fault offset on the San Cayetano fault compared to the smaller fault offsets for the Ventura fault and the SSCF, indicates that tectonics applies a significant control on patterns of relief and k_{sn} in the study area. The San Cayetano fault has significant stratigraphic separation with a maximum value of ~11 km across the fault at Fillmore, in combination with maximum relief of ~1700 m and maximum k_{sn} of 505 m (Fig. 4.12). Conversely, the Ventura fault has ~2 km of dip-slip separation at depth (Hubbard et al., 2014) and the SSCF has ~110 m of dip-slip separation (Chapter 3). Catchments in the hanging wall of the Ventura fault that do not have their drainage divides on Sulfur Mountain record a significantly lower maximum relief value of 475 m and maximum k_{sn} of 95 m (Fig.

4.11) compared to catchments in the hanging wall of the San Cayetano fault. Therefore, the higher values of relief and k_{sn} in the hanging wall of the San Cayetano fault, where much greater fault offsets are recorded are also recorded, imply that tectonic forcing is partly driving relief generation and increasing channel steepness.

Maximum k_{sn} values between 200–300 m are recorded in the lower reaches of streams to the north of the SSCF and south of the San Cayetano and Sisar faults (Fig. 4.11). The lower reaches of streams 12–18 are within the same Pliocene-Pleistocene sediments where values of k_{sn} of between 50–100 m are recorded to the west, along the western SSCF and the Ventura fault (Fig. 4.11). This observation is further evidence of a significant tectonic perturbation to channel steepness and relief because if channel steepness was controlled only by lithology, then streams 12–18 would have k_{sn} values for the lower reach similar to the k_{sn} values in streams to the west.

The non-lithological knickpoints identified in streams in the hanging wall of the San Cayetano fault can potentially provide insights into how changing tectonic conditions have affected patterns of relief and

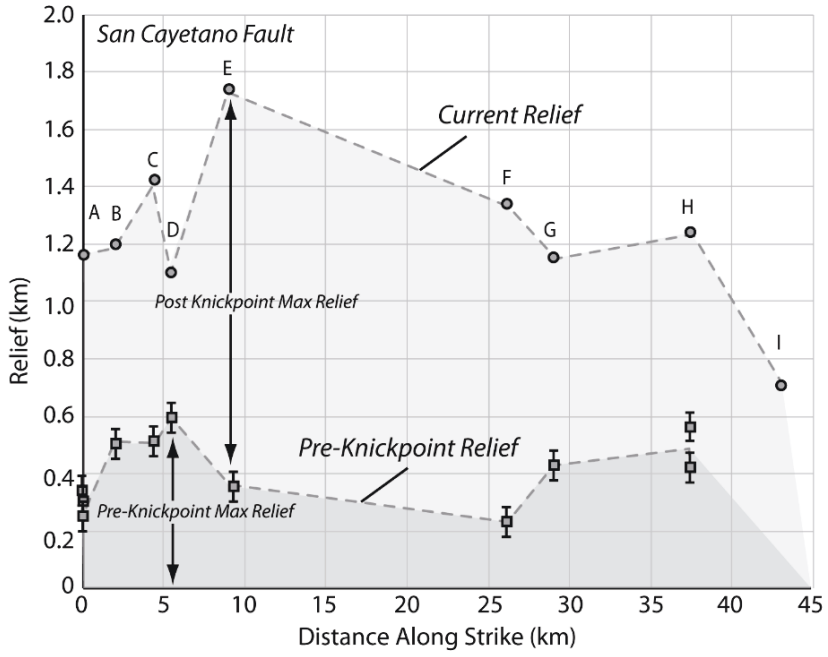

Figure 4.15 *Comparison of current catchment relief along strike of the San Cayetano fault with pre-existing relief prior to formation of the knickpoints. Pre-existing relief is calculated by subtracting the knickpoint height from the current relief. Uncertainties on pre-existing relief are based on +/- 50 m uncertainty assigned to knickpoint height. Letters refer to catchments in Table 4.5.*

k_{sn}. Non-lithological knickpoints develop in streams as a result of base-level change brought on by either a climatic or tectonic perturbation (Tucker and Whipple, 2002; Crosby and Whipple, 2006; Kirby and Whipple, 2012). Knickpoints formed by tectonic perturbations often result from an increase in fault slip rate, usually associated with fault linkage, as a river adjusts to the new boundary conditions imposed by the changing rate of fault motion (Boulton and Whittaker, 2009; Whittaker and Walker, 2015, Kent et al., 2017). In the case of the San Cayetano fault, the slip rates data in Figure 4.8 suggests a gradually decreasing fault slip rate since ~1.54 Ma, therefore, if the knickpoints in streams in the hanging wall of the San Cayetano fault did form in response to an increase in slip rate, it may well have occurred before ~1.54 Ma.

Insights into what may a have caused the increase in fault slip rates is provided in Figure 4.15, which is a plot of pre-knickpoint relief along strike of the San Cayetano fault calculated by subtracting the knickpoint height for the catchments from current maximum catchment relief. Previous workers have suggested that surface uplift related to the San Cayetano fault must have begun before ~3.3 Ma, based on the presence of diatoms dated at approximately 3.2–3.3 Ma in clasts of Miocene Modelo Formation recorded in turbidites near the base of the Pico Formation on the footwall of the San Cayetano fault in the Upper Ojai Valley (Rockwell, 1983). The presence of marine Modelo Formation clasts within the Pico Formation implies that the Modelo Formation must have been uplifted and eroded to the north of the present San Cayetano fault by at least 3.3 Ma as a result of activity on the San Cayetano fault (Rockwell, 1983). An interesting observation in Figure 4.15 is that there are two distinct peaks in the pattern of pre-knickpoint relief along strike with highest values recorded towards the eastern and western ends of current mapped trace of the San Cayetano fault, between 0–10 km and 25–40 km, respectively (Fig. 4.15). We suggest that the two peaks in pre-knickpoint relief represent surface uplift related to two separate faults; a proto-western San Cayetano fault between 0–10 km and a proto-eastern San Cayetano fault between 25–40 km (Fig. 4.15). We speculate that the increase in fault slip rate which generated the knickpoints was caused by fault linkage between what is now the ESCF and the WSCF to form one continuous fault at some point around or before 1.54 Ma.

A comparison of current catchment relief and pre-knickpoint relief along strike in the hanging wall of the San Cayetano fault indicates how fault slip has controlled relief generation since the formation of the knickpoints. In Figure 4.15, the catchment with maximum current relief (catchment E) may have been a local relief minimum at the time of knickpoint formation (Fig. 4.15a). Therefore, maximum post-knickpoint relief generation appears to have occurred along the WSCF (Fig. 4.15), where stratigraphic separation and late Pleistocene displacement rates are lowest (Fig. 4.12). We interpret this mismatch between relief and fault offset to be due to the presence of a blind fault in the footwall of the San Cayetano fault at depth (Chapter 3). We speculate that the blind fault may have propagated in the footwall of the San Cayetano fault around 0.95 Ma based on the pronounced decrease in slip rates for the San Cayetano fault observed around this time (Fig. 4.8a).

4.8 Conclusions

A multi-disciplinary geochronology and a detailed comparison between tectonic rock uplift and erosion signals allowed us to investigate the how spatial and temporal variability in tectonic forcing may control patterns of topographic relief development, channel morphology, and erosion rates in the Ventura basin, southern California. We calculated a basin-wide cosmogenic nuclide isochron burial dating geochronology for a key Quaternary strain marker, the Saugus Formation. The isochron burial ages demonstrate that both the top of the exposed Saugus Formation and the base of the underlying shallow marine equivalent increase in age systematically from west to east, with modal ages for the top and the base of $0.38\ ^{+.017}/_{-0.23} - 0.55\ ^{+0.08}/_{-0.10}$ Ma at Ventura, $0.95\ ^{+0.24}/_{-0.25} - 1.54\ ^{+0.11}/_{-0.10}$ Ma at Oak Ridge, and $\sim 2.49\ ^{+0.25}/_{0.29} - 3.30\ ^{+0.30}/_{-0.42}$ Ma in the eastern Ventura basin, respectively. Our burial ages indicate that the Saugus Formation in the eastern Ventura basin may be significantly older than previously thought.

The geochronology of the Saugus Formation was used in combination with fault offset amounts extracted from the published literature to re-evaluate fault displacement rates for several important active reverse faults, including the San Cayetano, Ventura, and Oak Ridge faults. Re-evaluated fault displacement rates were compared to ^{10}Be-derived basin-averaged erosion rates and show that erosion rates are generally significantly lower than rock uplift or fault throw rates in the Ventura basin. Additionally, we compared fault displacement rates and erosion rates with patterns of local relief

development, channel steepness, and an analysis of river long-profiles. The results indicate that catchments in Ventura basin are responding to fault activity but are yet to fully adjust to various tectonic perturbations. For example, catchments in the hanging wall of the Ventura fault and the Southern San Cayetano fault generally appear to be recording the tectonic uplift signal from before the onset of surface uplift related to the Ventura fault and the Southern San Cayetano fault at ~380 ka and ~58 ka, respectively. In the hanging wall of the San Cayetano fault, our data suggest that non-lithological knickpoints may have formed in streams at ~1.54 Ma or earlier due to an increase in fault slip rate resulting from fault linkage between what are now the eastern and western sections of the San Cayetano fault and that catchments in the hanging wall of the San Cayetano fault are still adjusting to the change in fault slip rate.

We also find that the highest values of local relief and channel steepness correspond to the oldest and most indurated lithological units, which implies that lithological distribution may have exerted a significant control on patterns of local relief generation and channel steepness. However, the distribution of bedrock lithological units in the Ventura basin is primarily controlled by tectonics. Therefore, we suggest on the local scale of catchments in the hanging wall of the San Cayetano, Ventura, and Southern San Cayetano faults, Quaternary fault activity and evolution has been the primary driver of Quaternary landscape evolution in the Ventura basin.

4.9 Acknowledgments

The authors thank C. Singer, R. Davey, and A. Seal for assistance in field work and sample collection. Work supported by funding from SCEC award numbers 15100 (to DHR and DDV), 17184 (to DHR), 16049 (to TKR), and 17024 (to TKR). The authors also acknowledge the financial support from the Australian Government for the Centre for Accelerator Science at the Australian Nuclear Science and Technology Organization (ANSTO) through the National Collaborative Research Infrastructure Strategy (NCRIS). This work was completed thanks to ANSTO award number 10125 (to DHR). Additional funding was supplied by a Royal Geological Society post-graduate research grant (to AH) and two post-graduate research grants from the British Society for Geomorphology (to AH). Corbett is

supported by a National Science Foundation EAR postdoctoral fellowship NSF-EAR-1735676 (to PRB).

Chapter 5: Discussion

This chapter will provide a discussion around some of the key findings from the research chapters in the context of the specific research questions in the Ventura basin and the broader research questions posed in Chapter 1. I first summarize the key research findings in section 5.1 before addressing the outstanding research questions in the Ventura basin, and the wider implications in terms of fault interaction and seismic hazard analysis.

5.1 Summary of key research findings

The research chapters presented in this thesis focus on the surface evidence and slip rate for the Southern San Cayetano fault (SSCF) (Chapter 2); the subsurface 3D geometry of the SSCF and stress interactions between the SSCF and neighbouring faults (Chapter 3); and how competing forces of tectonic uplift and erosion have controlled the Quaternary landscape evolution of the Ventura basin (Chapter 4).

- *Evidence for previously unconfirmed faults in the Ventura basin*

I have provided geological evidence to support the existence of two previously unconfirmed faults in the Ventura basin. In Chapter 2, I analysed high-resolution lidar data to characterize the surface expression of the SSCF based on fault scarps in Pleistocene and Holocene alluvial fans that cross the range front along the northern margin of the Ventura basin. The mapped trace of the SSCF potentially links the Ventura fault with the San Cayetano fault at the surface and creates an almost continuous ~150 km system of north-dipping faults along the northern margin of the Ventura basin, which may provide a pathway for large-magnitude multi-fault earthquakes (Chapter 2). I also suggested that an additional blind fault may be present in the footwall of the San Cayetano fault at some depth below ~5 km based on evidence from well data, microseismicity, and stratigraphic separation (Chapter 3; Fig. 3.9). I identified the presence of knickpoints in stream-profiles in the hanging wall of the San Cayetano fault, and I compared the position of the knickpoints relative to the San Cayetano fault surface trace to present day topographic relief development to suggest that significant relief (400–600m) was present in the hanging wall of the current San Cayetano fault before the knickpoints formed (Chapter 4; Fig. 4.13).

This pre-existing relief was compared to current relief to provide further evidence for the blind fault in the footwall of the San Cayetano fault (Chapter 4; Fig. 4.15). These observations indicate that blind faults have played a significant role in the evolution of the Ventura basin and could represent significant contemporary seismic hazards.

- *Spatial and temporal variations in patterns of deformation*

I calculated new estimates of slip rates for several major faults within the Ventura basin, over timescales of 10^3-10^6 years, to analyse spatial and temporal patterns of fault slip, strain accumulation, and stress distribution averaged over multiple earthquake cycles. I quantified fault offset across a suite of Pleistocene and Holocene alluvial surfaces (Chapter 2; Fig. 2.4) and calculated ages for this suite of terraces using ^{10}Be surface exposure dating of depth profiles (Chapter 2; Fig. 2.5). I calculated offsets of geomorphic surfaces of various ages across fault scarps resulting from flexural slip faults at Orcutt Canyon and used total offset on different timescales to identify a pattern of decreasing activity on the flexural slip faults since ~58 ka. I inferred that the decrease in activity of the flexural slip faults was linked to the initiation of activity on the SSCF at ~58 ka, which cut across the flexural slip faults (Chapter 2). I combined the offset amounts with the ^{10}Be geochronology to calculate slip rates for the SSCF since fault initiation at ~58 ka and showed that slip rates have been relatively constant over this period (Chapter 2; Fig. 2.6). Slip rates for the SSCF were compared with slip rates based on mechanical models and GPS data (Marshall et al., 2017), and demonstrate overlap with mechanical models that employ a mid-crustal ramp-flat geometry for the Pitas Point-Ventura fault (Chapter 2; Fig. 2.8). The ramp-flat geometry for the Pitas Point-Ventura fault implies a higher degree of subsurface structural connectivity and, consequently, a greater prospect of large-magnitude multi-fault earthquakes than a model where faults have constant dip to seismogenic depths.

The ^{10}Be surface geochronology was also combined with offsets and incision amounts for alluvial surfaces that cross the western San Cayetano fault (WSCF) in order to calculate rates and timing of Holocene and late Pleistocene activity on the WSCF (Chapter 4). In Chapter 3, I calculated static Coulomb stress change on the SSCF and the WSCF from ruptures on neighbouring faults. I compared the results of the stress modelling with the Holocene strain accumulation and geomorphic expression

of the faults to suggest that Holocene strain may have been focused on the SSCF rather than the upper WSCF and that Holocene earthquakes may propagate to the surface along the SSCF (Chapter 3; Fig. 3.8).

This thesis has also used cosmogenic isotope isochron burial dating to constrain the depositional age of the Saugus Formation. I used the resulting chronology to confirm that the Saugus Formation increases in age significantly from west to east (Chapter 4; Fig. 4.3) and to improve the slip rate estimates along strike of the Ventura basin. I combined the chronology of the Saugus Formation with published bedrock offsets for the San Cayetano, Ventura, and Oak Ridge faults to recalculate and refine existing fault slip rates (Chapter 4; Fig. 4.7, Table 4.3). I record a potential decrease in slip rate for the San Cayetano fault around 0.95 Ma (Chapter 4; Fig. 4.6). I speculate that the decrease in fault slip rates is indicative of a blind fault propagating in the footwall of the San Cayetano fault, which partitioned strain between the San Cayetano fault and a blind fault in the footwall.

The slip rates for the San Cayetano and Oak Ridge faults have been used by previous authors to compare patterns of regional long-term shortening with modern estimates from geodesy to assess contemporary strain accommodation (Donnellan et al., 1993a; Huftile and Yeats, 1995; Huftile and Yeats, 1996; Marshall et al., 2013; Marshall et al., 2017) and are included in regional seismic hazard assessments such as the Uniform California earthquake rupture forecast (UCERF 3) (Field et al., 2014; Field et al., 2015). The rates calculated here are based on a more robust geochronology (Chapter 4; Fig. 4.5) and are, therefore, a marked improvement on the previous estimates for these regionally important data. The above results also document temporal and spatial variations in slip rates for key faults in the Ventura basin, and indicate that deformation may have migrated over time from the San Cayetano fault in the east, to the Ventura fault in the west, potentially via the blind fault in the footwall. The evidence for this and the implications are discussed further in section 5.2.2 below.

- *Static stress transfer between reverse faults is highly sensitive to changes in fault geometry*

Previous models of static Coulomb stress transfer have generally applied planar faults in models of static Coulomb stress (e.g., King et al., 1994; Freed et al., 2007; Pace et al., 2014), which are not necessarily reasonable representations of true surface or subsurface fault geometry (Marshall et al.,

2008; Candela et al., 2011; Brodsky et al., 2016). The stress modelling I conducted here represents the first application of static Coulomb stress modelling where I attempted to recreate the three-dimensional complex geometry of faults based on field observations and subsurface data in the software *Coulomb 3.4* (Lin and Stein, 2004; Toda et al., 2005). Prior studies have established that patterns of modelled static stress change during earthquakes may be sensitive to both source and receiver fault down-dip geometry (Marshall and Morris, 2012; Mildon et al., 2016). The results presented here develop this theory because they provide the first case study of how fault geometry can influence patterns of modelled static Coulomb stress change on receiver when complex interacting faults are based on field observations and subsurface data (Chapter 3;). I used results from the stress modelling to demonstrate that static Coulomb stress transfer may partially facilitate multi-fault earthquakes if a ramp-flat model is adopted for the Pitas Point-Ventura fault, but that static Coulomb stress transfer is less significant contributor to the propagation of multi-fault earthquakes if the mid-crustal flat is not included (Chapter 3). These results imply that characterizing the deep structure of faults in the Ventura basin is essential to assess the prospects for multi-fault earthquakes (Chapter 3).

- *Catchment-averaged erosion rates in transient landscapes may not be reliable indicators of tectonic forcing*

I calculated ^{10}Be catchment-averaged erosion rates for catchments along strike of the hanging wall of the Ventura, San Cayetano, and SSCFs (Chapter 4). Current erosion rates are generally an order of magnitude lower than uplift rates, with the exception of the hanging wall of the eastern San Cayetano fault where erosion rates potentially overlap with uplift rates within uncertainties (Chapter 4). The difference between erosion rates and uplift rates, in combination with the presence of knickpoints in streams and the preservation of a large uplifted low-relief surface in the hanging wall of the San Cayetano fault, indicates a transient response to tectonic forcing (Chapter 4). The pattern of higher erosion rates for the ESCF compared to the WSCF (Chapter 4; Fig. 4.9) is similar to the pattern for uplift rates and stratigraphic separation which are both higher for the ESCF than the WSCF (Chapter 4; Fig. 4.12) and suggests that erosion rates may be effective for tracking tectonic uplift in the Ventura basin. However, in the hanging wall of the Ventura fault and the SSCF patterns of erosion rates show

no discernible pattern along-strike do not match patterns of relief and channel steepness indices, which both appear to be responding to the tectonic signal from the Lion Canyon, Sisar, and San Cayetano faults (Chapter 4; Fig. 4.11). Therefore, given short suggested timescales for activity on the Ventura (~380 ka) and SSCF (~58 ka) the erosion signal from catchments in the hanging wall of these faults may not have had sufficient time to fully adjust to the initiation of surface uplift related to the Ventura fault and the SSCF and the erosion signal in the fault hanging walls still reflects a component of activity on the Lion Canyon, Sisar, and San Cayetano faults. In summary, catchment averaged erosion rates in the Ventura basin appear to be good indicators of fault activity for older faults such as the San Cayetano fault but cannot necessarily be used to track rock uplift patterns in faults that have only been uplifting the surface for the past ~400 ka.

- *Fault evolution and interaction has controlled topographic relief development, channel morphology, and patterns of erosion in the Ventura basin*

By extracting hanging wall relief and channel steepness data from digital elevation models in the hanging wall of the Ventura, San Cayetano, and Southern San Cayetano faults, I was able to show that channel steepness is coupled to relief, and that variations in these two parameters appear to be controlled by lithology (Chapter 4; Fig. 4.10) and tectonics (Chapter 4; Fig. 4.11). However, relief generation and channel steepness in the hanging wall of the San Cayetano fault reach a maximum along the WSCF, whereas patterns of fault activity and erosion rates appear to reach a maximum along the ESCF (Chapter 4; Fig. 4.9 and 4.12). Furthermore, relief and channel steepness indices in the hanging wall of the Ventura and SSCFs have highest values in catchments which are intersected by the older and larger offset Lion Canyon, Sisar, and San Cayetano faults (Chapter 4; Fig. 4.11). Therefore, while relief and channel steepness for catchments in the study area do appear to be responding to tectonic forcing the transient response of the Ventura basin landscape to tectonic perturbations makes it difficult to attribute patterns of relief and channel steepness to individual faults.

I identified the presence of knickpoints in stream-profiles in the hanging wall of the San Cayetano fault and demonstrated that these knickpoints show a systematic relationship between upstream area and distance from the San Cayetano fault and, therefore, are likely to have a tectonic origin (Chapter 4; Fig.

4.14). Knickpoint height also shows a positive correlation with relief (Chapter 4; Fig. 4.14) and this correlation indicates that knickpoints are responding to the same signal as relief and channel steepness. Whereas it is not possible to attribute relief and channel steepness in isolation to the San Cayetano fault, the fact that the knickpoints show a systematic relationship with distance and area upstream from the fault indicates that relief, channel steepness, and knickpoint height may be responding in some way to tectonic forcing from the San Cayetano fault. I compared present day relief with knickpoint height to suggest that significant relief (400–600 m) was present in the hanging wall of the current San Cayetano fault before the knickpoints formed (Chapter 4; Fig. 4.15). I suggested that the pattern of relief development since knickpoint formation, with a maximum current value in what was a pre-knickpoint relief minimum, is further evidence for a blind fault in the footwall of the San Cayetano fault because this would explain the mismatch between was fault activity and relief development in the hanging wall of the San Cayetano fault (Chapter 4; Fig. 4.12). A comparison with fault slip rates suggests that propagation of the blind fault in the footwall of the San Cayetano fault may have cause an observed decrease in fault slip rates at 0.95 Ma, as strain became partitioned between the San Cayetano fault and the blind fault (Chapter 4; Fig. 4.8). I also hypothesize that knickpoints in the hanging wall of the San Cayetano fault may have formed as a result of fault linkage between what is now the western and eastern sections of the San Cayetano fault, at some point before 1.54 Ma (Chapter 4; Fig. 4.15).

5.2 Discussion of key research questions

The seismic hazard within tectonically active, earthquake-prone areas is often a result of the complex interaction of several faults (Field, 2005; Field et al., 2014; Field et al., 2015; Langridge et al., 2016). In many cases, devastating earthquakes occur on faults that are either blind or for which were unknown prior to the event (Shaw and Suppe, 1996; Beavan et al., 2011; Beavan et al., 2012; Li et al., 2014; Lu et al., 2016) and in many cases the slip rate and subsurface geometry of mapped faults are frequently not well characterized. As a result, even in well-studied areas such as the San Andreas fault and the eastern California shear zone (e.g., Dolan et al., 2007; Frankel et al., 2007a; Ganev et al., 2010; Rood et al., 2011b; Ganev et al., 2012; McAuliffe et al., 2013; Dolan et al., 2016) data are often lacking for a rigorous assessment of seismic hazards or to study how fault interaction affects spatial and temporal

patterns of deformation and landscape evolution. In this study, I focused on the Ventura basin to address some of these issues and improve the understanding of seismic hazards in this densely populated area of southern California.

5.2.1 To what extent do unidentified faults and blind faults inhibit accurate analysis of seismic hazard and what role do smaller faults play in stress transfer during multi-fault earthquakes?

In addressing the broad questions above I specifically focused on the SSCF to address the question for Chapter 1: **What field evidence is there for the proposed existence of the SSCF, are there any other unidentified faults in the Ventura Basin, and could the SSCF provide a pathway for potential large-magnitude multi-fault ruptures?**

Previously unrecognized faults or blind faults have been suggested as the seismic source for several recent moderately sized but damaging earthquakes. For example, the 2015 M_w 6.5 Pishan earthquake, China (Lu et al., 2016), and the 2011 M_w 6.2 Christchurch earthquake, New Zealand (Beavan et al., 2011; Beavan et al., 2012) were both recent destructive earthquakes that occurred on faults that were not known prior to the earthquake occurrence. Furthermore, both the Papatea fault and the Point Kean fault are previously unidentified faults which played role in transferring stress between other larger well-established faults during the 2017 M_w 7.8 Kaikōura earthquake (Clark et al., 2017; Hamling et al., 2017).

The SSCF was first proposed as either the eastward continuation of the Ventura fault, with a 45–55° dip from the shallow subsurface down to ~7 km where the fault flattens out onto a horizontal detachment surface, or an eastward extension of the south-dipping Sisar fault (Hubbard et al., 2014). However, no geological field data were provided in the Hubbard et al., (2014) study to confirm the existence of either possible interpretation. The scarps identified in Holocene and Pleistocene alluvial fans along the range front in Chapter 2 provide surface evidence for a north-dipping SSCF and indicates that the SSCF is active in the Holocene with a slip rate of $1.3\ ^{+0.5}/_{-0.3}$ mm yr^{-1} (Chapter 2). Furthermore, the investigation of the well-log data in Chapter 3 confirms that the SSCF is a north-dipping low-angle thrust fault that connects with the WSCF at a depth between 1.5–3.5 km (Chapter 3; Fig. 3.5). While the 3D geometry

for the SSCF presented in Chapter 3 is different from the proposed SSCF geometry of Hubbard et al., (2014), I present compelling evidence for the presence of a previously unconfirmed, seismically active, partially blind fault in an urbanized area of southern California.

In addition to the low-angle SSCF, I present well-log data, microseismicity, and stratigraphic separation data to argue for the presence of a blind fault located below a depth of ~5 km in the footwall of the San Cayetano fault (Chapter 3; Fig 3.10). Further evidence for this blind fault is provided in Chapter 4, because maximum post-knickpoint relief has been generated above the WSCF, where the lowest values of stratigraphic separation are observed (Chapter 4; Fig. 4.12 and 4.15). This blind fault may well be the north-dipping model of the SSCF originally proposed by Hubbard et al., (2014). Blind faults have been the source for damaging earthquakes just east of the Ventura basin beneath the San Fernando Valley, such as the 1994 Northridge earthquake (Tsutsumi and Yeats, 1999), and coseismic blind faults such as the Compton thrust are thought to represent a significant seismic hazard just south of the study area beneath the Los Angeles basin (Shaw and Suppe, 1996). All of the above demonstrates that blind faults may represent a significant poorly-quantified seismic hazard in the Ventura basin, particularly given that both the SSCF and a potential blind fault at depth may play a role in stress transfer during proposed large-magnitude multi-fault earthquakes (Section 5.2.3).

The propagation of the SSCF and potentially the blind fault, in the footwall of the main San Cayetano fault, provide an excellent field example of how the evolution of thrust fault system can alter the rupture hazard associated with well-established faults such as the San Cayetano fault (Chapters 2 and 3). Furthermore, the presence of well-developed fault scarps in Holocene surfaces associated with the SSCF compared to a lack of geomorphic evidence for activity on the uplifted central section of the main San Cayetano fault (Chapter 3, Figure 3.9), supports modelling studies of dynamic rupture propagation that suggest earthquake ruptures traveling up-dip from depth may preferentially propagate along low-angle faults compared to high angle faults (Ryan et al., 2015). When combined, the above findings add to the ongoing body of research on how small offset faults and blind faults can potentially alter the earthquake rupture hazards associated with well-established faults in complex tectonic systems with

multiple interacting faults (Fletcher et al., 2014; Fletcher et al., 2016; Clark et al., 2017; Hamling et al., 2017).

5.2.2 What evidence is there for proposed subsurface connectivity for faults in the Ventura basin, and can we use data from fault slip rates, erosion rates, or geomorphology to provide insights into subsurface fault connectivity and fault evolution?

Table 5.1 *Slip rates in the Ventura basin*

Fault	GPS Mechanical model rate: Ramp-flat) (mm yr^{-1})*	GPS Mechanical model rate: No-flat (mm yr^{-1})*	UCERF 3 Best estimate rate (mm yr^{-1})	Geomorphic rate: ~$10^{4–5}$ years (mm yr^{-1})	Geologic rate ~10^{6} years (mm yr^{-1})
North Dip					
San Cayetano (East)	5.4 +/- 2.1	3.8 +/- 1.3	6.0	n/c	3.9 +3.5/-2.0
San Cayetano (West)	5.4 +/- 2.1	3.8 +/- 1.3	6.0	1.8 +0.8/-0.5	3.9 +3.5/-2.0
Southern San Cayetano	2.6[+]	n/c	n/c	1.3–1.9	n/a
Ventura	3.5 +/- 3.3	2.6 +/- 1.1	1.6	4.4–6.9[a]	n/c
Pitas Point	n/a	0.5 +/- 0.8	1.6	2.3 +/- 0.3[b]	n/c
Red Mountain	1.6 +/- 0.7	6.5 +/- 1.7	2.0	n/c	n/c[++]
South Dip					
Sisar/Lion Canyon	1.6 +/- 0.6	0.6 +/- 0.7	0.4	n/a	n/c
Padre Juan	n/a	n/a	n/a	n/a	8.0[d]
Arroyo Parida	1.9 +/- 1.0	1.6 +/- 1.0	0.9	0.34 +/- 0.2[c]	n/c
Oak Ridge	3.1 +/- 1.0	4.5 +/- 1.5	3.0	n/c	2.0 +1.0/-0.6

**Mechanical model rates apply over decadal timescales. 'Ramp-flat' rates are from Marshall et al., (2017); 'No-flat' rates are from Marshall et al., (2013)*
[+]The slip rate for the Southern San Cayetano fault is not explicitly stated in the results but the rate is extracted from the Figure 3 of Marshall et al., (2017)
[++]I refer to approximate dip slip separation of the Red Mountain fault in the text but no slip rate is available because the sediments in the footwall run parallel to the fault so the precise amount of slip is not known (Yeats et al., 1977)
n/c = No rate calculated in this study or the literature (that I am aware of); n/a = not applicable
Geomorphic and geologic rates are from this study apart from a: Hubbard et al., (2014); b: Johnson et al., (2017); c: Rockwell et al., (1984); d: Nicholson et al., (2017)

One of the aims of this project outlined in Chapter 1 is to provide insights into the potential structural connectivity of faults within the Ventura basin because this has implications for the potential nucleation and propagation of large-magnitude earthquakes and seismic hazards (Chapter 1). The significance of the characterizing the deep structure of faults was highlighted further in Chapter 3, where the deep structure of faults has implications for the patterns of static stress transfer in potential multi-fault ruptures. By investigating the potential deep connectivity of faults, I also investigate wider questions from Chapter 1 such as: **To what degree are patterns of deformation over multiple earthquakes cycles variable in time and spaces and how do any potential variations impact our interpretation of seismic hazards?**

Recent studies argue that the Pitas Point, Ventura, Red Mountain, Lion Canyon, Southern San Cayetano, and San Cayetano faults are all connected at depth on some form of mid-crustal thrust ramp between 7–10 km depth (Hubbard et al., 2014; Marshall et al., 2017; Levy et al., in review). The existence of the mid-crustal thrust ramp is based on integrating data from surface geological maps and offshore seismic data in the upper ~5 km in kinematic structural modelling (Hubbard et al., 2014; Levy et al., in review). Geodetic studies indicate that that maximum surface uplift in the Western Transverse Ranges occurs ~20 km north of the Pitas Point, Ventura, and San Cayetano faults and maximum uplift in this location is predicted by geodetic models that include a mid-crustal thrust ramp (Marshall et al., 2017; Hammond et al., 2018). When faults are modelled without the mid-crustal thrust ramp, maximum uplift occurs 15 km south of where maximum uplift is observed in GPS data (Marshall et al., 2017). Hence, independent geodetic studies support a structural model which includes a mid-crustal thrust ramp.

In contrast, other workers have questioned the existence of the mid-crustal thrust ramp based on patterns of microseismicity at depth and the suggestion that subsurface structural connectivity is limited because some of the north-dipping faults are back-thrusts off south-dipping structures (Nicholson et al., 2017b). For example, the Ventura fault is suggested to be a back thrust off the Padre Juan and Lion Canyon faults, which are both suggested to be listric faults with south-dip (Yeats et al., 1988; Redin et al., 2005; Nicholson et al., 2017b). The Padre Juan fault has 2.8 km of dip-slip separation (Grigsby, 1986) and

the Lion Canyon fault has ~900 m of dip-slip separation (Huftile, 1988). Conversely, both the Pitas Point fault and the Ventura fault have maximum 250 m dip slip separation in the upper ~5 km recognized in seismic and well log data (Redin et al., 2005; Hubbard et al., 2014), although, the amount of slip on these faults is thought to increase with depth (Hubbard et al., 2014; Nicholson et al., 2017b).

The greater amount of dip-slip separation on the south-dipping faults in the upper 5 km is consistent with the suggestion that the Ventura fault could be a back thrust. However, my mapping of late Quaternary alluvial surfaces suggests that the Lion Canyon and Sisar faults (the Sisar fault is the eastward continuation of the Lion Canyon fault) do not offset any late Pleistocene or Holocene alluvial surfaces, whereas the San Cayetano fault and the SSCF both create scarps in Holocene surfaces (Chapter 2). The Ventura fault also has pronounced geomorphic expression in the form of a continuous fold scarp that runs through the city of Ventura (Sarna-Wojcicki, 1976; McAuliffe et al., 2015). Furthermore, wherever the south-dipping Lion Canyon or Sisar faults intersect the north-dipping San Cayetano fault or the SSCF, the south-dipping faults are overridden by the north-dipping faults (Chapter 3: Figs. 3.4, 3.5). This same pattern is observed offshore in 3D seismic data where the Pitas Point fault clearly offsets the Padre Juan fault by ~200 m (Nicholson et al., 2017b). At no point along the northern Ventura basin is there any evidence that a south-dipping fault offsets a north-dipping fault.

The observations in the above paragraph are not consistent with the Ventura fault being a back thrust. The large dip-slip separation, but limited geomorphic expression, on the south-dipping faults compared to the relatively small dip-slip separation, but pronounced geomorphic expression, on the north-dipping faults may instead be indicative of a switch from predominantly north-verging deformation to predominantly south-verging structures in the area around what is now Pitas Point at some point during the late Quaternary. This switch probably occurred after ~380 ka, which is the burial age for the top of the Saugus Formation at Ventura (Chapter 4) and is thought to represent the oldest age for folding of the Ventura Avenue anticline (Rockwell et al., 1988; Hubbard et al., 2014). The relatively small stratigraphic offset in the upper few kilometres for the Ventura and the Pitas Point faults can, therefore, be explained because these faults have only been propagating to the surface since at most ~380 ka. The implication is that the south-dipping faults do not appear to decrease fault connectivity between the

Pitas Point, Ventura, Southern San Cayetano, and San Cayetano faults. However, just because there is a continuous system of north-dipping faults does not necessarily mean that these faults are connected at depth. Further insights into the Quaternary structural evolution of the Ventura basin can therefore be gained from a comparison of fault slip rates in space and time.

In Chapter 1, I state that comparing fault slip rates on various time scales and comparing this data with data from geodesy is a common approach for assessment of patterns of strain accumulation in space and time. In Table 5.1, I present slip rate data from forward mechanical models based on geodetic data for all faults mapped along the northern margin of the Ventura basin and pertinent to this study (Marshall et al., 2013; Marshall et al., 2017). Table 5.1 also includes slip rates from geomorphic features and slip rates from geology (Chapter 2 and 4) and slip rates from the Uniform California earthquake rupture forecast (UCERF 3) report, an independent compilation and evaluation of all fault slip rates in California (Field et al., 2014).

A comparison of the rates in Table 5.1 was used by Marshall et al., (2017) in part to argue that a ramp-flat geometry for the Pitas Point-Ventura fault is more likely because slip rates for the Red Mountain and San Cayetano faults show better agreement with rates from the UCERF report than slip rates from forward models that do not incorporate a ramp-flat geometry (Marshall et al., 2017). I have not addressed the slip rates for the Red Mountain fault in this study, but the slip rates I calculated for the SSCF in Chapter 2 have better agreement with mechanical model-based rates from the 'ramp-flat' model (Chapter 2; Fig. 2.8). In contrast, the rates I calculated for the WSCF at Bear Canyon show better agreement with the 'no-flat' models (Table 5.1). However, my rates from the offset surface at Bear Canyon are towards the western end of the fault and may not record maximum slip on the WSCF. Regardless, the primary evidence from geodesy to argue in favour for a 'ramp-flat' geometry is the better match of model-derived rock uplift patterns to the north of the Pitas Point-Ventura fault for the 'ramp-flat' model compared to model-derived rock uplift for the 'no-flat' model (Marshall et al., 2017; Hammond et al., 2018).

The most significant broad trend in Table 5.1 is that the north-dipping faults have generally higher slip rates from both mechanical models and from geomorphic and geologic offsets. Generally higher slip

rates for the north-dipping faults suggest that these are the structures that are currently accommodating more strain compared to the south-dipping faults. The only exception is the blind south-dipping Padre Juan fault, which has a high proposed slip rate of ~8 mm yr^{-1} (Nicholson et al., 2017b). However, the slip rate for the Padre Juan fault assumes that all folding of the San Miguelito anticline in the hanging wall of the Padre Juan fault, and therefore slip on the Padre Juan fault, is post-Saugus Formation deposition and that the top of the Saugus Formation at Ventura is ~250 ka (Grigsby, 1986; Nicholson et al., 2017b). My burial age for the top Saugus at Ventura of 380 $^{+170}/_{-230}$ ka indicates that an age of 250 ka may be too young (Chapter 4). More significantly, the youngest strata folded by the San Miguelito anticline are the Pico Formation, and there is no evidence in cross sections or subsurface data that all folding of the San Miguelito anticline in the hanging wall of the Padre Juan fault at Pitas Point is entirely post-Saugus Formation in age (Grigsby, 1986; Redin et al., 2005). My isochron burial age for the base of the Las Posas Formation (roughly equivalent to the top of the Pico Formation) indicates that this horizon is at least 550 $^{+80}/_{-100}$ ka (Chapter 4). Consequently, existing data only prove that slip on the Padre Juan fault initiated at some point after ~550 ka and a slip rate of 8 mm yr^{-1} for the Padre Juan fault is probably too high.

Another important observation from the slip rates in Table 5.1 is that the slip rate for the Ventura fault from both geomorphic offsets (4.4–6.9 mm yr^{-1}) and from mechanical models (2.6–3.5 mm yr^{-1}) are higher than the Red Mountain fault (~2.0 mm yr^{-1}). The rate of 6.5 mm yr^{-1} from mechanical models using the 'no-flat' model for the Red Mountain fault is considered unrealistic because the fault has a limited geomorphic expression (i.e. no topographic fault scarps) and is therefore unlikely to be accommodating such a large proportion of contemporary strain (Marshall et al., 2017). In contrast, the Ventura fault has pronounced geomorphic expression (Chapter 2). However, the Red Mountain fault does have significant Quaternary dip-slip separation of ~7.5 km, which indicates that the Red Mountain fault has accommodated significant strain during the Quaternary (Yeats et al., 1977). When combined, the observation of high slip rates and pronounced geomorphic expression for the Ventura fault, compared to large dip-slip separation but relatively lower slip rates and limited geomorphic expression for the Red Mountain fault, point to a southward propagation of a north-dipping thrust front. This

southward propagation probably occurred after folding of the Ventura Avenue anticline commenced after ~380 ka (burial age for the Saugus Formation at Ventura; Chapter 4). A southward propagation in strain accumulation is also recorded in Chapters 2 and 3 by the propagation of the SSCF, and potentially the blind fault, in the footwall of the San Cayetano fault at 0.95 Ma (Chapter 4).

In addition to a southward propagation of the location of maximum strain accommodation, slip rates for the north-dipping faults also decrease westwards with the highest rates recorded onshore on the San Cayetano and Ventura faults and the lowest rates recorded offshore on the Pitas Point and Red Mountain faults (Table 5.1). This is highlighted by the Pitas Point fault which decreases in slip rates westward from 2.3 mm yr^{-1} at Pitas Point (Johnson et al., 2017) and becomes blind at increasing depth below the surface westward from 200 m below Pitas Point to a depth of ~2 km west of Santa Barbara (Sorlien and Nicholson, 2015).

The discussion in this section highlights a picture of southward strain migration and a decrease in strain accommodation westward. Such a pattern is consistent with southward propagating fold and thrust belt (Jordan et al., 1993; DeCelles et al., 2001; Alavi, 2004; Brandes and Tanner, 2014) and implies a high-degree of structural connectivity at depth as suggested by the 'ramp-flat' model. It is not clear why such strain migration would be observed if the faults were not connected at depth, as suggested by the 'no-flat' model because there is no continuous surface on which a systemic pattern of strain migration would develop. The suggestion of a southward propagation thrust front was first suggested by Rockwell (1983) and is supported by recent kinematic structural modelling (Levy et al., in review). Proposed structural connectivity at depth for faults in the Ventura basin has implications for the prospect of large-magnitude, multi-fault earthquakes in the Ventura basin and this is discussed in more detail in section 5.2.3 below. Furthermore, the discussion in the preceding paragraphs backs up the findings in section 5.2.1 and adds to a growing body of literature that describes how the ground motion or rupture hazards large-subsurface stratigraphic separation may be controlled or altered by interaction with younger, small offset faults.

5.2.3 How likely are proposed multi-fault earthquakes in the Ventura basin?

One of the main goals for this project set out in Chapter 1 was to investigate the potential for large-magnitude (M_w 7.5–~8) multi-fault earthquakes in the Ventura basin, and to explore the role the proposed SSCF could play in these proposed events. The distance a rupture can propagate along a fault or fault system, and hence the potential magnitude of the earthquake a fault can produce, is partly dependent upon the amount of segmentation along a fault system and the size of the steps between segments (Wesnousky, 2006; Oglesby, 2008; Wesnousky and Biasi, 2011; Lozos et al., 2012; Manighetti et al., 2015; Biasi and Wesnousky, 2016). Chapters 2 and 3 characterized the surface expression and subsurface 3D geometry of the SSCF and the degree of connectivity with surrounding faults. A first order observation is that the mapped surface trace for the SSCF appears to connect the Pitas Point-Ventura fault with the San Cayetano fault and create a continuous ~150 km long system of north-dipping faults (Chapter 2; Fig. 2.1). The discussion in the preceding section suggests that a 'ramp-flat' geometry may be more likely from the Pitas Point-Ventura fault (section 5.3). The ramp-flat geometry for the Pitas Point-Ventura fault implies a high degree of subsurface structural connectivity and, consequently, a greater prospect of large-magnitude multi-fault earthquakes compared to when the flat is not included in the Pitas Point-Ventura fault.

Further investigation, however, indicates the degree of subsurface connectivity in the upper 5 km between the Ventura and SSCF may be limited. The well investigation in Chapter 3 indicates that the SSCF is a low-angle thrust which dips ~15° north and connects with the San Cayetano fault in the subsurface at a maximum depth of around 3.5 km (Chapter 3; Fig. 3.5). The Ventura fault is characterized from well data and 2D onshore seismic data to dip 45–55° north (Hubbard et al., 2014). The geometry for the SSCF used to calculate mechanical model slip rates from GPS data assumed that the SSCF was hard-linked to the Ventura fault (Marshall et al., 2017). Despite an apparent surface connection between the Ventura fault and the SSCF outlined in Chapter 2, the subsurface well investigation does not provide evidence that the SSCF and the Ventura fault are hard-linked in the shallow subsurface. In Chapter 2, I suggested that a tear fault is present between the Ventura fault and the SSCF. Unfortunately, there are insufficient wells drilled in proximity to the proposed tear fault (n =

3) to investigate the potential existence of the tear fault using subsurface data (Chapter 3; Fig. 3.2). Given a pronounced change in dip eastwards between the Ventura fault and the SSCF, and in the absence of confirmed hard linkage between the Ventura fault and the SSCF in the subsurface, there is no obvious continuous pathway for rupture propagation to the surface between the Ventura fault and the San Cayetano fault, via the SSCF, unless the faults are all connected at depth below well control.

However, even when faults are not hard-linked in the shallow subsurface, dynamic rupture models (Oglesby, 2008; Lozos et al., 2012), empirical studies (Biasi and Wesnousky, 2016; Biasi and Wesnousky, 2017), and observed multi-fault earthquakes (Fletcher et al., 2014; Hamling et al., 2017) indicate that ruptures can re-nucleate across fault segment boundaries. At their minimum divergence near the surface the Ventura fault and the SSCF are ~3 km apart, and at their maximum divergence in the subsurface the Ventura fault and the SSCF are ~8 km apart (depending on whether the 'flat' or 'no flat' models are adopted) (Chapter 2; Fig. 3.1). Empirical studies have shown that ruptures on dip-slip faults with M_w > ~7.0 can cross stepovers as large as 10 km (Biasi and Wesnousky, 2016) and the recent M_w 7.8 Kaikōura earthquake in New Zealand suggested synchronous rupture on faults spaced up to 15 km apart within a multi-fault reverse and strike-slip earthquake (Hamling et al., 2017).

In Chapter 3, I presented data which suggests that maximum M_w for rupture of the entire Pitas Point/Ventura fault based on fault area scaling relationships would be M_w 7.5 (Chapter 3; Table 3.1). Accordingly, even a partial rupture of the Pitas Point-Ventura fault would be capable of producing a rupture with magnitude large enough (i.e. M_w >7.0) to theoretically rupture the stepover between the Ventura fault and the SSCF. This suggests that even in the absence of hard-linkage between the Ventura fault and the SSCF in the shallow subsurface, a multi-segment rupture between the Ventura fault and the SSCF may still be possible if the rupture nucleated at depth on some form of mid-crustal thrust ramp.

The modelling in Chapter 3 showed that the prospect of triggered seismicity on the SSCF and the WSCF due to static Coulomb stress change induced by ruptures on the Ventura and Pitas Point faults could depend on the location along-strike that the initial rupture occurs (Chapter 3). The same argument could also be made for the prospect of dynamic rupture propagation. Although the Pitas Point fault is almost

always described as the offshore extension of the Ventura fault (Sarna-Wojcicki, 1976; e.g. Hubbard et al., 2014; McAuliffe et al., 2015; Sorlien and Nicholson, 2015; Rockwell et al., 2016; Nicholson et al., 2017b), there is a bend in the fault trace from east-west to slightly southeast-northwest around Pitas Point, where the Pitas Point fault is thought to link with the Ventura fault (Chapter 3, Fig. 3.1). The subtle change in fault strike is the reason that modelled static stress decreases on the Ventura fault when ruptures are simulated on the Pitas Point fault in the 'no-flat' models (Chapter 3; Fig. 3.7). This indicates that the transition from the offshore Pitas Point fault to the onshore Ventura fault may be a segment boundary in the upper ~5 km, rather than one continuous fault (Sorlien and Nicholson, 2015).

Empirical modelling demonstrates that strike-slip or dip-slip ruptures rarely cross more than four stepovers and ruptures that do cross multiple stepovers are rare (Wesnousky, 2006; Wesnousky and Biasi, 2011; Biasi and Wesnousky, 2016). This is important because a dynamic rupture of the complete Pitas Point, Ventura, San Cayetano, and SSCF system would require that it crossed three separate segment boundaries. Consequently, while rupture propagation between the Pitas Point, Ventura, San Cayetano faults via the SSCFs is theoretically possible, events of this nature may be rare. The above observations are consistent with my suggestion in Chapter 2 that the SSCF is a rupture pathway that is predominantly, but not exclusively, active during through-going ruptures between the San Cayetano and Ventura faults. The implication is that only the larger (M_w >7.0) infrequent events that nucleate on the Pitas Point and/or Ventura faults also rupture the SSCF and the San Cayetano fault.

The primary lines of evidence for the occurrence of multi-fault earthquakes between the Pitas Point, Ventura, Southern San Cayetano, and San Cayetano faults comes from large coseismic slip events inferred from paleoseismic data. At Pitas Point, four 8–12 m uplift events are proposed from analysis of uplifted marine terraces since ~7 ka with the most recent event at ~950 years ago (Rockwell et al., 2016). At Ventura, two 5–6 m uplift events are suggested in the last 4 ka from stratigraphic analysis of the Ventura fault scarp, with the most recent event between 236–805 years ago (McAuliffe et al., 2015). Paleoseismic trenching on the ESCF at Piru revealed evidence for one 4–5 m uplift event during the period AD 1660–1813 (Dolan and Rockwell, 2001). This event could overlap in time with the youngest event recorded at Ventura data at 236–805 years ago, but assuming that the youngest event at Ventura

is the same event as the event recorded on the ESCF would mean that three large uplift events recorded at Pitas Point are not recorded at Ventura just ~15 km to the east. It is also worth noting that no tsunami deposits are record during a sedimentological investigation at Carpinteria, ~20 km west of Ventura, which would surely be associated with the occurrence of a M_w 7.5–8.0 earthquake in the offshore Santa Barbara channel (Reynolds, 2018).

Regardless of the precise timing of the events, there is a large degree of uncertainty associated with correlating the large (~5–12 m) paleoseismic uplift events for the Pitas Point, Ventura, and ESCF, which are key pieces of geological evidence for the occurrence of large-magnitude, multi-fault earthquakes within the Ventura basin. The uplift events at Pitas Point suggest that a ≥9 m uplift event has occurred at intervals of 1100–2300 years for the last 6.7 ka (Rockwell et al., 2016). Proposed intervals of this length further support the idea that if large-magnitude, multi-fault earthquakes do occur in the Ventura basin, they are infrequent. In summary, I outlined in section 5.2.2 that there are several lines of evidence from fault slip rates, geodesy, and geomorphology to argue in favour for a mid-crustal thrust ramp beneath the Ventura basin, which implies a high-degree of subsurface structural connectivity that and can, in theory, provide a pathway for large-magnitude (M_w 7.5–8.0) multi-fault earthquakes. However, the discussion in this section indicates that such events may well be rare given the large amount of segmentation in the upper ~5 km and difficulties correlating large uplift events identified at Pitas Point with events at Ventura and on the ESCF. Therefore, while the deep subsurface structure of faults in the Ventura basin may well provide a potential pathway for large-magnitude multi-fault earthquakes, the evidence that these events have occurred in the past remains unclear. One key piece of missing data to investigate the occurrence of suggested large-magnitude multi-fault earthquakes onshore between the Ventura, San Cayetano and SSCFs is paleoseismic data from the fault scarps on the SSCF and the WSCF.

5.3 Future work

In this final section I will discuss potential avenues for future work that would develop the ideas presented in this thesis and provide further insights into some of the questions investigated here.

5.3.1 Paleoseismic trenching of the SSCF and the WSCF

As I stated at the end of section 5.2.2, the key piece of missing data that may confirm whether multi-fault earthquakes have occurred on the Pitas Point, Ventura, San Cayetano, and SSCF is paleoseismic data for the SSCF and the WSCF. The ideal locations in which to excavate potential paleoseismic trenches are along the scarp in the Q4 alluvial fan at the mouth of Orcutt Canyon along the SSCF and along the scarp in the Bear Canyon fan on the WSCF (Chapter 2). The depth profile age of ~7.3 ka provides a maximum age for the fan surfaces (Chapter 2), but radiocarbon samples could be taken to date potential individual earthquake events if the scarps are multi-event scarps.

I would use paleoseismic data from the trench in the SSCF to:

a) Confirm that the SSCF is present beneath the scarp at Orcutt Canyon as suggested in Chapter 2 and whether the SSCF is emergent or blind at Orcutt Canyon;
b) Confirm the dip of the fault at the surface, which would help to reduce one of the major uncertainties in the inputs to my Monte Carlo simulations i.e. the fault dip;
c) Use radiocarbon dates to calculate potential recurrence intervals for the SSCF and examine the position of the fault in the seismic cycle; and
d) Attempt to match events recorded in the trench with either events on the Ventura fault or the ESCF, which would help investigate the question of whether these faults rupture synchronously.

I would use the data from the WSCF to:

a) Compare the timing of earthquakes on the WSCF with the late Holocene event on the ESCF (Dolan and Rockwell, 2001) to investigate whether the differences in geomorphic expression and stratigraphic separation between the ESCF and the WSCF (Chapter 3) indicate that the San Cayetano fault does not always rupture over its entire length;
b) Use radiocarbon samples to date past events on the WSCF and calculate a recurrence interval, which again could be used to ascertain the position of the WSCF in its seismic cycle; and
c) Compare the timing of events from the WSCF with potential data from the SSCF and the existing data on the Pitas Point (Rockwell et al., 2016) and Ventura faults (McAuliffe et al., 2015) to assess the timing of events between these faults and the potential for synchronous multi-fault earthquakes.

5.3.2 Refining the geochronology of the Saugus Formation

The geochronology for the Saugus Formation was used in this study to calculate fault slip rates for the San Cayetano and the Oak Ridge faults, and to calculate uplift rates in the hanging wall of the Ventura fault (Chapter 4). However, the age for the top of the Saugus Formation at Ventura of 0.38 $^{0.17}/_{-0.23}$ Ma has large associated uncertainty and consequently the uplift rates for the Ventura fault associated with this age of 7.0 $^{+11.9}/_{-2.5}$ mm yr^{-1} also have large associated uncertainty (Chapter 4). The reason for the large uncertainty in the age is that the Saugus Formation at Ventura is at the lower limit of the age range for isochron burial dating with the ^{26}Al-^{10}Be nuclide pair (Chapter 4) given the respective half-lives of ^{26}Al and ^{10}Be of 0.71 Ma and 1.36 Ma (Chapter 1). However, ^{36}Cl is produced in Ca- and K-bearing rocks and minerals and has a half-life of 0.30 Ma (Bentley et al., 1986). Because the half-life of ^{36}Cl is shorter than the half-life of ^{26}Al, the lower-limit in the burial age range of dateable sediments can, in theory, be decreased by constructing a ^{36}Cl-^{10}Be isochron. The Saugus Formation at Ventura would be an ideal location to test the feasibility of the ^{36}Cl-^{10}Be nuclide pair because sediment is sourced from the San Gabriel Mountains, which are primarily igneous and metamorphic rocks that should contain abundant co-existing quartz (for ^{10}Be) and feldspar (for ^{36}Cl). Furthermore, I have already dated the Saugus Formation at Ventura with the ^{26}Al-^{10}Be nuclide pair, which would serve as validation for the results from the ^{36}Cl-^{10}Be nuclide pair. Development of the ^{36}Cl-^{10}Be nuclide pair would not only decrease uncertainty in the age of the Saugus Formation at Ventura but would provide a valuable tool to date late Pleistocene sediments in many other geologic settings and geographic locations.

In Chapter 4, my isochron burial ages of 2.49 $^{+0.25}/_{0.29}$ Ma for the top and 3.30 $^{+0.30}/_{-0.42}$ Ma for the base of the Saugus Formation are considerably older than the previously published age of 0.5–2.3 Ma based on magnetostratigraphy and tephrochronology (Levi and Yeats, 1993). Further work should focus on collecting paleomagnetic transects in proximity to the locations of the isochron burial samples. I would compare the polarity of the resulting magnetic transect to the existing record of paleomagnetic reversals to evaluate whether the isochron burial ages agree with the chronology suggested by paleomagnetic reversals. This would either validate the burial age chronology in the eastern Ventura basin or indicate

that further work is needed to understand why the burial ages are not consistent with the previously published age.

Chapter 6: Conclusions

In this conclusion chapter I briefly summarize the findings of the three main research chapters. In Chapter 2, I attempted to address the question **to what extent do unidentified faults and blind faults inhibit accurate analysis of seismic hazard and what role do structurally immature faults play in stress transfer during multi-fault earthquakes?** To investigate this question I: i) used high-resolution lidar data to identify fault scarps along the trace of the Southern San Cayetano fault (SSCF); ii) employed cosmogenic nuclide exposure dating with depth profiles to produce a late Quaternary ^{10}Be geochronology for alluvial fans and river terraces along the northern Ventura basin; and iii) combined offsets across fault scarps with the ^{10}Be geochronology to calculate fault slip rates for the SSCF over multiple timescales. A summary of the main findings are as follows:

- The ^{10}Be geochronology dates a series of aggradational terraces along the northern Ventura basin with ages of ~7 ka, ~19 ka, and ~58 ka.
- I identified faults scarps with north-side-up along the range front of the northern Ventura basin, which run parallel to the proposed trace of the SSCF. I interpret these scarps to be related to activity on a north-dipping SSCF. I suggest that the SSCF is a young thrust fault, which has been active since at most ~58 ka and use limited well data to indicate that the SSCF has a shallow dip of ~20° north in the subsurface.
- Displacement rates averaged over multiple timescales for the SSCF have remained almost constant since ~58 ka with uplift rates of 1.6 $^{+0.6}/_{-0.4}$ mm yr^{-1} since ~58 ka, and 1.2 +/- 0.3 mm yr^{-1} since ~7 ka. I calculated slip rates which range from a maximum of 1.9 $^{+1.0}/_{-0.5}$ mm yr^{-1} for the interval ~19–7 ka, to 1.3 $^{+0.5}/_{-0.3}$ mm yr^{-1} since ~7 ka.
- I compared the slip rates calculated from geomorphic surfaces with slip rates from mechanical models based on GPS data (Marshall et al., 2017). The comparison shows good overlap between my results and model-derived rates that employ a mid-crustal ramp-flat geometry for the Pitas Point-Ventura fault. The ramp-flat geometry implies greater subsurface structural connectivity and, consequently, a greater prospect of large-magnitude multi-fault earthquakes than a model where faults have constant dip to seismogenic depths.

- I propose that it is possible that the SSCF enhances fault connectivity and facilitates multi-fault ruptures including the San Cayetano, Ventura, and Pitas Point faults. Although, given structural complexities, different slip histories, and different slip rates between the Ventura, San Cayetano, and Southern San Cayetano faults, I suggest that these faults may be less prone to synchronous rupture than previously suggested.

In Chapter 3, I attempted to address the questions i) **how does fault geometry effect stress transfer between faults?** and ii) **i static stress transference between reverse faults sensitive to changes in fault geometry?** To investigate these questions, I: i) examined petroleum well-log data to create a series of cross sections along strike of the SSCF and a three-dimensional subsurface model for the SSCF and ii) I used the fault model for the SSCF in conjunction with existing subsurface models for faults surrounding the SSCF as a base to model source and receiver faults for static Coulomb stress modelling. The main findings were as follows:

- I evaluated well-log evidence for the potential subsurface connection of the SSCF with the San Cayetano fault. I find that the SSCF has a 12–20° north dip along the northern Santa Clara River Valley and connects with the western San Cayetano fault (WSCF) at depths of 1.5–3.5 km. I concluded that the SSCF does not connect to the Ventura fault in the subsurface.
- From integration of subsurface data with surface data, I suggest that Holocene deformation appears to have been focused on the SSCF rather than the upper section of the western San Cayetano fault, which could imply that Holocene ruptures preferentially travel to the surface along the SSCF.
- The results of my static Coulomb stress modelling record complex patterns of stress change on receiver faults from various hypothetical rupture scenarios. My modelling is the first application of complex geometry faults based on field observations, surface data, and subsurface data for models of static Coulomb stress transfer on reverse or thrust faults.
- I propose that triggered seismicity may occur on the SSCF and the WSCF because of ruptures on the eastern San Cayetano fault (ESCF), due to large static stress increase on the SSCF and the WSCF from modelled ruptures on the ESCF. However, I suggest that different conclusions can be

drawn on the role of static stress in the prospect for multi-fault earthquakes in the Ventura basin depending on whether a mid-crustal flat is included in the Pitas Point and Ventura faults.

- My results provide an example of the extent to which variations in fault geometry produce different stress distribution of receiver faults in *Coulomb 3.4* and highlights the importance of incorporating variable dip faults into static Coulomb stress modelling. My results also indicate that an accurate understanding of 3D subsurface fault geometry is critical to a proper understanding of fault behaviour, the likelihood of multi-fault ruptures, and the long-term seismic hazard associated with faults.

In Chapter 4, I set out to investigate the broad question: **To what extent have Quaternary fault interactions shaped the landscape evolution of the Ventura basin?** By doing so, I also sought to investigate more specific questions about the suitability of catchment-averaged erosion rates and morphometric landscape parameters for extracting the tectonic signal from the landscape. In addition, I considered the specific question: **Over what time and length scales does the Saugus Formation vary in age across the Ventura basin and the extent to which the Saugus Formation can be used as a strain marker for late Quaternary tectonics in the Ventura basin?** To address these various problems: i) I collected samples for cosmogenic nuclide isochron burial dating on the Saugus Formation and used the resulting chronology to re-evaluate slip rates for several key faults in the Ventura basin; ii) I calculated ^{10}Be catchment-averaged erosion rates for catchments in the hanging wall of active reverse and thrust faults; iii) I undertook a quantitative analysis of hanging wall relief and channel steepness in the hanging wall of several key faults; and iv) I identified knickpoints in river long-profiles and investigated the relationship between the knickpoints and active faults in the Ventura basin.

The main findings are as follows:

- I show that both the base and the top of the exposed Saugus Formation are time-transgressive and increase in age from west to east along the axis of the Ventura basin. My burial ages for the top of the Saugus Formation are $0.38\ ^{+0.17}/_{-0.23}$ Ma in the western basin at Ventura and $2.49\ ^{+0.25}/_{-0.29}$ Ma in the eastern Ventura basin. My burial age for the base of the shallow marine Las Posas Formation,

which underlies the Saugus Formation at Ventura is 0.55 $^{+0.08}/_{-0.10}$ Ma, and the base of the Saugus Formation in the east Ventura basin is 3.30 $^{+0.30}/_{-0.42}$ Ma. My burial ages for the Saugus Formation in the east Ventura basin are significantly older than previous estimates of 0.5–2.3 Ma based on magnetostratigraphy and tephrochronology (Levi and Yeats, 1993).

- I calculate long-term slip rates for the San Cayetano fault of 7.1 +/- 1.0 mm yr^{-1} since ~1.54 Ma and I identified a potential decease in slip rate for the San Cayetano fault around 0.95 Ma, which I hypothesized could be caused by a blind fault propagating in the fault footwall.
- I find that ^{10}Be catchment-averaged erosion rates in the hanging walls of the San Cayetano, Ventura, and Southern San Cayetano faults are generally much lower than uplift or fault throw rates. I show that topographic relief is being built by multiple faults with complex surface and subsurface interactions and that channel steepness is responding to relief building.
- I demonstrated that the distance knickpoints have travelled upstream from the San Cayetano fault shows a strong power-law correlation with upstream area from the fault, which indicates the formation of the knickpoints is related to activity on the San Cayetano fault. I also show that knickpoint height is positively correlated with relief. Therefore, I conclude that relief, channel steepness, and knickpoints in the hanging wall of the San Cayetano fault are all responding to activity primarily on the San Cayetano fault, but also possibly a blind fault in the footwall.
- I found that topographic relief and channel steepness indices are lowest in areas of the lowest rock strength, which I took to indicate that lithology is also an important factor in controlling patterns of relief development and channel steepness. However, the distribution of lithological units in the Ventura basin is itself controlled by tectonics. Therefore, I conclude that tectonics forces are the most important driver of landscape evolution in the Ventura basin on the local scale.
- When combined, I suggest that the landscape analysis records a transient response to tectonic forcing where the erosional response recorded by the catchments reflects the current tectonic conditions as well as tectonic conditions from before various tectonics perturbations linked to fault linkage and evolution. These results indicate that on the local scale with uniform climate such as the hanging wall of the San Cayetano, Ventura, and Southern San Cayetano faults, tectonic

perturbations are the main drivers in patterns of topographic relief developments and channel steepness for periods up to 10^6 years.

The results in this thesis significantly reduce uncertainties in slip rates and subsurface geometry for several key faults and provide significant insights into the structural evolution the Ventura basin. My results demonstrate that patterns of deformation can demonstrate significant spatial variability on timescales between 10^3 to 10^6 years and that fault interactions and the migration of deformation exert significant control on landscape morphology and fault slip rates, which must both be accurately modelled for a robust analysis of seismic hazards.

Chapter 7: Bibliography

Adams, J., Ayodele, J., Bedford, J., Kaars-Sijpesteijn, C. and Watts, N., 1992. Application of dipmeter data in structural interpretation, Niger Delta. Geological Society, London, Special Publications, 65(1): 247-263.

Ahmad, S., Alam, A., Ahmad, B., Bhat, M. and Bhat, M.S., 2015. Geomorphic evidence of unrecognized Balapur fault segment in the southwest Kashmir basin of northwest Himalayas. Geomorphology, 250: 159-172.

Ahmadi, R., Ouali, J., Mercier, E., Mansy, J.-L., Lanoë, B.V.-V., Launeau, P., Rhekhiss, F. and Rafini, S., 2006. The geomorphologic responses to hinge migration in the fault-related folds in the Southern Tunisian Atlas. Journal of Structural Geology, 28(4): 721-728.

Airborne1, 2005. Ventura Rivers LiDAR dataset, project number A05-VENT-002.

Aki, K. and Richards, P., 1980. Quantitative Seismology, Vol. 2. WH Freeman, San Francisco.

Alavi, M., 2004. Regional stratigraphy of the Zagros fold-thrust belt of Iran and its proforeland evolution. American Journal of Science, 304(1): 1-20.

Allen, G. H., Barnes, J. B., Pavelsky, T. M., & Kirby, E., 2013. Lithologic and tectonic controls on bedrock channel form at the northwest Himalayan front. Journal of Geophysical Research: Earth Surface, 118(3), 1806-1825.

Amos, C.B., Kelson, K.I., Rood, D.H., Simpson, D.T. and Rose, R.S., 2010. Late Quaternary slip rate on the Kern Canyon fault at Soda Spring, Tulare County, California. Lithosphere, 2(6): 411-417.

Anderson, J.G. and Brune, J.N., 1999. Probabilistic seismic hazard analysis without the ergodic assumption. Seismological Research Letters, 70(1): 19-28.

Anderson, R.S., Repka, J.L. and Dick, G.S., 1996. Explicit treatment of inheritance in dating depositional surfaces using in situ ^{10}Be and ^{26}Al. Geology, 24(1): 47-51.

Armitage, J.J., Duller, R.A., Whittaker, A.C. and Allen, P.A., 2011. Transformation of tectonic and climatic signals from source to sedimentary archive. Nature Geoscience, 4(4): 231-235.

Atwater, T., 1970. Implications of plate tectonics for the Cenozoic tectonic evolution of western North America. Geological Society of America Bulletin, 81(12): 3513-3536.

Azor, 2002. Geomorphic indicators of active fold growth: South Mountain–Oak Ridge anticline, Ventura basin, southern California. GSA Bulletin, 114(6): 745-753.

Bailey, T.L., 1947. Origin and migration of oil into Sespe redbeds, California. AAPG Bulletin, 31(11): 1913-1935.

Balco, G., 2009. ^{26}Al–^{10}Be exposure age/erosion rate calculators: update from v. 2.1 to v. 2.2. World Wide Web Address: http://hess. ess. washington. edu/math/docs/al_be_v22/al_be_docs. html.

Balco, G. and Rovey, C.W., 2008. An isochron method for cosmogenic-nuclide dating of buried soils and sediments. American Journal of Science, 308(10): 1083-1114.

Balco, G. and Shuster, D.L., 2009. Production rate of cosmogenic ^{21}Ne in quartz estimated from ^{10}Be, ^{26}Al, and ^{21}Ne concentrations in slowly eroding Antarctic bedrock surfaces. Earth and Planetary Science Letters, 281(1): 48-58.

Balco, G., Soreghan, G.S., Sweet, D.E., Marra, K.R. and Bierman, P.R., 2013. Cosmogenic-nuclide burial ages for Pleistocene sedimentary fill in Unaweep Canyon, Colorado, USA. Quaternary Geochronology, 18: 149-157.

Balco, G., Stone, J.O., Lifton, N.A. and Dunai, T.J., 2008. A complete and easily accessible means of calculating surface exposure ages or erosion rates from ^{10}Be and ^{26}Al measurements. Quaternary geochronology, 3(3): 174-195.

Baldwin, J.N., Kelson, K.I. and Randolph, C.E., 2000. Late Quaternary fold deformation along the Northridge Hills fault, Northridge, California: Deformation coincident with past Northridge blind-thrust earthquakes and other nearby structures? Bulletin of the Seismological Society of America, 90(3): 629-642.

Barnes, J.B., Densmore, A.L., Mukul, M., Sinha, R., Jain, V. and Tandon, S.K., 2011. Interplay between faulting and base level in the development of Himalayan frontal fold topography. Journal of Geophysical Research: Earth Surface, 116(F3).

Beavan, J., Fielding, E., Motagh, M., Samsonov, S. and Donnelly, N., 2011. Fault location and slip distribution of the 22 February 2011 M_w 6.2 Christchurch, New Zealand, earthquake from geodetic data. Seismological Research Letters, 82(6): 789-799.

Beavan, J., Motagh, M., Fielding, E.J., Donnelly, N. and Collett, D., 2012. Fault slip models of the 2010–2011 Canterbury, New Zealand, earthquakes from geodetic data and observations of postseismic ground deformation. New Zealand Journal of Geology and Geophysics, 55(3): 207-221.

Behr, W., Rood, D., Fletcher, K., Guzman, N., Finkel, R., Hanks, T.C., Hudnut, K., Kendrick, K., Platt, J. and Sharp, W., 2010. Uncertainties in slip-rate estimates for the Mission Creek strand of the southern San Andreas fault at Biskra Palms Oasis, southern California. Geological Society of America Bulletin, 122(9-10): 1360-1377.

Bell, R.E., Jackson, C.A.L., Whipp, P.S. and Clements, B., 2014. Strain migration during multiphase extension: observations from the northern North Sea. Tectonics, 33(10): 1936-1963.

Bell, R.E., McNeill, L.C., Henstock, T.J. and Bull, J.M., 2011. Comparing extension on multiple time and depth scales in the Corinth Rift, Central Greece. Geophysical Journal International, 186(2): 463-470.

Bender, A.M., Amos, C.B., Bierman, P., Rood, D.H., Staisch, L., Kelsey, H. and Sherrod, B., 2016. Differential uplift and incision of the Yakima River terraces, central Washington State. Journal of Geophysical Research: Solid Earth, 121(1): 365-384.

Bentley, H.W., Phillips, F.M. and Davis, S.N., 1986. Chlorine-36 in the terrestrial environment. Handbook of Environmental Isotope Geochemistry, 2: 427-480.

Biasi, G.P. and Wesnousky, S.G., 2016. Steps and gaps in ground ruptures: Empirical bounds on rupture propagation. Bulletin of the Seismological Society of America, 106(3): 1110-1124.

Biasi, G.P. and Wesnousky, S.G., 2017. Bends and ends of surface ruptures. Bulletin of the Seismological Society of America, 107(6): 2543-2560.

Bie, L. and Ryder, I., 2014. Recent seismic and aseismic activity in the Ashikule stepover zone, NW Tibet. Geophysical Journal International, 198(3): 1632-1643.

Bierman, P. and Gillespie, A., 1991. Range fires: A significant factor in exposure-age determination and geomorphic surface evolution. Geology, 19(6): 641-644.

Bierman, P. and Steig, E.J., 1996. Estimating rates of denudation using cosmogenic isotope abundances in sediment. Earth Surface Processes and Landforms, 21(2): 125-139.

Borchers, B., Marrero, S., Balco, G., Caffee, M., Goehring, B., Lifton, N., Nishiizumi, K., Phillips, F., Schaefer, J. and Stone, J., 2016. Geological calibration of spallation production rates in the CRONUS-Earth project. Quaternary Geochronology, 31: 188-198.

Borgomeo, E., Hebditch, K. V., Whittaker, A. C., & Lonergan, L. (2014). Characterising the spatial distribution, frequency and geomorphic controls on landslide occurrence, Molise, Italy. Geomorphology, 226, 148-161.

Boulton, S.J. and Whittaker, A.C., 2009. Quantifying the slip rates, spatial distribution and evolution of active normal faults from geomorphic analysis: Field examples from an oblique-extensional graben, southern Turkey. Geomorphology, 104(3-4): 299-316.

Brandes, C. and Tanner, D.C., 2014. Fault-related folding: A review of kinematic models and their application. Earth-Science Reviews, 138: 352-370.

Braucher, R., Bourlès, D., Merchel, S., Romani, J.V., Fernadez-Mosquera, D., Marti, K., Leanni, L., Chauvet, F., Arnold, M. and Aumaître, G., 2013. Determination of muon attenuation lengths in depth profiles from in situ produced cosmogenic nuclides. Nuclear Instruments and Methods in Physics Research Section B: Beam Interactions with Materials and Atoms, 294: 484-490.

Brodsky, E.E., Kirkpatrick, J.D. and Candela, T., 2016. Constraints from fault roughness on the scale-dependent strength of rocks. Geology, 44(1): 19-22.

Campbell, R.H., Wills, C.J., Irvine, P.J. and Swanson, B.J., 2014. Preliminary geologic map of the Los Angeles 30'x 60'quadrangle, Southern California, 1: 100,000.

Candela, T., Renard, F., Schmittbuhl, J., Bouchon, M. and Brodsky, E.E., 2011. Fault slip distribution and fault roughness. Geophysical Journal International, 187(2): 959-968.

Carretier, S., Regard, V., Vassallo, R., Aguilar, G., Martinod, J., Riquelme, R., Christophoul, F., Charrier, R., Gayer, E. and Farías, M., 2015. Differences in ^{10}Be concentrations between river sand, gravel and pebbles along the western side of the central Andes. Quaternary Geochronology, 27: 33-51.

Cartwright, J.A., Trudgill, B.D. and Mansfield, C.S., 1995. Fault growth by segment linkage: an explanation for scatter in maximum displacement and trace length data from the Canyonlands Grabens of SE Utah. Journal of Structural Geology, 17(9): 1319-1326.

Carver, G.A. and McCalpin, J.P., 1996. Paleoseismology of compressional tectonic environments. International Geophysics, 62: 183-270.

Çemen, I., 1977. Geology of the Sespe-Piru Creek area, Ventura County, California. Masters Thesis, Ohio University, Athens, Ohio.

Çemen, I., 1989. Near-surface expression of the eastern part of the San Cayetano Fault: A potentially active thrust fault in the California Transverse Ranges. Journal of Geophysical Research, 94(B7): 9665-9677.

Chmeleff, J., von Blanckenburg, F., Kossert, K. and Jakob, D., 2010. Determination of the ^{10}Be half-life by multicollector ICP-MS and liquid scintillation counting. Nuclear Instruments and Methods in Physics Research Section B: Beam Interactions with Materials and Atoms, 268(2): 192-199.

Çiner, A., Doğan, U., Y ld r m, C., Akçar, N., Ivy-Ochs, S., Alfimov, V., Kubik, P.W. and Schlüchter, C., 2015. Quaternary uplift rates of the Central Anatolian Plateau, Turkey: insights from cosmogenic isochron-burial nuclide dating of the K z l rmak River terraces. Quaternary Science Reviews, 107: 81-97.

Clark, K., Nissen, E., Howarth, J., Hamling, I., Mountjoy, J., Ries, W., Jones, K., Goldstien, S., Cochran, U. and Villamor, P., 2017. Highly variable coastal deformation in the 2016 Mw 7. 8 Kaikōura earthquake reflects rupture complexity along a transpressional plate boundary. Earth and Planetary Science Letters, 474: 334-344.

Clark, M., Schoenbohm, L., Royden, L., Whipple, K., Burchfiel, B., Zhang, X., Tang, W., Wang, E. and Chen, L., 2004. Surface uplift, tectonics, and erosion of eastern Tibet from large-scale drainage patterns. Tectonics, 23(1).

Clarke, P., Davies, R., England, P., Parsons, B., Billiris, H., Paradissis, D., Veis, G., Cross, P., Denys, P. and Ashkenazi, V., 1998. Crustal strain in central Greece from repeated GPS measurements in the interval 1989–1997. Geophysical Journal International, 135(1): 195-214.

Collier, R.E., Pantosti, D., D'addezio, G., De Martini, P.M., Masana, E. and Sakellariou, D., 1998. Paleoseismicity of the 1981 Corinth earthquake fault: Seismic contribution to extensional strain in central Greece and implications for seismic hazard. Journal of Geophysical Research: Solid Earth, 103(B12): 30001-30019.

Corbett, L.B., Bierman, P.R. and Davis, P.T., 2016a. Glacial history and landscape evolution of southern Cumberland Peninsula, Baffin Island, Canada, constrained by cosmogenic ^{10}Be and ^{26}Al. Geological Society of America Bulletin, 128(7-8): 1173-1192.

Corbett, L.B., Bierman, P.R. and Rood, D.H., 2016b. An approach for optimizing in-situ cosmogenic ^{10}Be sample preparation. Quaternary Geochronology, 33: 24-34.

Cowgill, E., Gold, R.D., Xuanhua, C., Xiao-Feng, W., Arrowsmith, J.R. and Southon, J., 2009. Low Quaternary slip rate reconciles geodetic and geologic rates along the Altyn Tagh fault, northwestern Tibet. Geology, 37(7): 647-650.

Cowie, P., 1998. A healing–reloading feedback control on the growth rate of seismogenic faults. Journal of Structural Geology, 20(8): 1075-1087.

Cowie, P., Scholz, C., Roberts, G.P., Walker, J.F. and Steer, P., 2013. Viscous roots of active seismogenic faults revealed by geologic slip rate variations. Nature Geoscience, 6(12): 1036-1040.

Cowie, P.A. and Roberts, G.P., 2001. Constraining slip rates and spacings for active normal faults. Journal of Structural Geology, 23(12): 1901-1915.

Crosby, B.T. and Whipple, K.X., 2006. Knickpoint initiation and distribution within fluvial networks: 236 waterfalls in the Waipaoa River, North Island, New Zealand. Geomorphology, 82(1-2): 16-38.

Crowell, J.C., 1976. Implications of crustal stretching and shortening of coastal Ventura basin, California. In: D.G. Howell (Editor), Aspects of the Geologic History of the California Continental Borderland. AAPG Pacific Section, pp. 365-382.

Cyr, A.J., Granger, D.E., Olivetti, V. and Molin, P., 2010. Quantifying rock uplift rates using channel steepness and cosmogenic nuclide–determined erosion rates: Examples from northern and southern Italy. Lithosphere, 2(3): 188-198.

D'Arcy, M. and Whittaker, A.C., 2014. Geomorphic constraints on landscape sensitivity to climate in tectonically active areas. Geomorphology, 204: 366-381.

Das, S. and Scholz, C., 1983. Why large earthquakes do not nucleate at shallow depths. Nature, 305(5935): 621-623.

Davis, K., Burbank, D.W., Fisher, D., Wallace, S. and Nobes, D., 2005. Thrust-fault growth and segment linkage in the active Ostler fault zone, New Zealand. Journal of Structural Geology, 27(8): 1528-1546.

Dawers, N.H. and Anders, M.H., 1995. Displacement-length scaling and fault linkage. Journal of Structural Geology, 17(5): 607-614.

DeCelles, P.G., Robinson, D.M., Quade, J., Ojha, T., Garzione, C.N., Copeland, P. and Upreti, B.N., 2001. Stratigraphy, structure, and tectonic evolution of the Himalayan fold-thrust belt in western Nepal. Tectonics, 20(4): 487-509.

Deng, J. and Sykes, L.R., 1997a. Evolution of the stress field in southern California and triggering of moderate-size earthquakes: A 200-year perspective. Journal of Geophysical Research: Solid Earth, 102(B5): 9859-9886.

Deng, J. and Sykes, L.R., 1997b. Stress evolution in southern California and triggering of moderate-, small-, and micro-size earthquakes. Journal of Geophysical Research: Solid Earth, 102(B11): 24411-24435.

Densmore, A.L., Dawers, N.H., Gupta, S., Guidon, R. and Goldin, T., 2004. Footwall topographic development during continental extension. Journal of Geophysical Research: Earth Surface, 109(F3): 1-16.

Densmore, A.L., Ellis, M.A. and Anderson, R.S., 1998. Landsliding and the evolution of normal-fault-bounded mountains. Journal of Geophysical Research: Solid Earth, 103(B7): 15203-15219.

Densmore, A.L., Gupta, S., Allen, P.A. and Dawers, N.H., 2007. Transient landscapes at fault tips. Journal of Geophysical Research: Earth Surface, 112(F3): 1-16.

Densmore, A.L., Hetzel, R., Ivy-Ochs, S., Krugh, W.C., Dawers, N. and Kubik, P., 2009. Spatial variations in catchment-averaged denudation rates from normal fault footwalls. Geology, 37(12): 1139-1142.

Densmore, A.L., Li, Y., Richardson, N.J., Zhou, R., Ellis, M. and Zhang, Y., 2010. The role of late Quaternary upper-crustal faults in the 12 May 2008 Wenchuan earthquake. Bulletin of the Seismological Society of America, 100(5B): 2700-2712.

DeVecchio, D.E., Heermance, R.V., Fuchs, M. and Owen, L.A., 2012a. Climate-controlled landscape evolution in the Western Transverse Ranges, California: Insights from Quaternary geochronology of the Saugus Formation and strath terrace flights. Lithosphere, 4(2): 110-130.

DeVecchio, D.E., Keller, E.A., Fuchs, M. and Owen, L.A., 2012b. Late Pleistocene structural evolution of the Camarillo fold belt: Implications for lateral fault growth and seismic hazard in Southern California. Lithosphere, 4(2): 91-109.

Devilliers, M. and Werner, P., 1990. Example of fault identification using dipmeter data. Geological Society, London, Special Publications, 48(1): 287-295.

Dey, S., Thiede, R.C., Schildgen, T.F., Wittmann, H., Bookhagen, B., Scherler, D. and Strecker, M.R., 2016. Holocene internal shortening within the northwest Sub-Himalaya: Out-of-sequence faulting of the Jwalamukhi Thrust, India. Tectonics, 35(11): 2677-2697.

Dibblee, T., 1979. Geologic map of the Topatopa Mountains Quadrangle, Ventura County, California, 1: 24,000. United States Geological Survey (Preliminary) Open-file Report.

Dibblee, T., 1987. Geologic map of the Ojai Quadrangle, Ventura County, California, map number DF-13, 1: 24, 000. Dibblee Geological Foundation, Santa Barbara, California.

Dibblee, T., 1990a. Geologic map of the Fillmore quadrangle, Ventura County, California, map number DF-27, 1: 24,000. Dibblee Geological Foundation, Santa Barbara, California.

Dibblee, T., 1990b. Geologic map of the Santa Paula Peak quadrangle, Ventura County, California, map number DF-26, 1: 24,000. Dibblee Geological Foundation, Santa Barbara, California.

Dibblee, T., 1992. Geologic map of the Moorpark quadrangle, Ventura County, California, 1: 24, 000. Dibblee Geological Foundation, Santa Barbara, California.

Dibblee, T.W., 1950. Geology of Southwestern Santa Barbara County, California: Point Arguello, Lompoc, Point Conception, Los Olivos, and Gaviota quadrangles, 150. Department of Natural Resources, Division of Mines, San Francisco.

Dibblee, T.W. and Ehrenspeck, H.E., 1988a. Geologic map of the Ventura and Pitas Point quadrangles, Ventura County, California, 1: 24, 000. Dibblee Geological Foundation, Santa Barbara, California.

Dibblee, T.W. and Ehrenspeck, H.E., 1992a. Geologic map of the Oat Mountain and Canoga Park quadrangles, Los Angeles county, California, map number DF-36, 1:24,000. Dibblee Geological Foundation, Santa Barbara.

Dibblee, T.W. and Ehrenspeck, H.E., 1992b. Geologic Map of the Saticoy quadrangle: Ventura County, California, 1: 24, 000. Dibblee Geological Foundation, Santa Barbara, California.

DiBiase, R.A. and Whipple, K.X., 2011. The influence of erosion thresholds and runoff variability on the relationships among topography, climate, and erosion rate. Journal of Geophysical Research: Earth Surface, 116(F4): 1-17.

DiBiase, R.A., Whipple, K.X., Heimsath, A.M. and Ouimet, W.B., 2010. Landscape form and millennial erosion rates in the San Gabriel Mountains, CA. Earth and Planetary Science Letters, 289(1): 134-144.

Dixon, T.H., Norabuena, E. and Hotaling, L., 2003. Paleoseismology and Global Positioning System: Earthquake-cycle effects and geodetic versus geologic fault slip rates in the Eastern California shear zone. Geology, 31(1): 55-58.

Dolan, J.F., 2009. Paleoseismology and Seismic Hazards of the San Cayetano Fault Zone: NEHERP Final Technical Report: 02HQGR0041.

Dolan, J.F., Bowman, D.D. and Sammis, C.G., 2007. Long-range and long-term fault interactions in Southern California. Geology, 35(9): 855-858.

Dolan, J.F., Christofferson, S.A. and Shaw, J.H., 2003. Recognition of paleoearthquakes on the Puente Hills blind thrust fault, California. Science, 300(5616): 115-118.

Dolan, J.F., McAuliffe, L.J., Rhodes, E.J., McGill, S.F. and Zinke, R., 2016. Extreme multi-millennial slip rate variations on the Garlock fault, California: Strain super-cycles, potentially time-variable fault strength, and implications for system-level earthquake occurrence. Earth and Planetary Science Letters, 446: 123-136.

Dolan, J.F. and Rockwell, T.K., 2001. Paleoseismologic evidence for a very large ($M_w > 7$), post-AD 1660 surface rupture on the eastern San Cayetano fault, Ventura County, California: Was this the elusive source of the damaging 21 December 1812 earthquake? Bulletin of the Seismological Society of America, 91(6): 1417-1432.

Dolan, J.F., Sieh, K., Rockwell, T.K., Yeats, R.S., Shaw, J., Suppe, J., Huftile, G.J. and Gath, E.M., 1995. Prospects for larger or more frequent earthquakes in the Los-Angeles metropolitan region. Science, 267(5195): 199-205.

Donnellan, A., Hager, B.H. and King, R.W., 1993a. Discrepancy between geological and geodetic deformation rates in the Ventura Basin. Nature, 366(6453): 333-336.

Donnellan, A., Hager, B.H., King, R.W. and Herring, T.A., 1993b. Geodetic measurement of deformation in the Ventura Basin region, southern California. Journal of Geophysical Research: Solid Earth, 98(B12): 21727-21739.

Donnellan, A., Parker, J.W. and Peltzer, G., 2002. Combined GPS and InSAR models of postseismic deformation from the Northridge earthquake. Pure and Applied Geophysics, 159(10): 2261-2270.

Duffy, O.B., Bell, R.E., Jackson, C.A.-L., Gawthorpe, R.L. and Whipp, P.S., 2015. Fault growth and interactions in a multiphase rift fault network: Horda Platform, Norwegian North Sea. Journal of Structural Geology, 80: 99-119.

Dunai, T., 2001. Influence of secular variation of the geomagnetic field on production rates of in situ produced cosmogenic nuclides. Earth and Planetary Science Letters, 193(1): 197-212.

Dunai, T.J., 2000. Scaling factors for production rates of in situ produced cosmogenic nuclides: a critical reevaluation. Earth and Planetary Science Letters, 176(1): 157-169.

Duvall, A., Kirby, E., & Burbank, D., 2004. Tectonic and lithologic controls on bedrock channel profiles and processes in coastal California. Journal of Geophysical Research: Earth Surface, 109(F3).

Earth Consultants International, 2015. Fault trenching study of the Culbertson fault in the Timber Canyon area east of Santa Paula, Ventura County, California. Earth Consultants International, Inc.

Earth Systems Southern California, 2013. Geo-Technical Feasibility Report for tract 5475, Santa Paula.

Ellis, M. A., & Barnes, J. B., 2015. A global perspective on the topographic response to fault growth. Geosphere, 11(4), 1008-1023.

Erlanger, E.D., Granger, D.E. and Gibbon, R.J., 2012. Rock uplift rates in South Africa from isochron burial dating of fluvial and marine terraces. Geology, 40(11): 1019-1022.

Field, E., 2005. Probabilistic seismic hazard analysis (PSHA): A primer. Retrieved May, 17: 2011.

Field, E.H., Arrowsmith, R.J., Biasi, G.P., Bird, P., Dawson, T.E., Felzer, K.R., Jackson, D.D., Johnson, K.M., Jordan, T.H. and Madden, C., 2014. Uniform California earthquake rupture forecast, version 3 (UCERF3)—The time-independent model. Bulletin of the Seismological Society of America, 104(3): 1122-1180.

Field, E.H., Biasi, G.P., Bird, P., Dawson, T.E., Felzer, K.R., Jackson, D.D., Johnson, K.M., Jordan, T.H., Madden, C. and Michael, A.J., 2015. Long-term time-dependent probabilities for the third Uniform California Earthquake Rupture Forecast (UCERF3). Bulletin of the Seismological Society of America, 105(2A): 511-543.

Field, E.H., Milner, K.R., Hardebeck, J.L., Page, M.T., van der Elst, N., Jordan, T.H., Michael, A.J., Shaw, B.E. and Werner, M.J., 2017. A spatiotemporal clustering model for the third Uniform California Earthquake Rupture Forecast (UCERF3-ETAS): Toward an operational earthquake forecast. Bulletin of the Seismological Society of America, 107(3): 1049-1081.

Finnegan, N.J., Hallet, B., Montgomery, D.R., Zeitler, P.K., Stone, J.O., Anders, A.M. and Yuping, L., 2008. Coupling of rock uplift and river incision in the Namche Barwa–Gyala Peri massif, Tibet. Geological Society of America Bulletin, 120(1-2): 142-155.

Fletcher, J.M., Oskin, M.E. and Teran, O.J., 2016. The role of a keystone fault in triggering the complex El Mayor-Cucapah earthquake rupture. Nature Geoscience, 9(4): 303-307.

Fletcher, J.M., Teran, O.J., Rockwell, T.K., Oskin, M.E., Hudnut, K.W., Mueller, K.J., Spelz, R.M., Akciz, S.O., Masana, E. and Faneros, G., 2014. Assembly of a large earthquake from a complex fault system: Surface rupture kinematics of the 4 April 2010 El Mayor–Cucapah (Mexico) M_w 7.2 earthquake. Geosphere, 10(4): 797-827.

Flint, J., 1974. Stream gradient as a function of order, magnitude, and discharge. Water Resources Research, 10(5): 969-973.

Floyd, M., Billiris, H., Paradissis, D., Veis, G., Avallone, A., Briole, P., McClusky, S., Nocquet, J.M., Palamartchouk, K. and Parsons, B., 2010. A new velocity field for Greece: Implications for the kinematics and dynamics of the Aegean. Journal of Geophysical Research: Solid Earth, 115(B10): 1-25.

Frankel, K.L., Brantley, K.S., Dolan, J.F., Finkel, R.C., Klinger, R.E., Knott, J.R., Machette, M.N., Owen, L.A., Phillips, F.M., Slate, J.L. and Wernicke, B.P., 2007a. Cosmogenic Be-10 and Cl-36 geochronology of offset alluvial fans along the northern Death Valley fault zone: Implications for transient strain in the eastern California shear zone. Journal of Geophysical Research: Solid Earth, 112(B6): 1-18.

Frankel, K.L. and Dolan, J.F., 2007. Characterizing arid region alluvial fan surface roughness with airborne laser swath mapping digital topographic data. Journal of Geophysical Research, 112(F2): 1-14.

Frankel, K.L., Dolan, J.F., Finkel, R.C., Owen, L.A. and Hoeft, J.S., 2007b. Spatial variations in slip rate along the Death Valley-Fish Lake Valley fault system determined from LiDAR topographic data and cosmogenic ^{10}Be geochronology. Geophysical Research Letters, 34(18): 1-6.

Freed, A.M., 2005. Earthquake triggering by static, dynamic, and postseismic stress transfer. Annu. Rev. Earth Planet. Sci., 33: 335-367.

Freed, A.M., Ali, S.T. and Bürgmann, R., 2007. Evolution of stress in Southern California for the past 200 years from coseismic, postseismic and interseismic stress changes. Geophysical Journal International, 169(3): 1164-1179.

Friedrich, A.M., Wernicke, B.P., Niemi, N.A., Bennett, R.A. and Davis, J.L., 2003. Comparison of geodetic and geologic data from the Wasatch region, Utah, and implications for the spectral character of Earth deformation at periods of 10 to 10 million years. Journal of Geophysical Research: Solid Earth, 108(B4): 1-24.

Ganev, P.N., Dolan, J.F., Blisniuk, K., Oskin, M. and Owen, L.A., 2010. Paleoseismologic evidence for multiple Holocene earthquakes on the Calico fault: Implications for earthquake clustering in the Eastern California shear zone. Lithosphere, 2(4): 287-298.

Ganev, P.N., Dolan, J.F., McGill, S.F. and Frankel, K.L., 2012. Constancy of geologic slip rate along the central Garlock fault: Implications for strain accumulation and release in southern California. Geophysical Journal International, 190(2): 745-760.

Gawthorpe, R. and Leeder, M., 2000. Tectono-sedimentary evolution of active extensional basins. Basin Research, 12(3-4): 195-218.

Goltz, J.D., 1994. The Northridge, California earthquake of January 17, 1994: general reconnaissance report. National Centre for Earthquake Engineeering Research, State University of New York at Buffalo.

Gomez, B. and Livingston, D.M., 2012. The river it goes right on: Post-glacial landscape evolution in the upper Waipaoa River basin, eastern North Island, New Zealand. Geomorphology, 159: 73-83.

Gosse, J.C. and Phillips, F.M., 2001. Terrestrial in situ cosmogenic nuclides: theory and application. Quaternary Science Reviews, 20(14): 1475-1560.

Granger, D.E., Kirchner, J.W. and Finkel, R., 1996. Spatially averaged long-term erosion rates measured from in situ-produced cosmogenic nuclides in alluvial sediment. The Journal of Geology, 104(3): 249-257.

Granger, D.E., Lifton, N.A. and Willenbring, J.K., 2013. A cosmic trip: 25 years of cosmogenic nuclides in geology. Geological Society of America Bulletin, 125(9-10): 1379-1402.

Granger, D.E. and Muzikar, P.F., 2001. Dating sediment burial with in situ-produced cosmogenic nuclides: theory, techniques, and limitations. Earth and Planetary Science Letters, 188(1): 269-281.

Griffith, W. and Cooke, M., 2004. Mechanical validation of the three-dimensional intersection geometry between the Puente Hills blind-thrust system and the Whittier fault, Los Angeles, California. Bulletin of the Seismological Society of America, 94(2): 493-505.

Grigsby, F.B., 1986. Quaternary tectonics of the Rincon and San Miguelito oil fields area, western Ventura basin, California. Masters Thesis, Oregon State University, Corvallis, Oregon.

Gudmundsdottir, M.H., Blisniuk, K., Ebert, Y., Levine, N.M., Rood, D.H., Wilson, A. and Hilley, G.E., 2013. Restraining bend tectonics in the Santa Cruz Mountains, California, imaged using ^{10}Be concentrations in river sands. Geology, 41(8): 843-846.

Gupta, S., Cowie, P.A., Dawers, N.H. and Underhill, J.R., 1998. A mechanism to explain rift-basin subsidence and stratigraphic patterns through fault-array evolution. Geology, 26(7): 595-598.

Hager, B.H., Lyzenga, G.A., Donnellan, A. and Dong, D., 1999. Reconciling rapid strain accumulation with deep seismogenic fault planes in the Ventura basin, California. Journal of Geophysical Research: Solid Earth, 104(B11): 25207-25219.

Hall, J.F., Holmes, W. and Somers, P., 1994. Northridge earthquake, January 17, 1994, Preliminary reconnaissance report, California Institute of Technology, Pasedena, California.

Hamling, I.J., Hreinsdóttir, S., Clark, K., Elliott, J., Liang, C., Fielding, E., Litchfield, N., Villamor, P., Wallace, L. and Wright, T.J., 2017. Complex multifault rupture during the 2016 M_w 7.8 Kaikōura earthquake, New Zealand. Science, 356(6334): eaam7194.

Hammond, W.C., Burgette, R.J., Johnson, K.M. and Blewitt, G., 2018. Uplift of the Western Transverse Ranges and Ventura Area of Southern California: A Four-Technique Geodetic Study Combining GPS, InSAR, Leveling, and Tide Gauges. Journal of Geophysical Research: Solid Earth, 123(1): 836-858.

Harris, R.A., 1998. Introduction to special section: Stress triggers, stress shadows, and implications for seismic hazard. Journal of Geophysical Research: Solid Earth, 103(B10): 24347-24358.

Harris, R.A. and Simpson, R.W., 1992. Changes in static stress on southern California faults after the 1992 Landers earthquake. Nature, 360(6401): 251-254.

Hauksson, E., Andrews, J., Plesch, A., Shaw, J.H. and Shelly, D.R., 2016. The 2015 Fillmore earthquake swarm and possible crustal deformation mechanisms near the bottom of the Eastern Ventura basin, California. Seismological Research Letters, 87(4): 807-815.

Haviv, I., Enzel, Y., Whipple, K., Zilberman, E., Matmon, A., Stone, J. and Fifield, K., 2010. Evolution of vertical knickpoints (waterfalls) with resistant caprock: Insights from numerical modeling. Journal of Geophysical Research: Earth Surface, 115(F3): 1-22.

Heisinger, B., Lal, D., Jull, A., Kubik, P., Ivy-Ochs, S., Knie, K. and Nolte, E., 2002a. Production of selected cosmogenic radionuclides by muons: 2. Capture of negative muons. Earth and Planetary Science Letters, 200(3): 357-369.

Heisinger, B., Lal, D., Jull, A., Kubik, P., Ivy-Ochs, S., Neumaier, S., Knie, K., Lazarev, V. and Nolte, E., 2002b. Production of selected cosmogenic radionuclides by muons: 1. Fast muons. Earth and Planetary Science Letters, 200(3): 345-355.

Heyman, J., Applegate, P.J., Blomdin, R., Gribenski, N., Harbor, J.M. and Stroeven, A.P., 2016. Boulder height–exposure age relationships from a global glacial ^{10}Be compilation. Quaternary Geochronology, 34: 1-11.

Hidy, A.J., Gosse, J.C., Pederson, J.L., Mattern, J.P. and Finkel, R.C., 2010. A geologically constrained Monte Carlo approach to modeling exposure ages from profiles of cosmogenic nuclides: An example from Lees Ferry, Arizona. Geochemistry, Geophysics, Geosystems, 11(9): 1-18.

Hodgkinson, K.M., Stein, R.S. and King, G.C., 1996. The 1954 Rainbow Mountain-Fairview Peak-Dixie Valley earthquakes: A triggered normal faulting sequence. Journal of Geophysical Research: Solid Earth, 101(B11): 25459-25471.

Hollingsworth, J., Ye, L. and Avouac, J.P., 2017. Dynamically triggered slip on a splay fault in the M_w 7.8, 2016 Kaikoura (New Zealand) earthquake. Geophysical Research Letters, 44(8): 3517-3525.

Hopps, T., E, Stark, H., E and Hindle, R., J, 1992. Subsurface geology of Ventura Basin, California, Ventura Basin Study Group Report. Rancho Energy Consultants, Inc, Santa Paula, California.

Hubbard, J., Shaw, J.H., Dolan, J., Pratt, T.L., McAuliffe, L. and Rockwell, T.K., 2014. Structure and seismic hazard of the Ventura Avenue anticline and Ventura fault, California: prospect for large, multisegment ruptures in the Western Transverse Ranges. Bulletin of the Seismological Society of America, 104(3): 1070-1087.

Hubbard, J., Shaw, J.H. and Klinger, Y., 2010. Structural setting of the 2008 M_w 7.9 Wenchuan, China, earthquake. Bulletin of the Seismological Society of America, 100(5B): 2713-2735.

Huftile, G.J., 1988. Geologic structure of the Upper Ojai Valley and Chaffee Canyon areas, Ventura County, California. Masters Thesis, Oregon State University, Corvallis, Oregon.

Huftile, G.J. and Yeats, R.S., 1995. Convergence rates across a displacement transfer zone in the western Transverse Ranges, Ventura basin, California. Journal of Geophysical Research: Solid Earth, 100(B2): 2043-2067.

Huftile, G.J. and Yeats, R.S., 1996. Deformation rates across the Placerita (Northridge M_w 6.7 aftershock zone) and Hopper Canyon segments of the western Transverse Ranges deformation belt. Bulletin of the Seismological Society of America, 86(1B): S3-S18.

Hughes, A., Rood, D.H., Whittaker, A.C., Bell, R.E., Rockwell, T.K., Levy, Y., Wilcken, K.M., Corbett, L.B., Bierman, P.R., DeVecchio, D.E., Marshall, S.T., Gurrola, L.D. and Nicholson, C., 2018. Geomorphic evidence for the geometry and slip rate of a young, low-angle thrust fault: Implications for hazard assessment and fault interaction in complex tectonic environments. Earth and Planetary Science Letters, 504: 198-210.

Izett, G., Naeser, C. and Obradovich, J., 1974. Fission-track age of zircons from an ash bed in the Pico Formation (Pliocene and Pleistocene) near Ventura, California, Geological Society of America Abstract and Programs.

Izett, G.A., 1981. Volcanic ash beds: Recorders of upper Cenozoic silicic pyroclastic volcanism in the western United States. Journal of Geophysical Research: Solid Earth, 86(B11): 10200-10222.

Jackson, C.A.-L., Bell, R.E., Rotevatn, A. and Tvedt, A.B., 2017. Techniques to determine the kinematics of synsedimentary normal faults and implications for fault growth models. Geological Society, London, Special Publications, 439(1): 187-217.

Jackson, C.A.-L. and Rotevatn, A., 2013. 3D seismic analysis of the structure and evolution of a salt-influenced normal fault zone: a test of competing fault growth models. Journal of Structural Geology, 54: 215-234.

Jennings, C. and Bryant, W., 2010. Fault activity map of California: California Geological Survey Geologic Data Map No. 6, 1: 750, 000. California Department of Conservation, California.

Jennings, P.C., 1997. Enduring lessons and opportunities lost from the San Fernando earthquake of February 9, 1971. Earthquake Spectra, 13(1): 25-44.

Johnson, S.Y., Hartwell, S.R., Sorlien, C.C., Dartnell, P. and Ritchie, A.C., 2017. Shelf evolution along a transpressive transform margin, Santa Barbara Channel, California. Geosphere, 13(6): 2041-2077.

Jordan, T., Allmendinger, R., Damanti, J. and Drake, R., 1993. Chronology of motion in a complete thrust belt: the Precordillera, 30-31 S, Andes Mountains. The Journal of Geology, 101(2): 135-156.

Jull, A.T., Scott, E.M. and Bierman, P., 2015. The CRONUS-Earth inter-comparison for cosmogenic isotope analysis. Quaternary Geochronology, 26: 3-10.

Kamb, B., Silver, L., Abrams, M., Carter, B., Jordan, T.H. and Minster, J.B., 1971. Pattern of faulting and nature of fault movement in the San Fernando earthquake. US Geological Survey Profesional Paper, 733: 41-54.

Kamerling, M., Sorlien, C. and Nicholson, C., 2003. 3D development of an active oblique fault system, northern Santa Barbara Channel, California. Seismological Research Letters, 74(2): 248.

Kenner, S.J. and Segall, P., 2000. A mechanical model for intraplate earthquakes: Application to the New Madrid seismic zone. Science, 289(5488): 2329-2332.

Kent, E., Boulton, S.J., Whittaker, A.C., Stewart, I.S. and Cihat Alçiçek, M., 2017. Normal fault growth and linkage in the Gediz (Alaşehir) Graben, Western Turkey, revealed by transient river long-profiles and slope-break knickpoints. Earth Surface Processes and Landforms, 42(5): 836-852.

Kew, W.S., 1924. Goelogy and oil rescources of a part of Los Angeles and Ventura Counties, California. USGS Bulletin 753.

Kilb, D., Gomberg, J. and Bodin, P., 2002. Aftershock triggering by complete Coulomb stress changes. Journal of Geophysical Research: Solid Earth, 107(B4): 2-1 - 2-14.

King, G.C., Stein, R.S. and Lin, J., 1994. Static stress changes and the triggering of earthquakes. Bulletin of the Seismological Society of America, 84(3): 935-953.

Kirby, E. and Whipple, K., 2001. Quantifying differential rock-uplift rates via stream profile analysis. Geology, 29(5): 415-418.

Kirby, E., Whipple, K. and Harkins, N., 2008. Topography reveals seismic hazard. Nature Geoscience, 1(8): 485-487.

Kirby, E. and Whipple, K.X., 2012. Expression of active tectonics in erosional landscapes. Journal of Structural Geology, 44: 54-75.

Kirby, E., Whipple, K.X., Tang, W. and Chen, Z., 2003. Distribution of active rock uplift along the eastern margin of the Tibetan Plateau: Inferences from bedrock channel longitudinal profiles. Journal of Geophysical Research: Solid Earth, 108(B4): 1-24.

Klinger, Y., Le Béon, M. and Al-Qaryouti, M., 2015. 5000 yr of paleoseismicity along the southern Dead Sea fault. Geophysical Journal International, 202(1): 313-327.

Kohl, C. and Nishiizumi, K., 1992. Chemical isolation of quartz for measurement of in-situ-produced cosmogenic nuclides. Geochimica et Cosmochimica Acta, 56(9): 3583-3587.

Korup, O., 2006. Rock-slope failure and the river long profile. Geology, 34(1): 45-48.

Korup, O., 2008. Rock type leaves topographic signature in landslide-dominated mountain ranges. Geophysical Research Letters, 35(11): 1-5.

Lajoie, K.R., Sarna-Wojcicki, A.M. and Yerkes, R.F., 1982. Quaternary chronology and rates of crustal deformation in the Ventura area, California. AAPG Pacific Section SEPM: 43-51.

Lal, D., 1988. In situ-produced cosmogenic isotopes in terrestrial rocks. Annual Review of Earth and Planetary Sciences, 16(1): 355-388.

Lal, D., 1991. Cosmic ray labeling of erosion surfaces: in situ nuclide production rates and erosion models. Earth and Planetary Science Letters, 104(2-4): 424-439.

Lal, D. and Peters, B., 1967. Cosmic ray produced radioactivity on the earth, Cosmic Rays II. Springer, pp. 551-612.

Lamb, M.P., Howard, A.D., Dietrich, W.E. and Perron, J.T., 2007. Formation of amphitheater-headed valleys by waterfall erosion after large-scale slumping on Hawai ‘i. Geological Society of America Bulletin, 119(7-8): 805-822.

Langridge, R., Ries, W., Litchfield, N., Villamor, P., Van Dissen, R., Barrell, D., Rattenbury, M., Heron, D., Haubrock, S. and Townsend, D., 2016. The New Zealand active faults database. New Zealand Journal of Geology and Geophysics, 59(1): 86-96.

Lavé, J. and Avouac, J., 2001. Fluvial incision and tectonic uplift across the Himalayas of central Nepal. Journal of Geophysical Research: Solid Earth, 106(B11): 26561-26591.

Leonard, M., 2010. Earthquake fault scaling: Self-consistent relating of rupture length, width, average displacement, and moment release. Bulletin of the Seismological Society of America, 100(5A): 1971-1988.

Leonard, M., 2014. Self-consistent earthquake fault-scaling relations: Update and extension to stable continental strike-slip faults. Bulletin of the Seismological Society of America, 104(6): 2953-2965.

Levi, S. and Yeats, R.S., 1993. Paleomagnetic constraints on the initiation of uplift on the Santa-Susana fault, Western Transverse Ranges, California. Tectonics, 12(3): 688-702.

Levi, S. and Yeats, R.S., 2003. Paleomagnetic definition of crustal fragmentation and Quaternary block rotations in the east Ventura Basin and San Fernando valley, southern California. Tectonics, 22(5).

Levy, Y., Rockwell, T.K., Shaw, J.H., Plesch, A., Driscoll, N.W. and Perea, H., in review. Structural modeling of the Western Transverse Ranges: an imbricated thrust ramp architecture. Tectonophysics.

Li, Y., Jia, D., Wang, M., Shaw, J.H., He, J., Lin, A., Xiong, L. and Rao, G., 2014. Structural geometry of the source region for the 2013 Mw 6.6 Lushan earthquake: Implication for earthquake hazard assessment along the Longmen Shan. Earth and Planetary Science Letters, 390(Supplement C): 275-286.

Lifton, N., Caffee, M., Finkel, R., Marrero, S., Nishiizumi, K., Phillips, F.M., Goehring, B., Gosse, J., Stone, J. and Schaefer, J., 2015. In situ cosmogenic nuclide production rate calibration for the CRONUS-Earth project from Lake Bonneville, Utah, shoreline features. Quaternary Geochronology, 26: 56-69.

Lifton, N., Sato, T. and Dunai, T.J., 2014. Scaling in situ cosmogenic nuclide production rates using analytical approximations to atmospheric cosmic-ray fluxes. Earth and Planetary Science Letters, 386: 149-160.

Lifton, N.A., Bieber, J.W., Clem, J.M., Duldig, M.L., Evenson, P., Humble, J.E. and Pyle, R., 2005. Addressing solar modulation and long-term uncertainties in scaling secondary cosmic rays for in situ cosmogenic nuclide applications. Earth and Planetary Science Letters, 239(1): 140-161.

Lin, J. and Stein, R.S., 2004. Stress triggering in thrust and subduction earthquakes and stress interaction between the southern San Andreas and nearby thrust and strike-slip faults. Journal of Geophysical Research: Solid Earth, 109(B2): 1-19.

Loveless, J.P. and Meade, B.J., 2011. Stress modulation on the San Andreas fault by interseismic fault system interactions. Geology, 39(11): 1035-1038.

Lozos, J.C., Oglesby, D.D., Brune, J.N. and Olsen, K.B., 2012. Small intermediate fault segments can either aid or hinder rupture propagation at stepovers. Geophysical Research Letters, 39(18): 1-4.

Lu, R., Xu, X., He, D., Liu, B., Tan, X. and Wang, X., 2016. Coseismic and blind fault of the 2015 Pishan Mw 6.5 earthquake: Implications for the sedimentary-tectonic framework of the western Kunlun Mountains, northern Tibetan Plateau. Tectonics, 35(4): 956-964.

Luyendyk, B.P., 1991. A model for Neogene crustal rotations, transtension, and transpression in southern California. Geological Society of America Bulletin, 103(11): 1528-1536.

Luyendyk, B.P., Kamerling, M.J. and Terres, R., 1980. Geometric model for Neogene crustal rotations in southern California. Geological Society of America Bulletin, 91(4): 211-217.

Mackey, B.H., Scheingross, J.S., Lamb, M.P. and Farley, K.A., 2014. Knickpoint formation, rapid propagation, and landscape response following coastal cliff retreat at the last interglacial sea-level highstand: Kaua ‘i, Hawai ‘i. Bulletin, 126(7-8): 925-942.

Manighetti, I., Caulet, C., De Barros, L., Perrin, C., Cappa, F. and Gaudemer, Y., 2015. Generic along-strike segmentation of Afar normal faults, East Africa: Implications on fault growth and stress heterogeneity on seismogenic fault planes. Geochemistry, Geophysics, Geosystems, 16(2): 443-467.

Marshall, S.T., Cooke, M.L. and Owen, S.E., 2008. Effects of nonplanar fault topology and mechanical interaction on fault-slip distributions in the Ventura Basin, California. Bulletin of the Seismological Society of America, 98(3): 1113-1127.

Marshall, S.T., Funning, G.J., Krueger, H.E., Owen, S.E. and Loveless, J.P., 2017. Mechanical models favor a ramp geometry for the Ventura-pitas point fault, California. Geophysical Research Letters, 44(3): 1311-1319.

Marshall, S.T., Funning, G.J. and Owen, S.E., 2013. Fault slip rates and interseismic deformation in the western Transverse Ranges, California. Journal of Geophysical Research: Solid Earth, 118(8): 4511-4534.

Marshall, S.T. and Morris, A.C., 2012. Mechanics, slip behavior, and seismic potential of corrugated dip-slip faults. Journal of Geophysical Research: Solid Earth, 117(B3): 1-19.

Matthews, N. E., Vazquez, J. A., & Calvert, A. T., 2015. Age of the L ava C reek supereruption and magma chamber assembly at Yellowstone based on $^{40}Ar/^{39}Ar$ and U-P b dating of sanidine and zircon crystals. Geochemistry, Geophysics, Geosystems, 16(8), 2508-2528.

McAuliffe, L.J., 2014. Paleoseismologic and slip rate studies of three major faults in southern California: understanding the complex behavior of plate boundary fault systems over millenial timescales. PhD Thesis, University of Southern California, Los Angeles.

McAuliffe, L.J., Dolan, J.F., Kirby, E., Rollins, C., Haravitch, B., Alm, S. and Rittenour, T.M., 2013. Paleoseismology of the southern Panamint Valley fault: Implications for regional earthquake occurrence and seismic hazard in southern California. Journal of Geophysical Research: Solid Earth, 118(9): 5126-5146.

McAuliffe, L.J., Dolan, J.F., Rhodes, E.J., Hubbard, J., Shaw, J.H. and Pratt, T.L., 2015. Paleoseismologic evidence for large-magnitude (Mw7.5–8.0) earthquakes on the Ventura blind thrust fault: Implications for multifault ruptures in the Transverse Ranges of southern California. Geosphere, 11(5): 1629-1650.

McGill, S. and Rockwell, T., 1998. Ages of late Holocene earthquakes on the central Garlock fault near El Paso Peaks, California. Journal of Geophysical Research: Solid Earth, 103(B4): 7265-7279.

McGill, S.F., Wells, S.G., Fortner, S.K., Kuzma, H.A. and McGill, J.D., 2009. Slip rate of the western Garlock fault, at Clark Wash, near Lone Tree Canyon, Mojave Desert, California. Geological Society of America Bulletin, 121(3-4): 536-554.

Meade, B.J. and Hager, B.H., 2005. Block models of crustal motion in southern California constrained by GPS measurements. Journal of Geophysical Research: Solid Earth, 110(B3).

Meigs, A., Yule, D., Blythe, A. and Burbank, D., 2003. Implications of distributed crustal deformation for exhumation in a portion of a transpressional plate boundary, Western Transverse Ranges, Southern California. Quaternary International, 101: 169-177.

Meyer, V., Nicol, A., Childs, C., Walsh, J. and Watterson, J., 2002. Progressive localisation of strain during the evolution of a normal fault population. Journal of Structural Geology, 24(8): 1215-1231.

Mildon, Z.K., Roberts, G.P., Faure Walker, J.P. and Iezzi, F., 2017. Coulomb stress transfer and fault interaction over millennia on non-planar active normal faults: the Mw 6.5–5.0 seismic sequence of 2016–2017, central Italy. Geophysical Journal International, 210(2): 1206-1218.

Mildon, Z.K., Toda, S., Faure Walker, J.P. and Roberts, G.P., 2016. Evaluating models of Coulomb stress transfer: Is variable fault geometry important? Geophysical Research Letters, 43(24): 12407-12414.

Miller, S.R., Baldwin, S.L. and Fitzgerald, P.G., 2012. Transient fluvial incision and active surface uplift in the Woodlark Rift of eastern Papua New Guinea. Lithosphere, 4(2): 131-149.

Miller, S.R., Sak, P.B., Kirby, E. and Bierman, P.R., 2013. Neogene rejuvenation of central Appalachian topography: Evidence for differential rock uplift from stream profiles and erosion rates. Earth and Planetary Science Letters, 369: 1-12.

Mudd, S.M., Harel, M.-A., Hurst, M.D., Grieve, S.W. and Marrero, S.M., 2016. The CAIRN method: automated, reproducible calculation of catchment-averaged denudation rates from cosmogenic nuclide concentrations. Earth Surface Dynamics, 4(3): 655-674.

Muzikar, P., 2011. Geological constraints and ^{26}Al–^{10}Be burial dating isochrons. Earth Surface Processes and Landforms, 36(7): 946-952.

Namson, J. and Davis, T., 1988. Structural transect of the western Transverse Ranges, California: Implications for lithospheric kinematics and seismic risk evaluation. Geology, 16(8): 675-679.

Nicholson, 1994. Microplate capture, rotation of the western Transverse Ranges, and initiation of the San Andreas transform as a low-angle fault system. Geology, 22: 491-495.

Nicholson, C., Kamerling, M.J., Sorlien, C.C., Hopps, T.E. and Gratier, J.-P., 2007. Subsidence, compaction, and gravity sliding: implications for 3D geometry, dynamic rupture, and seismic hazard of active basin-bounding faults in Southern California. Bulletin of the Seismological Society of America, 97(5): 1607-1620.

Nicholson, C., Plesch, A. and Shaw, J.H., 2017a. Community Fault Model Version 5.2: Updating & expanding the CFM 3D fault set and its associated fault database, 2017 SCEC Annual Meeting Proceedings & Abstracts, XXVII.

Nicholson, C., Plesch, A., Sorlien, C.C., Shaw, J.H. and Hauksson, E., 2015. The SCEC Community Fault Model Version 5.0: An Updated And Expanded 3D Fault Set For Southern California, Pacific Section AAPG Convention.

Nicholson, C., Sorlien, C., Kamerling, M.J. and Hopps, T., E, 2017b. An integrated onshore-offshore reevaluation of 3D fault and fold geometry, coastal uplift and seismic hazard in the Santa Barbara-Ventura area, United States Geological Survey, Santa Barbara.

Nicol, A., Childs, C., Walsh, J., Manzocchi, T. and Schöpfer, M., 2017. Interactions and growth of faults in an outcrop-scale system. Geological Society, London, Special Publications, 439(1): 23-39.

Niemann, J.D., Gasparini, N.M., Tucker, G.E. and Bras, R.L., 2001. A quantitative evaluation of Playfair's law and its use in testing long-term stream erosion models. Earth Surface Processes and Landforms: The Journal of the British Geomorphological Research Group, 26(12): 1317-1332.

Niemi, N.A., Oskin, M., Burbank, D.W., Heimsath, A.M. and Gabet, E.J., 2005. Effects of bedrock landslides on cosmogenically determined erosion rates. Earth and Planetary Science Letters, 237(3-4): 480-498.

Nishiizumi, K., 2004. Preparation of ^{26}Al AMS standards. Nuclear Instruments and Methods in Physics Research Section B: Beam Interactions with Materials and Atoms, 223: 388-392.

Nishiizumi, K., Imamura, M., Caffee, M.W., Southon, J.R., Finkel, R.C. and McAninch, J., 2007. Absolute calibration of ^{10}Be AMS standards. Nuclear Instruments and Methods in Physics Research Section B: Beam Interactions with Materials and Atoms, 258(2): 403-413.

Nishiizumi, K., Winterer, E., Kohl, C., Klein, J., Middleton, R., Lal, D. and Arnold, J., 1989. Cosmic ray production rates of ^{10}Be and ^{26}Al in quartz from glacially polished rocks. Journal of Geophysical Research: Solid Earth, 94(B12): 17907-17915.

Ogata, Y., 2005. Synchronous seismicity changes in and around the northern Japan preceding the 2003 Tokachi-oki earthquake of M8. 0. Journal of Geophysical Research: Solid Earth, 110(B8): 1-10.

Oglesby, D., 2008. Rupture termination and jump on parallel offset faults. Bulletin of the Seismological Society of America, 98(1): 440-447.

Oglesby, D.D., Archuleta, R.J. and Nielsen, S.B., 1998. Earthquakes on dipping faults: the effects of broken symmetry. Science, 280(5366): 1055-1059.

Oglesby, D.D. and Day, S.M., 2001. Fault geometry and the dynamics of the 1999 Chi-Chi (Taiwan) earthquake. Bulletin of the Seismological Society of America, 91(5): 1099-1111.

Olson, E.L. and Cooke, M.L., 2005. Application of three fault growth criteria to the Puente Hills thrust system, Los Angeles, California, USA. Journal of Structural Geology, 27(10): 1765-1777.

Oskin, M., Perg, L., Shelef, E., Strane, M., Gurney, E., Singer, B. and Zhang, X., 2008. Elevated shear zone loading rate during an earthquake cluster in eastern California. Geology, 36(6): 507-510.

Ouimet, W.B., 2010. Landslides associated with the May 12, 2008 Wenchuan earthquake: Implications for the erosion and tectonic evolution of the Longmen Shan. Tectonophysics, 491(1-4): 244-252.

Ouimet, W.B., Whipple, K.X. and Granger, D.E., 2009. Beyond threshold hillslopes: Channel adjustment to base-level fall in tectonically active mountain ranges. Geology, 37(7): 579-582.

Owen, L.A., Clemmens, S.J., Finkel, R.C. and Gray, H., 2014. Late Quaternary alluvial fans at the eastern end of the San Bernardino Mountains, Southern California. Quaternary Science Reviews, 87: 114-134.

Pace, B., Bocchini, G.M. and Boncio, P., 2014. Do static stress changes of a moderate-magnitude earthquake significantly modify the regional seismic hazard? Hints from the L'Aquila 2009 normal-faulting earthquake (M_w 6.3, central Italy). Terra Nova, 26(6): 430-439.

Parsons, T., Stein, R.S., Simpson, R.W. and Reasenberg, P.A., 1999. Stress sensitivity of fault seismicity: A comparison between limited-offset oblique and major strike-slip faults. Journal of Geophysical Research: Solid Earth, 104(B9): 20183-20202.

Pei, Y., Paton, D.A., Knipe, R.J., Lickorish, W.H., Li, A. and Wu, K., 2018. Unraveling the influence of throw and stratigraphy in controlling subseismic fault architecture of fold-thrust belts: An example from the Qaidam Basin, northeast Tibetan Plateau. AAPG Bulletin, 102(6): 1091-1117.

Peltzer, G., Crampé, F., Hensley, S. and Rosen, P., 2001. Transient strain accumulation and fault interaction in the Eastern California shear zone. Geology, 29(11): 975-978.

Peruccacci, S., Brunetti, M. T., Luciani, S., Vennari, C., & Guzzetti, F., 2012. Lithological and seasonal control on rainfall thresholds for the possible initiation of landslides in central Italy. Geomorphology, 139: 79-90.

Phillips, F.M., Argento, D.C., Balco, G., Caffee, M.W., Clem, J., Dunai, T.J., Finkel, R., Goehring, B., Gosse, J.C. and Hudson, A.M., 2016. The CRONUS-Earth project: a synthesis. Quaternary Geochronology, 31: 119-154.

Pike, A. S., Scatena, F. N., & Wohl, E. E. (2010). Lithological and fluvial controls on the geomorphology of tropical montane stream channels in Puerto Rico. Earth Surface Processes and Landforms, 35(12), 1402-1417.

Plesch, A., Shaw, J.H., Benson, C., Bryant, W.A., Carena, S., Cooke, M., Dolan, J., Fuis, G., Gath, E. and Grant, L., 2007. Community fault model (CFM) for southern California. Bulletin of the Seismological Society of America, 97(6): 1793-1802.

Pollitz, F., Vergnolle, M. and Calais, E., 2003. Fault interaction and stress triggering of twentieth century earthquakes in Mongolia. Journal of Geophysical Research: Solid Earth, 108(B10): 16-1 - 16-14.

Pollitz, F.F., 1992. Postseismic relaxation theory on the spherical earth. Bulletin of the Seismological Society of America, 82(1): 422-453.

Portenga, E.W., Bierman, P.R., Duncan, C., Corbett, L.B., Kehrwald, N.M. and Rood, D.H., 2015. Erosion rates of the Bhutanese Himalaya determined using in situ-produced ^{10}Be. Geomorphology, 233: 112-126.

Pritchard, D., Roberts, G., White, N. and Richardson, C., 2009. Uplift histories from river profiles. Geophysical Research Letters, 36(24): 1-5.

Redin, T., Forman, J. and Kamerling, M., 2005. Santa Barbara Channel structure and correlation sections, Pacific Section AAPG Cross Sections CS-32 through CS-42, Bakersfield, California.

Regalla, C., Kirby, E., Fisher, D. and Bierman, P., 2013. Active forearc shortening in Tohoku, Japan: Constraints on fault geometry from erosion rates and fluvial longitudinal profiles. Geomorphology, 195: 84-98.

Reid, H.F., 1910. The mechanics of the earthquake, 2. Carnegie Institution of Washington.

Reynolds, L.C., 2018. The late Quaternary evolution of the southern California coast: sea-Level change, storms, and subsidence. PhD Thesis, University of California: Santa Barbara, Santa Barbara.

Rice, J.R., 1992. Fault stress states, pore pressure distributions, and the weakness of the San Andreas fault, International Geophysics. Elsevier, pp. 475-503.

Rockwell, T., 1983. Soil chronology, geology, and neotectonics of the northcentral Ventura basin. PhD Thesis, University of California: Santa Barbara, Santa Barbara.

Rockwell, T., 1988. Neotectonics of the San-Cayetano Fault, Transverse Ranges, California. Geological Society of America Bulletin, 100(4): 500-513.

Rockwell, T., 2011. Large co-seismic uplift of coastal terraces across the Ventura Avenue anticline: Implications for the size of earthquakes and the potential for tsunami generation, SCEC Annual Meeting, Palm Springs.

Rockwell, T., Keller, E., Clark, M. and Johnson, D., 1984. Chronology and rates of faulting of Ventura River terraces, California. Geological Society of America Bulletin, 95(12): 1466-1474.

Rockwell, T., Keller, E. and Dembroff, G., 1988. Quaternary rate of folding of the Ventura Avenue anticline, western Transverse Ranges, southern California. Geological Society of America Bulletin, 100(6): 850-858.

Rockwell, T., Lindvall, S., Herzberg, M., Murbach, D., Dawson, T. and Berger, G., 2000. Paleoseismology of the Johnson Valley, Kickapoo, and Homestead Valley faults: Clustering of earthquakes in the eastern California shear zone. Bulletin of the Seismological Society of America, 90(5): 1200-1236.

Rockwell, T.K., Clark, K., Gamble, L., Oskin, M.E., Haaker, E.C. and Kennedy, G.L., 2016. Large Transverse Range earthquakes cause coastal upheaval near Ventura, Southern California. Bulletin of the Seismological Society of America, 106(6): 2706-2720.

Roda-Boluda, D.C., D'Arcy, M., Whittaker, A.C., Gheorghiu, D.M. and Rodés, Á., 2019. ^{10}Be erosion rates controlled by transient response to normal faulting through incision and landsliding. Earth and Planetary Science Letters, 507: 140-153.

Roda-Boluda, D.C., D'Arcy, M., McDonald, J. and Whittaker, A.C., 2019. Lithological controls on hillslope sediment supply: Insights from landslide activity and grain size distributions. Earth Surface Processes and Landforms, 45(5): 956-977.

Rood, D.H., Burbank, D.W. and Finkel, R.C., 2011a. Chronology of glaciations in the Sierra Nevada, California, from ^{10}Be surface exposure dating. Quaternary Science Reviews, 30(5-6): 646-661.

Rood, D.H., Burbank, D.W. and Finkel, R.C., 2011b. Spatiotemporal patterns of fault slip rates across the Central Sierra Nevada frontal fault zone. Earth and Planetary Science Letters, 301(3): 457-468.

Rood, D.H., Hall, S., Guilderson, T.P., Finkel, R.C. and Brown, T.A., 2010. Challenges and opportunities in high-precision Be-10 measurements at CAMS. Nuclear Instruments and Methods in Physics Research Section B: Beam Interactions with Materials and Atoms, 268(7): 730-732.

Ryan, K.J., Geist, E.L., Barall, M. and Oglesby, D.D., 2015. Dynamic models of an earthquake and tsunami offshore Ventura, California. Geophysical Research Letters, 42(16): 6599-6606.

Rydelek, P.A. and Sacks, I.S., 1999. Large earthquake occurrence affected by small stress changes. Bulletin of the Seismological Society of America, 89(3): 822-828.

Sarna-Wojcicki, 1976. Geology of the Ventura Fault, Ventura County, California, 1: 6,000. United States Geological Survey, Reston, Virginia.

Sarna-Wojcicki, A., Morrison, S.D., Meyer, C. and Hillhouse, J., 1987. Correlation of upper Cenozoic tephra layers between sediments of the western United States and eastern Pacific Ocean and comparison with biostratigraphic and magnetostratigraphic age data. Geological Society of America Bulletin, 98(2): 207-223.

Sarna-Wojcicki, A. and Yerkes, R., 1982. Comment on Article by RS Yeats on "Low-Shake Faults of the Ventura Basin, California. 78th Cordilleran Section Annual Meeting, Guide Book. Geological Society of America.

Sarna-Wojcicki, A.M., 1984. Chemical analyses, correlations, and ages of upper Pliocene and Pleistocene ash layers of east-central and southern California.

Schlueter, J.C., 1976. Geology of the Upper Ojai-Timber Canyon Area Ventura County, California, Ohio University, December.

Scholz, C.H., 1990. The mechanics of earthquakes and faulting. Cambridge University Press.

Schwarcz, H.P., 1989. Uranium series dating of Quaternary deposits. Quaternary International, 1: 7-17.

Schwartz, D., Tauxe, L. and Driscoll, N., 2018. Macroplate Versus Microplate Deformation of the Western Transvers Range: New Constraints from Directional Paleomagnetic Data, AGU Fall Meeting Abstracts.

Shaw, J.H. and Suppe, J., 1994. Active faulting and growth folding in the eastern Santa Barbara Channel, California. Geological Society of America Bulletin, 106(5): 607-626.

Shaw, J.H. and Suppe, J., 1996. Earthquake hazards of active blind-thrust faults under the central Los Angeles basin, California. Journal of Geophysical Research: Solid Earth, 101(B4): 8623-8642.

Shimazaki, K. and Nakata, T., 1980. Time-predictable recurrence model for large earthquakes. Geophysical Research Letters, 7(4): 279-282.

Sieh, K., Stuiver, M. and Brillinger, D., 1989. A more precise chronology of earthquakes produced by the San Andreas fault in southern California. Journal of Geophysical Research: Solid Earth, 94(B1): 603-623.

Snyder, N.P., Whipple, K.X., Tucker, G.E. and Merritts, D.J., 2000. Landscape response to tectonic forcing: Digital elevation model analysis of stream profiles in the Mendocino triple junction region, northern California. Geological Society of America Bulletin, 112(8): 1250-1263.

Sorlien, C.C., Gratier, J.-P., Luyendyk, B.P., Hornafius, J.S. and Hopps, T.E., 2000. Map restoration of folded and faulted late Cenozoic strata across the Oak Ridge fault, onshore and offshore Ventura basin, California. Geological Society of America Bulletin, 112(7): 1080-1090.

Sorlien, C.C. and Nicholson, C., 2015. Post-1 Ma deformation history of the Pitas Point-North Channel-Red Mountain fault system and associated folds in Santa Barbara Channel, California, Santa Barbara.

Spotila, J.A., Farley, K.A. and Sieh, K., 1998. Uplift and erosion of the San Bernardino Mountains associated with transpression along the San Andreas fault, California, as constrained by radiogenic helium thermochronometry. Tectonics, 17(3): 360-378.

Stein, R.S., Barka, A.A. and Dieterich, J.H., 1997. Progressive failure on the North Anatolian fault since 1939 by earthquake stress triggering. Geophysical Journal International, 128(3): 594-604.

Stein, R.S., King, G.C. and Lin, J., 1992. Change in failure stress on the southern San Andreas fault system caused by the 1992 M_w 7.4 Landers earthquake. Science, 258(5086): 1328-1332.

Stock, G.M., Frankel, K.L., Ehlers, T.A., Schaller, M., Briggs, S.M. and Finkel, R.C., 2009. Spatial and temporal variations in denudation of the Wasatch Mountains, Utah, USA. Lithosphere, 1(1): 34-40.

Stone, J.O., 2000. Air pressure and cosmogenic isotope production. Journal of Geophysical Research: Solid Earth, 105(B10): 23753-23759.

Strader, A. and Jackson, D.D., 2014. Near-prospective test of Coulomb stress triggering. Journal of Geophysical Research: Solid Earth, 119(4): 3064-3075.

Strader, A. and Jackson, D.D., 2015. Static coulomb stress-based southern California earthquake forecasts: A pseudoprospective test. Journal of Geophysical Research: Solid Earth, 120(3): 1667-1676.

Suppe, J., 1983. Geometry and kinematics of fault-bend folding. American Journal of Science, 283(7): 684-721.

Swanson, B.J. and Irvine, P.J., 2015. Updated Nomenclature for Plio-Pleistocene Formations in the Onshore Ventura Basin, Los Angeles and Santa Barbara 30′× 60′ Quadrangles, Pacific Section AAPG, SEG and SEPM Joint Technical Conference, Oxnard, California.

Tan, S., Clahan, K. and Irvine, P., 2004. Geologic map of the Santa Paula 7.5-minute quadrangle, Ventura County, California, 1: 24, 000. California Geological Survey, California.

Thibert, B., Gratier, J.-P. and Morvan, J.-M., 2005. A direct method for modeling and unfolding developable surfaces and its application to the Ventura Basin (California). Journal of Structural Geology, 27(2): 303-316.

Thompson, S.C., Weldon, R.J., Rubin, C.M., Abdrakhmatov, K., Molnar, P. and Berger, G.W., 2002. Late Quaternary slip rates across the central Tien Shan, Kyrgyzstan, central Asia. Journal of Geophysical Research: Solid Earth, 107(B9): 7-1 - 7-33.

Toda, S. and Enescu, B., 2011. Rate/state Coulomb stress transfer model for the CSEP Japan seismicity forecast. Earth, Planets and Space, 63(3): 171-185.

Toda, S. and Stein, R., 2003. Toggling of seismicity by the 1997 Kagoshima earthquake couplet: A demonstration of time-dependent stress transfer. Journal of Geophysical Research: Solid Earth, 108(B12): 7-1 - 7-12.

Toda, S., Stein, R.S., Reasenberg, P.A., Dieterich, J.H. and Yoshida, A., 1998. Stress transferred by the 1995 Mw= 6.9 Kobe, Japan, shock: Effect on aftershocks and future earthquake probabilities. Journal of Geophysical Research: Solid Earth, 103(B10): 24543-24565.

Toda, S., Stein, R.S., Richards-Dinger, K. and Bozkurt, S.B., 2005. Forecasting the evolution of seismicity in southern California: Animations built on earthquake stress transfer. Journal of Geophysical Research: Solid Earth, 110(B5): 1-17.

Tsutsumi, H. and Yeats, R.S., 1999. Tectonic setting of the 1971 Sylmar and 1994 Northridge earthquakes in the San Fernando Valley, California. Bulletin of the Seismological Society of America, 89(5): 1232-1249.

Tucker, G. and Whipple, K., 2002. Topographic outcomes predicted by stream erosion models: Sensitivity analysis and intermodel comparison. Journal of Geophysical Research: Solid Earth, 107(B9): 1-1 - 1-16.

Tucker, G.E., 2009. Natural experiments in landscape evolution. Earth Surface Processes and Landforms, 34(10): 1450-1460.

Van Der Woerd, J., Klinger, Y., Sieh, K., Tapponnier, P., Ryerson, F.J. and Mériaux, A.S., 2006. Long-term slip rate of the southern San Andreas fault from ^{10}Be-^{26}Al surface exposure dating of an offset alluvial fan. Journal of Geophysical Research: Solid Earth, 111(B4): 1-17.

Vance, D., Bickle, M., Ivy-Ochs, S. and Kubik, P.W., 2003. Erosion and exhumation in the Himalaya from cosmogenic isotope inventories of river sediments. Earth and Planetary Science Letters, 206(3-4): 273-288.

Vedder, J., Wagner, H. and Schoellhamer, J., 1969. Geologic framework of the Santa Barbara Channel region. US Geological Survey Professional Paper, 679: 1-11.

Verdecchia, A. and Carena, S., 2016. Coulomb stress evolution in a diffuse plate boundary: 1400 years of earthquakes in eastern California and western Nevada, USA. Tectonics, 35(8): 1793-1811.

Wagner, H., Lander, E., Roeder, M., Prothero, D. and McDaniel, G., 2007. A new Irvingtonian land mammal assemblage from the Saugus Formation, Moorpark, Ventura County, California. Bulletin: Southern California Academey of Sciences, 106(2): 143A.

Wallace, R.E., 1987. Grouping and migration of surface faulting and variations in slip rates on faults in the Great Basin province. Bulletin of the Seismological Society of America, 77(3): 868-876.

Wang, Y., Schoenbohm, L.M., Zhang, B., Granger, D.E., Zhou, R., Zhang, J. and Hou, J., 2017. Late Cenozoic landscape evolution along the Ailao Shan Shear Zone, SE Tibetan Plateau: Evidence from fluvial longitudinal profiles and cosmogenic erosion rates. Earth and Planetary Science Letters, 472: 323-333.

Weber, F., Kiessling, E., Sprotte, E., Johnson, J., Sherburne, R. and Cleveland, G., 1976. Seismic hazards study of Ventura County. California: California Department of Conservation, California Division of Mines and Geology Open-File Report: 76-5.

Wedmore, L., Walker, J.F., Roberts, G.P., Sammonds, P., McCaffrey, K. and Cowie, P., 2017. A 667 year record of coseismic and interseismic Coulomb stress changes in central Italy reveals the role of fault interaction in controlling irregular earthquake recurrence intervals. Journal of Geophysical Research: Solid Earth, 122(7): 5691-5711.

Wehmiller, J., Lajoie, K., Sarna-Wojcicki, A., Yerkes, R., Kennedy, G., Stephens, T., Kohl, R. and Zartman, R., 1978. Amino acid racemization dating of Quaternary mollusks, Pacific coast United States. US Geological Survey Open-File Report, 78(701): 445-448.

Wehmiller, J.F., 1992. Aminostratigraphy of southern California Quaternary marine terraces. SEPM Special Publications, 48: 317-321.

Wells, D.L. and Coppersmith, K.J., 1994. New empirical relationships among magnitude, rupture length, rupture width, rupture area, and surface displacement. Bulletin of the seismological Society of America, 84(4): 974-1002.

Wesnousky, S.G., 2006. Predicting the endpoints of earthquake ruptures. Nature, 444(7117): 358.

Wesnousky, S.G. and Biasi, G.P., 2011. The length to which an earthquake will go to rupture. Bulletin of the Seismological Society of America, 101(4): 1948-1950.

Wesnousky, S.G., Briggs, R.W., Caffee, M.W., Ryerson, F., Finkel, R.C. and Owen, L.A., 2016. Terrestrial cosmogenic surface exposure dating of glacial and associated landforms in the Ruby Mountains-East Humboldt Range of central Nevada and along the northeastern flank of the Sierra Nevada. Geomorphology, 268: 72-81.

West, A.J., Hetzel, R., Li, G., Jin, Z., Zhang, F., Hilton, R.G. and Densmore, A.L., 2014. Dilution of 10Be in detrital quartz by earthquake-induced landslides: Implications for determining denudation rates and potential to provide insights into landslide sediment dynamics. Earth and Planetary Science Letters, 396: 143-153.

Whipple, K., Wobus, C., Crosby, B., Kirby, E. and Sheehan, D., 2007. New tools for quantitative geomorphology: extraction and interpretation of stream profiles from digital topographic data, GSA short course, GSA Annual Meeting, Boulder, Colorado.

Whipple, K.X., 2004. Bedrock rivers and the geomorphology of active orogens. Annu. Rev. Earth Planet. Sci., 32: 151-185.

Whipple, K.X., 2009. The influence of climate on the tectonic evolution of mountain belts. Nature Geoscience, 2(2): 97-104.

Whipple, K.X., DiBiase, R.A., Ouimet, W.B. and Forte, A.M., 2017. Preservation or piracy: Diagnosing low-relief, high-elevation surface formation mechanisms. Geology, 45(1): 91-94.

Whipple, K.X. and Tucker, G.E., 1999. Dynamics of the stream-power river incision model: Implications for height limits of mountain ranges, landscape response timescales, and research needs. Journal of Geophysical Research: Solid Earth, 104(B8): 17661-17674.

Whittaker, A.C., 2012. How do landscapes record tectonics and climate? Lithosphere, 4(2): 160-164.

Whittaker, A.C., Attal, M., Cowie, P.A., Tucker, G.E. and Roberts, G., 2008. Decoding temporal and spatial patterns of fault uplift using transient river long profiles. Geomorphology, 100(3-4): 506-526.

Whittaker, A.C. and Boulton, S.J., 2012. Tectonic and climatic controls on knickpoint retreat rates and landscape response times. Journal of Geophysical Research: Earth Surface, 117(F2): 1-19.

Whittaker, A.C., Cowie, P.A., Attal, M., Tucker, G.E. and Roberts, G.P., 2007. Bedrock channel adjustment to tectonic forcing: Implications for predicting river incision rates. Geology, 35(2): 103-106.

Whittaker, A.C. and Walker, A.S., 2015. Geomorphic constraints on fault throw rates and linkage times: Examples from the Northern Gulf of Evia, Greece. Journal of Geophysical Research: Earth Surface, 120(1): 137-158.

Wilcken, K., Fink, D., Hotchkis, M., Garton, D., Button, D., Mann, M., Kitchen, R., Hauser, T. and O'Connor, A., 2017. Accelerator Mass Spectrometry on SIRIUS: New 6MV spectrometer at ANSTO. Nuclear Instruments and Methods in Physics Research Section B, 406: 278-282.

Winterer, E.L. and Durham, D.L., 1962. Geology of southeastern Ventura Basin, Los Angeles County, California.

Wobus, C., Whipple, K.X., Kirby, E., Snyder, N., Johnson, J., Spyropolou, K., Crosby, B., Sheehan, D. and Willett, S., 2006a. Tectonics from topography: Procedures, promise, and pitfalls. Geological Society of America: Special Papers, 398: 55-74.

Wobus, C.W., Crosby, B.T. and Whipple, K.X., 2006b. Hanging valleys in fluvial systems: Controls on occurrence and implications for landscape evolution. Journal of Geophysical Research: Earth Surface, 111(F2): 1-14.

Woessner, J., Hainzl, S., Marzocchi, W., Werner, M., Lombardi, A., Catalli, F., Enescu, B., Cocco, M., Gerstenberger, M. and Wiemer, S., 2011. A retrospective comparative forecast test on the 1992 Landers sequence. Journal of Geophysical Research: Solid Earth, 116(B5): 1-22.

Wright, T.L., 1991. Structural geology and tectonic evolution of the Los Angeles basin, California. Active Margin Basins, 52: 35-134.

Xu, S., Freeman, S.P., Rood, D.H. and Shanks, R.P., 2015. Decadal 10Be, ^{26}Al and ^{36}Cl QA measurements on the SUERC 5 MV accelerator mass spectrometer. Nuclear Instruments and Methods in Physics Research Section B: Beam Interactions with Materials and Atoms, 361: 39-42.

Xu, X., Wen, X., Yu, G., Chen, G., Klinger, Y., Hubbard, J. and Shaw, J., 2009. Coseismic reverse-and oblique-slip surface faulting generated by the 2008 M_w 7.9 Wenchuan earthquake, China. Geology, 37(6): 515-518.

Yanites, B.J., Tucker, G.E. and Anderson, R.S., 2009. Numerical and analytical models of cosmogenic radionuclide dynamics in landslide-dominated drainage basins. Journal of Geophysical Research: Earth Surface, 114(F1): 1-20.

Yeats, R., 1981. Deformation of a 1 Ma Datum, Ventura Basin, California: US Geological Survey Technical Report. contract(14-08): 0001-18283.

Yeats, R., Butler, M. and Schlueter, J., 1977. Santa Susana-San Cayetano-Red Mountain fault system: Subsurface geology, mechanical analysis, and displacement rates. Part III, Geology of the central Santa Susana fault area, Ventura and Los Angeles counties, United States Geological Survey: Final technical report, contract 14-08-0001-15886, 29 pp.

Yeats, R.S., 1982. Low-Shake faults of the Ventura Basin, California. In: J.D. Cooper (Editor), 78th Cordilleran Section Annual Meeting, Guide Book. Geological Society of America, pp. 21-23.

Yeats, R.S., 1988. Late Quaternary slip rate on the Oak Ridge fault, Transverse Ranges, California: Implications for seismic risk. Journal of Geophysical Research, 93(B10): 12137-12149.

Yeats, R.S. and Huftile, G.J., 1995. The Oak Ridge fault system and the 1994 Northridge earthquake. Nature, 373(6513): 418-420.

Yeats, R.S., Huftile, G.J. and Grigsby, F.B., 1988. Oak-Ridge Fault, Ventura Fold Belt, and the Sisar Decollement, Ventura Basin, California. Geology, 16(12): 1112-1116.

Yeats, R.S., Huftile, G.J. and Stitt, L.T., 1994. Late Cenozoic tectonics of the east Ventura basin, Transverse Ranges, California. AAPG Bulletin, 78(7): 1040-1074.

Yerkes, R., Sarna-Wojcicki, A. and Lajoie, K., 1987. Geology and Quaternary deformation of the Ventura area. Recent reverse faulting in the Transverse Ranges, California. US Geological Survey Professional Paper, 1139: 169-178.

Yerkes, R.F. and Lee, W.H.K., 1979. Late Quaternary deformation in the western Transverse Ranges, California, Circular 799-B. US Department of the Interior, Geological Survey.

Yue, L.-F., Suppe, J. and Hung, J.-H., 2005. Structural geology of a classic thrust belt earthquake: The 1999 Chi-Chi earthquake Taiwan (M_w 7.6). Journal of Structural Geology, 27(11): 2058-2083.

Zechar, J.D. and Frankel, K.L., 2009. Incorporating and reporting uncertainties in fault slip rates. Journal of Geophysical Research: Solid Earth, 114(B12): 1-9.

Zhao, Z., Granger, D., Zhang, M., Kong, X., Yang, S., Chen, Y. and Hu, E., 2016. A test of the isochron burial dating method on fluvial gravels within the Pulu volcanic sequence, West Kunlun Mountains, China. Quaternary Geochronology, 34: 75-80.

Ziv, A. and Rubin, A.M., 2000. Static stress transfer and earthquake triggering: No lower threshold in sight? Journal of Geophysical Research: Solid Earth, 105(B6): 13631-13642.

Appendices

Appendix A: Supplementary Materials to Chapter 2

A1 Field Sampling Methods

Depth profiles were used to improve the geochronology for alluvial terraces and alluvial fans at Orcutt, Timber, and Bear Canyons, and for the fold in the Santa Clara River Valley. Existing geomorphic mapping (Rockwell, 1983) was digitized using ArcGIS and refined using outputs from the lidar dataset. A well-developed soil profile and little evidence of modification to the terrace tread were interpreted to indicate that a surface has undergone little erosion since abandonment. The strength and thickness of soil profile development and, if appropriate, the elevation relative to the level of the modern Orcutt Canyon channel were used to field check the approximate age of terraces, following Rockwell (1983). Older surfaces are interpreted to have a strongly developed soil profile, including a well-developed argillic horizon and increasing development of the B horizon with increasing age. Q4 surfaces at Orcutt Canyon are generally 6–10 m above the current stream level, Q5 terraces are generally situated 25–35 m above the current stream level, and the Q6 surfaces are up to 100 m above the current stream level.

All deposits were poorly sorted and consist of a range of grain sizes from silt to boulders. The Q4 and Q5 sample locations at Orcutt Canyon and the Q4 locality on the Bear Canyon fan are river cut exposures. The Q6 sample at Timber Canyon was collected from a hillside terrace tread exposure, and the Q5 sample from the fold in the Santa Clara River Valley was taken from a train track exposure.

At each sample site, the outer ~50 cm of surface cover was removed to prevent contamination from material washed down from above and to negate the effect of nuclide accumulation from the sidewall. Level lines were set up every 40 cm, from a depth of 40 cm below the terrace

surface down to 200 cm below the terrace surface. Samples of the bulk sediment were collected from ~5 cm above and below of the level line (i.e. a range of ~10 cm). Samples were collected from bottom to top to avoid lower samples being contaminated by sediment from above during sample collection. A compass and clinometer were used to measure the topographic shielding at each of the sample localities. Latitude, longitude, and elevation for each sample were measured using a handheld GPS.

A2 Sample preparation and laboratory methods

During quartz separation in the CosmIC laboratory at Imperial College London, bulk sediment samples were sieved to isolate the 250–500 μm fraction. For samples with a low 250–500 μm yield, the 500–1000 μm fraction was included to increase the sample yield. Sample purity was measured using an Agilent 5100 SVDV inductively coupled plasma-optical emission spectrometer (ICP-OES) prior to sample dissolution.

Beryllium isolation took place at the University of Vermont using the methodology of Corbett et al (2016). Firstly, an in house ^{9}Be carrier solution produced from beryl was added to samples. Ten samples were processed alongside a blank to account for laboratory background contamination and a sample of the CRONUS-N sand (Jull et al., 2015) to assess inter-laboratory reproducibility in results. Pure quartz was dissolved in concentrated HF before being converted into chloride form by fuming in $HClO_4$ and drying down in HCl. Be was isolated in the samples using ion exchange chromatography. Anion exchange chromatography with HCl was employed to remove Fe from the samples. Cation exchange chromatography, firstly with H_2SO_4 and secondly with HCl was conducted to isolate Be. Be in solution was precipitated as a beryllium hydroxide gel which is ignited using a Bunsen burner to produce beryllium oxide. Beryllium oxide was mixed with Nb powder and transferred into copper cathodes ready for analysis using accelerator mass spectrometry (AMS).

During $^{10}Be/^{9}Be$ AMS measurements at the Centre for Accelerator Science at the Australian Nuclear Science and Technology Organization average BeO^- ion beam currents were 2.5–6.5 μA for the samples and 3–10 μA for the standards. The average BeO^- ion beam current for the samples was 62% of the average beam current for the primary standard and the range in 1σ analytical $^{10}Be/^{9}Be$ measurement uncertainties was 2.7–8.2%. Measured $^{10}Be/^{9}Be$ AMS ratios for the three process blanks were 6.94×10^{-16}, 5.47×10^{-16}, and 4.93×10^{-16}. This equates to total ^{10}Be atoms in each of the three process blanks of 8857 +/- 2288 atoms, 11187 +/- 2388 atoms, and 7876 +/- 2786 atoms. Blank corrected 1σ analytical uncertainties for all samples ranged from 2.9–9.3%.

A3 Data reduction and application of a Monte Carlo Simulation to calculating surface ages

Measured AMS $^{10}Be/^{9}Be$ ratios were converted to concentrations and samples were blank corrected relative to the batch-specific process blank, assuming that the main source of ^{10}Be contamination came from either (i) within the laboratory during sample processing, (ii) a small amount of potential ^{10}Be in the carrier itself, or (iii) background ^{10}Be within the AMS. Background ^{10}Be in the AMS is most likely from ^{10}B isobaric interference, but ^{10}B corrections were <1%. The measured ratio of $^{10}Be/^{9}Be$ in the carrier is ~8.19×10^{-17} to 1.62×10^{-16}. This equates to 1329 +/- 1329 to 2622 +/- 1854 atoms of ^{10}Be in the carrier. The mean ^{10}Be atoms for all process blanks was 9307 +/- 2487 atoms. This equates to 0.2–9.9% atoms ^{10}Be in the process blanks compared to total atoms ^{10}Be in each of the samples. A complete list of all sample parameters, constants, production rates, carrier concentrations, measured AMS ratios, and reduced ^{10}Be concentrations for all samples is includes in Table ST1 and sample parameters for the blanks are included in Table ST2.

Exposure ages along with associated uncertainties were calculated using a Monte Carlo simulator (Hidy et al., 2010). Density is modelled ranging from 1.7–1.8 g cm^{-3}, based on average values of soil samples from both published and unpublished work, encompassing a dataset of hundreds of soil samples from various geographical locations (Eric McDonald, pers comm). The only previous depth profile from the Ventura Basin employed a density range of 2.2–2.5 g cm^{-3} (DeVecchio et al., 2012a). However, we do not employ this range as we feel these values are too high for the poorly consolidated late Pleistocene-Holocene alluvial terrace and fan deposits sampled here. A comparison of output ages using the higher density range of 2.2–2.5 g cm^{-3} (DeVecchio et al., 2012a) is included in Table ST4.

Corrections for topographic shielding were made using the CRONUS-Earth online geometric shielding calculator, version 1.1 (available at: http://hess.ess.washington.edu/math/general/skyline_input.php). We employ a reference production rate of 4.24 +/- 0.12 atoms g^{-1} yr^{-1} in our Monte Carlo age simulations. The reference production rate was calculated by inputting the Promontory Point (PPT) location reference production rate calibration data from Lake Bonneville, Utah, USA (Lifton et al., 2015) into the CRONUS-Earth online exposure-age calculator version 2.3 (available at: https://hess.ess.washington.edu/) (Balco, 2009). We prefer the 4.24 +/- 0.12 atoms g^{-1} yr^{-1} value as opposed to alternative reference production rates (e.g. Balco, 2009; Borchers et al., 2016) as these alternative values are normalized values based on global calibration data from a range of geographical locations and latitudes. The PPT data is the closest calibration dataset to our sample locations, both geographically and in terms of latitude, and has a consistently higher measured ^{10}Be reference production rate than other calibration datasets from other geographic locations, latitudes, and altitudes (see Figure 1 from Borchers et al., 2016). Ages output from Monte Carlo simulations employing various reference production rates all overlap within the uncertainties and are presented in Table ST4.

No published rates of erosion are available for the specific sample localities. Consequently, we have assumed zero erosion of the fill terraces at the locations we sampled in our Monte Carlo simulator model inputs. We acknowledge that zero erosion across an entire terrace surface is unlikely. However, as we have no data to quantify erosion rates at our specific sample locations, figures S4 to S7 are included to demonstrate the basis for little erosion being a reasonable assumption for each of the specific depth profile localities. The Q4 fan at Bear Canyon has a relatively smooth, convex, cross profile, with the exception of the most northerly 200 m, which is raised in elevation by ~8 m relative the rest of the profile (Fig. S3 A-A'). Radial long profiles across the fan show a smooth surface with a constant dip of around 5° to the southwest. The fan profile is truncated sharply by a steep sub-vertical dip where the fan is cut by Sisar Creek (Fig. S3 B-B' to E-E'). The 5° dip in the fan surface is significantly perturbed at the south west end of profile B-B'. At roughly 400 m distance profile B-B' levels off for ~100 m before a steep 15 m drop where the fan meets Sisar Creek. We interpret this mound to be man-made ground, resulting from construction of the houses in Fig. S3F. The made ground terminates 50 m north of our sample site. We conclude that a small variation in both fan cross profiles and radial profiles in conjunction with complete Q4 soil profile development justifies the assumption of zero erosion.

The Q5 sample at Orcutt Canyon is located on the edge of a subsidiary channel, 200 m west from the main Orcutt Canyon channel (Fig. S4 A-A'). A colluvial wedge is draped over the western section of the terrace (Fig. S4). If sampled, the colluvial wedge would record a younger event than abandonment of the Q5 fill terrace. However, cross profiles B-B' to D-D' in Figure S5 clearly show that the colluvium terminates about 30 m west of the Q5 sample location. The flat morphology of the topography in profiles B-B' to D-D' and the presence of a complete Q5 soil profile is taken to indicate that the surface has not undergone significant erosion.

For the Q6 sample locality at Timber Canyon, we use standard deviation in slope as a proxy for the amount of erosion that has occurred (Frankel and Dolan, 2007). We assume that highly eroded surfaces will have higher variation in slope and analyse the fan remnant surface in three sections; a more eroded southern section (range in slope 49°), a moderately eroded middle section (range in slope 39°), and a relatively uneroded northern section (range in slope 30°) (Fig. S5). Using this analysis and observing the proximity of the sample location to a channel in the cross profile in D-D' (Fig. S5), it would appear that our Q6 sample is taken from an eroded portion of the fan. However, detailed analysis of long profiles demonstrates that an un-eroded fan surface is a reasonable assumption. Long profile E-E' in Figure S6 is oriented north-south through a planar section of the surface not cut by channels. This profile has a slope of 26° (Fig. S5). Long profile F-F' in Fig. S5 runs along the western edge of the surface and passes through our sample location for the Q6 terrace age. Profile F-F' has an almost identical slope (25°) to profile E-E at our Q6 sample location, and also has a planar, smooth surface. We interpret the similarity in slope and smoothness between the profile E-E' and profile F-F' in Figure S6, along with the presence of a complete Q6 soil profile, to indicate that sample locality for Q6 has not been affected by channel incision and assume no erosion.

The fold in the Santa Clara River Valley warps the valley floor for 2 km along the line of the east to west trending fold axial trace (Fig. S6). A section of the middle portion of the fold has been removed by river erosion leaving two-fold segments separated by a ~350 m wide gap. The larger eastern section of the fold is 1300 m along the fold axial trace and the smaller western section of the fold is 350 m along the fold axial trace. The larger eastern section of the fold has been heavily eroded along its southern limb, with the amount of erosion decreasing westward along strike of the fold axial trace (Fig. S6). Profile B-B' in Figure S7 demonstrates that the crest of the fold has been eroded away in the area where maximum uplift has occurred. However, profile A-A' in Figure S7 shows a complete, rounded fold hinge which does not

appear to have been significantly affected by erosion. Profile A-A' is taken through the location of our depth profile for the Q5 fold. We take the presence of a complete Q5 soil profile and the complete fold profile in section A-A' (Fig. S6) to indicate that this portion of the fold has not undergone significant erosion.

The above discussion demonstrates that minimal erosion has occurred at all of our sample locations. A depth profile has previously been used to model landscape evolution in the Ventura Basin (DeVecchio et al., 2012a). Erosion in this instance was modelled between 0 and 0.1 cm ka^{-1}. Using a range of 0 to 0.1 cm ka^{-1} for our samples and including a maximum potential erosion value of 10 or 20 cm (values most likely far higher than is realistic given the well-developed soil profiles) does not significantly alter the ages output from Monte Carlo simulations (Table ST5). A comparison between our preferred rates incorporating no erosion and rates incorporating a range of small amounts of erosion is included in Table ST5.

A4 Lidar data and description of parameters used to calculate displacement rates

The Ventura County lidar dataset was collected during February 2005 using a swath width of 560 m and a laser pulse rate of 25,000 Hz. The lidar data was collected with a 15 cm vertical precision and a 45 cm horizontal precision. Bare earth topography was extracted from the raw laser returns using techniques proprietary to Airborne1 (Airborne1, 2005).

Monte Carlo simulations incorporate uncertainties in various different input parameters by assigning a suitable probability density function (PDF) to each input (Zechar and Frankel, 2009). The type of PDF applied to each input variable should be the PDF that best defines the uncertainty associated with the specific variable. Five different input parameters were used to calculate most likely values and uncertainties in slip rates and throw rates for the Q4 and Q5 scarps at Orcutt Canyon, and uplift rates for the Q6 surfaces at Timber Canyon and Santa Paula

Creek. These parameters are geomorphic surface age, geomorphic surface slope, geomorphic surface slope projection (intercept), fault position along the scarp, and fault dip. All Monte Carlo simulations were performed in Oracle Crystal Ball, a spreadsheet-based program for modelling uncertainty.

Geomorphic surface slope and intercept were calculated by applying a least squares linear regression to x-y coordinates derived from topographic cross profiles extracted from the lidar dataset (e.g. Rood et al., 2011b). The least squares linear regression was applied to the appropriate geomorphic surface in both the hanging wall and footwall of the fault. Uncertainty in slope and intercept is modelled using a PDF with a normal distribution under the assumption that scatter in the data either side of the regression line has a normal distribution defined by a mean and standard deviation.

For the Q4 and Q5 surfaces at Orcutt Canyon, a linear regression was applied to surfaces both immediately north and south of the fault scarp, assuming that surfaces correlate across the fault. This assumption was verified by comparing soil profiles in the field. The southern and northern sections of the Q5 surface in the hanging wall of the fault have been lost to erosion. Therefore, we plot a linear regression through the flat middle section of the Q5 surface and project this surface to the fault. A similar approach is applied to calculate uplift rates for Q6 fan surfaces at Timber Canyon and Santa Paula Creek. However, we use a linear regression through the surface of Q3 deposits in the footwall of the fault at these locations, as no Q6 deposits are preserved in the footwall.

Uncertainties in the age of the geomorphic surface are modelled for all surfaces using a custom PDF derived from the range and frequency of surface ages output from Monte Carlo age simulations (Hidy et al., 2010). A custom PDF is used as it encompasses all possible outputs for age from 100,000 trial runs during the depth profile Monte Carlo simulations. This approach

facilitates the incorporation of variation in positively and negatively-skewed uncertainties within the age.

No paleoseismic trenching has been conducted across the main trace of SSCF. Consequently, the position of the fault within the fault scarp is unquantified. We model fault position within the scarp using a custom trapezoidal PDF. A trapezoidal PDF assumes that the fault position is most likely between one half to one third scarp height, measured from the base of the scarp, with likelihood decreasing to zero at the top and base of the scarp. This assumption is based on the most likely fault position within the scarp derived from published trenching studies of active reverse faults and a literature review faulting on compressional tectonic regimes (Carver and McCalpin, 1996; Thompson et al., 2002).

In our slip rate Monte Carlo simulations, we also assign a custom trapezoidal PDF to model fault dip between 50° and 90°. The trapezoidal PDF assumes an equal likelihood of occurring between 60-80°, with likelihood decreasing to zero at 50° and 90°. Faults observed in shallow boreholes at the range front, west of Santa Paula Creek range from 54-90° (Earth Systems Southern California, 2013). Table ST3 includes the depth and sense of displacement for all faults observed in the shallow boreholes. The majority of faults recorded in the shallow boreholes have a steep northward dip of between 70–90° and the mean dip is ~77° (Table ST3). Most faults have either 'north-side up' or 'reverse left-lateral' displacement. We have excluded small splay faults with shallow dips, south dipping faults, and faults that have normal displacement from our calculations (5 out of a total of 20 faults discarded). We cannot confirm if any individual fault in this dataset is the SSCF, but the data defines a steeply north dipping zone of faulting, ~15 m deep, from 5-20 m depth below the surface (Table ST3). The assumption of a steep fault dip at the surface is also supported by observations that faults scarps in the Q4 and Q5 fans at the mouth of Orcutt Canyon are not significantly offset from the range front or from each other. Furthermore, by projecting the topographic profile across the Q5 scarp

above the topographic profile of the Q4 scarp and modelling the fault position on both scarps as one third- and one-half scarp height, we suggest an apparent fault dip at the surface of 51-64 degrees (Fig S1). Additionally, the 50-90° range includes the geometry of the SSCF used in previous modelling of ~60° (Nicholson et al., 2015; Marshall et al., 2017) facilitating a more rigorous comparison of our data with previous modelling.

Conversely, evidence from subsurface datasets suggests the fault has a ~20° dip in the subsurface. Including a fault dip as low as 20° in our Monte Carlo simulations for slip rates across the Q4 scarp at Orcutt Canyon does not significantly alter the slip rate values output from the simulations (Table ST6). However, the positively-skewed uncertainty increases as a lower fault dip creates a long tail in the frequency histogram output from the simulation (Table ST6). We have not included the additional uncertainty resulting from a shallow subsurface dip in Monte Carlo simulations as we are measuring the offset of geomorphic features at the surface and the evidence highlighted above does not support a shallow fault dip in the upper ~100 m. We have included comparison of output slip rates from Monte Carlo simulations encompassing various fault dips in Table ST6 to demonstrate that the output slip rates all overlap within uncertainties.

A5 Calculating displacement rates

Slip rates for the SSCF across the Q4 and Q5 terraces are calculated following the method of Thompson et al (2002). The fan or terrace is assumed to have initially formed a single planar surface, which has since been offset by activity on the SSCF to leave an uplifted hanging wall above a downthrown footwall (Fig. S7). A topographic profile is extracted from the lidar data across the scarp, perpendicular to the surface trace of the fault. Data in x-y coordinates, where x is the distance from the start of the profile and y is elevation (both in meters), is used to plot a linear regression through the hanging wall terrace tread ($y_h = m_h x + b_h$), footwall terrace tread ($y_f = m_f x + b_f$), and fault scarp surface ($y_s = m_s x + b_s$) (Fig. S7). The resulting linear regression

is used to calculate the mean and standard deviation of the slope of the line, and the intercept of the line with the y axis. Fault dip at the surface (d) is modelled between 50-90°. Across all the scarps the terrace tread in the hanging wall is tilted southwards relative to the footwall, therefore, the amount of dip-slip (s) on the fault is calculated using both a hanging wall and footwall component:

$$\boldsymbol{s = s_h + s_f}$$

ES1

where s_h is the hanging wall component of dip slip:

$$\boldsymbol{s_h = \frac{v_h}{\sin\delta + m_h \cos\delta}}$$

ES2

and s_f is the footwall component of dip slip:

$$\boldsymbol{s_f = \frac{v_f}{\sin\delta + m_f \cos\delta}}$$

ES3

In equation ES2, v_h is the hanging wall component of vertical separation (or fault throw):

$$\boldsymbol{v_h(x) = x(m_h - m_s) + b_h - b_s}$$

ES4

and in equation ES3, v_f is the footwall component of vertical separation (or fault throw):

$$\boldsymbol{v_f(x) = x(m_s - m_f) + b_s - b_f}$$

ES5

Both equations ES4 and ES5 require quantification of the mid-point in the scarp (x). To calculate x, we use the following equation:

$$\boldsymbol{x} = \boldsymbol{i_{hs}} + (\frac{\boldsymbol{x_r}}{\boldsymbol{2}})$$

ES6

Where i_{hs} is the intercept between the projection of the linear regression through the hanging wall tread with the projection of the linear regression through the scarp face, and x_r is the distance between i_{hs} and the intercept of the projection linear regression through the scarp face with the projection of the linear regression through the footwall (i_{fs}):

$$\boldsymbol{x_r} = \boldsymbol{i_{sf}} - \boldsymbol{i_{hs}}$$

ES7

Equations ES6 and ES7 require that topographic profiles are extracted with the highest values for y corresponding to the lowest values for x (i.e. elevation decreases from left to right). Slip rate (u) is then calculated by dividing the total dip slip on the fault by the time of abandonment of the offset surface (t):

$$\boldsymbol{u} = \frac{\boldsymbol{s}}{\boldsymbol{t}}$$

ES8

All parameters used in equations ES1-ES8 are described in Figure S7.

The same method is employed to calculate uplift for the Q6 fan surfaces at Timber Canyon and Santa Paula Creek. However, as no corresponding Q6 surfaces are preserved in the fault footwall we calculate minimum vertical separation (v) of the hanging wall relative to Q3 fans

surfaces in the footwall. We do not calculate slip rates for these surfaces as we cannot correlate the Q6 surfaces across the fault.

A simpler Monte Carlo simulation is employed to calculate most likely uplift rates for the Q6 strath at Orcutt Canyon and the Q5 fold in the Santa Clara River Valley. Uncertainties in the uplift are modelled using a normally distributed PDF with a mean and standard deviation. Uncertainties in age are modelled in the same way as for the fault slip rates by using a custom PDF based on the output histogram for the depth profile age simulation (Hidy et al., 2010). Uplift rate (i) is calculated by dividing the uplift (h) amount by the time of abandonment of the uplifted surface (t):

$$\boldsymbol{i = \frac{h}{t}}$$

ES9

Positive uncertainty is calculated by subtracting the modal value from the highest value with 95 % confidence limits. Negative uncertainty is calculated by subtracting the minimum value within the 95 % confidence limit from the modal value. The resulting output is either a displacement amount or displacement rate with a specific positive uncertainty and a specific negative uncertainty.

Interval uplift rates, fault throw rates, and fault slip rates, which represent the rate of activity for time intervals between the formation of two proximal offset terraces, are also calculated using Monte Carlo simulations. We use the output histogram for the amount of total displacement (throw, uplift, or slip) for each individual marker and the PDF for each individual marker age. An iterative Monte Carlo simulation models the most likely time interval between the terrace formation, and the amount of displacement that has occurred during that time interval, all with associated uncertainties. The final interval displacement rate and uncertainties

are then modelled using a Monte Carlo simulation incorporating the interval time and amount of displacement (with uncertainties) output from the iterative simulation.

Fault movements in the Ventura Basin are thought to include a strike-slip component (Nicholson, 1994; Marshall et al., 2008). However, we model deformation rates as purely reverse slip because there is little geomorphic evidence for lateral offset of geomorphic features, such as laterally offset channels or shutter ridges and we have no data to quantify strike-slip movements. Furthermore, differential rates of hanging wall and footwall subsidence are not considered in our displacement rates (Nicholson et al., 2007). We calculate displacement of the hanging wall relative to the footwall assuming that any regional non-tectonic subsidence is affecting both the hanging wall and the footwall in equal amounts.

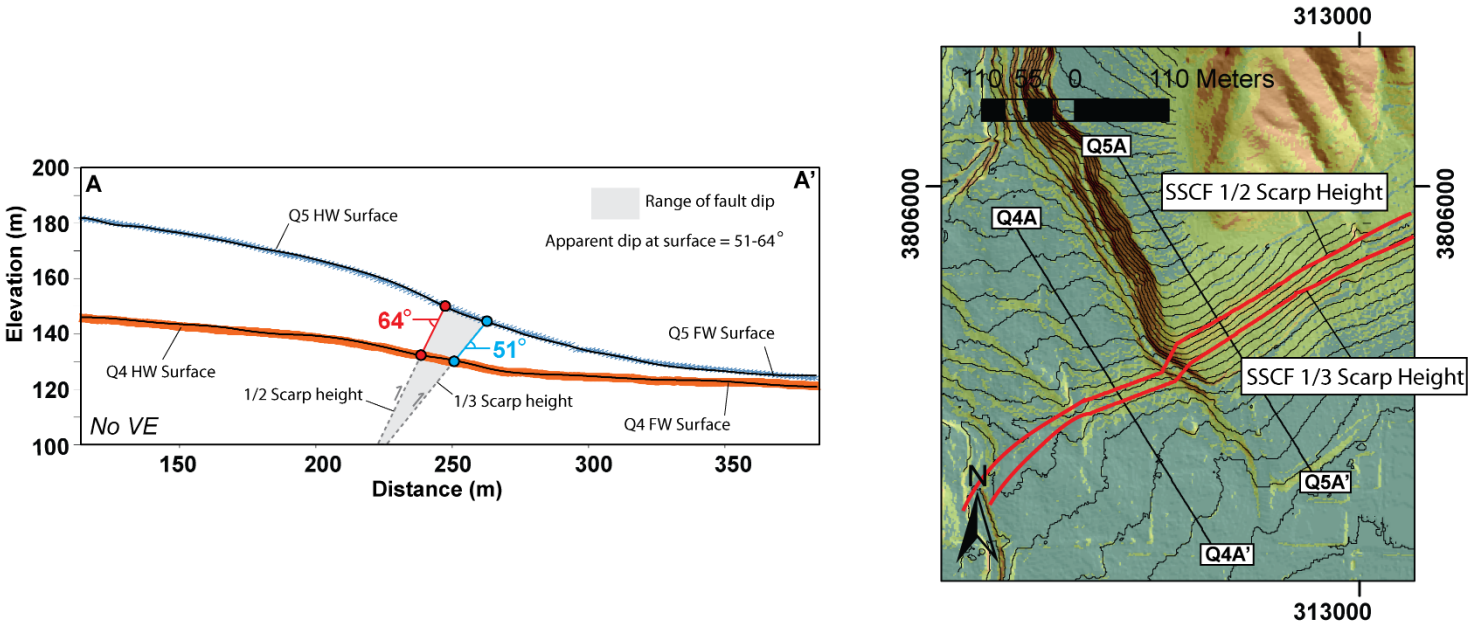

Figure S1 Range of apparent dips for the SSCF at the surface from topographic analysis of fault scarps in Q4 and Q5 alluvial fans assuming a fault position within the scarp of between one half and one third scarp height. The slope map on the right shows the fault trace if the fault intersected the scarp at one half or one third scarp height and the location of the cross sections across the Q4 and Q5 fault scarps at the mouth of Orcutt Canyon. Section A-A' is a section through the Q4 scarp in orange projected below the Q5 scarp in blue. The apparent dip of the SSCF at half scarp height is shown in red and the apparent dip for the SSCF at one third scarp height is shown in blue to define a range of apparent surface dips of the fault of 51–64°. VE = Vertical exaggeration.

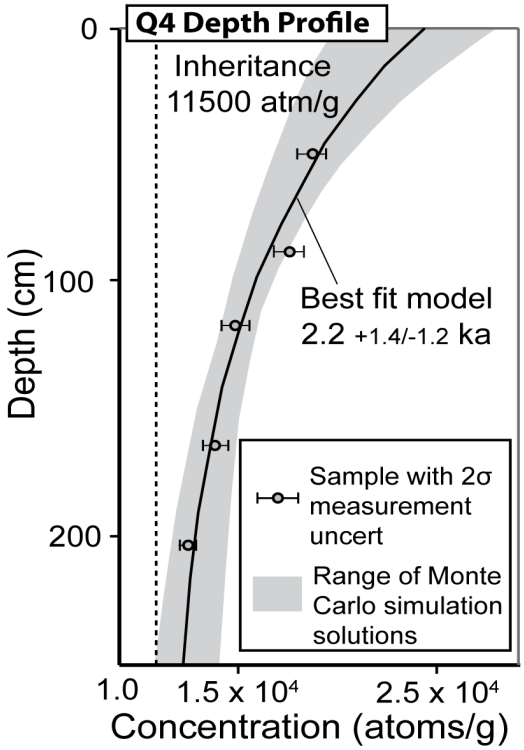

Figure S2 Depth profile for a Q4 (?) alluvial terrace at Orcutt Canyon

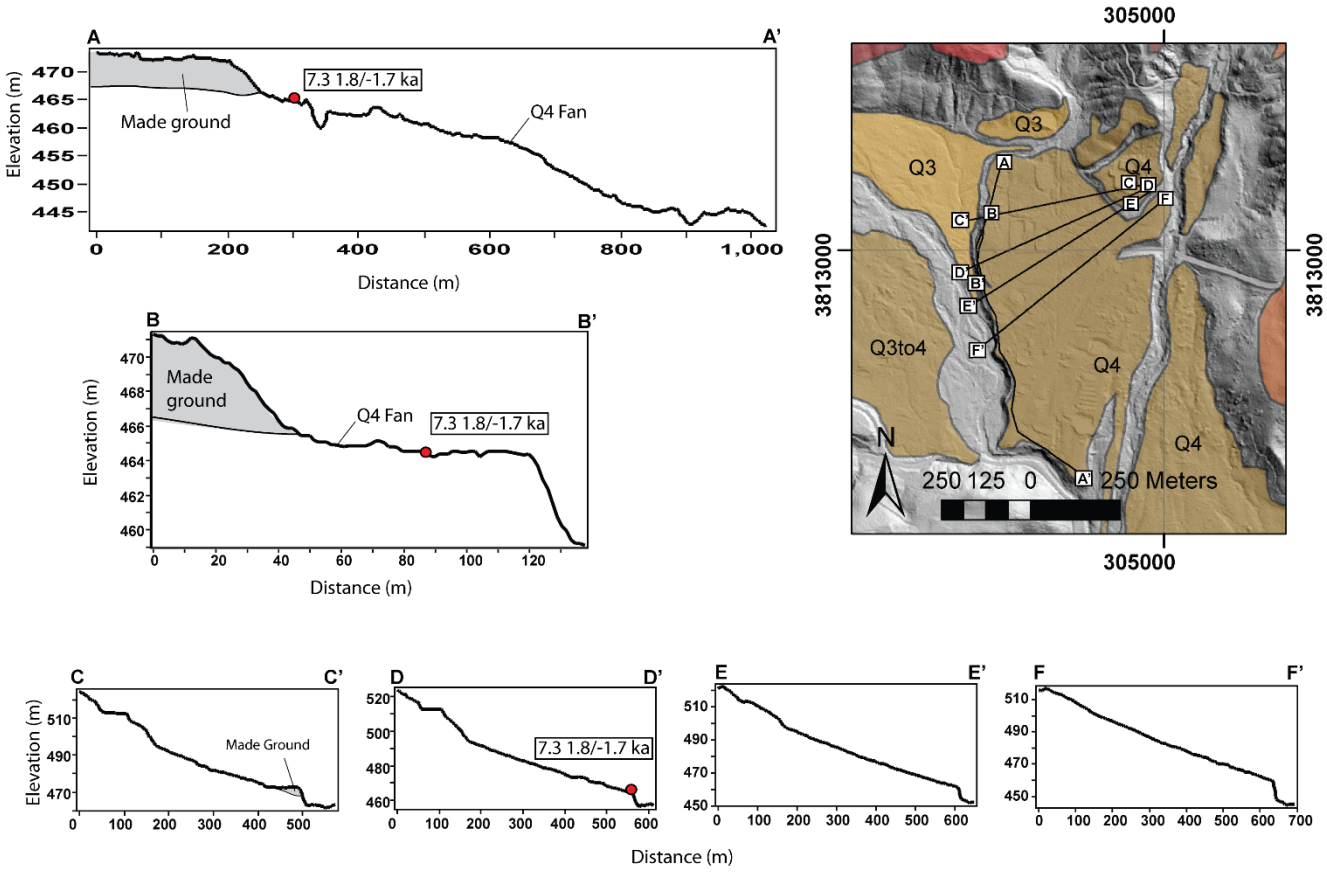

Figure S3 Erosion of the Q4 fan at Bear Canyon. (F) shows the extent of alluvial fans mapped at the mouth of the canyon and the lines of section for topographic profiles A-A' through E-E'. A-A' is a cross profile through the Bear Canyon fan showing the Q4 depth profile sample location and the extent of possible made ground. Sections B-B' through E-E' are long profiles through the Bear Canyon fan. B-B' shows the morphology of the fan around the made ground. C-C' shows the long profile of the fan through the Q4 depth profile sample location. D-D' and E-E' show the general long profile of the Bear Canyon fan.

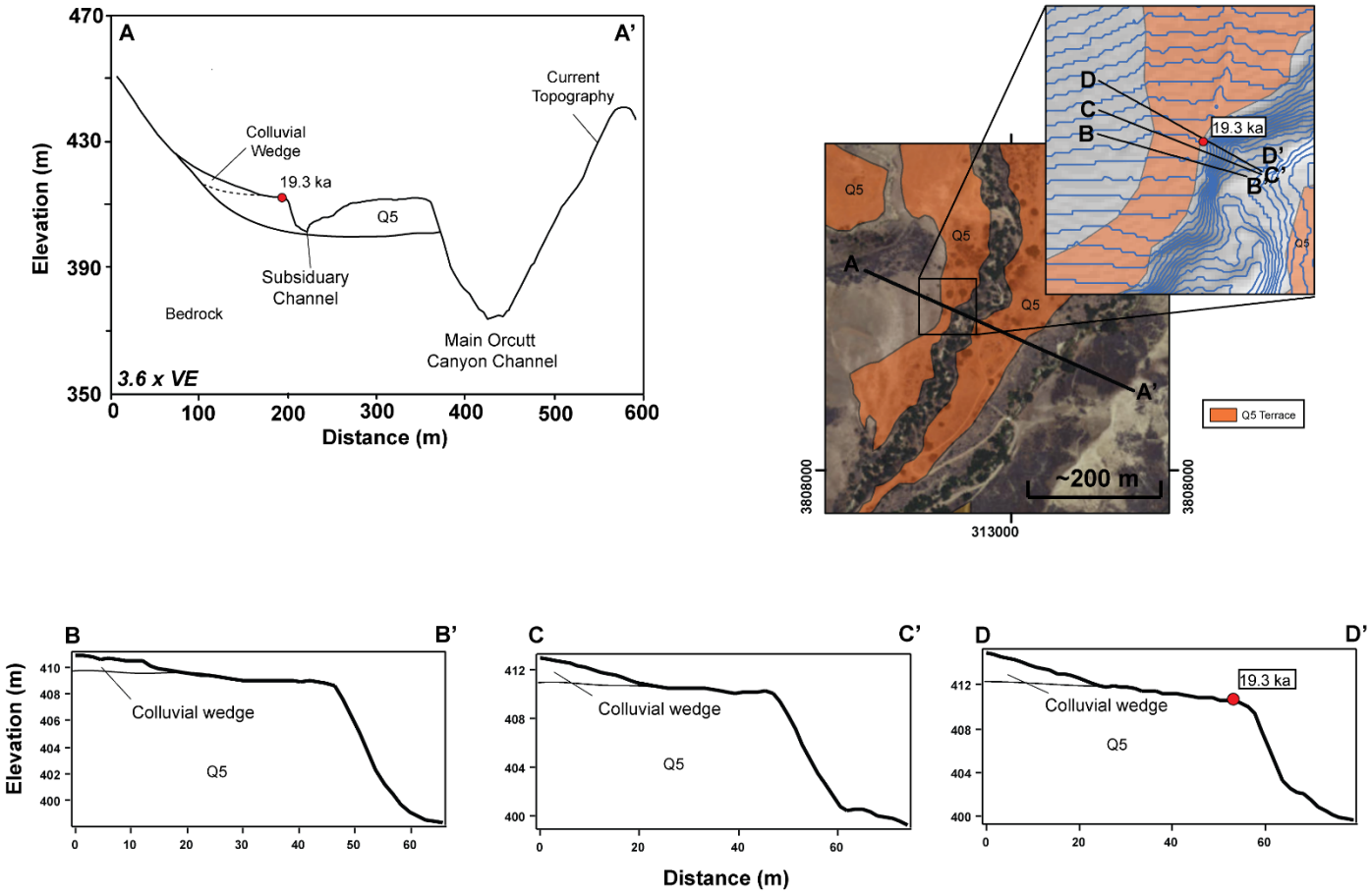

Figure S4 Erosion of the Q5 sample location at Orcutt Canyon. The aerial photograph in the top right shows the extent of the Q5 terrace around the Q5 depth profile sample and the line of section of profile A-A'. The extent of the inset contour map with a light hillshade is also shown. The inset contour map contains the line of section for cross profiles B-B' through D-D' and the location of depth profile sample for the Q5 terrace. Cross section A-A' shows the position of the subsidiary channel in relation to the main Orcutt Canyon channel. It also shows the thickness of the Q5 fill terrace, depth profile sample location for the Q5 terrace, and the extent of a colluvial wedge draped over the Q5 terrace. Sections B-B' through D-D' are zoomed in cross profiles through the Q5 terrace where the terrace is cut by a subsidiary of Orcutt Canyon and where our depth profile was taken. Sections C-C' through D-D' show that the colluvial wedge terminates roughly 30 m west of the sample location highlighted in section D-D'. VE = Vertical exaggeration.

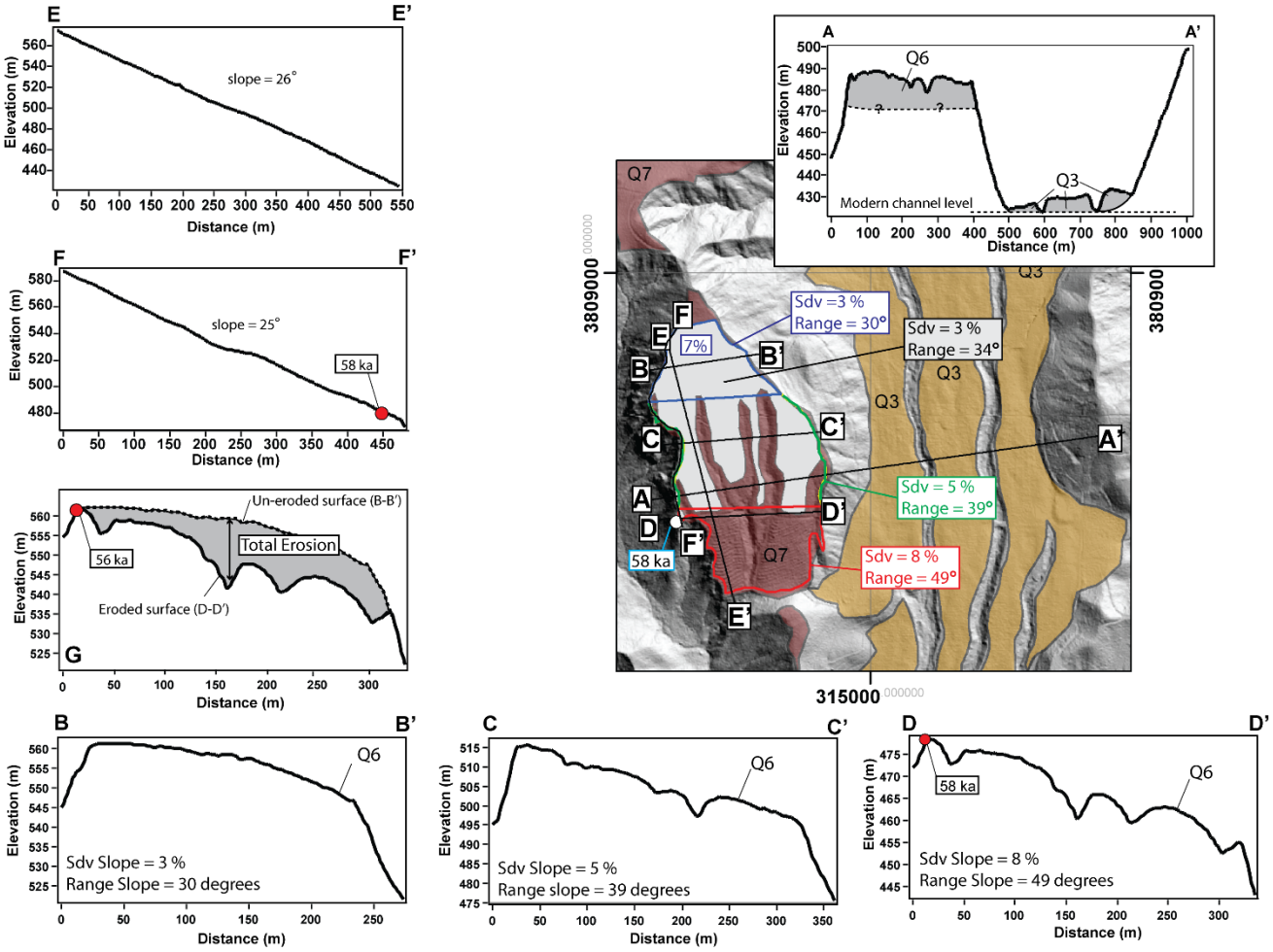

Figure S5 Erosion of the Q6 depth profile location at Timber Canyon. The hillshade map in the top right shows the extent of the Q6 and Q3 fans at Timber Canyon along with the lines of cross sections A-A' through F-F'. The highly eroded lower section of the Q6 fan is highlighted in red, the moderately eroded middle section is highlighted in green, and the smooth upper section in highlighted in blue. The grey polygon shows the area in the top two thirds of the fan which has not been incised by channels. Section A-A' is a cross profile showing the relative elevations and approximate thicknesses across the Q6 and Q3 fans. Cross sections B-B' through D-D' are taken through the lower (D-D'), middle (C-C'), and upper (B-B') sections of the Q6 fan and show the relative channel incision. The depth profile sample location is shown in section D-D'. E-E' and F-F' are long profiles down the Q6 fan. E-E' is a long profile down a smooth section of the fan and F-F' is taken along the edge of the fan through the depth profile sample location. G is a schematic correlative cross section which compares the amount of erosion is section D-D' to the smoothed cross profile in section B-B'.

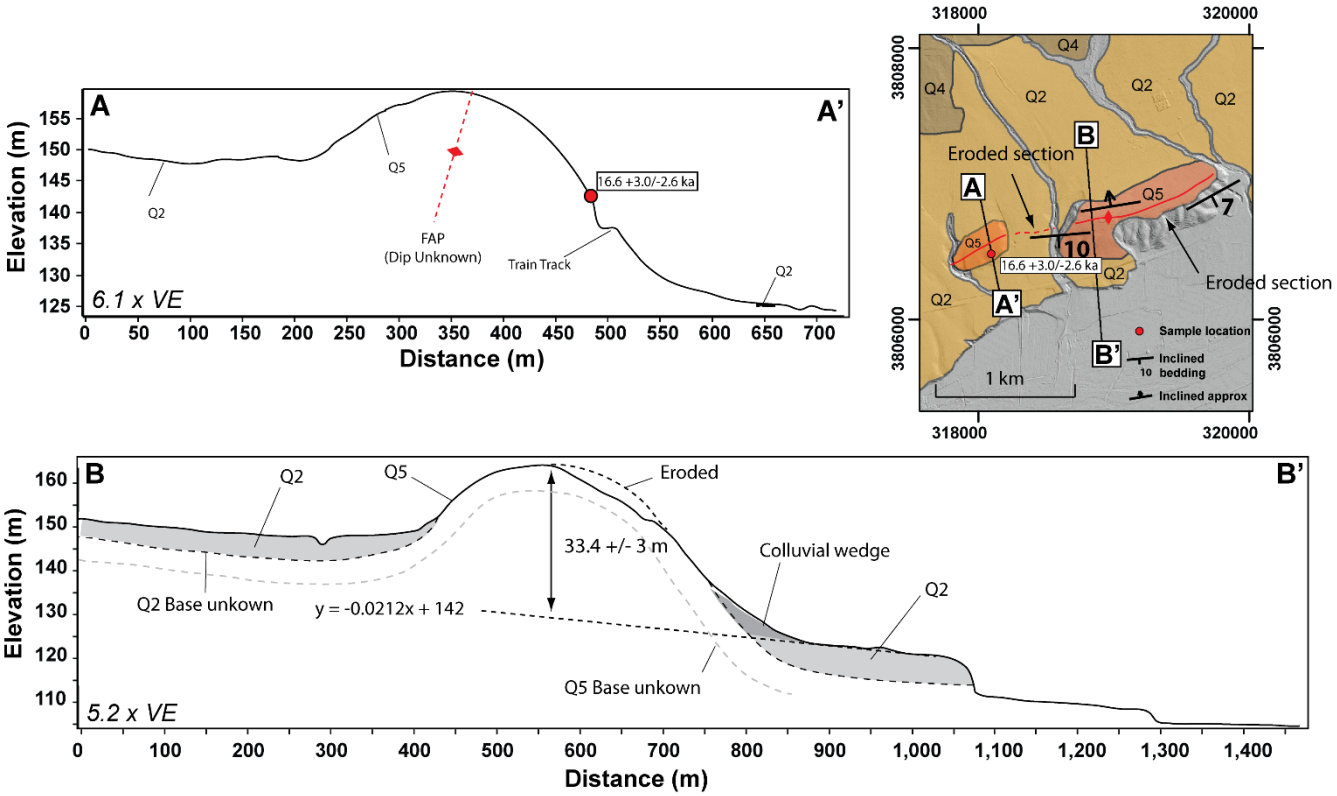

Figure S6 Morphology and erosion of the Q5 fold at the location of our depth profile in the Santa Clara River Valley. The inset hillshade map in the top right shows the line of cross sections A-A' and B-B' along with the axial trace of the fold and the dip of beds in the Q5 deposits. Section A-A' is taken through the fold at the location where our depth profile sample was located. Section B-B' is taken through the area of maximum uplift of the fold. Section B-B' shows the eroded area on the top of the fold and the projection of the top of the Q2 surface used to calculate uplift. We cannot measure the thickness of the Q5 or Q2 fill deposits in the subsurface but approximate geometries are shown to schematically demonstrate our structural interpretation of the fold. VE = Vertical exaggeration, FAP = Fold axial plane.

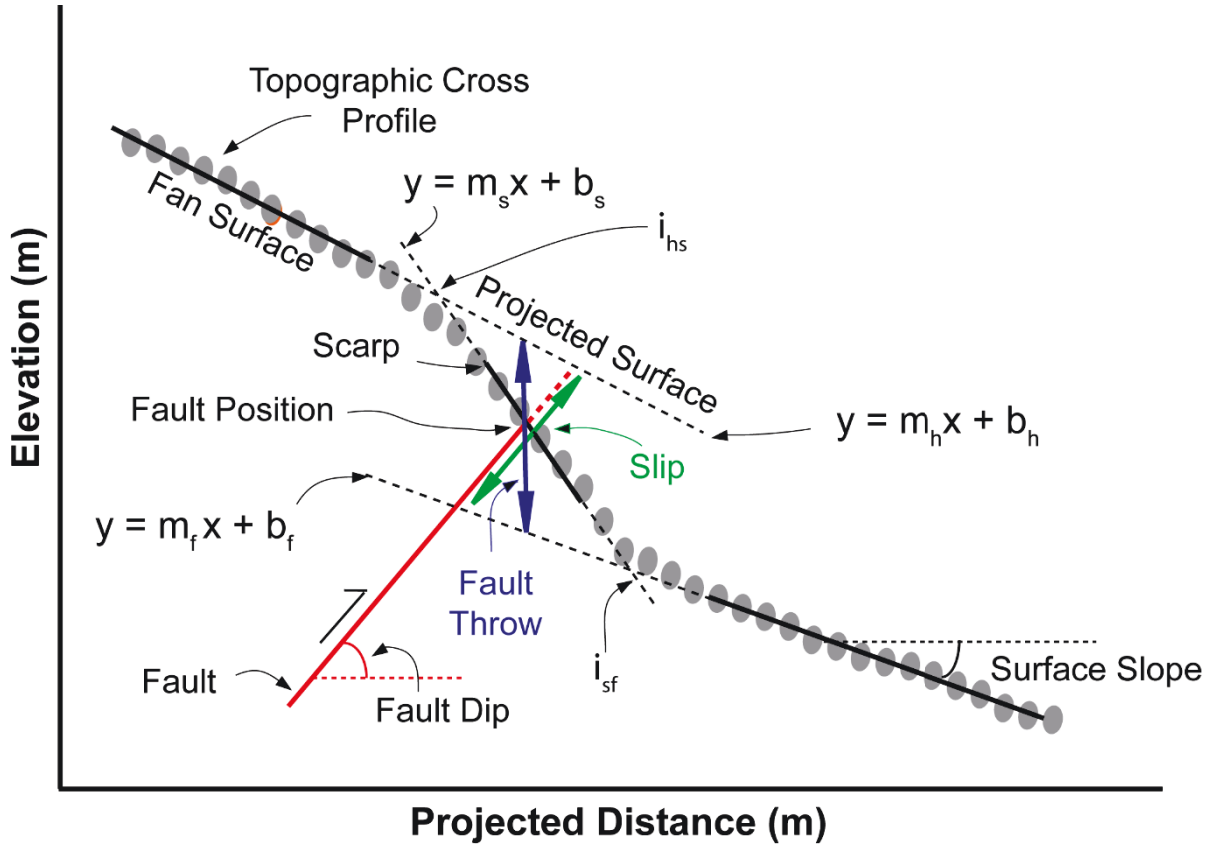

Figure S7 Parameters and equations used to calculate slip rates and throw rates using Monte Carlo simulations across the scarps at Orcutt Canyon and Q6 fan surfaces at Timber Canyon and Santa Paula Creek.

Table ST1 Full sample parameters used for data reduction

Sample	Cathode Number	Location		Elevation above SL (m)	Depth (cm)	Thickness [a] (cm)	Production Rate (atom/g/yr)		Shielding Factor [d]	Denudation Rate (mm/yr)	Quartz (g)	Be Carrier [e] (g)	$^{10}Be/^{9}Be$ [f,g]			^{10}Be Concentration (atoms/g SiO_2) [g, h, i]			Age (ka) [g, j, k]		
		°N	°W				Spallation [b]	Muons [c]													
KR 1	BE740	34.4397	-119.1282	459	39	6	5.54	0.212	0.998	0	16.029	0.8431	2.741E-14	+/-	1.067E-15	26925	+/-	1110	7.3	+/-	1.8/1.7
KR 2	BE741	34.4397	-119.1282	459	74	10	5.54	0.212	0.998	0	20.517	0.8369	3.057E-14	+/-	1.505E-15	23559	+/-	1205	7.3	+/-	1.8/1.7
KR 3	BE742	34.4397	-119.1282	459	116	12	5.54	0.212	0.998	0	19.873	0.8375	1.859E-14	+/-	8.150E-16	14560	+/-	681	7.3	+/-	1.8/1.7
KR 4	BE744	34.4397	-119.1282	459	153	12	5.54	0.212	0.998	0	14.049	0.8405	9.722E-15	+/-	5.765E-16	10496	+/-	681	7.3	+/-	1.8/1.7
KR 5	BE745	34.4397	-119.1282	459	182	13	5.54	0.212	0.998	0	10.631	0.8391	5.848E-15	+/-	4.769E-16	8028	+/-	743	7.3	+/-	1.8/1.7
OCN 1	BE734	34.3994	-119.0356	416	42	6	5.96	0.209	0.997	0	21.094	0.8359	9.653E-14	+/-	2.718E-15	72312	+/-	2177	19.3	+/-	2.7
OCN 2	BE735	34.3994	-119.0356	416	84	9	5.96	0.209	0.997	0	19.796	0.8375	7.008E-14	+/-	1.987E-15	55892	+/-	1699	19.3	+/-	2.7
OCN 3	BE737	34.3994	-119.0356	416	124	10	5.96	0.209	0.997	0	21.135	0.8393	3.804E-14	+/-	1.337E-15	28230	+/-	1054	19.3	+/-	2.7
OCN 4	BE738	34.3994	-119.0356	416	169	9	5.96	0.209	0.997	0	20.559	0.8343	2.311E-14	+/-	1.054E-15	17336	+/-	839	19.3	+/-	2.7
OCN 5	BE739	34.3994	-119.0356	416	212	11	5.96	0.209	0.997	0	20.619	0.8295	1.391E-14	+/-	8.764E-16	10135	+/-	685	19.3	+/-	2.7
TC 1	BE758	34.4011	-119.0171	430	39	8	6.54	0.210	0.995	0	20.671	0.8369	2.656E-13	+/-	7.740E-15	204712	+/-	6316	58.4	+/-	12.7/9.0
TC 2	BE759	34.4011	-119.0171	430	76	6	6.54	0.210	0.995	0	17.770	0.8375	1.751E-13	+/-	5.273E-15	156845	+/-	4986	58.4	+/-	12.7/9.0
TC 3	BE760	34.4011	-119.0171	430	112	11	6.54	0.210	0.995	0	20.525	0.8387	1.419E-13	+/-	3.836E-15	110114	+/-	3186	58.4	+/-	12.7/9.0
TC 4	BE761	34.4011	-119.0171	430	153	7	6.54	0.210	0.995	0	21.315	0.8386	8.411E-14	+/-	2.451E-15	62617	+/-	1942	58.4	+/-	12.7/9.0
TC 5	BE763	34.4011	-119.0171	430	196	8	6.54	0.210	0.995	0	20.229	0.8326	6.242E-14	+/-	1.976E-15	48588	+/-	1629	58.4	+/-	12.7/9.0
FW 1	BE752	34.3832	-118.9784	139	41	11	4.50	0.190	0.999	0	14.712	0.8417	4.455E-14	+/-	1.503E-15	48179	+/-	1720	17.1	+/-	3.5/2.5
FW 3	BE754	34.3832	-118.9784	139	116	9	4.50	0.190	0.999	0	20.270	0.8361	3.199E-14	+/-	1.184E-15	24940	+/-	978	17.1	+/-	3.5/2.5
FW 4	BE755	34.3832	-118.9784	139	150	11	4.50	0.190	0.999	0	13.292	0.8376	1.356E-14	+/-	7.434E-16	15717	+/-	927	17.1	+/-	3.5/2.5
FW 5	BE757	34.3832	-118.9784	139	196	7	4.50	0.190	0.999	0	20.525	0.8389	1.409E-14	+/-	7.567E-16	10662	+/-	614	17.1	+/-	3.5/2.5
OC4 1	BE746	34.3859	-119.0360	225	45	10	4.06	0.196	0.984	0	20.822	0.8388	2.361E-14	+/-	9.777E-16	17849	+/-	790	2.2	+/-	1.4/1.2
OC4 2	BE747	34.3859	-119.0360	225	82	10	4.06	0.196	0.984	0	20.793	0.8398	2.232E-14	+/-	1.006E-15	16895	+/-	811	2.2	+/-	1.4/1.2
OC4 3	BE748	34.3859	-119.0360	225	114	6	4.06	0.196	0.984	0	21.267	0.8426	1.99E-14	+/-	9.089E-16	14733	+/-	720	2.2	+/-	1.4/1.2
OC4 4	BE750	34.3859	-119.0360	225	160	10	4.06	0.196	0.984	0	20.747	0.8432	1.837E-14	+/-	8.857E-16	13918	+/-	719	2.2	+/-	1.4/1.2
OC4 5	BE751	34.3859	-119.0360	225	202	6	4.06	0.196	0.984	0	21.325	0.8361	1.763E-14	+/-	8.549E-16	12866	+/-	670	2.2	+/-	1.4/1.2

a: Thickness is the range of depth over which sample was collected i.e. 6 cm = +/- 3cm above stated depth.

b: Constant (time-invariant) scaling scheme of Lal (1991) and Stone (2000) with a reference production rate of 4.24 +/- 0.12 atoms/g/yr based on calibratoin data from Lifton et al, (2015) and the CRONUS online calculator version 2.3 (Balco, 2009).

c: Muonogenic ^{10}Be production is modelled after Heisinger (2002a, 2002b).

d: Calculated using the CRONUS-Earth Geometric Shielding Calculator version 1.1 (available online at: http://hess.ess.washington.edu/).

e: In-house produced Be carrier has density of 1.012 g/ml and Be concentration of 291 µg/ml.

f: AMS measured ratios were normalized to standard 01-5-2 with a assumed $^{10}Be/^{9}Be$ ratio of 8.558×10^{-12} (Nishiizumi et al, 2007).

g: All uncertainties are 1σ confidence level.

h: ^{10}Be concentrations and associated measurement uncertainties are blank corrected relative to batch specific process blanks. Total atoms ^{10}Be in process blanks (atoms): KR & OC4 = 8857 +/- 2288, OCN = 11187 +/- 2388, TC & FW = 7876 +/- 2786.

i: Uncertainties include error in the blank, carrier mass (1%), and samples propogated in quadrature.

j: A ^{10}Be half-life of 1.387 +/- 0.012 My (Chmeleff et al., 2010) was used but we apply a greater uncertainty of 5% to the half-life in our simulations.

k: We plotted depth profiles using a Monte Carlo simulator following the methods of Hidy et al, (2010) assuming a density of 1.7-1.8 g/cm^3 and an attenuation length of 160 g/cm^2.

Table ST2 Sample parameters for blanks

Sample	Cathode Number	Be Carrier [a] (g)	$^{10}Be/^{9}Be$ [b, c]			^{10}Be atoms [c]		
B597I	BE736	0.8390	6.94E-16	+/-	1.49E-16	11187	+/-	2388
B599J	BE749	0.8424	5.47E-16	+/-	1.42E-16	8857	+/-	2288
B600K	BE762	0.8353	4.93E-16	+/-	1.75E-16	7876	+/-	2786

a: In-house produced be carrier has density of 1.012 g/ml and Be concentration of 291 µg/ml.

b: AMS measured ratios were normalized to standard 01-5-2 with an assumed $^{10}Be/^{9}Be$ ratio of 8.558 x 10^{-12} (Nishiizumi et al, 2007).

c: All uncertainties are 1σ confidence level.

Table ST3 Faults identified in shallow boreholes

Depth (ft)	Dip (°, azimuth)	Offset	Evidence
30.5	77 NW	Strike slip	8'' inch wide carbonate cemented zone
60	75 NW	n/a	6' wide fault zone with splays
64	74 NW	Reverse-left lateral	6'' wide strongly expressed fault zone, polished surfaces, slicken lines oriented 31/043
65	29 NE	n/a	1/2 to 1/4" minor splay from clay gouge
65.25	59 NW	n/a	6" wide clay gouge zone
65.75	54 NW	Reverse-left lateral	1/16" wide slicken lines and polished surfaces
67	77 (NE or SE?)	n/a	1/16" clay gouge
15.75	77 NW	n/a	1" cemented carbonate gouge
15.75	90	n/a	2" cemented carbonate gouge
18.5	69 NW	North side up	Clay gouge
22	76 NE	North side up	2.5" Clay gouge
27	85 NE	North side up	0.5" clay gouge
34.5	77 NE	n/a	3" wide cc cemented clay gouge
16.5	90	n/a	2.5" wide
20.5	72 SW	n/a	3 splays
20.5	90	n/a	3 splays
20.5	65 SW	n/a	3 splays
28	90	North side up	2" thick anastomosing splays of clay gouge
31.5	69 NW	Normal displacement	1/8 " thick clay gouge
32.5	12 NE	North side up	Laminae

Greyed out rows have been discounted from the data due to demonstrating either normal displacement, dipping southwards, being labelled as minor splays, or having anomalously low dip angles. All data is taken from an unpublished geo-technical report (Earth Systems Southern California, 2013).

Table ST4 Comparison of output ages calculated using various reference calibration production rates and densities

Surface	Age (4.24 atoms g^{-1} yr^{-1}) (ka)*	Age (4.0 atoms g^{-1} yr^{-1}) (ka)+	Age (4.46 atoms g^{-1} yr^{-1}) (ka)**	Age (2.2-2.5 g cm^3) (ka)++
Q4 OC	7.3 +/- 1.8/1.7	7.6 +/- 2.3/1.5	6.8 +/- 1.9/1.4	7.6 +/- 2.3/1.7
Q5 OC	19.3 +/- 2.7	20.2 +/- 2.1/2.9	18.3 +/- 3.2/2.3	26.7 +/- 5.7/4.4
Q6 OC	58.4 +/- 12.7/9.0	63.3 +/- 12.7/10.1	55.6 +/- 12.2/8.4	68.0 +/- 16.8/11.3
Q5 Fold	17.1 +/- 3.5/2.5	18.0 +/- 3.7/2.8	16.6 +/- 3.0/2.6	20.1 +/- 5.2/3.4

** Preferred ages calculated using reference calibration production rate data from Promontory Point, Utah, USA, after Lifton et al., 2015*

+ Ages calculated using reference calibration production rate data from a global dataset after Borchers et al., 2016

*** Ages calculated using reference calibration production rate data from a global dataset after Balco, 2009*

++ All ages calculated using a density of 1.7-1.8 g cm^{-3} except ++ which is calculated using a reference production rate of 4.24 atoms g^{-1} (Lifton et al., 2015) but a higher density of 2.2-2.5 g cm^{-3} after DeVecchio et al 2012.

Table ST5 Comparison of output ages based on zero erosion vs low erosion rates after DeVecchio et al, 2012.

Surface	Age (Zero Erosion) (ka)	Age (0-0.1 cm ka^{-1} erosion) (ka)
Q4 BC	6.8 +/- 1.9/1.4	6.8* +/- 1.9/1.4
Q5 OC	18.3 +/- 3.2/2.3	18.5* +/- 3.1/2.5
Q5 Fold	16.6 +/- 3.0/2.6	16.5* +/- 3.2//2.5
Q6 TC	55.6 +/- 12.2/8.4	56.6+ +/- 12.3/8.8

Ages calculated using a reference production rate of 4.46 atoms g^{-1}

** Calculated incorporating a maximum total erosion of 10 cm to reflect current bar and swale morphology*

+ Calculated incorporating a maximum total erosion of 20 cm to reflect greater amount of

Table ST6 Comparison of output slip rates from Monte Carlo simulations using various fault dips

Age (ka)				Fault Dip (°)	Slip Rate (mm yr^{-1})			Fault dip PDF
Q4	7.3	+/-	1.8/1.7	50-90	1.3	+/-	0.5/0.3	Trapezoidal
Q5	19.3	+/-	2.7	50-90	1.7	+/-	0.6/0.2	Trapezoidal
Q4	6.8	+/-	1.9/1.4	50-90	1.4	+/-	0.5/0.3	Trapezoidal
Q5	18.3	+/-	3.2/2.3	50-90	1.8	+/-	0.5/0.3	Trapezoidal
Q4	6.8	+/-	1.9/1.4	40-65	1.7	+/-	0.7/0.5	Boxcar
Q5	18.3	+/-	3.2/2.3	40-65	2.2	+/-	1.0/0.4	Boxcar
Q4	6.8	+/-	1.9/1.4	20-80	1.5	+/-	2.8/0.3	Boxcar
Q5	18.3	+/-	3.2/2.3	20-80	1.9	+/-	4.4/0.3	Boxcar
Q4	6.8	+/-	1.9/1.4	20-65	1.7	+/-	4.4/1.3	Boxcar
Q5	18.3	+/-	3.2/2.3	20-65	2.1	+/-	4.4/0.3	Boxcar

Rates in grey are preferred ages and preferred rates.

Boxcar probability density function (PDF) assumes equal probability for all values within the range.

Trapezoidal PDF assumes an equal probability of fault dip between 60-80° with probability decreasing to zero at 50° and 90°.

Appendix B: Supplementary materials to Chapter 3

B1 Fault construction

Faults are constructed for use in *Coulomb 3.4* following the methodology outlined in Mildon et al 2016. Fault surface traces are drawn in Google Earth™ and a fault projection direction is selected perpendicular to the mean fault strike to create a 3D fault plane. Full details of modelled fault parameters including average fault strike, fault dip, and projection direction are included in Table S2. We use a depth to the seismogenic zone of 17 km, based on the deepest recorded seismicity on the San Cayetano fault, and project the fault planes to 17 km depth (Yerkes and Lee, 1979). A rake of 90° appropriate for reverse faults is assigned to the faults (Aki and Richards, 1980). Faults throughout the Ventura basin are thought to contain a component of oblique slip (Nicholson et al., 2007; Marshall et al., 2008), however, because the exact component of oblique slip is poorly characterized we model slip as purely reverse. Fault planes are modelled using 1 km rectangular elements. Different element size affects the resolution of the calculated stress field output from modelling (Lin and Stein, 2004; Toda et al., 2005), but a 1 km size is selected to obtain sufficiently high resolution whilst minimizing computational time.

Table S 3 *Additional well data for fault cuts with medium and low confidence*

Well Name	Well No [a]	API	Latitude (°) [b]	Longitude (°) [b]	Evidence	Fault Depth (m [c])	Data Source	Notes and confidence level	Cross Section [d]
McCloskey 2	7	11105512	34.421722	-119.065223	*Suggested fault zone on core log at 1580 m just below spike in resistivity log.*	1580	This study	Moderate (could be represent Sisar fault)	n/a
Loel Maxwell 1	9	11104107	34.427402	-119.012906	*Core dips 60–90° throughout but 45° at 1470 m*	1470*	This study	Low	n/a
Loel Maxwell 3	10	11106048	34.422668	-118.989439	*Shattered core with multiple slickensides noted in core log.*	1550*	This study	Low	n/a
Thorpe 81–30	28	11106066	34.406706	-119.008792	*n/a*	n/a	This study	No evidence; No dip-meter data and only sporadic core data	n/a
Ex Mission X12	11	11102390	34.410069	-119.088399	*Core dips 40–55° throughout log but drop to 15–30° between 715–1600*	714-1600*	This study	Low	n/a
Ex Mission 2	12	11120629	34.410889	-119.093961	*Subtle change in dip-meter data from 45–50°S to 65–75° at 1725 m.*	1725	Hopps et al (1992)	Low	C-C'
Adams 48	15	11120810	34.410846	-119.104841	*Decrease in unprotected dip-meter data from ~70° to ~40° at 1175 m.*	1175*	This study	Low; probably too shallow for SSCF	n/a
Ex mission X4	16	11102377	34.398022	-119.142536	*Gouge zone with variable dips noted in core logs at 1300 m, which corresponds to subtle variation in dip-meter data*	1300	This study, Hopps et al (1992)	Moderate	D-D'
Ex mission X5	17	11102385	34.391794	-119.158113	*Core dips from 30–40° throughout log but decrease to 20–30 at bottom of log at 1320 m.*	1320	This study	Low	n/a
Ex mission X14	18	11120035	34.35284	-119.101001	*n/a*	~300	This study, Hopps et al (1992)	Dip data too deep to evidence fault	D-D'
Ex mission X17	19	11120275	34.359636	-119.10312	*n/a*	400–500	This study, Hopps et al (1992)	Dip data too deep to evidence fault	D-D'
Ex mission X3	20	11105922	34.352067	-119.167092	*Fault planes and/or gouge zones noted a in core logs at 1400, and 1580 m.*	n/a	This study	No evidence; gouge zones and fault planes too deep for SSCF in this location	n/a
Ex mission X10	21	11105925	34.35688	-119.18584	*Increase in dip-meter data from 20 °S at 700 m to 50°S at 990 m.*	n/a	This study, Hopps et al (1992)	Low; interpreted as an unconformity in Hopps et al (1992)	n/a
Ex mission X7	22	11102386	34.388888	-119.192512	*Fractures noted on core log at 2075 m with spike in R at 2050 m. Dipmeter*	n/a	This study, Hopps et al (1992)	Low	n/a

					consistent throughout.				
Willoughby 1	23	11120365	34.381758	-119.201149	*n/a*	n/a	This study	No evidence	n/a
ACL 1	24	11100511	34.382493	-119.234515	*n/a*	n/a	This study	No evidence	n/a
ACL 2	25	11100512	34.381265	-119.235369	*n/a*	n/a	This study	No evidence	n/a
Good ACL 1	26	11105935	34.370525	-119.25202	*n/a*	n/a	This study	No evidence	n/a
Canet 1	27	11105939	34.360451	-119.251238	*n/a*	n/a	This study	No evidence	n/a

a: Well No refers to location on map in Figure 2 and is also noted in Figures 3, 4, & 5 (if applicable)

b: Latitude and longitude refer to the surface location of the well. The actual location of the fault evidence may be away from this location if the well has significant drift

c: Fault depth in meters below sea level

d: See Figures 5 and 6 for cross sections

** Indicates that well depth has not been corrected for well drift and true depth may be less than indicated*

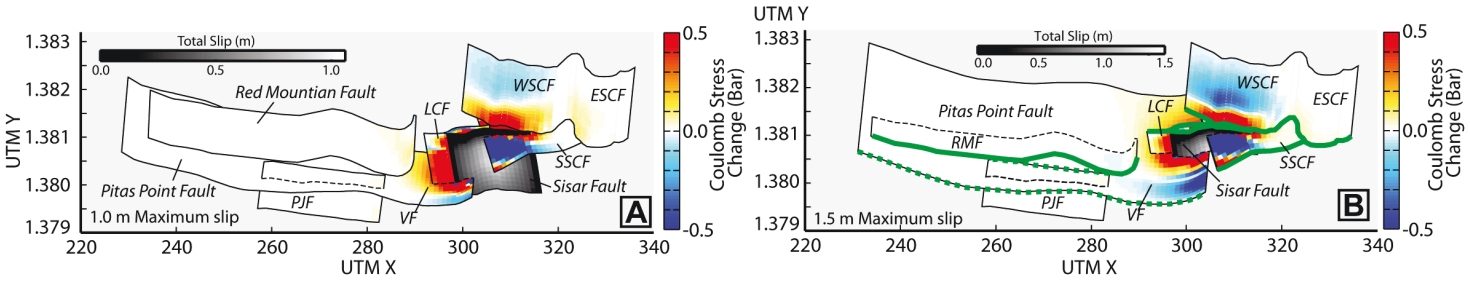

Figure S0-1 Stress imparted on faults resulting from ruptures in on the Sisar fault in the 'no-flat' model (A) and the 'ramp-flat' model (B)

Table S2 Fault model construction parameters

Fault	Dip profile*	Average strike (°)	Projection direction (°)
Pitas Point (n-f)	50° to 5.25 km, 40° to 7.0 km, 30° to 9.0 km, 42° to 10 km, 50° to 17 km	275	005
Ventura (n-f)	60° to 6 km, 50° to 12 km, 60° to 17 km	277	007
Entire Pitas Point/Ventura (r-f)	50° to 6 km, 25° to 6.5 km, 06° to 7.5 km, 25° to 8.0 km, 35° to 17 km	276	006
Eastern San Cayetano	25° to 1.0 km, 40° to 1.6 km, 50° to 17 km	278	006
Western San Cayetano	40° to 1.0 km, 45° to 1.6 km, 50° to 17 km	274	006
Southern San Cayetano	15° to WSCF	253	343
Red Mountain (n-f)	60° to 17 km	263	003
Red Mountain (r-f)	60° to PPVF	263	003
Sisar (n-f)	60° to 6.0 km, 30° to 6.5 km, 10° to 7 km, 03° to 7.3 km	080	170
Sisar (r-f)	60° to 6.0 km, 30° to 7 km	080	170
Lion Canyon (r-f)	60° to 6.0 km, 30° to 7 km	080	170
Lion Canyon (n-f)	60° to 6.0 km, 30° to 6.5 km, 10° to 7 km,	080	170

	03° to 7.3 km		
Padre Juan	40° to 3.0 km, 60° to 6.3 km, 30° to 6.9 km, 10° to 7.0 km, 03° to 7.15 km	098	188

** Degrees from horizontal and distance is depth below 0*

(r-f): 'Ramp-flat model, (n-f): 'no flat' model

All faults have a rake of 90

ESCF and WSCF are projected in same direction to minimize overlap between separate faults at depth

WSCF = Western San Cayetano fault, PPVF = Pitas Point/Ventura fault

Appendix C: Supplementary Materials to Chapter 4

C1. Cosmogenic nuclide measurement techniques: background and sampling methods

This study incorporates ^{26}Al–^{10}Be isochron burial dating, cosmogenic ^{10}Be derived erosion rates, and ^{10}Be surface exposure dating. All three techniques are based on the same basic physics where rocks and soils near the Earth's surface accumulate terrestrial cosmogenic nuclides (TCN) by nuclear spallation reactions via the interaction of cosmic rays from space with minerals contained in rocks or soils (Lal, 1991; Lal and Peters, 1967). In this study, we focus on the nuclides ^{10}Be and ^{26}Al, which are formed by the interaction of cosmic rays with ^{16}O and ^{28}Si in quartz (Lal, 1988). The penetration of cosmogenic ray-derived secondary neutrons, and the production rate of spallation-induced cosmogenic nuclides decreases exponentially with depth to approximately 2–3 m below the surface (depending on material density), and the concentration of cosmogenic nuclides in a sample should reflects the time the sample has spent within the zone of production. Using this basic theory, different sampling strategies and methods of data reduction can be applied to calculate burial or exposure ages, or to quantify rates of erosion.

C1.1 Isochron burial dating on the Saugus Formation: background

Isochron burial dating is a key tool for dating late Quaternary sediments and can be applied to a wide range of terrestrial and marine deposits (e.g. Balco and Rovey, 2008; Balco et al., 2013; Bender et al., 2016; Çiner et al., 2015; Erlanger et al., 2012). Once a deposit is buried to a depth below the penetration zone depth of cosmic rays, cosmogenic nuclide production will cease, and the nuclide concentration becomes primarily a function of radioactive decay, which occurs at a rate dependent on the radioactive half-life of the specific cosmogenic nuclide. The currently-accepted value for the half-life of 10Be is currently measured at 1.387 +/- 0.012 x 106 yr^{-1} (Chmeleff et al., 2010) and for ^{26}Al the half-life is 0.708 +/- 0.017 x 106 yr^{-1} (Nishiizumi, 2004). The respective half-lives of ^{10}Be and ^{26}Al define an ideal age range for cosmogenic isotope isochron burial dating between ~0.2–5 Ma, although this figure range is dependent upon initial nuclide concentrations within the samples prior to deposition. The Saugus

Formation is an ideal target for isochron burial dating because the formation has an estimated age of between 0.2–2.3 Ma (Levi and Yeats, 1993; Wehmiller et al., 1978). Additionally, the provenance for much of the Saugus Formation is the San Gabriel Mountains or the Topatopa Mountains (Levi and Yeats, 1993), which is composed of igneous and metamorphic rocks or Tertiary sandstones, respectively, that provides abundant quartz, as required for the measurement of ^{10}Be and ^{26}Al (Campbell et al., 2014).

Simple burial dating assumes minimal post-burial production has affected a single sample, which limits the application to very specific settings such as cave deposits (Granger and Muzikar, 2001). The advantage of the isochron burial dating method is that post-burial production is treated as a constant that can be empirically measured by analysing a suite of multiple, therefore, samples with the same burial age, but varying pre-depositional exposure and erosion histories can be analysed simultaneously (Balco and Rovey, 2008). Several assumptions are required to use isochron burial dating. Firstly, the period of exposure prior to deposition in the current deposit should be short enough that no significant radioactive decay occurred during transportation. The ~3600 m thick succession of Saugus sediments within the central Ventura basin, all of which are thought to be Pleistocene in age, suggests high sedimentation rates and associated rapid erosion rates (Yeats, 1977; Yeats, 1988). High sedimentation rates suggest that the Saugus Formation was transported and deposited rapidly, and that minimal decay will have occurred prior to deposition.

A second assumption is that all clasts should share the same post-burial history and, therefore, post-burial nuclide production can be treated as a constant. Sampling from the same depth horizon (within +/- 30 cm) addresses this issue because it ensures that although all clasts likely have different prior depositional and erosional histories, they should all share the same post-burial history. Additionally, samples must have been rapidly buried to a depth below the cosmogenic nuclide production zone to ensure that post-burial production by neutron spallation does not overprint the signal of post-burial decay. Sampling from a depth of > 2 m from the surface increases the probability that post-burial production by neutron spallation does not overprint the decay signal (Balco and Rovey, 2008).

C1.2 Exposure dating using boulder sampling; background and sampling strategy

Total cosmogenic nuclide (TCN) exposure ages for surface clasts, including boulders, is a well-established technique for dating various Pleistocene sedimentary landforms such as glacial surfaces (Rood et al., 2011a; e.g. Corbett et al., 2016a; Wesnousky et al., 2016) or alluvial fans (e.g. Frankel et al., 2007a; Behr et al., 2010; Owen et al., 2014). Post-depositional exhumation of a clast from the subsurface by the erosion of surrounding material can affect the measured nuclide concentration within a boulder and, consequently, the apparent age. Specifically, if a boulder has been exhumed, then the production rate will have varied through time as the amount of shielding from the surrounding soils decreased. Consequently, an exhumed boulder will give an apparent age that will underestimate the true age for the deposit and surface (Behr et al., 2010; Heyman et al., 2016). Moreover, significant erosion of the outer surface of a boulder can reduce measured nuclide concentrations and will yield apparent exposure ages that will underestimate the true exposure age, which would be measured from an uneroded boulder (Rood et al., 2011a; DeVecchio et al., 2012a). In contrast, a large inherited nuclide concentration can artificially increase the apparent exposure age of the boulder surface.

The upper 2–5 cm of the tops of each boulder were sampled from the centre of flat topped boulders to reduce the effects of fire spallation (Bierman and Gillespie, 1991) and uncertainties relating to surface geometry (Nishiizumi et al., 1989). Where possible, anomalously fresh, unweathered boulder surfaces with minimal case-hardening or polishing or a low surface relief that suggested recent material loss were avoided because erosion of the outer surface decreases the apparent age of the boulder and underestimates the age of deposition. The latitude, longitude, and elevation of each boulder was measured using a handheld GPS and topographic shielding was measured at each boulder using a clinometer and compass.

C1.3 ^{10}Be catchment-averaged erosion rates background and sampling

Sediment stored in an actively eroding landscape accumulates cosmogenic nuclides (including ^{10}Be) as it passes upwards through the production zone of cosmogenic nuclides before being eroded from the

hillslope, transported, and deposited in an active channel. In eroding landscapes, where both nuclide production during transportation and radioactive decay can be ignored and sediment is well mixed, the concentration of ^{10}Be within a sand sample from an active fluvial channel is proportional to the catchment-averaged ^{10}Be production rate and is inversely proportional to the spatially averaged erosion rate (Lal, 1991; Bierman and Steig, 1996; Granger et al., 1996). Consequently, rapidly eroding catchments will have low nuclide concentrations and slowly eroding catchments will have high nuclide concentrations.

The relationship between nuclide concentration and spatially averaged erosion rates depends upon an approximately uniform and evenly distributed upstream lithology to ensure that the supply of quartz to the catchment is evenly sourced (Bierman and Steig, 1996). Variations in grain sizes are observed within individual catchments within the Ventura basin but not significant changes in lithology, such as changes from sediments to igneous or metamorphic rocks. Accordingly, we assume that quartz is sourced evenly from throughout the catchments in the study area and that the sediment is well-mixed and homogenized during transport.

An additional assumption when deriving catchment-averaged erosion rates is that catchments are in isotopic equilibrium where the ingoing and outgoing isotope (or sediment) fluxes are equal (Bierman and Steig, 1996). Perturbations in the ratio of ingoing and outgoing isotope flux can arise in areas with high density, deep-seated landslides that mobilize nuclide-depleted sediments from beneath the nuclide production zone (Niemi et al., 2005; Yanites et al., 2009; Roda-Boluda et al., 2019). TCN catchment-averaged erosion rates can still be a true reflection of the average erosion signal if landslides are a significant contributor to the erosion signal in small (<100 km^2) catchments with frequent, shallow (< 2m), low-volume landslides (Niemi et al., 2005; Yanites et al., 2009; Roda-Boluda et al., 2019).

C1.3.1 Erosion rates calculated using the CAIRN method

The Catchment-Averaged Denudation Rates from Cosmogenic Nuclides (CAIRN) software calculates easily reproducible erosion rates and facilitates the incorporation of both internal and external uncertainties to the final catchment wide erosion rate (Mudd et al., 2016). CAIRN calculates erosion

rates using topographic shielding and nuclide production on a pixel-by-pixel basis. Each pixel's output value for production and shielding is used to calculate an expected nuclide concentration for the catchment, assuming that erosion is constant throughout the catchment. CAIRN then uses Newton iteration to calculate the erosion rate that best matches the predicted nuclide concentration (Mudd et al., 2016). Catchment wide erosion rates were calculated using a digital elevation model extracted from 30 m Shuttle Radar Topography Mission (SRTM) data. For the shielding and production rate calculations step values for zenith (Φ) and azimuth (θ) were 10° and 15°, respectively. These were selected to maintain a high degree of accuracy whilst reducing computational time. CAIRN propagates uncertainties in ^{10}Be concertation, ^{10}Be production rate, and muon production in quadrature to record a 1σ uncertainty following the method of Balco (2008).

C2. Laboratory analysis and accelerator mass spectrometry details

C2.1 Laboratory analysis

Beryllium and aluminium isolation followed the methodology of Corbett et al (2016). Firstly, an in house ^{9}Be carrier spike produced from Beryl was added to samples. For burial dating samples a commercial SPEX aluminium carrier was also added to the samples. For samples processed at the University of Vermont (UVM), Burlington, ten samples were processed alongside a blank to account for laboratory background contamination and a sample of the CRONUS-N sand (Jull et al., 2015) to assess inter-laboratory uncertainties in results. Samples processed at Imperial College London (ICL) were processed in batches of nine alongside one process blank. Prior to dissolution and isotope separation, quartz aliquots were tested for purity using an inductively coupled plasma-optical emission spectrometer (ICP-OES). Pure quartz was dissolved in concentrated HF before being converted into chloride form by fuming in $HClO_4$ and drying down in HCl. Be and, if appropriate, Al were isolated in the samples using ion exchange chromatography. Anion exchange with HCl was employed to remove Fe from the samples prior to cation exchange, firstly with H_2SO_4 and secondly with HCl to isolate Be and Al. Be and Al in solution was precipitated as a beryllium or aluminium hydroxide gel which is

either burnt using a Bunsen burner or heated in a furnace to produce beryllium or aluminium oxide. Be a Beryllium oxide was mixed with Nb powder and Al as aluminium oxide was mixed with Ag powder and transferred into copper cathodes ready for analysis using accelerator mass spectrometry.

C2.2 Accelerator mass spectrometry details

Accelerator mass spectrometry (AMS) analysis for sample suites HCR, SLC, OCS, SI5 and BCB took place at the Centre for Accelerator Science at the Australian Nuclear Science and Technology Organization (ANSTO). Be standard 01-5-2 with an assumed $^{10}Be/^{9}Be$ ratio of 8.558×10^{-12} (Nishiizumi et al., 2007) was used to calibrate $^{10}Be/^{9}Be$ ratios measured in the samples. Measured $^{26}Al/^{27}Al$ ratios for the burial dating samples were calibrated against Al standard KN 01-4-2 with a nominal $^{26}Al/^{27}Al$ ratio of 3.096×10^{-11} (Nishiizumi, 2004). For sample suites HCR, SLC, OCS, and BCB, during $^{10}Be/^{9}Be$ AMS measurements at BeO^- ion beam currents were 1.2–8.0 μA for the samples and 2.9-9.7 μA for the standards. The average BeO^- ion beam current for the samples was 59% of the average beam current for the primary standard. 1σ analytical uncertainties with the AMS measurements for the samples ranged from 3–12%. Boron corrections were <1%. During $^{26}Al/^{27}Al$ AMS measurements at Al^- ion beam currents were 0.2–0.6 μA for the samples and 0.3-0.7 μA for the standards. The average Al^- ion beam current for the samples was 77 % of the average beam current for the primary standard. 1σ analytical uncertainties associated with the AMS measurements for the samples ranged from 4–29 %.

Sample suites HCR, SLC, and OCS were blank corrected for Be using the average of three associated process blanks with measured $^{10}Be/^{9}Be$ AMS ratios of 5.56×10^{-16}, 6.93×10^{-16}, and 5.87×10^{-16}. Total ^{10}Be atoms in each of the three blanks processed alongside these samples was 9190 +/- 2200 atoms, 11180 +/- 2400 atoms, and 9150 +/- 2600 atoms and the average values used for the blank correction was 9970 +/- 1000 atoms. The range in 1σ analytical uncertainties for measurement of ^{10}Be concentrations was 3–116 %. Sample suites HCR, SLC, and OCS were blank corrected for Al using the average of four associated process blanks with measured $^{26}Al/^{27}Al$ AMS ratios of 1.31×10^{-15}, 9.74×10^{-16}, 9.27×10^{-16}, and 1.31×10^{-15}. Total ^{26}Al atoms in each of the four blanks processed alongside these samples was 76200 +/- 34100 atoms, 52948 +/- 37440 atoms, 50430 +/- 50440, and 72070 +/-

41620 atoms and the average values used for the blank correction was 62720 +/- 10070 atoms. The range in 1σ analytical uncertainties for measurement of ^{26}Al was 4–42 %.

Sample suite BCB was the boulder samples, which were blank corrected using the concentration of the process blank that was processed alongside the specific sample. Measured $^{10}Be/^{9}Be$ AMS ratio for these two process blanks were 7.50 x 10^{-16} and 6.62 x 10^{-16}. Total ^{10}Be atoms in these two blanks processed alongside these samples was 12110 +/- 4030 atoms and 10700 +/- 3100 atoms. The range in 1σ analytical uncertainties for measurement of $^{10}Be/^{9}Be$ was 3–4 %.

Sample suite SI5 during $^{10}Be/^{9}Be$ AMS measurements at BeO^- ion beam currents were 3.8–5.4 μA for the samples. 1σ analytical uncertainties with the AMS measurements for the samples ranged from 5–11%. Boron corrections were <1%. During $^{26}Al/^{27}Al$ AMS measurements at Al^- ion beam currents were 0.3–0.5 μA for the samples. 1σ analytical uncertainties associated with the AMS measurements for the samples ranged from 16–27 %. Sample suite SI5 was blank corrected for Be and Al using the concentration of the process blank that was processed alongside the specific sample. The measured $^{10}Be/^{9}Be$ AMS ratio for the Be blank was 1.29 x 10^{-15}. Total ^{10}Be atoms in the blank was 22489 +/- 2726 atoms. The range in 1σ analytical uncertainties for measurement of $^{10}Be/^{9}Be$ was 6–27 %. The measured $^{26}Al/^{27}Al$ AMS ratio for the Al blank was 1.21 x 10^{-15}. Total ^{126}Al atoms in the blank was 72572 +/- 36293 atoms. The range in 1σ analytical uncertainties for measurement of $^{26}Al/^{27}Al$ was 23–73 %.

Accelerator mass spectrometry (AMS) analysis for sample suites SGR, SVF, TP, SCQ, STL took place at the Scottish Universities Environmental Research Centre (SUERC). Measured $^{10}Be/^{9}Be$ ratios were calibrated using Be standard 01-5-4 with an assumed Be ratio of 2.851 x 10^{-12} (Nishiizumi et al., 2007) and $^{26}Al/^{27}Al$ ratios were calibrated using standard KN 01-4-3 with a nominal $^{26}Al/^{27}Al$ ratio of 4.110 x 10^{-11} (Nishiizumi, 2004). For sample suite STL, the average BeO^- ion beam current for the samples was 54% of the average beam current for the primary standard. 1σ analytical uncertainties with the AMS measurements for the samples ranged from 3–10%. During $^{26}Al/^{27}Al$ AMS measurements the average Al^- ion beam current for the samples was 69 % of the average beam current for the primary standard. 1σ analytical uncertainties associated with the AMS measurements for the samples ranged from 3–15 %. Sample suites STL was blank corrected for Be using the average of two associated process blanks

with measured $^{10}Be/^{9}Be$ AMS ratios of 2.73 x 10^{-15} and 3.12 x 10^{-15}. Total ^{10}Be atoms in each of the two blanks processed alongside these samples was 46366 +/- 7425 atoms and 40645 +/- 6075 atoms and the average values used for the blank correction was 43510 +/- 6751 atoms. The range in 1σ analytical uncertainties for measurement of ^{10}Be concentrations was 4–15 %. Sample suites STL was blank corrected for Al using the average of two associated process blanks with measured $^{26}Al/^{27}Al$ AMS ratios of 6.30 x 10^{-16} and 3.07 x 10^{-16}. Total ^{26}Al atoms in each of the two blanks processed alongside these samples was 27755 +/- 19627 atoms and 13254 +/- 13253 atoms and the average values used for the blank correction was 62720 +/- 10070 atoms. The range in 1σ analytical uncertainties for measurement of ^{26}Al was 9–17 %.

For sample suites SGR, SVF, TP, SCQ, the average BeO^- ion beam current for the samples was 53 % of the average beam current for the primary standard. 1σ analytical uncertainties with the AMS measurements for the samples ranged from 3–6%. During $^{26}Al/^{27}Al$ AMS measurements the average Al^- ion beam current for the samples was 87 % of the average beam current for the primary standard. 1σ analytical uncertainties associated with the AMS measurements for the samples ranged from 3–7 %. Sample suites SGR, SVF, TP, SCQ were blank corrected for Be using the specific process blank measured with the samples. For STP and SGR the measured $^{10}Be/^{9}Be$ AMS ratio for the process blank was 2.13 x 10^{-15} and for SVF and SCQ the measured $^{10}Be/^{9}Be$ AMS ratio for the process blank was 1.97 x 10^{-15}. Total ^{10}Be atoms in each of the two blanks processed alongside these samples was 27114 +/- 3906 atoms for sample suites SVF and SCQ, and 29245 +/- 8120 atoms for sample suites STP and SGR. The range in 1σ analytical uncertainties for measurement of ^{10}Be concentrations for these four samples was 3–25 %. Sample suites SGR, SVF, TP, SCQ were blank corrected for Al using the specific process blank measured with the samples. For STP and SGR the measured $^{26}Al/^{27}Al$ AMS ratio for the process blank was 1.56 x 10^{-15} and for SVF and SCQ the measured $^{26}Al/^{27}Al$ AMS ratio for the process blank was 8.35 x 10^{-16}. Total ^{26}Al atoms in each of the two blanks processed alongside these samples was 36414 +/- 21018 atoms for sample suites SVF and SCQ, and 65073 +/- 26582 atoms for sample suites STP and SGR. The range in 1σ analytical uncertainties for measurement of ^{26}Al concentrations for these four samples was 3–19 %.

AMS ratios for the erosion rate samples were measured at Lawrence Livermore National Laboratory AMS facility and were calibrated using Be standard 01-5-4 with an assumed $^{10}Be/^{9}Be$ ratio of 2.851 x 10^{-12} (Nishiizumi et al., 2007). During $^{10}Be/^{9}Be$ AMS measurements at BeO^- ion beam currents were 12–22 μA for the samples. 1σ analytical uncertainties with the AMS measurements for the samples ranged from 2–22%. The erosion rate samples were blank corrected for Be using the process blank processed alongside the sample in the laboratory with measured $^{10}Be/^{9}Be$ AMS ratios of 1.82 x 10^{-15} and 1.83 x 10^{-15}. Total ^{10}Be atoms in each of these blanks was 30933 +/- 4391 atoms and 31126 +/- 4227 atoms. The range in 1σ analytical uncertainties for measurement of ^{10}Be concentrations was 2–32 %.

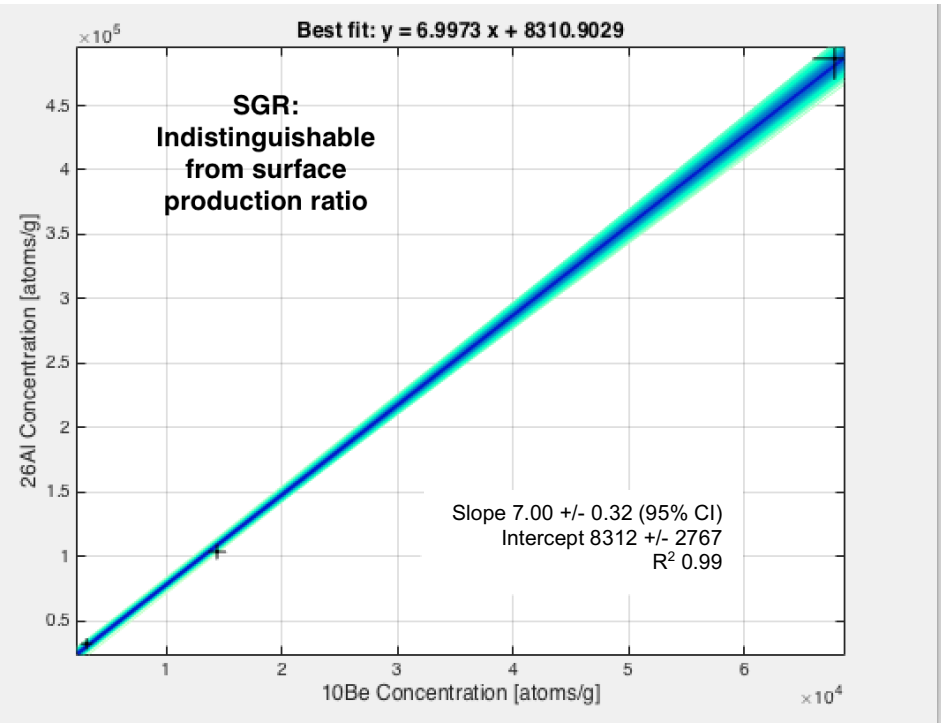

Figure CS1 *^{26}Al-^{10}Be isochron results for sediment samples from the modern San Gabriel river used to confirm production ratio for $^{26}Al/^{10}Be$ of 6.75 in the study area. The slope of 7.00 +/- 0.32 is indistinguishable from the assumed surface production ratio of 6.75 within 95 % confidence limits. Individual samples with 1σ error (crosses) and range of Bayesian linear regression fits (blue and green).* CI = Confidence interval

C3. Published cross sections used for fault offsets

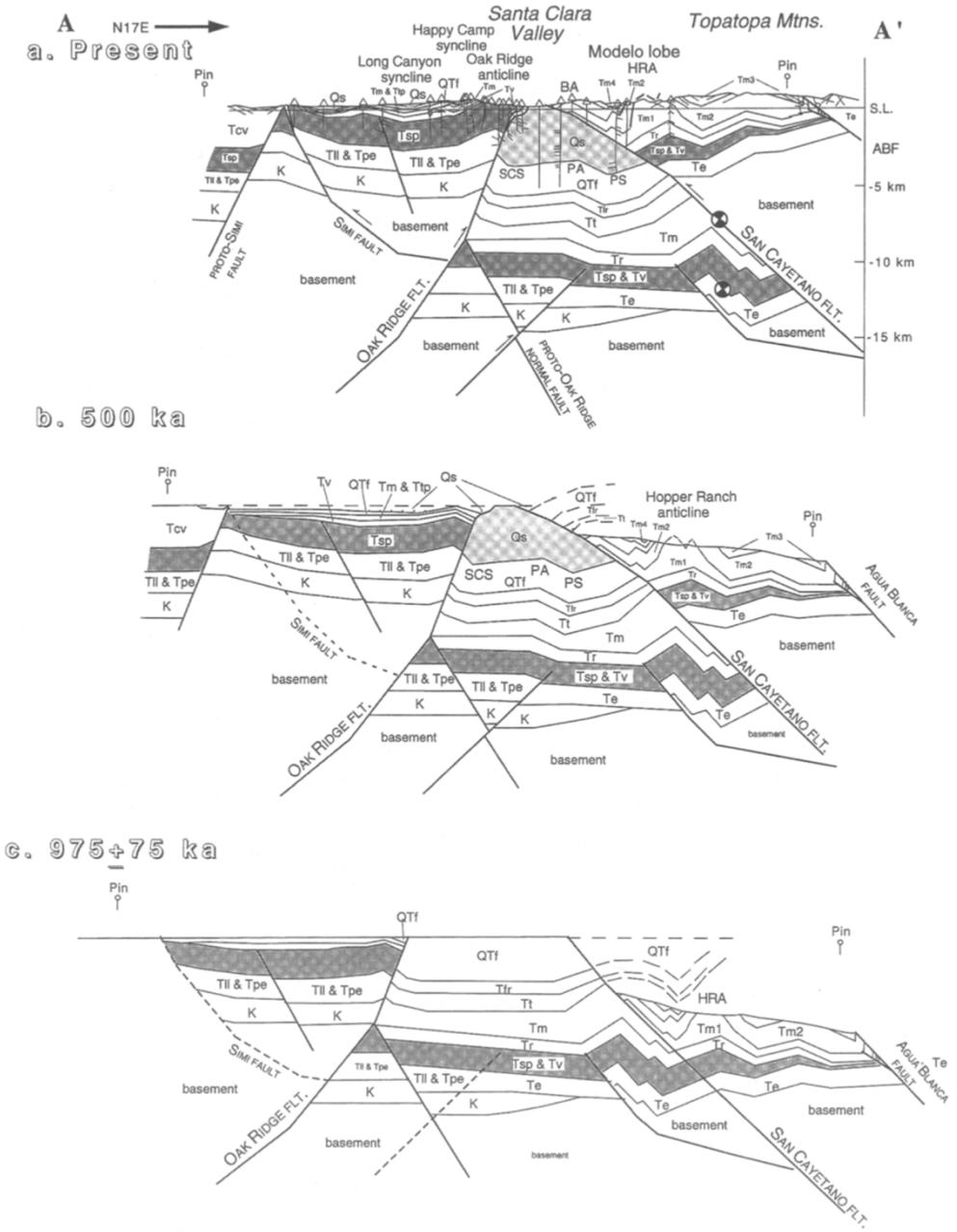

Figure CS2 *Cross sections through the Happy Camp Syncline from Huftile and Yeats (1996) used to measure dip-slip displacement for slip rates for the Oak Ridge and San Cayetano faults. Cross sections were initially retro-deformed to 500 ka and 975 ka by Huftile and Yeats (1996) but these ages were recalculated here using isochron burial ages for the Saugus Formation from of 950 ka (initially 500 ka) and from 1540 ka (initially 975 ka). See Huftile and Yeats (1996) for stratigraphic units and lines of section.*